Master Thesis of Science

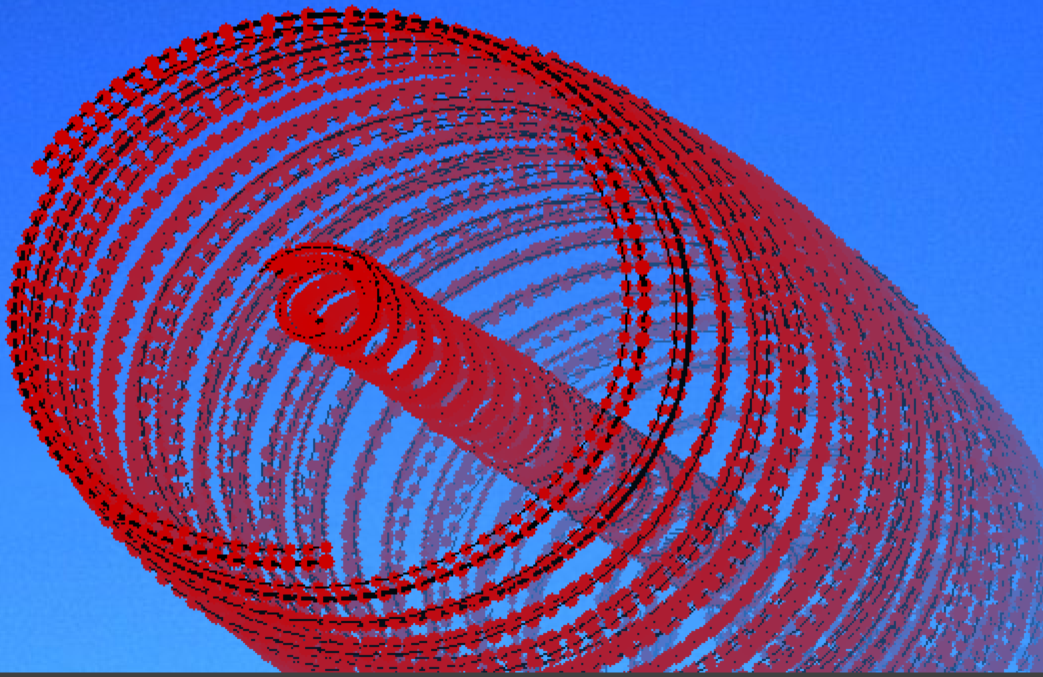

3D Lagrangian VPM-FMM for Modelling the Near-Wake of a HAWT

The development of a stable, accurate, and efficient numerical solver for large-scale wind energy purposes

T.J. Berdowski

May 07, 2015

European Wind Energy Master - EWEM- Rotordesign Track

3D Lagrangian VPM-FMM for Modelling the Near-Wake of a HAWT

The development of a stable, accurate, and efficient numerical solver for large-scale wind energy purposes

MASTER OF SCIENCE THESIS

For obtaining the degree of Master of Science in Engineering Wind Energy at Technical University of Denmark and in Aerospace Engineering at Delft University of Technology.

T.J. Berdowski

May 07, 2015

European Wind Energy Master - EWEM

Copyright © T.J. Berdowski
All rights reserved.

European Wind Energy Master - EWEM
Of
Rotordesign Track

The undersigned hereby certify that they have read and recommend to the European Wind Energy Master - EWEM for acceptance a thesis entitled **“3D Lagrangian VPM-FMM for Modelling the Near-Wake of a HAWT”** by **T.J. Berdowski** in partial fulfillment of the requirements for the degree of **Master of Science**.

Dated: May 07, 2015

Supervisor:
Dr.ir. C.J. Simão Ferreira of TU Delft

Supervisor:
Dr.ir. J.H. Walther of DTU Denmark

Reader:
Dr.ir. S. Mayer of DTU Denmark

Reader:
Prof.Dr.Ir. G.A.M. van Kuik of TU Delft

Reader:
Dr.Ir. F. Meng of Fraunhofer IWES

Summary

Traditionally, the design of the Horizontal Axis Wind Turbine (HAWT) has relied on momentum-based methods such as the Blade Element-Momentum (BEM) models. With the growth of computational power, optimization of wind turbines by using Computational Fluid Dynamics (CFD) for the explicit wake modelling is becoming more mainstream. Wake modelling is also conveniently handled by Lagrangian vortex methods, which offer the advantage of auto-adaptivity regarding multi-scale vortical flows and distribution of vorticity in space. The current thesis work focusses on the class of Vortex Particle Methods (VPM) which allows for the efficient treatment of complex wake aerodynamics, especially when the connectivity of vortex filaments plays a significant role, such as with blade-wake interactions and viscous or turbulent diffusion.

The objective of the present thesis work was to develop and demonstrate the capabilities of a Lagrangian, 3D, free-wake VPM for modelling the near-wake of a HAWT. This has been achieved by identifying and applying different numerical approaches of handling the wake convection and diffusion, and to validate these approaches along an actuator disk and 3-bladed turbine configuration of a HAWT.

To this extent, a numerical VPM code has been developed. For mitigation of the computational effort, an existing Fast Multipole Method (FMM) has been modified and implemented. This FMM, along with some other routines regarding distributed memory allocation and parallelization, are part of the Parallel Particle-Mesh (PPM) library [30] which served as the backbone for the current code implementation. The modification of the FMM involved the acquisition of the velocity and vortex stretching terms as partial derivatives of the vector potential.

Investigation of the FMM showed that at least $\mathcal{O}(10^4)$ particles are required in the domain to obtain speedup over a direct calculation in the 3D wake. It was also found that it was computationally more efficient for the presently modified FMM to obtain the velocity and stretching terms through finite differences than through the directly derived expressions from the vector potential.

Simulations have been carried out with an axi-symmetrical actuator disk for a thrust coefficient between $C_t = 4/9 - 8/9$. Comparisons with momentum theory, PIV results [20], and a potential flow model [33] showed an accurate modelling of the axial velocity deficit over the wake. The auto-adaptivity of the VPM was demonstrated through a physically correct modelling of the shear layer. This involved the onset of the Kelvin-Helmholtz instability, the subsequent vortex break-down, and a stabilized but expanding shear layer with the phenomenon of vortex pairing arising. Due to the break-down of the shear layer, the final wake expansion as dictated by momentum theory was not reached. The VPM was also able to simulate highly loaded actuator disks. Results have been obtained between $C_t = 9/9 - 16/9$, for which flow reversal and periodic vortex shedding appeared. The simulations showed a departure from momentum theory and a rough comparison with Glauert's correction for highly loaded rotors.

The investigation with simple vortex geometries indicated that the numerical stability of the VPM forms a major issue. The local divergence of particles often resulted in a break-down of the full simulation (strength vectors diverging and growing to infinite values). Especially critical were flow regions consisting of vortices with sharp curvatures, such as with roll-up structures and entangled filaments, and regions of highly stretched flow with intense rotation. Treatment of divergence and the mitigation of rotation from these critical flow regions were proven to be essential for the success of the 3D wake simulation over time. Especially valuable was the application of a Particle Strength Exchange (PSE) scheme for the viscous diffusion of vorticity out of these distorted regions.

In this context, the 3D near-wake of the MEXICO [22] rotor has been modelled with the VPM, for a tip speed ratio of $\lambda = 6.67$. Stable and accurate simulations have been obtained using PSE with a rotor based Reynolds number of $1.9 \cdot 10^4$, using the FMM and up to about $0.5 - 1.5 \cdot 10^5$ number of particles on a single CPU core. Moreover, relaxation [24] has been applied for the successful treatment of divergence in the root vortex. Comparisons with experimental results of the MEXICO rotor [23] showed a close agreement for the axial and radial velocity profile over the near-wake.

Acknowledgements

I would like to express my gratitude to my supervisors. Carlos, thank you for your support and valuable insights throughout my thesis, and for helping pushing the quality of the work to a higher level. And Jens Walther, I have to thank you for the countless hours that we have spent in your office trying to debug the PPM and (re)checking the lengthy derivations for the FMM.

Gael, thank you for your tremendous effort in helping me setting up the whole project, and for your continuous support throughout the thesis work. Any time I knocked on the door, you would give me as much time as needed to solve the many troubles I had with the code development. Your help has been truly indispensable. Fanzhong, thank you for your supervision at Fraunhofer IWES. The experience and insights obtained during the internship proved to be very valuable for my thesis work. And Johannes, thank you for making time to help me out with understanding the Naga code.

Dieter, I have to thank you especially, for reminding me every now and then that there is more in the world than equations and derivations (although I still tend to disagree). Any time I got stuck, whether it was in life or with my thesis (and life=thesis for me lately), I could count on you. It has been a real pleasure working with you over the course of the Master thesis. Furthermore, I would like to thank Oriol for his precious advice and hospitality in Denmark; Rody and Danuta for the good company in office; Bram for helping me out with the cluster and accompanying me in the UB during the last days of my thesis writing (and also Esmeralda, thank you for offering your photoshop skills); and Lukas, Kumayl, Maarten, and many others for the distraction from my thesis work every now and then.

Last, but certainly not least, I would like to thank my parents for their unconditional support of any kind throughout my academic adventure, the endless patience with my graduation, and the kind hospitality in Delft during the ”laatste loodjes” of my thesis. I guess I also need to apologize for all the times I have been so close at home and yet so far away with my mind at the same time. And Maaike and Max, success with the remainder of your study; I am really looking forward to your thesis presentations!

Contents

Summary v

Acknowledgements vii

List of Figures xviii

List of Tables xix

Nomenclature xxi

1 Introduction 1
- 1.1 Motivation and objective . . . 1
- 1.2 Research questions . . . 2
- 1.3 Research plan . . . 4
- 1.4 State-of-the-art . . . 5
- 1.5 Report outline . . . 6

2 Wake Aerodynamics 9
- 2.1 Actuator Disk and Blade Element Momentum theory . . . 10
- 2.2 Wake aerodynamics of a HAWT . . . 11
  - 2.2.1 Near-wake . . . 11
  - 2.2.2 Far-wake . . . 12
- 2.3 Motivation for the application of a VPM for modelling the wake of a VAWT 13

3 Theory of the 3D Vortex Particle Method 15
- 3.1 Introduction . . . 15
  - 3.1.1 The basis of vortex theory . . . 15
  - 3.1.2 Vorticity described by filament elements . . . 16
  - 3.1.3 The limitations of a filament method . . . 17

3.2 The 3D VPM 18
    3.2.1 The fundamental equations of the vortex particle method 18
    3.2.2 Regularization of the singular particles 19
    3.2.3 Vorticity stretching 21
3.3 Maintaining the divergence-free vorticity field 22
    3.3.1 Relaxation of the particle divergence by Novikov 23
    3.3.2 Relaxation of the particle divergence by Pedrizzetti 23
3.4 Viscous diffusion 24
    3.4.1 The Random Walk Method 24
    3.4.2 Core Spreading Methods 25
    3.4.3 Particle Strength Exchange 25
3.5 Lagrangian grid distortions 26
    3.5.1 Remeshing by particle splitting 26
3.6 Performance parameters 27
    3.6.1 Linear invariants and diagnostics 27
    3.6.2 Quadratic invariants and diagnostics 29
3.7 Conclusions 31

4 The Application of an $\mathcal{O}(N \log N)$ Fast Multipole Method 33
4.1 Summary of the FMM algorithm 33
4.2 Analytical description of the FMM 36
4.3 Derivation of the velocity 40
4.4 Conclusions 41

5 Introduction to the Numerical VPM Code 43
5.1 The Parallel Particle-Mesh (PPM) library 43
5.2 The Fast Multipole Method (FMM) routines 44
5.3 Structure of the VPM program 45

6 Verification and Validation 47
6.1 Single vortex ring 49
    6.1.1 Motivation 49
    6.1.2 Problem statement 49
    6.1.3 Discussion on the ring velocity and overlapping condition by the direct method 50
6.2 Double or leapfrogging rings 52
    6.2.1 Motivation 52
    6.2.2 Problem statement 52
    6.2.3 Verification of the vorticity stretching by the direct method 54
    6.2.4 Verification of the velocity by the FMM using finite differences . . 55
    6.2.5 Verification of the velocity by the FMM using the direct derivative expressions 56

6.2.6 Discussion on the verification of the stretching by the FMM using finite differences . . . 57
6.2.7 Analysis of the computational effort of the FMM . . . 57
6.3 The knot problem of linked vortex rings . . . 61
6.3.1 Motivation . . . 61
6.3.2 Problem Statement . . . 62
6.3.3 Comparison of the knot problem with numerical results from literature 64
6.3.4 Analysis of the results with the classic stretching scheme . . . 66
6.3.5 Analysis of the results with the transpose scheme and divergence relaxation applied . . . 68
6.3.6 Comparison between the classic and transpose scheme regarding the diagnostics . . . 70
6.3.7 Analysis of the results with the PSE scheme applied for mitigation of intensely stretched flow structures . . . 72
6.3.8 Analysis of the results with different core types applied . . . 73
6.4 Actuator disk combined with an analytical model for the far-wake . . . 77
6.4.1 Motivation . . . 77
6.4.2 Problem statement . . . 77
6.4.3 Analysis of the wake and shear layer for $C_t = 8/9$ . . . 78
6.4.4 Analysis of the results for a direct computation versus the FMM . 82
6.4.5 Analysis of the results for different core sizes and overlapping ratios 83
6.4.6 Analysis of results for different thrust coefficients . . . 85
6.5 Simulation of the 3-bladed MEXICO rotor with prescribed circulation . . 88
6.5.1 Motivation . . . 88
6.5.2 Problem statement . . . 88
6.5.3 Qualitative discussion of the wake . . . 89
6.5.4 Comparison between results with and without PSE applied for the classic scheme . . . 90
6.5.5 Analysis of the results with a PSE scheme applied using the transpose scheme . . . 91
6.5.6 Comparison between the numerical and experimental wake . . . 97
6.5.7 Comparison between the numerical and empirical results of the axial and radial velocity . . . 97
6.5.8 Analysis of the computational effort . . . 99

7 Conclusions and Recommendations 101
7.1 Conclusions . . . 101
7.2 Recommendations . . . 104

A Regularized Evolution Equations 109

B Profound Derivation of the Velocity 111

C The Analytical Expressions for a System of Coaxial Vortex Rings 115

D The Analytical Expressions for the Semi-Infinite Circular Vortex Tube 117

E Results over Time for the Knot Problem 119

F Actuator Disk Results over Time for the Betz Limit and Highly Loaded Rotors 121

F.1 Results for $C_t = 8/9$ (Betz limit) 122

F.2 Results for $C_t = 9/9$ 124

F.3 Results for $C_t = 12/9$ 126

F.4 Results for $C_t = 16/9$ 128

G Results over Time for the MEXICO Rotor 131

G.1 Results for the classic scheme 132

G.2 Results for the classic scheme with PSE applied 135

G.3 Results for the classic scheme with the PSE scheme applied using a small time step size 138

G.4 Results for the transpose scheme with PSE applied 141

G.5 Results for the transpose scheme with relaxation and PSE applied 144

List of Figures

2.1 Impression of the actuator disk and BEM theory (Hansen [15]). 11

2.2 A schematic layout of the near and far-wake of a HAWT (Sanderse [28]). . 13

2.3 The motion of a VAWT: (a) Schematic overview of the velocity and force vectors over the rotation (Castelein [3]). (b) Demonstration of the periodic motion of the angle of attack over the rotation for $\lambda = 4.5$ (Ferreira et al. [10]). 14

3.1 (a) Vorticity described by filaments carrying a scalar circulation. Each filament section shares its computational nodes with its direct neighbours, and thus connectivity is maintained implicitly. (b) Vorticity described by particles carrying a vector strength. Connectivity is maintained explicitly as long as the particles remain aligned. 17

4.1 The construction of a quad-tree (or an octa-tree in 3D) takes place by subsequent subdivisions of the parent (or root) box into 4 (or 8) child boxes as long as the number of respective particles in the root box exceeds a threshold. Once this threshold has been reached, the subdivision of the parent box stops, and a child box at the finest subdivision is called a leaf box as shown in green. 34

4.2 For each leaf box, the influence of each individual particle within the box is collected at the center of the box as a multipole expansion (a). Thereafter, the multipole expansions from the 8 child boxes (but depicted as 4 boxes in 2D) at level n are collected at the center of the box of the parent box at level n-1 of the tree, starting from the leafs down to level 2 (b). 35

4.3 Interactions between the multipole expansions around source Q with target point P can take place as long as the ratio of D/d is greater than the acceptance factor θ (a). Figure (b) shows that further away, multipole expansions of boxes lower in the tree can be taken. In the near-field (shown as the box around target point P) the interactions have to be taken directly, though, as the centers of the surrounding boxes are too close to P. 36

4.4 Spherical coordinates centered around the origin are used throughout the analytical description of the FMM, with the angles defined as in (a). The vectors describing the target P, the centers Q_0 and Q_1 of two boxes at different levels in the tree, and a source particle q_i within box Q_0 are shown, along with two vectors describing the distance between Q_1 and P, and Q_0 and Q_1. 39

5.1 Flowchart of the VPM program 46

6.1 A schematic overview of the ring decomposition by particles. Visible are 20 particles with the corresponding strength vector and core radius. The particle spacing h in this example equals two core radii, such that the overlap is $\lambda = \sigma/h = 0.5$. 49

6.2 The error for the velocity as taken at the center of the ring relative to an analytical approximation versus the overlapping ratio. 51

6.3 The front and side view of the initial position of the two vortex rings. The core size, number of particles, and circulation is equal for both rings. . . . 52

6.4 Demonstration of the evolution of the leapfrogging configuration over time 53

6.5 The application of a 3-point central difference stencil in 3 dimensions, results in 7 nodes for the first partial derivatives, and 25 nodes for the second partial derivatives. 54

6.6 The radius of both simulated rings over time compared to the analytical result. 55

6.7 The convergence of the velocity error over the expansion order for a range of acceptance factors, whereby the velocity is taken through finite differences. 56

6.8 The convergence of the velocity error over the expansion order for a range of acceptance factors, whereby the velocity is taken through the direct derivative expressions. 57

6.9 The convergence of the stretching error over the expansion order for a range of acceptance factors, whereby the velocity is taken via the direct derivative expressions and the stretching through finite differences from the velocity partial derivatives. 58

6.10 The computational effort of the FMM normalized to the computational effort of a direct simulation, with a growth rate between $0.52 \sim 0.58$ in computational effort over the expansion order, and a growth rate of about $0.56 \sim 0.65$ in computational effort over the acceptance factor. 58

6.11 Two possibilities of computing the interactions in a box: (a) via direct interactions between the target P and all the individual particles, or (b) between the multipole expansion around the box center Q and target P. . 59

6.12 The front and side view of the initial position of the two vortex rings. The core size, number of particles, and circulation is equal for both rings. . . . 62

6.13 Impression of the knot problem over time. Red indicates regions of filament stretching, and blue regions of compression. The second ring is in a perpendicular plane to the observer. 62

6.14 Demonstration of the phenomenon of blow-up in a simulation. Visible is a single vortex ring subject to some anomalies in the particle alignment. In a short amount of time these anomalies make the whole structure unstable and the simulation ceases to exist. 63

6.15 Impression of the reconnection process, whereby the two rings form one ring through viscous diffusion. The encircled areas show the reconnection points, and the vectors indicate the opposite circulation of the aligned filaments. These are critical regions regarding stability. 63

6.16 The knot problem as simulated by the VPM (frame (a) through (d)) and simulated by Winckelmans and Leonard [37] (frame (e) through (h)). . . . 65

6.17 A comparison of quadratics for the knot problem between the VPM code from this thesis and the numerical results from Winckelmans and Leonard [37]. 66

6.18 Vertically, 4 different cases are shown: (a-c) constant amount of particles, (d-f) particle splitting applied, (g-i) reduction of time step size, (j-l) reduction of both time step size and overlapping ratio. Horizontally, the frames of the last 0.3 seconds before blow-up are visualized. Red indicates a region of stretching, and blue indicates compression. 67

6.19 Vertically, 3 different cases are shown with the transpose scheme applied: (a-c) constant amount of particles, (d-f) particle splitting and relaxation applied, (g-i) reduction of time step size and relaxation increased. Horizontally, the frames of the last instances in time before blow-up are visualized. Red indicates a region of stretching, and blue indicates compression. . . . 69

6.20 The linear and quadratic diagnostics for several cases of the knot problem. 71

6.21 Mitigation of the divergence during stretching with the transpose scheme applied 72

6.22 Vertically, 4 different cases are shown, all with a PSE scheme applied: (a-c) classic scheme with a real (time dependent) core, (d-f) classic scheme with a constant core (vorton), (g-i) transpose scheme with a real (time dependent) core, (j-l) transpose scheme with a constant core (vorton). For the cases with the transpose scheme, a relaxation factor of $f = 0.02$ is applied. Horizontally, for each case 3 images in time are shown. Red indicates a region of stretching, and blue indicates compression. 74

6.23 The linear and quadratic diagnostics for several cases of the knot problem. 76

6.24 The axial velocity contour plot with the particle street projected on top for $C_t = 8/9$ and the semi-infinite vortex tube applied. 79

6.25 The vorticity contour plot with the particle street projected on top for $C_t = 8/9$ and the semi-infinite vortex tube applied. Close-up of the near-wake. 79

6.26 Kelvin-Helmholtz instability of a vortex sheet (Lewis [19]). Sheet modelled by 30 vortex elements of strength $\Delta\Gamma = 1.0$, $\Delta t = 0.001$. 80

6.27 The mean axial velocity contour plot (100 samples) with the particle street projected on top for $C_t = 8/9$ and the semi-infinite vortex tube applied. Close-up of the near-wake. 81

6.28 The mean axial velocity contour plot of the reference experiment (Lignarolo et al. [20]). 81

6.29 The difference in mean axial velocity between figures 6.27 and 6.28. 81

6.30 A comparison between the direct simulation and the simulation with the FMM applied for the centerline velocity over the wake, with $C_t = 8/9$. Note, NS stands for No far-field Stretching applied. 83

6.31 The axial velocity deficit for different axial positions over the wake at $C_t = 8/9$. Comparison between the direct simulation, the FMM, and the FMM with No Stretching (NS) applied. 84

6.32 The axial velocity deficit for different axial positions over the wake at $C_t = 8/9$. Comparison between different overlapping ratios. 84

6.33 The axial velocity deficit for different axial positions over the wake at $C_t = 8/9$. Comparison between different core sizes. 84

6.34 A comparison between different overlapping ratios and core sizes for the centerline velocity over the wake, with $C_t = 8/9$. 85

6.35 The contour map of the axial velocity over a range of thrust coefficients. The semi-infinite vortex tube is only applied for thrust coefficients of $C_t = 8/9$ and lower. 86

6.36 (a) The centerline velocity over the wake for different thrust coefficients. (b) The induction factor versus the thrust coefficient for theoretical, empirical, and simulated results. 87

6.37 The configuration of the MEXICO rotor and the normalized trailing circulation over each blade. Image (a) is borrowed from Micallef et al. [22]. Note, The diameter of the MEXICO turbine is 2.25 [m] with $c_{\max}$ being 0.24 [m]. 88

6.38 A typical illustration of the wake of a HAWT as modelled through the VPM. As the particle vectors are alligned, a representation of the trailing vortex filaments is visible. The thickness is an indication of the circulation strength. 89

6.39 Demonstration of the wake of the 3-bladed MEXICO turbine, simulated by the VPM. The black lines represent the trailing vortices discretized by particle vectors. 90

6.40 The wake with the classic scheme, without PSE applied. Visualization after 9 rotations. 92

6.41 The wake with the classic scheme, with PSE applied. Visualization after 14 rotations. 93

6.42 The wake with the classic scheme, with PSE applied. Visualization after 12 rotations. 94

6.43 The wake with the transpose scheme without relaxation, but with PSE applied. Visualization after 12 rotations. 95

6.44 The wake with the transpose scheme with relaxation ($f = 0.1$) and PSE applied. Visualization after 13 rotations. 96

6.45 Axial velocity of a VPM simulation with the transpose stretching scheme, a numerical core, and the PSE scheme applied. 97

6.46 Axial velocity of a physical 2-bladed turbine, obtained by PIV (Lignarolo et al. [20]). 97

6.47 The axial and radial velocity for different radial positions in the near-wake. The rotor is positioned at $z/D = 0$. The empirical results are borrowed from Nilsson et al. [23] 98

6.48 (a) Impression of the number of particles over the number of turbine rotations. (b) The speedup of the FMM relative to a direct simulation versus the number of particles in the domain. 99

E.1 Demonstration of the time evolution of the knot-problem. 120

F.1 Axial velocity. $C_t = 8/9$. NP stands for Number of Particles, of which 1 particle is shown per shed vortex ring (50 particles per ring). 122

F.2 Continuation of figure F.1. Axial velocity. $C_t = 8/9$. NP stands for Number of Particles, of which 1 particle is shown per shed vortex ring (50 particles per ring). 123

F.3 Axial velocity. $C_t = 9/9$. NP stands for Number of Particles, of which 1 particle is shown per shed vortex ring (50 particles per ring). 124

F.4 Continuation of figure F.3. Axial velocity. $C_t = 9/9$. NP stands for Number of Particles, of which 1 particle is shown per shed vortex ring (50 particles per ring). 125

F.5 Axial velocity. $C_t = 12/9$. NP stands for Number of Particles, of which 1 particle is shown per shed vortex ring (50 particles per ring). 126

F.6 Continuation of figure F.5. Axial velocity. $C_t = 12/9$. NP stands for Number of Particles, of which 1 particle is shown per shed vortex ring (50 particles per ring). 127

F.7 Axial velocity. $C_t = 16/9$. NP stands for Number of Particles, of which 1 particle is shown per shed vortex ring (50 particles per ring). 128

F.8 Continuation of figure F.7. Axial velocity. $C_t = 16/9$. NP stands for Number of Particles, of which 1 particle is shown per shed vortex ring (50 particles per ring). 129

G.1 Filaments. Set-up: classic stretching scheme, $\Delta t = 0.05(s)$. NR and NP stand for Number of Rotations and Number of Particles respectively. . . . 132

G.2 Axial velocity. Set-up: classic stretching scheme, $\Delta t = 0.05(s)$. NR and NP stand for Number of Rotations and Number of Particles respectively. 133

G.3 Vorticity. Set-up: classic stretching scheme, $\Delta t = 0.05(s)$. NR and NP stand for Number of Rotations and Number of Particles respectively. . . . 134

G.4 Filaments. Set-up: classic stretching scheme, $\Delta t = 0.05(s)$, $\nu = 0.0001[m^2/s]$. NR and NP stand for Number of Rotations and Number of Particles respectively. 135

G.5 Axial velocity. Set-up: classic stretching scheme, $\Delta t = 0.05(s)$, $\nu = 0.0001[m^2/s]$. NR and NP stand for Number of Rotations and Number of Particles respectively. 136

G.6 Vorticity. Set-up: classic stretching scheme, $\Delta t = 0.05(s)$, $\nu = 0.0001[m^2/s]$. NR and NP stand for Number of Rotations and Number of Particles respectively. 137

G.7 Filaments. Set-up: classic stretching scheme, $\Delta t = 0.02(s)$, $\nu = 0.0001[m^2/s]$. NR and NP stand for Number of Rotations and Number of Particles respectively. 138

G.8 Axial velocity. Set-up: classic stretching scheme, $\Delta t = 0.02(s)$, $\nu = 0.0001[m^2/s]$. NR and NP stand for Number of Rotations and Number of Particles respectively. 139

G.9 Vorticity. Set-up: classic stretching scheme, $\Delta t = 0.02(s)$, $\nu = 0.0001[m^2/s]$. NR and NP stand for Number of Rotations and Number of Particles respectively. 140

G.10 Filaments. Set-up: transpose stretching scheme, $\Delta t = 0.05(s)$, $\nu = 0.0001[m^2/s]$. NR and NP stand for Number of Rotations and Number of Particles respectively. 141

G.11 Axial velocity. Set-up: transpose stretching scheme, $\Delta t = 0.05(s)$, $\nu = 0.0001[m^2/s]$. NR and NP stand for Number of Rotations and Number of Particles respectively. 142

G.12 Vorticity. Set-up: transpose stretching scheme, $\Delta t = 0.05(s)$, $\nu = 0.0001[m^2/s]$. NR and NP stand for Number of Rotations and Number of Particles respectively. 143

G.13 Filaments. Set-up: transpose stretching scheme, $f = 0.1$, $\Delta t = 0.05(s)$, $\nu = 0.0001[m^2/s]$. NR and NP stand for Number of Rotations and Number of Particles respectively. 144

G.14 Axial velocity. Set-up: transpose stretching scheme, $f = 0.1$, $\Delta t = 0.05(s)$, $\nu = 0.0001[m^2/s]$. NR and NP stand for Number of Rotations and Number of Particles respectively. 145

G.15 Vorticity. Set-up: transpose stretching scheme, $f = 0.1$, $\Delta t = 0.05(s)$, $\nu = 0.0001[m^2/s]$. NR and NP stand for Number of Rotations and Number of Particles respectively. 146

List of Tables

6.1 Overview of parameters as applied for the thin vortex ring problem 50

6.2 Overview of parameters as applied for the leapfrogging problem 53

6.3 Computational efforts of a box (expansion) interaction relative to a direct (particle-particle) interaction 60

6.4 Overview of parameters as applied for the knot problem 64

6.5 Overview of parameters as applied for the actuator disk problem 78

6.6 Overview of parameters as applied for the simulation of the MEXICO rotor 89

A.1 Overview of several relevant terms of common regularization functions . . 109

A.2 Terms used in the calculation of the particle evolution equations, for a variety of smoothing kernels 110

E.1 Overview of parameters as applied for the knot problem in figure E.1 . . . 119

Nomenclature

List of abbreviations

AD	Actuator Disk
BEM	Blade Element-Momentum
CCSM	Corrected Core Spreading Method
CSM	Core Spreading Method
DFM	Divergence Filtering Method
DNS	Direct Numerical Simulation
DNW	Deutsch-Niederländische Windkanälen (German-Dutch Wind Tunnels)
CFD	Computational Fluid Dynamics
FMM	Fast Multipole Method
FFT	Fast Fourier Transform
HAWT	Horizontal Axis Wind Turbine
MEXICO	Model rotor EXperIments under COntrolled conditions
MPI	Message Passing Interface
NP	Number of Particles
NR	Number of Rotations
NS	Navier-Stokes
ODE	Ordinary Differential Equation
PIV	Particle Image Velocimetry
PPM	Parallel Particle-Mesh
PSE	Particle Strength Exchange
RHS	Right Hand Side
RK2	Second order Runge-Kutta
RK4	Fourth order Runge-Kutta
RWM	Random Walk Method
TSR	Tip Speed Ratio
VAWT	Vertical Axis Wind Turbine
VFM	Vortex Filament Method
VIC	Vortex-In-Cell
VPM	Vortex Particle Method

List of symbols

Latin symbols

$\boldsymbol{A}$	General matrix	–
$\boldsymbol{A}$	Angular momentum	–
A_n^m	Translation function	–
a	Axial induction factor	–
C	Core-specific function for the angular momentum	–
C_n^m	Multipole expansion coefficients	–
C_t	Thrust coefficient	–
c_{max}	maximum chord length	$[m]$
D	Volume of an elementary domain	$[m^3]$
D	Distance between source and target	$[m]$
D	Distance between two ring centers	$[m]$
D_n^m	Multipole expansion coefficients	–
d	Dimension	–
d	Diameter of a tree-box	$[m]$
E	Elliptic integral of the second kind	–
$\mathscr{E}$	Enstrophy	–
f	Mixing factor between stretching schemes, from 0 to 1	–
f	Relaxation factor for the DFM, from 0 to 1	–
G	Green's function	–
G	Gaussian probability density function	–
g	Regularization for the velocity	–
h	Inter-particle distance	$[m]$
$\mathscr{H}$	Helicity	–
$\boldsymbol{I}$	Identity matrix	–
$\boldsymbol{I}$	Linear momentum	–
I_i^j	Elliptic function	–
I_n^m	Inner translation function	–
i	Imaginary number: $sqrt{-1}$	–
$\boldsymbol{K}$	Biot-Savart kernel	–
K	Elliptic integral of the first kind	–
k	Elliptic parameter	–
k_i^j	Elliptic parameter	–
$\boldsymbol{l}$	Filament length vector	$[m]$
L	Filament length	$[m]$
M	Number of childs for the CCSM	–
M_n^m	Multipole expansion coefficients	–
N	Number of particles	–
NB	Number of blades	–
NP	Number of particles	–
NR	Number of rotations	–
O_n^m	Outer translation function	–
$\mathscr{O}$	Order	–

P	Target point	$[m]$
P_n	Legendre polynomials	–
P_n^m	Associated Legendre polynomials	–
p	Pressure	$[Pa]$
Q	Multipole source point	$[m]$
q	Particle source point	$[m]$
R	Ring radius	$[m]$
R	Rotation matrix from Cartesian to spherical coordinates	–
R^{-1}	Rotation matrix from spherical to Cartesian coordinates	–
Re	Reynolds number	–
r	Spanwise position	$[m]$
$\boldsymbol{r}$	Relative position vector	$[m]$
$\boldsymbol{r_0}$	Position vector from filament start to end	$[m]$
$\boldsymbol{r_1}$	Position vector from target to filament start	$[m]$
$\boldsymbol{r_2}$	Position vector from target to filament end	$[m]$
$\boldsymbol{S}$	Surface of the filament cross-section	$[m^2]$
t	time	$[s]$
$\boldsymbol{u}$	Velocity	$[ms^{-1}]$
U	Velocity	$[ms^{-1}]$
vol	Particle volume	$[m^3]$
$\boldsymbol{x}$	Position	$[m]$
$\boldsymbol{x^p}$	Particle position	$[m]$
$\boldsymbol{x_1}$	Position of the filament start	$[m]$
$\boldsymbol{x_2}$	Position of the filament end	$[m]$
Y_n^m	Spherical harmonics	–
Z	Axial position of the ring	$[m]$
z_{tube}	Position of the analytical vortex tube in axial direction	$[m]$

Greek symbols

$\boldsymbol{\alpha^p}$	Particle strength	$[m^3s^{-1}]$
α	Scaling factor for the CCSM from 0 to 1	–
β	Core-specific velocity constant	$[ms^{-1}]$
Γ	Circulation	$[m^2s^{-1}]$
γ	Circulation per unit length	$[ms^{-1}]$
γ	Spherical angle between the target and source	$[rad]$
δ	Dirac delta function	–
ε	Variance	–
ε	Error	–
ζ	Regularization for the vorticity	–
θ	Acceptance factor	–
θ	Spherical component	$[rad]$
λ	Overlapping ratio	–
λ	Tip Speed Ratio (TSR)	–
ν	Kinematic viscosity	$[m^2s^{-1}]$
$\boldsymbol{\xi}$	Stochastic position for the Brownian motion	$[m]$

Π	Elliptic integral of the third kind	–
ρ	Density	$[kgm^{-3}]$
ρ	Distance non-dimensionalized by the smoothing radius	–
ρ	Spherical component	$[m]$
σ	Smoothing radius of the particle core	$[m]$
Φ	Scalar potential	–
ϕ	General scalar	–
ϕ	Spherical component	$[rad]$
χ	Regularization for the stream function	–
$\boldsymbol{\Psi}$	Vector potential	–
$\boldsymbol{\psi}$	Stream function	$[m^2s^{-1}]$
$\boldsymbol{\Omega}$	Total vorticity	–
$\boldsymbol{\omega}$	Vorticity	$[s^{-1}]$
$\boldsymbol{\omega^p}$	Particle vorticity	$[s^{-1}]$

Sub- and superscripts

∞	Free-stream conditions
.	Time evolution
˜	Discretized field subject to divergence
c	Child particle
i	Particle identifier
m	Order of the multipole expansion
n	Time step
n	Level in the tree
n	Order of the multipole expansion
P	Target
p	Particle identifier
p	Parent particle
Q	Source
q	Particle identifier
qp	Distance from q to p
r	Real core representation
v	Vorton representation
σ	Smooth field

Chapter 1

Introduction

1.1 Motivation and objective

Blade Element Momentum (BEM) methods, which are based on blade discretization and the momentum balance over the flow, are the most commonly applied design tools for wind energy applications. BEM models have been proven to be fast and accurate in case of HAWT design. However, with BEM theory a 2D description of the rotor is assumed and the wake is not explicitly modelled. To include transient aerodynamics and 3D flow effects, one has to divert to empirical models and corrections.

With the rise of computational power, it is becoming more attractive to apply Computational Fluid Dynamics (CFD), by which the flow is discretized on a regular grid and solved through the Navier-Stokes equations. The fluid dynamics are explicitly taken into account, through which viscous phenomena such as dynamic stall and flow separation can be numerically calculated. CFD is valuable in case of wall-boundary conditions, but the Eulerian description poses problems over the whole flow domain as a large range of flow scales persist over the wake. I.e. a very fine mesh is required at locations of small vortical structures at the blade, and a mesh that is decreasing in coarseness in the wake, where larger scales of eddies dominate.

A more physical way to describe the wake is by applying a Lagrangian (not bound to a regular grid) vortex method. The Lagrangian description makes the vortex method auto-adaptive, by which it is meant that the range of flow scales is automatically accounted for, and that the flow is only described there where information is present. Especially in turbulent wakes, vortex methods are potentially both more accurate and faster than classic CFD. On the contrary, CFD is more suitable for the treatment of wall-boundary conditions. Hybrid methods, where CFD is applied at the rotor and vortex methods in the wake, are therefore an important topic of research.

When vortex methods are applied, often the vortices are described through a filament representation. Filaments have the benefit of being implicitly connected, resulting in less algorithmic terms needed to be resolved. On the contrary, vorticity can also be projected on particle (or blob) elements, through which the connectivity has to be explicitly computed. This property makes the modelling more challenging as unstable numerical divergence is manifested, but the lack of connectivity also gives rise to opportunities due to a larger degree in modelling freedom. As particles are not implicitly linked to their neighbours, issues such as turbulence, viscous diffusion, and blade-wake or tower-wake interactions are more naturally incorporated, without having the need to apply special measures such as filament surgery. Applications include the modelling of wind turbines subject to unsteady conditions, wind turbines operating in the wake of a wind farm, but also the modelling of the inherently unsteady and complex aerodynamics of VAWT machines, which operate in their own wake.

Hence, Lagrangian Vortex Particle Methods (VPM) offer potential computational and accuracy advantages over both CFD and filament methods in case of complex, vortical wakes. On top of that, the computational efficiency can get further increased by the application of a Fast Multipole Method (FMM), whereby the far-field interactions are calculated through clusters of particles. As such, the following thesis objective is formulated:

Objective of the present Master thesis research:

- **To develop and demonstrate the capabilities of a computationally efficient, accurate, and stable implementation of a Vortex Particle Method combined with a Fast Multipole Method for the 3D Lagrangian wake modelling of a HAWT.**

1.2 Research questions

In support of the proposed research as defined in the objective, the following four research questions are composed:

Research questions:

1. **What issues regarding stability of the VPM can be addressed, and what constraints drive the convergence of the model?**
2. **Is an FMM effective in improving the computational efficiency of a VPM in the context of the 3D wake of a HAWT?**
3. **Can the auto-adaptivity of the VPM be exploited to obtain an accurate description of the wake and shear layer of an actuator disk, including heavily loaded rotors?**

4. **Can accurate and stable near-wake flow solutions be obtained for a 3D rotating HAWT with prescribed circulation?**

The rationale behind the research questions is briefly addressed:

What issues regarding stability of the VPM can be addressed, and what constraints drive the convergence of the model?
The objective describes the development of a VPM code, for which the Lagrangian flow description offers the advantage of auto-adaptivity. This makes the design challenging, as no regular grid is available for remeshing (opposed to for instance VIC) whenever the flow becomes a poor representation of the real solution over time. Moreover, the particle description is prone to divergence due to the vortex stretching which is present in 3D, and unstable behaviour related to a non-smooth vorticity distribution. These issues have to be addressed, and subsequently different set-ups with the VPM using simple vortex geometries are simulated to analyze the stability and convergence over time. In this way, directives are drafted for a successful development of a VPM regarding stability, accuracy, and computational effort.

Is an FMM effective in improving the computational efficiency of a VPM in the context of the 3D wake of a HAWT?
To reduce the computational effort, the VPM is combined with an existing FMM. This FMM is modified, whereby the computation of the vector potential is replaced by the computation of the velocity and vortex stretching. The FMM is optimally capable of reducing the computational effort from $\mathcal{O}(N^2) \rightarrow \mathcal{O}(NlogN)$. Nevertheless, the performance of the FMM is very dependent on the particle distribution in space and the overhead involved in constructing the data-tree. Moreover, the computation of the velocity and stretching is significantly more expensive than the computation of the vector potential. For these reasons, it is investigated how effective the FMM is in reducing the computational efficiency of the 3D wake of a HAWT.

Can the auto-adaptivity of the VPM be exploited to obtain an accurate description of the wake and shear layer of an actuator disk, including heavily loaded rotors?
To assess the capability of the VPM in modelling the near-wake of the HAWT, the analysis of the wake consisting of shed vortex rings by a constant-force actuator disk is considered. Validation is carried out by comparing the wake expansion and flow deficit over the wake with the solutions from momentum theory and a potential flow model. The axisymmetry of the problem allows for a large number of particles and elimination of particle divergence, such that numerical stable and accurate results are obtained for a limited computational effort. The shear layer formed by vortex rings is inherently unstable, and the auto-adaptivity of the VPM is exploited for modelling the on-set of the Kelvin-Helmholtz instability and the subsequent break-down of the vortex sheet. The capability of the VPM is also demonstrated for highly loaded rotors for which flow-reversal takes place and where the momentum theory is no longer valid.

Can accurate and stable near-wake flow solutions be obtained for a 3D rotating HAWT subject to prescribed circulation?
The wake of a 3-bladed HAWT is modelled through a constant-in-time bound circulation over the blades, which is obtained from the MEXICO experiment [22]. As such, the investigation can be focussed on the wake as the rotor aerodynamics do not have to be resolved. Opposed to the axisymmetric actuator disk, the wake of this experiment consists of helical trailing vortices and is therefore purely 3D. The lack of axisymmetry significantly increases the computational effort, and particle divergence is manifested making the stable modelling of the wake challenging. Several modelling implementations are therefore investigated with the VPM, and the wake is compared to experimental results from the MEXICO rotor and PIV results from a 2-bladed turbine.

1.3 Research plan

To answer the research questions and subsequently to fulfil the objective, a numerical VPM code has to be developed and assessed. The following tasks can be distinguished:

1. Obtain knowledge of the theoretical background of the VPM and the functionality of the PPM library and FMM routines.
2. Derive the relevant output expressions for the FMM, and modify the routines accordingly.
3. Develop the combined VPM and FMM code (hereafter simply referred to as the VPM).
4. Verify the accuracy of the evolution equations of the VPM, and assess the computational effort and stability of the VPM over time.
5. Validate the VPM for the wake of a HAWT along analytical, numerical, and experimental results from literature.

For verification and validation of the VPM code, five test cases are simulated, which are stated below. A detailed motivation for each test case is presented in the introduction of chapter 6.

- Single circular thin vortex ring (torus)
- Double coaxial vortex rings (leapfrogging)
- Double linked vortex rings (knot)
- Axi-symmetrical wake of an actuator disk
- 3D wake of a 3-bladed HAWT with prescribed circulation

1.4 State-of-the-art

In this section, an overview of recent work in the field of wake modelling for wind turbines is presented, whereby the rationale for a Vortex Particle Method is outlined. It is also indicated that most work related to wind turbine wakes have focussed on either CFD or Eulerian-Lagrangian vortex methods, supporting the novelty of a purely Lagrangian VPM for the treatment of 3D flows of wind turbine wakes.

Lignarolo et al. [20] notes that a poor modelling of the wake, usually by actuator disk or line models, results in large inaccuracies in the kinetic energy recovery and that CFD models show a large dispersion in the prediction of the wind farm power by different turbulence models. To investigate the influence of periodic and random wake motions, stereoscopic PIV has been carried out on an actuator disk and rotating turbine model, allowing for a statistical analysis of the mixing process in the wake, up to 5 diameters downstream. It is found that wake instabilities affect all of the flow properties, and that these have an important effect on turbulence, leading to more effective mixing. Ferreira et al. [11] notes that the development of VAWTs is hindered by the lack of fast and accurate simulation models. Therefore, the accuracy and physical validity of 6 types of VAWT performance models has been investigated: a single and double multiple streamtube model, an actuator cylinder model, a 2D potential flow panel method, a 3D lifting line method, and a 2D conformal mapping unsteady vortex technique. It was found that the BEM-based streamtube models were proven both inaccurate and fundamentally physically incorrect, and should have to be discontinued unless empirically corrected for. On the other hand, the vortex based methods where the wake is explicitly modelled showed a good agreement between models. Yu et al. [38] investigated the validity of the momentum theory for dynamic and non-uniform loads, by a vortex ring analysis of an actuator disk. Moreover, the far-wake was replaced by a semi-infinite analytical vortex tube for computational mitigation. It is noted that the BEM and independent annuli assumption is acceptable for steady non-uniform loads, but that unsteady models are required in case of dynamics loading.

Voutsinas [35] notes that Eulerian CFD is by far the most popular simulation method for (wind energy) aerodynamics. Wall boundary conditions are easily accounted for, but CFD is bound to a grid and suffers from numerical diffusion in the wake. On the other hand, vortex methods are not well suited for the incorporation of wall boundary conditions, but are far better suited for the vortical wake modelling due to the Lagrangian, physical representation and the lack of numerical diffusion. With the philosophy of combining the best of both worlds, Manickathan [21] applied a 2D hybrid Eulerian-Lagrangian coupling for resolving both the small-scale flow around the blades and the large-scale dynamics of the far wake of a VAWT, resulting in the pHyFlow model. In this way, the blade aerodynamics and wall-boundary conditions are handled through CFD, while vortex particles represent the wake of the turbine.

Apart from the fact that CFD can be incorporated into the aerodynamic modelling, a Eulerian-Lagrangian description is also applied for allowing remeshing, the computation of partial derivatives, and the application of Fast Fourier Transform (FFT) solvers, as will be outlined here. Hejlesen et al. [16] notes that often tree algorithms are applied for computational reductions, whereby the FMM optimally obtains an $\mathcal{O}(N)$ scaling, though it is subject to a large pre-factor. This notion makes the FMM less attractive, especially in 3D, where the translations of multipole expansions becomes expensive. Hence, recent developments in particle methods have focussed on hybrid Eulerian-Lagrangian approaches. In this sense, Rasmussen [25] applied a Vortex-In-Cell (VIC) method combined with a Fast Fourier Transform (FFT) method, whereby the advection is treated through Lagrangian particles, while remeshing on a grid is used for resolving the differential operators. Chatelain et al. [5] coupled a VIC with immersed lifting lines for the LES simulation of tandem wind turbine wakes, whereby a RANS solver was applied for the near-blade region. Chatelain et al. [4] has applied a vortex particle method regarding the investigation of aircraft wake instabilities, whereby regular remeshing was still applied for treating divergence. A massive parallel computation using 16.000 CPUs was carried out, whereby the largest ever Direct Numerical Simulation (DNS) of a vortex particle method was achieved with a total of 6 billion particles, and up to a Reynolds number of 6000.

1.5 Report outline

Chapter 2 - Wake aerodynamics:
A discussion of the aerodynamic properties of the wake of a Horizontal Axis Wind Turbine is presented, including an introduction into the Actuator Disk and Blade Element Momentum theory. Alongside, an overview of fundamental aerodynamic properties of the Vertical Axis Wind Turbine is given to support the rationale of a Vortex Particle Method.

Chapter 3 - Theory on the 3D vortex particle method:
In this chapter the Vortex Particle Method theory is outlined, as implemented in the numerical model. Relevant topics that are dealt with include the introduction of the vorticity transport equation, a comparison between filament and particle vorticity descriptions, the handling of the evolution equations, the smoothing of the singular particle field, the treatment of Lagrangian and solenoidal distortions, viscous diffusion, and an introduction into useful performance parameters.

Chapter 4 - The application of an $\mathcal{O}(N \log N)$ fast multipole method:
In this chapter the theoretical background of the currently implemented $\mathcal{O}(N \log N)$-type Fast Multipole Method (FMM) is outlined. A discussion on the derivation of the partial derivatives of the vector potentials for obtaining the velocity and vorticity stretching terms is added.

Chapter 5 - Introduction to the numerical VPM code:
An introduction is given into the numerical VPM method, including the PPM library and the FMM routines.

Chapter 6 - Verification and validation:
The results, verification, and validation are altogether presented in this chapter. Three

test-cases consisting of vortex geometries have been simulated for the verification of both the VPM and the added FMM. Of interest are the assessment of the correct calculation of the velocity and vorticity stretching field, along with an insight into the computational efficiency of the FMM, and the stability and accuracy of the VPM over time. For validation, the results and discussion of the simulations with an actuator disk and 3-bladed HAWT are presented.

Chapter 7 - Conclusions and recommendations:
The conclusions and recommendations are stated in this chapter

Appendix
The thesis is completed with the addition of several appendices, containing fundamental expressions and derivations used throughout the VPM and the application of the FMM. Finally, visualizations over time of the knot problem, the actuator disk, and the 3-bladed HAWT are added.

Chapter 2

Wake Aerodynamics

Generally, the design of wind turbines is based on the Blade Element Momentum (BEM) theory, which forms the basis for all modern wind turbine design codes (Vermeer et al. [34]). Over the years, BEM has proven to be a valuable and generally accepted tool for the design of HAWT machines as it is fast, and reasonably accurate under steady conditions. However, wind turbines operate in a stochastic atmosphere and often in the wake of other turbines in a wind-farm setting. For optimization it is thus necessary to include unsteady (or transient) aerodynamic effects. BEM does not take the modelling of the wake explicitly into account, although this is necessary if transient effects are of importance. Methodologies that are suitable for the explicit wake modelling are offered by the numerical CFD and vortex based methods, of which the Vortex Particle Method is the research topic of the present thesis work.

To be able to both model and assess the simulated wake, it is necessary to understand the origin and flow characteristics of the wake of a HAWT machine. To this extent, an introduction is given in the concept of Froude's momentum theory, through which the rotor is modelled as an Actuator Disk (AD) and only the global momentum properties of the wake are taken into account. Replacing the AD by a rotor with a finite number of radially discretized blades results in the BEM theory. Understanding the AD concept is also relevant as it is used in the validation of the numerical VPM code.

Momentum theory assumes an expanding wake with an infinitely thin shear layer, although a real wake is of interest. For the current thesis work, the modelling of this wake is limited to that of HAWT machines and up to about 5 diameters downstream, which delimits the so called near-wake region. To be able to assess the quality of the wake, it is necessary to have an understanding of the flow origin, properties, and arising phenomena. Therefore, in this chapter a qualitative description is presented of the wake development originating from a HAWT. Finally, some attention is paid to the aerodynamics of a Vertical Axis Wind Turbine (VAWT), as this turbine supports the motivation for the development of a particle method.

2.1 Actuator Disk and Blade Element Momentum theory

A classical concept for describing the working principle of a wind turbine is given by the Actuator Disc (AD) model (Glauert [13]), see figure 2.1a. Hereby, the 3D HAWT rotor is simplified into a 2D infinitely thin disk that exerts a constant thrust on the through-flow. The AD represents the configuration of a HAWT, but with the rotor modelled as being infinitesimally thin, having an infinite amount of blades, being subject to a constant loading, and rotating at infinite velocity. Furthermore, the AD is exposed to an inviscid, incompressible flow. As the fluid passing the AD travels downstream, the velocity is decreased through induction, forming an expanding streamtube separated from the ambient free stream by an infinitesimally thin shear layer. This decrement in velocity expresses the extraction of kinetic energy from the flow by the turbine. At the same time a sudden drop of pressure is distinguishable at the actuator disk as a direct result of the applied axial thrust. This drop in pressure recovers over the expanding wake, back to the free stream level.

The AD concept gives a relationship between energy extraction and rotor thrust for a HAWT under ideal circumstances, but the rotor geometry, and real flow and operational conditions are ignored. A well-known method linking the energy extraction through the momentum balance to the physical rotor geometry is given by the Blade Element Momentum (BEM) theory. The uniform thrust production is replaced by a rotor with a finite rotational speed, producing a local 2D blade loading which is discretized over the span of each blade, where the airfoil properties are obtained through tabulated empirical lift and drag polars. The blade loading stands at the basis of the wake induction, though the induction field on its turn changes the local blade loading. This relationship between loading and induction is included in the blade loading calculations via induction factors a and a', as described in figure 2.1b. These factors give the ratio of the induced velocity components over the free stream velocity components in horizontal and vertical direction respectively, thereby describing the reduction of local velocity due to induction. As the induction and blade loading are interdependent, an iterative solution method is required.

The BEM theory allows for a simple analysis of the performance of a turbine and can give satisfying results for a HAWT under the conditions of steady aerodynamics. In reality, a wide range of complex aerodynamics are of importance which can not be captured by BEM theory alone (unless maybe empirically accounted for, such as with dynamic stall models), and in the case of a VAWT the aerodynamics are inherently unstable, for which simple BEM-based models are absolutely inadequate for a proper analysis (Ferreira et al. [11]). To be able to model the unsteady aerodynamics, it is necessary to include the calculation of the wake explicitly, which gives rise to the class of numerical CFD and vortex based methods. In the following sections of this chapter, an attempt is made to capture and describe the relevant occurring aerodynamic phenomena in the wake of a HAWT.

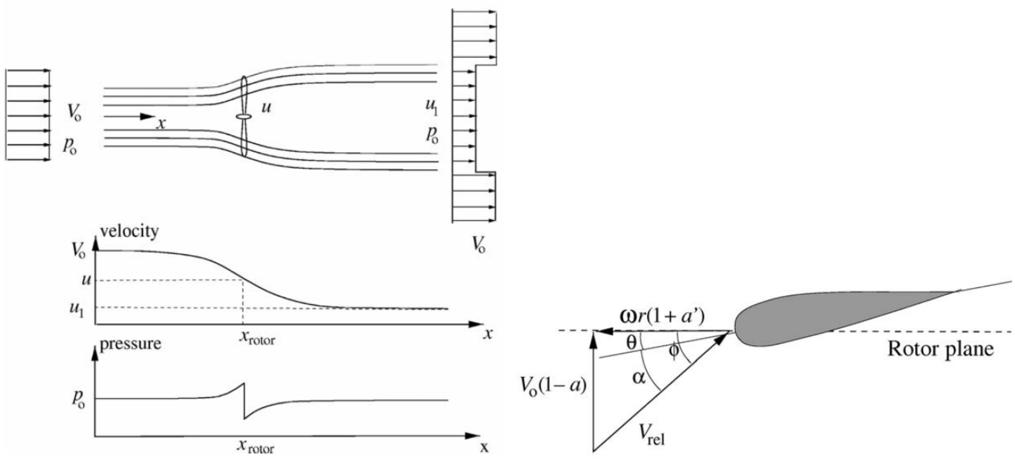

(a) The actuator disk concept (b) A 2D blade element

Figure 2.1: *Impression of the actuator disk and BEM theory (Hansen [15]).*

2.2 Wake aerodynamics of a HAWT

Good reviews on the topic of wind turbine wake aerodynamics are given by Vermeer et al. [34] and Sanderse [28], on which the following analysis is based. The wake of a wind turbine can be subdivided into two distinguishable regions, namely the near-wake just downstream the rotor up to a few rotor diameters, and the far-wake beyond (where sometimes also a transitional region is recognized in between). The near-wake is characterized and directly influenced by the rotor geometry, and vice versa, and is therefore related to the performance of the turbine itself. In contrast, the significance of the far-wake lies in wind-farm modelling, where the actual rotor geometry is far less important and can be greatly simplified. As the near and far-wake have such different properties, those are treated separately hereafter.

2.2.1 Near-wake

Consider a physical HAWT geometry, with a circular wake cross section, demarcated by an initially thin shear layer, subject to atmospheric conditions. The following topics describe the associated near-wake of this turbine, which is often taken from the rotor to about two to five rotor diameters downstream. A visualization is given in figure 2.2.

- **An expanding wake.** As a direct consequence of the thrust on the rotor and the accompanying kinetic energy extraction from the wind, the flow velocity decreases through the rotor. Regarding the continuity equation, the wake has to expand up till a point downstream where the pressure has recovered to ambient conditions.
- **An expanding shear layer.** The wake is separated from the free stream by a shear layer that is initially very thin and thus steep. As the shear layer has a steep gradient, it is unstable, and it is prone to turbulent eddy creation. Due

to turbulent diffusion, the shear layer expands rapidly up to a point where the wake is fully covered by this shear layer, about 2 to 5 rotor diameters downstream. Another distinct observation attributed to the shear layer is the phenomenon of vortex pairing, where the helical tip vortices start sticking together. It turns out that vortex pairing is an important factor in the turbulent mixing and the growth of the shear layer.

- **Instabilities originating from the turbine geometry.** Though the most important source of turbulence lies in the unstable shear layer within the wake, also the turbine geometry has an influence on the stability of the wake. For instance, variations in thrust and torque over the rotor result in a non-uniform flow profile with deficits of pressure and velocity. Besides, important contributors to the wake turbulence are the trailing vortices, the turbulent boundary layer leaving the trailing edge, flow separation from the nacelle and tower, and unsteady aerodynamics through for instance aero-elastic effects and vortex shedding.
- **Atmospherical and operational conditions.** A turbine operating in the Earth's boundary layer is subject to an asymmetrical free stream velocity profile and of course atmospheric turbulence. Along with these conditions, wind shear and yawed conditions may arise.

2.2.2 Far-wake

Beyond the near-wake the flow reaches a state where the wake is deemed fully developed, called the far-wake. Where the near-wake is directly related to the performance of the rotor itself, the analysis of the far-wake is more interesting in the context of the wind-farm. The far-wake can be described as follows:

- **A fully developed, self-similar wake.** The wake is assumed to be fully developed, as both the wake and the shear layer have expanded to their final state. Under the absence of the Earth's boundary layer and ambient turbulence, the profile of both the velocity deficit and the turbulence intensity approximate a Gaussian shape, and can be considered axi-symmetric and self-similar.
- **Re-energizing of the flow.** As the wake travels downstream, turbulent mixing assures re-energizing of the flow, and as such a slow dissipation of the velocity deficit and the turbulence intensity.
- **A negligible influence of the rotor geometry.** In the far-wake, the influence of the rotor geometry is not visible anymore, due to diffusion of individual effects. The modelling of the rotor can be greatly simplified, where the only important parameters of the original rotor are the total thrust and the turbulent kinetic energy.
- **Wake meandering.** The far-wake will experience a wake instability, much like the periodic vortex shedding behind a cylinder (Kármán vortex shedding). The wake will start meandering through the creation of large scale eddies.

- **A Significance for wind-farm modelling.** As the far-wake has to be analyzed over a large region on the level of a wind-farm, topics like wake interference, and atmospheric and topographic effects dictate the wake behaviour.

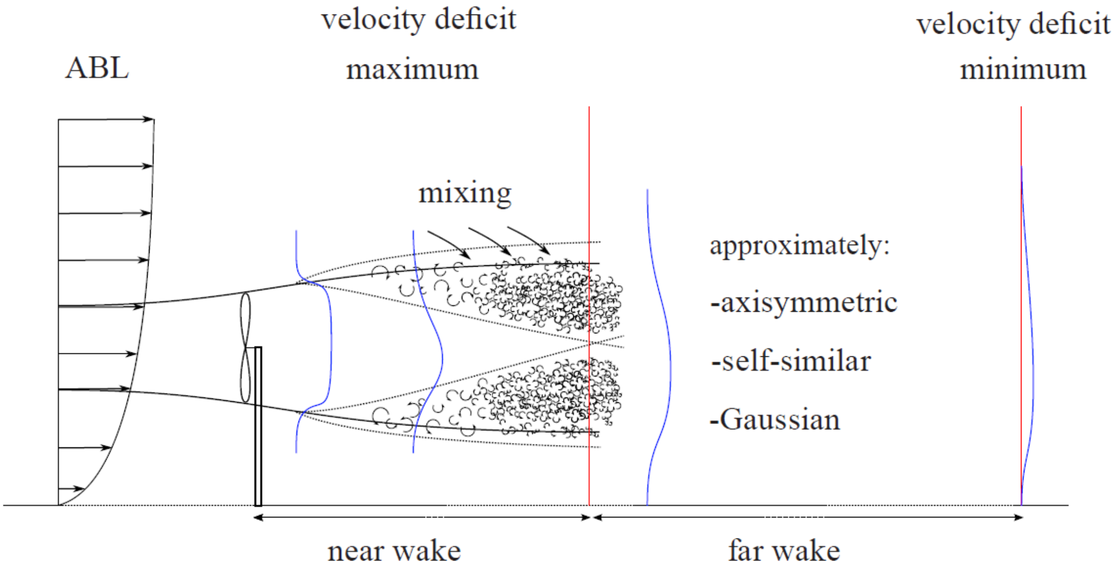

Figure 2.2: *A schematic layout of the near and far-wake of a HAWT (Sanderse [28]).*

2.3 Motivation for the application of a VPM for modelling the wake of a VAWT

Although the objective describes the assessment of the near-wake of a HAWT for the present thesis, the larger aim is to be able to model the wake of large-scale wind turbines in general, including that of the Vertical Axis Wind Turbine (VAWT). The VAWT differs considerably from the HAWT in the operational mechanism and the characteristics of the wake. In this section, the motivation for modelling the wake of the VAWT by a VPM is briefly outlined.

Figure 2.3a schematically shows the velocity and force vectors on the blades over the rotation of a VAWT. It is visible that the velocity vector is periodically changing direction relative to the blade. As a result, the magnitude of the angle of attack is also periodic, as visible in figure 2.3b.

Due to the periodic blade loading, vorticity is continuously shed at the trailing edge. This leads to the fact that, opposed to the HAWT, the VAWT is inherently operating under unstable conditions (Simão Ferreira [31]). Dynamic stall takes place with the shedding of vortex bubbles. The shed vortices and vortex bubbles originating from the upstream part of the rotation will results in the occurrence of blade-wake interactions downstream. It is mainly for this phenomenon that a VPM would be considered for VAWT modelling, as

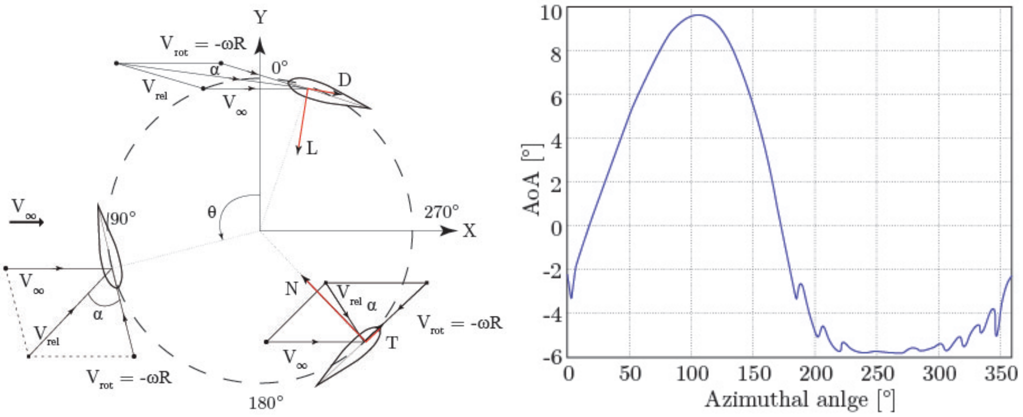

(a) (b)

Figure 2.3: *The motion of a VAWT: (a) Schematic overview of the velocity and force vectors over the rotation (Castelein [3]). (b) Demonstration of the periodic motion of the angle of attack over the rotation for* $\lambda = 4.5$ *(Ferreira et al. [10]).*

the blade-wake interactions will result in disconnection of vortex filaments. Nevertheless, it is stated again that the research for the present thesis is limited to the investigation of the near-wake of the HAWT.

Chapter 3

Theory of the 3D Vortex Particle Method

3.1 Introduction

In this chapter, the theory of the 3D Vortex Particle Method (VPM) is outlined, which forms the basis of the numerical code developed for this thesis work. First, an introduction is given into the fundamental equations and principles of the vortex theory, whereby the vector notation of the Navier-Stokes (NS) equations is presented in vorticity formulation. Accordingly, a short discussion is presented on the use of filaments and particles in vortex modelling. The fundamental theory of the VPM is then presented which describes the solution to the NS-equations in vorticity formulation for particles. Important topics include the handling of the singular particle field by regularization, the handling of divergence and grid distortions, and the treatment of viscous diffusion. Alongside, a section is devoted to the linear and quadratic diagnostics, by which the conservation laws can be tracked giving valuable information about the quality of the simulation.

3.1.1 The basis of vortex theory

Equation 3.1 shows the NS momentum equations in vector notation, for a viscid incompressible flow without body forces.

$$\frac{D\boldsymbol{u}}{Dt} = \frac{d\boldsymbol{u}}{dt} + \boldsymbol{u} \cdot \nabla \boldsymbol{u} = -\nabla \frac{p}{\rho} + \nu \nabla^2 \boldsymbol{u} \tag{3.1}$$

Note the convective derivative notation of $D/Dt = d/dt + \boldsymbol{u} \cdot \nabla$, which describes the evolution of a property in a Lagrangian framework. The NS-equations can be rewritten in the form of equation 3.2, using the identity of $\boldsymbol{u}\times\boldsymbol{\omega} = \frac{1}{2}\nabla\boldsymbol{u}^2 - \boldsymbol{u}\cdot\nabla\boldsymbol{u}$, where $\boldsymbol{\omega} = \nabla\times\boldsymbol{u}$ is the vorticity.

$$\frac{d\boldsymbol{u}}{dt} = \boldsymbol{u}\times\boldsymbol{\omega} - \frac{1}{\rho}\nabla\left(p + \frac{1}{2}\rho\boldsymbol{u}^2\right) + \nu\nabla^2\boldsymbol{u} \tag{3.2}$$

By taking the curl, and using the identities $\nabla\times(\nabla\phi) = 0$ (hence, the pressure term disappears as it is a scalar), and $\nabla\times\left(\nabla^2\boldsymbol{A}\right) = \nabla^2\left(\nabla\times\boldsymbol{A}\right)$, we are left with equation 3.3.

$$\frac{d\boldsymbol{\omega}}{dt} = \nabla\times(\boldsymbol{u}\times\boldsymbol{\omega}) + \nu\nabla^2\boldsymbol{\omega} \tag{3.3}$$

A simplification of this expression is obtained by applying the identity $\nabla\times(\boldsymbol{u}\times\boldsymbol{\omega}) = \boldsymbol{\omega}\cdot\nabla\boldsymbol{u} - \boldsymbol{u}\cdot\nabla\boldsymbol{\omega} + \boldsymbol{u}\left(\nabla\cdot\boldsymbol{\omega}\right) - \boldsymbol{\omega}\left(\nabla\cdot\boldsymbol{u}\right)$, and by observing that the last two terms of this identity drop out due to the incompressibility assumption (the vorticity and velocity field are divergence-free). Equation 3.3 is rewritten in the vorticity transport equation (equation 3.4).

$$\frac{D\boldsymbol{\omega}}{Dt} \equiv \frac{d\boldsymbol{\omega}}{dt} + \boldsymbol{u}\cdot\nabla\boldsymbol{\omega} = \boldsymbol{\omega}\cdot\nabla\boldsymbol{u} + \nu\nabla^2\boldsymbol{\omega} \tag{3.4}$$

.

We have now arrived at the NS-equations in vorticity-velocity formulation (notice that the pressure term is not explicitly apparent anymore). Equation 3.4 describes the evolution of vorticity. Along with the relationship between the velocity and vorticity $\boldsymbol{\omega} = \nabla\times\boldsymbol{u}$ and the evolution equation of the flow position $\boldsymbol{u} = d\boldsymbol{x}/dt$, a full flow description is obtained. The first term on the Right Hand Side (RHS), $\boldsymbol{\omega}\cdot\nabla\boldsymbol{u}$, is called the (vortex) stretching term, and the second term, $\nu\nabla^2\boldsymbol{\omega}$, is denoted as the viscous diffusion term. Vortex stretching is a phenomenon that is specific for 3D flows; in 2D the stretching term disappears mathematically. Stretching is also often seen to be at the basis of the turbulent energy cascade whereby energy is transferred to the smaller scales, and it thus forms an important modelling aspect of the 3D VPM. It will become apparent over the course of this thesis work that vortex stretching forms a source of instabilities for the numerical VPM, and therefore the handling of stretching is extensively discussed (see section 3.2.3).

3.1.2 Vorticity described by filament elements

A classic approach for application of the vortex theory is offered by describing the vorticity on a filament (figure 3.1a). This filament is discretized into a chain of straight segments, whereby each filament segment is fully described by the position of its two extremes and the amount of vorticity contained in the cross-section of the filament. Connectivity is guaranteed by the fact that each computational node in the chain is shared between two neighbouring filament ends. Instead of explicitly computing the vorticity, the circulation strength of a filament is used which is related to the vorticity as shown by equation 3.5, with $\boldsymbol{S}$ the cross-sectional area of the filament:

$$\Gamma = \iint\limits_{\boldsymbol{S}} \boldsymbol{\omega}\cdot d\boldsymbol{S} \tag{3.5}$$

Circulation can thus be seen as the flux of vorticity, or the other way around: the vorticity is circulation per unit area over the cross-section of a filament. The circulation is related to the velocity through the well-known Biot-Savart law:

$$\boldsymbol{u} = \frac{\Gamma}{4\pi} \int \frac{\boldsymbol{dl} \times (\boldsymbol{r}_0 - \boldsymbol{r}_1)}{\|\boldsymbol{r}_0 - \boldsymbol{r}_1\|^3} \approx \frac{\Gamma}{4\pi} \sum \frac{\boldsymbol{r}_1 \times \boldsymbol{r}_2}{\|\boldsymbol{r}_1 \times \boldsymbol{r}_2\|^2} \boldsymbol{r}_0 \cdot \left(\frac{\boldsymbol{r}_1}{\|\boldsymbol{r}_1\|} - \frac{\boldsymbol{r}_2}{\|\boldsymbol{r}_2\|} \right) \tag{3.6}$$

The Biot-Savart law thus describes the complete velocity field in the domain, and also the evolution of the filament position in space, as the computational nodes move as material elements through the fluid. Computation of the evolution of circulation in space and time is not required; according to Helmholtz, the strength of circulation remains constant along the filament line for an inviscid flow, and according to Kelvin, the circulation remains constant in time for an ideal fluid:

$$\frac{D\Gamma}{Dt} = 0 \tag{3.7}$$

Calculation of the velocity field via the concept of circulation is thus convenient: only the evolution of the interconnected computational nodes has to be computed through the Biot-Savart law. Evolution of the length of a filament element is not of importance, as it is implicitly taken into account through the mutual distance of a computational node pair. This inherited connectivity leads to some issues, as will be described in section 3.1.3.

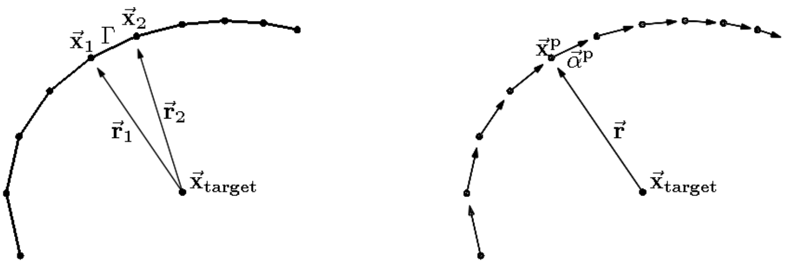

(a) Filament representation

(b) Particle representation

Figure 3.1: *(a) Vorticity described by filaments carrying a scalar circulation. Each filament section shares its computational nodes with its direct neighbours, and thus connectivity is maintained implicitly. (b) Vorticity described by particles carrying a vector strength. Connectivity is maintained explicitly as long as the particles remain aligned.*

3.1.3 The limitations of a filament method

The inherited connectivity attributed to filaments gives rise to some limitations:

- Viscous diffusion of filaments can be simulated to a certain extent by allowing the regularized core to grow. Other viscous phenomena, and then in particular the process of vortex filament reconnection, are not so easily accounted for.

- Blade-wake interactions (or interactions with any solid body in general) infringe on the connectivity of filaments.
- Regions of intense vortex stretching and very sharp curvatures will often arise, such as in the case of vortex roll-up. The only mechanisms counteracting these extreme conditions are offered by viscous diffusion and dissipation at the smallest flow scales. Filament methods are not well suited for handling these conditions.

A solution is to describe the fluid by vorticity carrying particles, denoted here as $\boldsymbol{\alpha}^p$. These particles form the basis of the so-called Vortex Particle Method (VPM), see figure 3.1b. Like filaments, particles move as material elements with the flow, and carry a volume of vorticity. The volume of vorticity is known as the particle strength, and it is related to the filament circulation through equation 3.9.

$$\boldsymbol{\alpha}^p = \int_D \boldsymbol{\omega}^p(t) dD = \Gamma d\boldsymbol{l} \tag{3.8}$$

In contrast to filament methods, the connectivity is not implicitly taken into account, but as long as the vorticity field remains divergence-free ($\nabla \cdot \boldsymbol{\omega} = 0$) and the particle density is sufficient, the solution is equivalent to that of filaments. The modelling of a VPM is therefore also very challenging: if the divergence-free condition is not well maintained, the method is prone to become unstable and inaccurate. However, if properly modelled, the VPM can offer a very interesting and powerful tool for the treatment of viscous or complex wake flows.

3.2 The 3D VPM

In the following sections, the particle method is outlined for the 3D case. The framework of the presented theory is to a large extent based on the work of Winckelmans [36] and Cottet and Koumoutsakos [8]. Special emphasis is put on handling the vorticity evolution equations (vortex stretching), as the solenoidal condition is important for obtaining a stable solution over time.

3.2.1 The fundamental equations of the vortex particle method

In an incompressible and inviscid flow singular particles possess two properties, namely the particle location $\boldsymbol{x}^p(t)$ and the particle strength $\boldsymbol{\alpha}^p(t)$ with the latter defined in equation 3.9 as the integration of the particle vorticity over the volume, such that the discretized vorticity field is described by equation 3.10. The particle description is demonstrated in figure 3.1b. Note that the tilde ($\tilde{\ }$) represents the solution due to a discretized field, and that $\delta(\boldsymbol{x})$ stands for the Dirac delta function.

$$\boldsymbol{\alpha}^p = \int_D \boldsymbol{\omega}^p(t) dD \tag{3.9}$$

$$\tilde{\boldsymbol{\omega}}(\boldsymbol{x},t) = \sum_p \boldsymbol{\omega}^p = \sum_p \boldsymbol{\alpha}^p(t)\delta(\boldsymbol{x} - \boldsymbol{x}^p(t)) \tag{3.10}$$

The evolution equations over time of $\boldsymbol{x}^p$ and $\boldsymbol{\alpha}^p$ are described by equations 3.11 and 3.12. Note that $[\nabla \boldsymbol{u}]$ is a 3x3-matrix containing the gradient terms of the velocity as in $[\partial u_i/\partial x_j]$, i.e. it is the gradient tensor of $\boldsymbol{u}$. The evolution of the particle strength over time is also known as vortex stretching. In the remainder of this section, the construction of the velocity field from the particle vorticity is presented. The handling of the vortex stretching follows in subsection 3.2.3. Generally, the notation of the tilde is dropped in case of the velocity, for reasons that become apparent during the discussion of the divergence of the discretized particle field in subsection 3.3 (i.e. $\tilde{\boldsymbol{u}} = \boldsymbol{u}$).

$$\frac{d\mathbf{x}^p}{dt} = \mathbf{u}(\boldsymbol{x}^P, t) \tag{3.11}$$

$$\frac{d\boldsymbol{\alpha}^p}{dt} = \boldsymbol{\alpha}^p \cdot \nabla \boldsymbol{u}(\boldsymbol{x}^p, t) = [\nabla \boldsymbol{u}(\boldsymbol{x}^p, t)]\,[\boldsymbol{\alpha}^p] \tag{3.12}$$

As the flow is assumed incompressible (from now on referred to as divergence-free or solenoidal), a stream function $\tilde{\boldsymbol{\psi}}$ should exist which is related to the vorticity through the Poisson equation: $\nabla^2\tilde{\boldsymbol{\psi}}(\boldsymbol{x},t) = -\tilde{\boldsymbol{\omega}}(\boldsymbol{x},t)$. The solution to the Poisson equation is given in equation 3.13 in the form of a convolution ($*$) of the Green's function with the source function, given here as the particle vorticity. The 3D Green's function solution for the Laplacian operator is $G(\boldsymbol{x}) = 1/(4\pi \left\|\boldsymbol{x}\right\|)$.

$$\tilde{\boldsymbol{\psi}}(\boldsymbol{x},t) = G(\boldsymbol{x}) * \tilde{\boldsymbol{\omega}}(\boldsymbol{x},t) = \sum_p G(\boldsymbol{x} - \boldsymbol{x}^p(t))\boldsymbol{\alpha}^p(t) = \frac{1}{4\pi}\sum_p \frac{\boldsymbol{\alpha}^p(t)}{\left\|\boldsymbol{x} - \boldsymbol{x}^p(\boldsymbol{t})\right\|} \tag{3.13}$$

By taking the curl of the stream function of equation 3.13, the Biot-Savart law for a particle description is obtained. The gradient of the Green's function itself is usually described by $\boldsymbol{K}(\boldsymbol{x})$, called the Biot-Savart kernel, and is equal to $\boldsymbol{K}(\boldsymbol{x}) = \nabla G(\boldsymbol{x}) = -\boldsymbol{x}/(4\pi \left\|\boldsymbol{x}\right\|^3)$:

$$\begin{aligned}\boldsymbol{u}(\boldsymbol{x},t) &= \nabla \times \tilde{\boldsymbol{\psi}}(\boldsymbol{x},t) = \nabla \times (G(\boldsymbol{x}) * \tilde{\boldsymbol{\omega}}(\boldsymbol{x},t)) = \sum_p \nabla G(\boldsymbol{x} - \boldsymbol{x}^p(t)) \times \boldsymbol{\alpha}^p(t) \\ &= \sum_p \boldsymbol{K}(\boldsymbol{x} - \boldsymbol{x}^p(t)) \times \boldsymbol{\alpha}^p(t) = \frac{-1}{4\pi}\sum_p \frac{\boldsymbol{x} - \boldsymbol{x}^p(t)}{\left\|\boldsymbol{x} - \boldsymbol{x}^p(t)\right\|^3} \times \boldsymbol{\alpha}^p(t)\end{aligned} \tag{3.14}$$

3.2.2 Regularization of the singular particles

The representation of the vorticity field by singular particles is non-physical in the sense that singular vorticity with an infinite rotational velocity cannot sustain over time and diffusion of vorticity will occur. More important, the singularities will probably lead to an unstable simulation. Therefore, smoothing of the vorticity around its particle center is presented here through the use of regularization functions, which smear out the vorticity mathematically as shown in equation 3.15.

$$\tilde{\boldsymbol{\omega}}_\sigma(\boldsymbol{x},t) = \zeta_\sigma(\boldsymbol{x}) * \tilde{\boldsymbol{\omega}}(\boldsymbol{x},t) = \sum_p \boldsymbol{\alpha}^p(t)\zeta_\sigma(\boldsymbol{x} - \boldsymbol{x}^p(t)) \tag{3.15}$$

$\zeta_\sigma(\boldsymbol{x})$ is called the regularized smoothing kernel. It is related to the (unregularized) smoothing function as in equation 3.16.

$$\zeta_\sigma(\boldsymbol{x}) = \frac{1}{\sigma^3}\zeta\left(\frac{\|\boldsymbol{x}\|}{\sigma}\right) \tag{3.16}$$

The smoothing function $\zeta(\rho)$, with $\rho = \|\boldsymbol{x}\|/\sigma$ and σ being the smoothing radius, contains certain properties that ensure the conservation of momenta up to a certain order. These moment conditions are directly related to the convergence of the method. The zeroth moment condition, known as the normalization constraint, ensures conservation of vorticity. The first and second moment conditions deal with the linear and angular momentum conservation respectively. Higher order conditions are usually not relevant, as an order above 2 results in the loss of positivity of the smoothing function (meaning that the function is not strictly positive over the full domain, resulting in areas of negative vorticity). smoothing functions that fulfil these requirements, and therefore also often implemented, are for instance the zeroth and second order Gaussian and algebraic functions. Apart from the regularization function with respect to the vorticity, two more regularization function types are of interest, namely the regularization for the stream function $\chi_\sigma(\boldsymbol{x})$, and the regularization function for the velocity $g_\sigma(\boldsymbol{x})$, as shown in equations 3.17, and 3.18. The regularization functions are interrelated through equation 3.19.

$$\chi_\sigma(\boldsymbol{x}) = \frac{1}{\sigma}\chi\left(\frac{\|\boldsymbol{x}\|}{\sigma}\right) \tag{3.17}$$

$$g_\sigma(\boldsymbol{x}) = g\left(\frac{\|\boldsymbol{x}\|}{\sigma}\right) \tag{3.18}$$

$$\nabla^2\chi(\rho) = \frac{2}{\rho}\chi'(\rho) + \chi''(\rho) = -\frac{g'(\rho)}{\rho^2} = -\zeta(\rho) \tag{3.19}$$

$\chi_\sigma(\boldsymbol{x})$ is used to form a smoothed representation of the stream function and is basically the regularized Green's function. $g_\sigma(\boldsymbol{x})$ on its turn is used in the regularization of the velocity field, and appears in the regularized Biot-Savart kernel, as in equations 3.20 through 3.22. It will become apparent that mainly the $g_\sigma(\rho)$-function is of interest, due to its use in the regularized evolution equations of $\boldsymbol{x}^p$ and $\boldsymbol{\alpha}^p$.

$$\tilde{\boldsymbol{\psi}}_\sigma(\boldsymbol{x},t) = G(\boldsymbol{x}) * \tilde{\boldsymbol{\omega}}_\sigma(\boldsymbol{x},t) = \chi_\sigma(\boldsymbol{x}) * \tilde{\boldsymbol{\omega}}(\boldsymbol{x},t) = \sum_p \chi_\sigma(\boldsymbol{x} - \boldsymbol{x}^p(t))\boldsymbol{\alpha}^p(t) \tag{3.20}$$

$$\begin{aligned}\boldsymbol{u}_\sigma(\boldsymbol{x},t) = \nabla\times\tilde{\boldsymbol{\psi}}_\sigma(\boldsymbol{x},t) &= \sum_p \nabla\chi_\sigma(\boldsymbol{x}-\boldsymbol{x}^p(t))\times\boldsymbol{\alpha}^p(t)\\ = \sum_p \boldsymbol{K}_\sigma(\boldsymbol{x}-\boldsymbol{x}^p(t))\times\boldsymbol{\alpha}^p(t) &= -\sum_p \frac{g_\sigma(\boldsymbol{x}-\boldsymbol{x}^p(t))}{\|\boldsymbol{x}-\boldsymbol{x}^p(t)\|^3}(\boldsymbol{x}-\boldsymbol{x}^p(t))\times\boldsymbol{\alpha}^p(t)\end{aligned} \tag{3.21}$$

$$\boldsymbol{K}_\sigma(\boldsymbol{x}) = \frac{-g_\sigma(\boldsymbol{x})}{\|\boldsymbol{x}\|^3} \tag{3.22}$$

Smoothing kernels can be constructed in various ways. For the ease of calculation one is often interested in smoothing kernels that are radially symmetric; and taking into account the positivity constraint mentioned earlier on, the order of the smoothing kernel should not be higher than 2. As a result, the most used kernels are the second order Gaussian kernels, and the zeroth and second order algebraic kernels. As these kernels are used extensively for various numerical scheme implementations in the VPM code, an overview of expressions is given in appendix A.

3.2.3 Vorticity stretching

Recall equation 3.11 for the vortex stretching:

$$\frac{D\boldsymbol{\alpha}^p}{Dt} = \left[\nabla\boldsymbol{u}(\boldsymbol{x}^P(t),t)\right][\boldsymbol{\alpha}^p] \tag{3.11}$$

Now that the equation for the velocity field is known, it is used to derive the equation for the vortex stretching. In case of a singular particle field, the result is given in equation 3.23.

$$\frac{D\boldsymbol{\alpha}^p}{Dt} = -\frac{1}{4\pi}\sum_q\left\{\frac{1}{\|\boldsymbol{r}_{qp}\|^3}\boldsymbol{\alpha}^p\times\boldsymbol{\alpha}^q - \frac{3}{\|\boldsymbol{r}_{qp}\|^5}(\boldsymbol{\alpha}^p\cdot\boldsymbol{r}_{qp})\cdot(\boldsymbol{r}_{qp}\times\boldsymbol{\alpha}^q)\right\} \tag{3.23}$$

Referring again to equation 3.11, it can be observed that $[\nabla\boldsymbol{u}][\boldsymbol{\omega}]-[\nabla\boldsymbol{u}]^{\boldsymbol{T}}[\boldsymbol{\omega}] = \boldsymbol{\omega}\times(\nabla\times\boldsymbol{u}) = \boldsymbol{\omega}\times\boldsymbol{\omega} = 0$ (The proof is written out in appendix A). This identity shows that the original stretching scheme can be replaced by a transpose variant $[\nabla\boldsymbol{u}]^{\boldsymbol{T}}[\boldsymbol{\omega}]$ which holds equivalent information. Any combination of both the original and transpose scheme can be constructed, resulting in a so-called mixed scheme as in $f[\nabla\boldsymbol{u}][\boldsymbol{\omega}]+(1-f)[\nabla\boldsymbol{u}]^{\boldsymbol{T}}[\boldsymbol{\omega}]$ (whereby the original scheme is referred to as the classic scheme from now on). The discrete expressions for these schemes are given in equations 3.24 through 3.26 for a regularized particle field, in which f is a mixing factor between 0 and 1. Although the classic and transpose scheme are equivalent by construction, this is not the case in a discretized form, where the vorticity field is generally not divergence-free. In other words: $\tilde{\boldsymbol{\omega}} \neq \nabla\times\boldsymbol{u}$. This is an important observation, as it leads to the fact that the choice of stretching scheme will affect the convergence of the simulation. Therefore, in the verification and validation part of the thesis, attention is paid to both scheme implementations.

$$\left.\frac{D\boldsymbol{\alpha}^p}{Dt}\right|_{\sigma}^{classic} = -\sum_q \left\{ \frac{1}{\sigma^3}\frac{g(\rho)}{\rho^3}\boldsymbol{\alpha}^p \times \boldsymbol{\alpha}^q + \frac{1}{\sigma^5 \rho}\frac{d}{d\rho}\left(\frac{g(\rho)}{\rho^3}\right)(\boldsymbol{\alpha}^p \cdot \boldsymbol{r}_{qp}) \cdot (\boldsymbol{r}_{qp} \times \boldsymbol{\alpha}^q) \right\} \tag{3.24}$$

$$\left.\frac{D\boldsymbol{\alpha}^p}{Dt}\right|_{\sigma}^{transpose} = \sum_q \left\{ \frac{1}{\sigma^3}\frac{g(\rho)}{\rho^3}\boldsymbol{\alpha}^p \times \boldsymbol{\alpha}^q + \frac{1}{\sigma^5 \rho}\frac{d}{d\rho}\left(\frac{g(\rho)}{\rho^3}\right)(\boldsymbol{\alpha}^p \cdot (\boldsymbol{r}_{qp} \times \boldsymbol{\alpha}^q)) \cdot \boldsymbol{r}_{qp} \right\} \tag{3.25}$$

$$\begin{aligned}\left.\frac{D\boldsymbol{\alpha}^p}{Dt}\right|_{\sigma}^{mixed} = \sum_q \Bigg\{ \frac{1}{\sigma^5 \rho}\frac{d}{d\rho}\left(\frac{g(\rho)}{\rho^3}\right) \Big[&(1-f)\,(\boldsymbol{\alpha}^p \cdot (\boldsymbol{r}_{qp} \times \boldsymbol{\alpha}^q)) \cdot \boldsymbol{r}_{qp} \\ &-f\,(\boldsymbol{\alpha}^p \cdot \boldsymbol{r}_{qp}) \cdot (\boldsymbol{r}_{qp} \times \boldsymbol{\alpha}^q)\Big]\Bigg\}\end{aligned} \tag{3.26}$$

3.3 Maintaining the divergence-free vorticity field

As stated in subsection 3.2.3, a particle representation leads to a vortex particle field that is generally not divergence-free ($\nabla \cdot \tilde{\boldsymbol{\omega}} \neq 0$). The stream function is therefore also generally not divergence-free, as it is related to the vorticity field as $-\nabla^2 \tilde{\boldsymbol{\psi}} = \tilde{\boldsymbol{\omega}} \rightarrow \nabla \cdot \tilde{\boldsymbol{\psi}} \neq 0$. On the contrary, the velocity field is actually divergence-free as it is the curl of the stream function, and thus it is 0 by construction: $\nabla \cdot \boldsymbol{u} = \nabla \cdot \left(\nabla \times \tilde{\boldsymbol{\psi}}\right) = 0$ (explaining why the tilde is dropped in the notation of $\boldsymbol{u}$ throughout this thesis work). The exact same reasoning applies for a regularized particle field. This is an important difference between particles and filaments, where the latter provide a solenoidal field by construction. No matter the refinement, the vorticity field discretized by particles will inevitably become a poor representation of the real vorticity field as time elapses.

Cottet and Koumoutsakos [8] however note that the classic stretching scheme manages to keep the flow divergence-free reasonably well by construction. As long as the particles maintain sufficient overlap (see section 3.5), the initial disturbance at time zero of the divergence is not significantly amplified. Moreover, the implementation of viscous diffusion seems to have a very positive effect on the treatment of divergence. The transpose scheme on the other hand does not seem to share these properties, and the handling of divergence most probably has to be considered.

Fortunately, due to the fact that the velocity field is actually divergence-free, a divergence-free vorticity field can be reconstructed from the velocity field. By observing the vector identity $\nabla \times (\nabla \times \boldsymbol{A}) = \nabla(\nabla \cdot \boldsymbol{A}) - \nabla^2 \boldsymbol{A}$, the following relationship is obtained:

$$\boldsymbol{\omega} = \nabla \times \boldsymbol{u} = \nabla \times \left(\nabla \times \tilde{\boldsymbol{\psi}}\right) = -\nabla^2 \tilde{\boldsymbol{\psi}} + \nabla\left(\nabla \cdot \tilde{\boldsymbol{\psi}}\right) = \tilde{\boldsymbol{\omega}} + \nabla\left(\nabla \cdot \tilde{\boldsymbol{\psi}}\right) \tag{3.27}$$

It is clear that the second term in the RHS drops out for a solenoidal field, as the divergence of the stream function would be zero then, but for the discretized case this term has to be taken into account. Two methods are presented for the relaxation of the particle divergence. The first method employs the relationship above and provides a physical explanation for relaxation, but relies on solving a system of linear equations. The second method is on a purely mathematical basis and is not supported by vortex theory, but it seems that good results are obtained with just a limited computational effort.

3.3.1 Relaxation of the particle divergence by Novikov

The following method has been outlined by Winckelmans and Leonard [37]. For a regularized particle field, equation 3.27 becomes:

$$\begin{aligned}
\boldsymbol{\omega}_\sigma(\boldsymbol{x},t) &= \tilde{\boldsymbol{\omega}}_\sigma(\boldsymbol{x},t) + \nabla\left(\nabla\cdot\tilde{\boldsymbol{\psi}}(\boldsymbol{x},t)\right)\\
&= \sum_p \boldsymbol{\alpha}^p(t)\zeta_\sigma(\boldsymbol{x}-\boldsymbol{x}^p(t)) + \sum_p \nabla\left(\boldsymbol{\alpha}^p(t)\cdot\nabla G_\sigma(\boldsymbol{x}-\boldsymbol{x}^p(t))\right)\\
&= \sum_p \boldsymbol{\alpha}^p(t)\zeta_\sigma(\boldsymbol{x}-\boldsymbol{x}^p(t)) + \sum_p \left[\frac{-g_\sigma(\boldsymbol{x}-\boldsymbol{x}^p(t))}{\|\boldsymbol{x}-\boldsymbol{x}^p(t)\|^3}\boldsymbol{\alpha}^p\right.\\
&\quad\left. + \left(3\frac{g_\sigma(\boldsymbol{x}-\boldsymbol{x}^p(t))}{\|\boldsymbol{x}-\boldsymbol{x}^p(t)\|^3} - \zeta_\sigma(\boldsymbol{x}-\boldsymbol{x}^p(t))\right)\times\frac{(\boldsymbol{x}-\boldsymbol{x}^p(t))\cdot\boldsymbol{\alpha}^p(t)}{\|\boldsymbol{x}-\boldsymbol{x}^p(t)\|^2}(\boldsymbol{x}-\boldsymbol{x}^p(t))\right]
\end{aligned} \tag{3.28}$$

Now a set of linear equations can be introduced, that solve equation 3.28 for all p:

$$\begin{aligned}
\sum_q \boldsymbol{\alpha}^q_{\text{new}}(t)\zeta_\sigma(\boldsymbol{x}^p(t)-\boldsymbol{x}^q(t)) = \sum_q &\left[\boldsymbol{\alpha}^q_{\text{old}}(t)\zeta_\sigma(\boldsymbol{x}^p(t)-\boldsymbol{x}^q(t))\right.\\
&\left.+\nabla\left(\boldsymbol{\alpha}^q_{\text{old}}(t)\cdot\nabla G_\sigma(\boldsymbol{x}^p(t)-\boldsymbol{x}^q(t))\right)\right]
\end{aligned} \tag{3.29}$$

The set of linear equations is probably large, and therefore most conveniently solved by an iterative approach. By writing $\boldsymbol{A}\boldsymbol{\alpha}_{\text{new}} = \boldsymbol{\alpha}_{old}$ and by assuming that the old and new particle strengths are close to each other, it follows that $\boldsymbol{A}$ has to lie close to the identity matrix $\boldsymbol{I}$. Using the fact that $\boldsymbol{A} = \boldsymbol{I} + (\boldsymbol{A}-\boldsymbol{I})$, a convergent scheme now follows for all p, with the initial condition of $\boldsymbol{\alpha}^{p,(0)}_{\text{new}} = \boldsymbol{\alpha}^p_{old}$ and a^{pq} the respective term from matrix $\boldsymbol{A}$:

$$\boldsymbol{\alpha}^{p,(n)}_{\text{new}} = \left(\boldsymbol{\alpha}^p_{old} + \boldsymbol{\alpha}^{p,(n-1)}_{\text{new}}\right) - \sum_q a^{pq}\boldsymbol{\alpha}^{p,(n-1)}_{\text{new}} \tag{3.30}$$

3.3.2 Relaxation of the particle divergence by Pedrizzetti

The necessity of solving a linear set of equations can be avoided by a more practical approach, called the Divergence Filtering Method (DFM) by Pedrizzetti [24]. Each time step, the particles are updated along equation 3.31, with Δt being the size of the time step and f a time step dependent frequency factor.

$$\boldsymbol{\alpha}^p_{\text{new}}(t) = (1 - f\Delta t)\, \boldsymbol{\alpha}^p_{\text{old}}(t) + f\Delta t \frac{\boldsymbol{\omega}_\sigma(\boldsymbol{x}^p(t), t)}{\|\boldsymbol{\omega}_\sigma(\boldsymbol{x}^p(t), t)\|} \left\|\boldsymbol{\alpha}^p_{\text{old}}(t)\right\| \tag{3.31}$$

There is not a clear-cut physical explanation as a justification for this method other than a mathematical relaxation, but in practice the results obtained with the DFM seem to be satisfactory. Effectively, this method provides a smoothing of the strength vector by aligning with neighbouring particles, and as such simulates the connectivity aspect of the vortex filament. The frequency factor f has to be manually tuned along the time step size used, but it turns out that a very small f often already provides desirable results ($f \approx 0.02$).

3.4 Viscous diffusion

Vortex methods are particularly suited for describing turbulent flows. Filaments provide a Lagrangian description of the NS-equations in vorticity form, which result in a physical description of vortical flows over a range of scales. In the case of lower Reynolds numbers, particles offer a more convenient way to handle viscous diffusion due to the lack of connectivity. The motivation for the current thesis work lies however in the large-scale wind turbine applications, but even in the case of turbulent flow, handling of viscous diffusion has to be considered. On the one hand, viscous effects are at the origin of vorticity creation for bluff bodies, but more important in the current situation: intense vortex stretching will form prohibitive small scales of complexity within the flow, and viscous diffusion provides the only mechanism for dissipating these small scale energies (Cottet and Koumoutsakos [8]). The phenomenon of intense vortex stretching has been encountered extensively during carrying out of the simulations for the present thesis work, and viscous diffusion has indeed been found to be essential for the treatment of small flow scales.

3.4.1 The Random Walk Method

An attractive solution for high-Reynold number flows is offered by the Random Walk Method (RWM) as proposed by Chorin [7], whereby an extra random component is added to the particle velocities to simulate diffusion. In this sense, diffusion of the vorticity field has to be seen in the mean of the random particle motion, but the RWM converges to that of the NS-equations, with conservation of vorticity. A large amount of particles is however required, to keep the statistical error low, and applicability is constrained to high Reynolds numbers where the gradients over time are small. For the application of the RWM, viscous splitting is applied, whereby the convection of the flow is first resolved. Then, the particle location is updated as $\boldsymbol{x}^{p,(n+1)} = \boldsymbol{x}^{p,(n)} + \boldsymbol{\xi}^{p,(n)}$, with $\boldsymbol{\xi}^{p,(n)}$ being the extra term due to Brownian motion along the following Gaussian probability distribution with zero mean and the variance as $\varepsilon = 2\nu\Delta t$:

$$G = \frac{1}{\left(\sqrt{2\pi\varepsilon}\right)^d} e^{\frac{-x^2}{2\varepsilon}} \tag{3.32}$$

3.4.2 Core Spreading Methods

The RWM is attractive and often applied due to its simplicity while still converging to the NS-equations, but other methods provide a more physical interpretation. In this sense, Leonard [18] introduced the Core Spreading Method (CSM). Hereby, the core is allowed to grow to simulate viscous diffusion (much like the viscous core growth as discussed in the former section). This method, however, does not converge to the NS equations as time elapses as the core grows beyond the characteristic length scales. Rossi [27] introduced the Corrected Core Spreading Method (CCSM), where the particles are allowed to split and reposition in the cross-sectional plane, as soon as the initial particle grows beyond a specific threshold core size. Thereby, convergence of the method is ensured. Rossi envisioned a splitting of the parent particle into M evenly distributed child parents circumferentially around the parent particle (whereby the parent particle itself loses all its strength and thus vanishes). To conserve both viscosity and the angular momentum, the conditions of equations 3.33 through 3.35 have to be fulfilled (where the indices p and c denote parent and child particles respectively, and α denotes a scaling factor between 0 and 1):

$$\|\boldsymbol{x}^c - \boldsymbol{x}^p\| = \sqrt{(1-\alpha^2)}\sigma^p \tag{3.33}$$

$$\boldsymbol{\alpha}^c = \frac{\boldsymbol{\alpha}^p}{M} \tag{3.34}$$

$$\sigma^c = \alpha\sigma^p \tag{3.35}$$

3.4.3 Particle Strength Exchange

A final method that will be discussed is the Particle Strength Exchange (PSE) method by Degond [9]. Where the Random Walk Method and Core Spreading Methods rely on updating either the particle position or the core size, the Particle Strength Exchange method maintains these properties. Instead, the circulation is exchanged with neighbouring particles to simulate viscous diffusion. A great advantage of this method is that it allows the particles to represent numerical volumes of vorticity, rather than being physical cores. On the other hand, the PSE method requires neighbouring particles to be able to diffuse vorticity. The general formulation of the PSE scheme is presented in equation 3.36, and the result for the high-order algebraic kernel is given in equation 3.37.

$$\left.\frac{d\boldsymbol{\alpha}^p}{dt}\right|_{\text{visc.}} = -2\nu\sum_q \frac{1}{\sigma^5\rho}\frac{d\zeta(\rho)}{d\rho}\left(\text{vol}^p\boldsymbol{\alpha}^q - \text{vol}^q\boldsymbol{\alpha}^p\right) \tag{3.36}$$

$$\left.\frac{d\boldsymbol{\alpha}^p}{dt}\right|_{\text{visc, HOA}} = \frac{105\nu}{4\pi}\sum_q \frac{1}{\sigma^5(\rho^2+1)^{\frac{9}{2}}}\left(\mathrm{vol}^p\boldsymbol{\alpha}^q - \mathrm{vol}^q\boldsymbol{\alpha}^p\right) \qquad (3.37)$$

For the current thesis work, multiple variants of the core spreading method have been experimented with, but it turned out that the implementation of a PSE scheme always gave the most satisfactory results in the end. Especially regarding the stability of the simulation, the PSE mechanism is a welcoming measure to mitigate instabilities as stresses resulting from intense stretching, sharp curvatures, vortex roll-up, and entanglement are effectively dealt with.

3.5 Lagrangian grid distortions

An important topic regarding both the accuracy and stability of the vortex particle method is to maintain the integrity of the Lagrangian grid. This has to be understood as keeping the field smooth enough, such that both under- and over-resolved areas of vorticity areas are avoided or corrected for. As the essence of the vortex particle method lies in the communication of information between particles, a minimum particle overlap is obliged for the success of the simulation. If the overlapping condition is violated, a computation is bound to become inaccurate. Apart from case-specific initial particle distributions (e.g. concentric rings), this loss of overlap is an inherent problem of purely Lagrangian methods. Especially in filament direction major problems will arise regarding both accuracy and stability. For instance, the particles may start to diverge, such that the explicit connection between particles ceases to exist. As a result the simulation is prone to instabilities and will most probably blow-up (loss of particle alignment and an unbounded growth of particle strength vectors). On the other hand, the particles might succeed in staying connected, but extremely fine and unstable filament structures will appear through (non-physical) intense stretching due to vortex roll-up behaviour. Another example is given by the fact that for instance the PSE scheme requires a basis of particles to diffuse vorticity over the domain, or that filaments (as discretized by particles) loose energy if the overlap is under-resolved. Hence, large errors in the velocity field will appear.

Two types of methods are usually applied for correcting the grid distortion. One can either redistribute the vorticity by remeshing the particles over the domain, or on the other hand by maintaining the current particle positions through redistribution of the circulations. Often Eulerian remeshing strategies are applied, although in the current thesis work it is of interest to maintain the full Lagrangian description. Another form of remeshing is however implemented, through which particles are added in filament direction, whenever the overlap is at the verge of becoming under-resolved. This method is outlined below.

3.5.1 Remeshing by particle splitting

In an inviscid fluid, the volume of vorticity represented by the particle has to remain constant over time ($d(\sigma^2 L)/dt = 0$). As a consequence, the core radius shrinks during stretching of the filament. In a vortex particle method this core shrinking is in conflict with the overlapping condition ($\lambda = \sigma/h$), which requires the core to grow linear with stretching. Viscous diffusion allows for some core growth in the physical sense, but especially in high-Reynolds number flows this will not assure particle overlap in the longitudinal direction for all times. Let σ_r be the real core radius, and σ_v the core radius of a vortex model to satisfy the overlapping condition. The core growth rate for both cases is given in equations 3.38 and 3.39 respectively.

$$\frac{d\sigma_v}{dt} = \lambda \frac{dL}{dt} \tag{3.38}$$

$$\frac{d\sigma_r}{dt} = -\frac{\sigma_r}{2L}\frac{dL}{dt} + \frac{2\nu}{\sigma_r} \tag{3.39}$$

λ is the overlapping factor. As a rule of thumb it should be larger than 1. A method to satisfy both the real and the overlapping condition, is to split the particles in longitudinal direction on a regular base, such that in the new case $\sigma_v = \sigma_r$. If volume is conserved, it follows that splitting has to occur if $L \geqslant 2^{2/3} L_0$, with L the current filament length, and L_0 the original filament length at initiation. Each of the two children is positioned a quarter of the parent filament length on each side of the parent particle, and receives half of the strength, length, and core radius. In this way, the physical meaning of the core radius is conserved. Pedrizzetti [24]

3.6 Performance parameters

Over de course of this chapter, several physical and numerical aspects of vortex particle methods have been discussed. Topics like the solenoidal vorticity field, and the particle regularization and overlap, are of paramount importance regarding the stability of the VPM. It is thus important to assess the performance of the VPM over time. Relevant parameters are offered by the linear and quadratic invariants of the flow, such as the conservation of vorticity and energy. As the name indicates, invariants are conserved for a real fluid, but for a discretized particle field these invariants will divert from the real solution. In the discretized case the invariants are called diagnostics, and it turns out in the following discussion that these diagnostics are valuable in the verification process, as the performance of each diagnostic is dependent on specific attributes of the quality of the simulation. A separate analysis is presented for both the linear and the quadratic diagnostics, with the notion that either an inviscid or a viscous incompressible flow is considered, with a unit density and unbounded flow conditions (thus, the vorticity approaches zero at infinity).

3.6.1 Linear invariants and diagnostics

Both the total vorticity $\boldsymbol{\Omega}$, the linear momentum $\boldsymbol{I}$, and the angular momentum $\boldsymbol{A}$ are conserved for both the inviscid and viscous flow conditions, see equations 3.40 through

3.42.

$$\boldsymbol{\Omega} = \int \boldsymbol{\omega} d\boldsymbol{x} = 0 \quad ; \quad \frac{d\boldsymbol{\Omega}}{dt} = 0 \tag{3.40}$$

$$\boldsymbol{I} = \int \boldsymbol{u} d\boldsymbol{x} = \frac{1}{2} \int \boldsymbol{x} \times \boldsymbol{\omega} d\boldsymbol{x} \quad ; \quad \frac{d\boldsymbol{I}}{dt} = 0 \tag{3.41}$$

$$\boldsymbol{A} = \int \boldsymbol{x} \times \boldsymbol{u} d\boldsymbol{x} = \frac{1}{3} \int \boldsymbol{x} \times (\boldsymbol{x} \times \boldsymbol{\omega}) \, d\boldsymbol{x} \quad ; \quad \frac{d\boldsymbol{A}}{dt} = 0 \tag{3.42}$$

After discretization of the vorticity field by particles, the linear invariants are generally not conserved anymore due to the violation of the divergence-free condition of the vorticity field ($\tilde{\boldsymbol{\omega}} \neq \boldsymbol{\omega}$). Instead, the invariants are now referred to as diagnostics, see equations 3.43 through 3.46. The expression for the singular and regularized case are similar, except for the angular momentum which is dependent on a regularization-specific function C. This extra term vanishes if the particle divergence is maintained well, thus when $\boldsymbol{\Omega} \approx 0$. In any other case, C has to be obtained which is usually not straightforward, with the exception of the high order algebraic kernel for which $C = \frac{3}{2}$.

$$\tilde{\boldsymbol{\Omega}} = \tilde{\boldsymbol{\Omega}}_\sigma = \sum_p \boldsymbol{\alpha}^p(t) \tag{3.43}$$

$$\tilde{\boldsymbol{I}} = \tilde{\boldsymbol{I}}_\sigma = \frac{1}{2} \sum_p \boldsymbol{x}^p(t) \times \boldsymbol{\alpha}^p(t) \tag{3.44}$$

$$\tilde{\boldsymbol{A}} = \frac{1}{3} \sum_p \boldsymbol{x}^p(t) \times (\boldsymbol{x}^p(t) \times \boldsymbol{\alpha}^p(t)) \tag{3.45}$$

$$\tilde{\boldsymbol{A}}_\sigma = \tilde{\boldsymbol{A}} - \frac{2}{9} C \sigma^2 \boldsymbol{\Omega} \tag{3.46}$$

With:

$$C = 4\pi \int_0^\infty \zeta(\rho) \rho^4 d\rho \tag{3.47}$$

As the linear diagnostics are not conservative in general, the time-derivatives do not equal 0. An exception is formed by the transpose scheme, for which the total vorticity is actually conserved for the singular case, as $d\boldsymbol{\Omega}/dt|_T = 0$ by construction. This result implies that the transpose scheme is favoured over any other stretching scheme for the singular case, but in the regularized case there is no clear-cut best practice. Regarding the other invariants, as long as one manages to keep the divergence of the vorticity small, it turns out that also the linear and angular moments are conserved reasonably well for all schemes.

3.6.2 Quadratic invariants and diagnostics

In this section, the three quadratic properties of total kinetic energy E, helicity $\mathscr{H}$, and enstrophy $\mathscr{E}$ are discussed, see equations 3.48 through 3.50 (E is also referred to as the generalized Hamiltonian and it is actually only truly the total kinetic energy in case of zero total vorticity). The total kinetic energy and the helicity are invariants for the inviscid case, as those are conserved in an inviscid flow. The enstrophy is a measure of stretching, and is therefore understandably not conserved whenever stretching is manifested. For viscous flows, the kinetic energy decays by a rate directly proportional to the enstrophy as in $dE/dt = -\nu\mathscr{E}$. This property makes E very suitable as an indicator for viscous flow computations. Also the helicity is not conserved in the viscous case, as it has to be qualitatively understood as the net linkage of vortex lines, which can break up in viscous flows (vortex reconnection).

$$E = \frac{1}{2}\int \boldsymbol{u}\cdot\boldsymbol{u}d\boldsymbol{x} \quad ; \quad \frac{dE}{dt} = -\nu\mathscr{E} \tag{3.48}$$

$$\mathscr{H} = \int \boldsymbol{\omega}\cdot\boldsymbol{u}d\boldsymbol{x} \tag{3.49}$$

$$\mathscr{E} = \int \boldsymbol{\omega}\cdot\boldsymbol{\omega}d\boldsymbol{x} \tag{3.50}$$

The case with singular particles:

The expression for the total energy E can be rewritten as a function of the vorticity and the stream function (3.51).

$$\begin{aligned} E &= \frac{1}{2}\int \boldsymbol{u}\cdot\boldsymbol{u}d\boldsymbol{x} = \frac{1}{2}\int (\nabla\times\boldsymbol{\psi})\cdot(\nabla\times\boldsymbol{\psi})\,d\boldsymbol{x} = \frac{1}{2}\int \boldsymbol{\psi}\cdot(\nabla\times(\nabla\times\boldsymbol{\psi}))\,d\boldsymbol{x} \\ &= \frac{1}{2}\int \boldsymbol{\psi}\cdot\left(-\nabla^2\boldsymbol{\psi} + \nabla(\nabla\cdot\boldsymbol{\psi})\right)d\boldsymbol{x} = \frac{1}{2}\int \boldsymbol{\psi}\cdot\boldsymbol{\omega}d\boldsymbol{x} + \frac{1}{2}\int \boldsymbol{\psi}\cdot\nabla(\nabla\cdot\boldsymbol{\psi})\,d\boldsymbol{x} \end{aligned} \tag{3.51}$$

The second term in the final expression vanishes for a solenoidal particle field ($\nabla\cdot\boldsymbol{\psi} = 0$). As expression 3.51 is effectively only a function of $\boldsymbol{u}$, which is solenoidal by construction, it is thus possible to reconstruct the total divergence-free energy E from a discretized particle field. For the singular case (with $\rho = \|\boldsymbol{r}_{qp}\|/\sigma$ and $\boldsymbol{r}_{qp} = \boldsymbol{x}^p - \boldsymbol{x}^q$) this results in equations 3.52 and 3.53.

$$\tilde{E} = \frac{1}{2}\int \tilde{\boldsymbol{\psi}}\cdot\tilde{\boldsymbol{\omega}}d\boldsymbol{x} = \frac{1}{8\pi}\sum_p\sum_q \frac{\boldsymbol{\alpha}^p\cdot\boldsymbol{\alpha}^q}{\|\boldsymbol{r}_{qp}\|} \quad ; \quad p \neq q \tag{3.52}$$

$$E = \tilde{E} + \frac{1}{16\pi}\sum_p\sum_q \frac{1}{\boldsymbol{r}_{qp}}\left(\frac{\boldsymbol{r}_{qp}\cdot\boldsymbol{\alpha}^p}{\|\boldsymbol{r}_{qp}\|}\times\frac{\boldsymbol{r}_{qp}\cdot\boldsymbol{\alpha}^p}{\|\boldsymbol{r}_{qp}\|} - \boldsymbol{\alpha}^p\cdot\boldsymbol{\alpha}^q\right) \quad ; \quad p \neq q \tag{3.53}$$

Equation 3.53 is a good indicator for the performance of the simulation regarding divergence. If the solenoidal conditions is well maintained, the second term in the RHS has to vanish. I.e. only $\tilde{E}$ remains.

In contrast to the total energy, the helicity is directly a function of the vorticity which is generally not divergence-free. However, when applying equation 3.28, one re-obtains the correct vorticity field as $\tilde{\boldsymbol{\omega}} \to \boldsymbol{\omega}$, and thus $\tilde{\mathscr{H}} \to \mathscr{H}$. This results in the concise expression for the helicity in equation 3.54.

$$\mathscr{H} = \frac{1}{4\pi} \sum_p \sum_q \frac{\boldsymbol{r}_{qp}}{\|\boldsymbol{r}_{qp}\|^3} \cdot \left(\boldsymbol{\alpha}^p \times \boldsymbol{\alpha}^q\right) \tag{3.54}$$

The enstrophy $\mathscr{E}$ is undefined for singular particles, as an infinitesimally small core would result in an infinitely large vortical rotation.

The case with regularized particles:

Obtaining expressions for regularized quadratic diagnostics is not so straightforward as it was for the linear case. A double regularization is required as each quadratic diagnostic is dependent on two regularized terms, e.g. $E_{\sigma\sigma} = \frac{1}{2} \int \boldsymbol{u}_\sigma \cdot \boldsymbol{u}_\sigma d\boldsymbol{x}$, but exact solutions of double-regularized diagnostics are generally not available. One is thus compelled to considering approximations by once-regularized functions instead, where only solutions are known in the case of the higher order algebraic kernel, for which the expressions for the total energy and helicity are presented in equations 3.55 through 3.56.

$$\tilde{E}_\sigma = \frac{1}{2} \int \tilde{\boldsymbol{\psi}}_\sigma \cdot \tilde{\boldsymbol{\omega}} d\boldsymbol{x} = \frac{1}{8\pi} \sum_p \sum_q \frac{1}{\sigma} \frac{\rho^2 + \frac{3}{2}}{\left(\rho^2 + 1\right)^{\frac{3}{2}}} \boldsymbol{\alpha}^p \cdot \boldsymbol{\alpha}^q \tag{3.55}$$

$$\begin{aligned} E_\sigma = \tilde{E}_\sigma + \frac{1}{16\pi} \sum_p \sum_q \frac{1}{\|\boldsymbol{r}_{qp}\|} \Bigg[& \frac{-\rho}{\left(\rho^2 + 1\right)^{\frac{3}{2}}} \boldsymbol{\alpha}^p \cdot \boldsymbol{\alpha}^q \\ & + \frac{\rho^3}{\left(\rho^2 + 1\right)^{\frac{3}{2}}} \times \left(\frac{\left(\boldsymbol{r}_{qp} \cdot \boldsymbol{\alpha}^p\right)}{\|\boldsymbol{r}_{qp}\|} \frac{\left(\boldsymbol{r}_{qp} \cdot \boldsymbol{\alpha}^q\right)}{\|\boldsymbol{r}_{qp}\|} - \boldsymbol{\alpha}^p \cdot \boldsymbol{\alpha}^q \right) \Bigg] \end{aligned} \tag{3.56}$$

$$\mathscr{H}_\sigma = \frac{1}{4\pi} \sum_p \sum_q \frac{1}{\sigma^3} \frac{\left(\rho^2 + \frac{5}{2}\right)}{\left(\rho^2 + 1\right)^{\frac{5}{2}}} \times \left(\boldsymbol{r}_{qp} \cdot \left(\boldsymbol{\alpha}^p \times \boldsymbol{\alpha}^q\right)\right) \tag{3.57}$$

Opposed to the singular case, an expression for the once-regularized enstrophy is actually available. Like the helicity, the enstrophy is a function of the vorticity, and a similar approach is followed by forcing $\tilde{\boldsymbol{\omega}} \to \boldsymbol{\omega}$ and $\tilde{\boldsymbol{\omega}}_\sigma \to \boldsymbol{\omega}_\sigma$. That way, an exact result for the enstrophy is obtained and shown in equations 3.58 and 3.59.

$$\tilde{\mathscr{E}}_\sigma = \int \tilde{\boldsymbol{\omega}} \cdot \tilde{\boldsymbol{\omega}}_\sigma d\boldsymbol{x} = \frac{1}{4\pi} \sum_p \sum_q \frac{15}{2\sigma^3} \frac{1}{\left(\rho^2 + 1\right)^{\frac{7}{2}}} \boldsymbol{\alpha}^p \cdot \boldsymbol{\alpha}^q \tag{3.58}$$

$$\begin{aligned} \mathscr{E}_\sigma = \tilde{\mathscr{E}}_\sigma + \frac{1}{4\pi} \sum_p \sum_q \frac{1}{\sigma^3} \Bigg[& \frac{-\left(\rho^2 + \frac{5}{2}\right)}{\left(\rho^2 + 1\right)^{\frac{5}{2}}} \boldsymbol{\alpha}^p \cdot \boldsymbol{\alpha}^q \\ & + 3 \frac{\rho^2 \left(\rho^2 + \frac{9}{2}\right) + \frac{7}{2}}{\left(\rho^2 + 1\right)^{\frac{9}{2}}} \times \left(\left(\boldsymbol{x}^p \cdot \boldsymbol{x}^q\right) \cdot \boldsymbol{\alpha}^p\right) \left(\boldsymbol{r}_{qp} \cdot \boldsymbol{\alpha}^q\right) \Bigg] \end{aligned} \tag{3.59}$$

Again, for a solenoidal field, the second term in the RHS of equation 3.59 vanishes.

Note that because the single-regularized expressions are used instead of the correct double-regularized ones, E_σ and $\mathscr{H}_\sigma$ will not be conservative, even for a well discretized, nearly divergence-free, inviscid flow.

3.7 Conclusions

The vorticity transport equation is presented, which serves as the evolution equation of vorticity over space and time. Along with the Biot-Savart law for the velocity, these equations for the basis of vortex theory. With vortex filaments, the evolution of vorticity (vortex stretching) is implicitly treated through the conservation of circulation, easing the computational difficulty of the fluid. With vorticity carrying particles, the vorticity stretching actually has to be taken into account explicitly, making the problem more complex, but at the same time more versatile through a lack of connectivity. Hence, particles are better suited for the handling of viscous or turbulent diffusion, blade-wake interactions, and regions of intense vortex stretching.

Several topics within the theory of Lagrangian vortex particle theory are addressed. First, the smoothing of the singular particle field by applying regularization cores, to prevent unintended small rotational scales and to assure particle overlap for communication between particles. Regarding the vorticity stretching, different numerical implementations are presented that are physically equal under the condition of a solenoidal particle field, but do posses different modelling qualities otherwise. The handling of the solenoidal condition and grid distortions is discussed, and finally the importance of viscous diffusion (even for turbulent flows) along with viscous schemes are presented.

The last section of the theoretical content covers the relevance of tracking the linear and quadratic diagnostics of the simulation, to obtain a quantitative insight into the modelling performance. These include the linear momenta up to the second order, which should remain constant in the flow, and the quadratic total energy, helicity, and enstrophy. The latter two quadratics are indicators for the amount of stretching and rotation in the flow, and are especially useful for viscous computations.

Chapter 4

The Application of an $\mathcal{O}(N \log N)$ Fast Multipole Method

The vortex particle method scales as $\mathcal{O}(N^2)$, which requires the use of fast summation methods once the simulation size falls in the range of tens of thousands of particles and beyond. An attractive solution is offered by the Fast Multipole Method (FMM), which is based on the recognition that the effect of a cluster of particles at a certain distance can be approximated by a finite series expansion. The domain is then decomposed into groups of varying spatial sizes containing particles. The near-interactions are calculated directly, but far-interactions between clusters are handled through multipole expansions. The larger the inter-cluster distance, the courser the resolution of the interaction which is justifiable. Greengard and Rokhlin [14] have introduced the technique of the FMM, and their algorithm could theoretically improve the computational cost up to $\mathcal{O}(N)$. Currently an $\mathcal{O}(N \log N)$-version of the FMM is implemented, however, as discussed hereafter.

4.1 Summary of the FMM algorithm

In this section, an informal description of an $\mathcal{O}(N \log N)$ version of the FMM is presented, which has been implemented into the VPM for the present thesis work. The method requires a profound bookkeeping of the computational domain into a complete data structure. To this extent, several subsequent steps can be distinguished. First, the data structure is defined by construction of a tree, where the computational domain is (sub)divided into layers of refinement holding an increasing amount of boxes dependent on the local particle density. When the domain structure is defined, the local multipole expansions are calculated around the centers of the boxes in the finest levels, and subsequently these expansions are translated to the centers of the boxes in the coarser levels below. After this step, the source field is fully described in terms of multipole expansions, and the potential or its derivatives are computed at each target point by taking far-field interactions through multipole expansions, while near-field interactions are still taken directly between particles.

In the method by Greengard and Rokhlin [14], the multipole expansions are turned into local expansions after translation during traversing of the tree, such that all the target points in a box obtain the far-field interactions through the local expansion around the center of its own box, instead of interaction with all the individual multipole expansions of all far-field boxes. In the optimal case this reduces the computational effort down to $\mathcal{O}(N)$, but it requires extra traversing steps in the tree to compute the set of local expansions, and as such increases the overhead.

Step 1: Defining the data structure:
The computational domain is subdivided into a quad-tree in two dimensions or an octa-tree in three dimensions. As the current implementation of the FMM is in 3D, the explanation continues with a description of the octa-tree, although the corresponding figures show the 2D case for clarity. This means that for each dimension the domain is cut in half into equally sized boxes which is repeated for each level (level 1: 1 box, level 2: 8 boxes, level 3: 64 boxes, etc.). This defines the topology of the computational domain with increasing levels of refinement. Each box therefore holds 8 children, or 8 children have a common parent box in the level below. As long as a certain criterion is not fulfilled (which usually yields a maximum amount of particles allowed in a box, or a maximum level of refinement), the subdivision continues. The children at the finest levels are then called the leafs of the tree. The construction of the data tree is shown in figure 4.1.

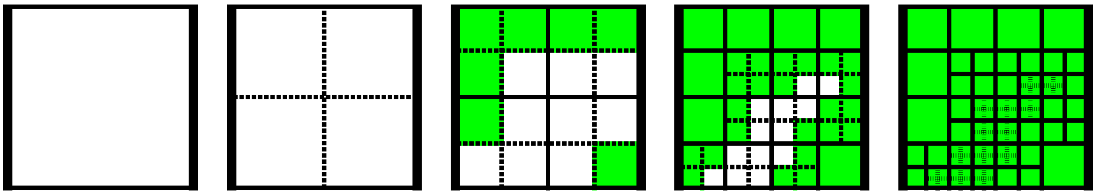

(a) Level 1 (b) Level 2 (c) Level 3 (d) Level 4 (e) Level 5

Figure 4.1: *The construction of a quad-tree (or an octa-tree in 3D) takes place by subsequent subdivisions of the parent (or root) box into 4 (or 8) child boxes as long as the number of respective particles in the root box exceeds a threshold. Once this threshold has been reached, the subdivision of the parent box stops, and a child box at the finest subdivision is called a leaf box as shown in green.*

Along with the division of the computational domain, relevant properties are obtained simultaneously that identify the local domain structure, such as data-lists holding the relationship between neighbouring boxes, which particles are in the box, and the box dimensions (radius, center, and mass).

Step 2: Calculating and shifting the multipole expansions:
For the finest level, the multipole expansions of the potential of all the particles being hold in a certain leaf box are calculated around that box' center (figure 4.2a). These multipole

expansions are then shifted downwards and translated from the centers of the children to that of the parent boxes at the level below, so that the parent box holds a combination of the 8 multipole expansions of its childs (figure 4.2b). This is called traversing of the multipole expansions over the tree, and it is carried out down to level 2 in the current implementation.

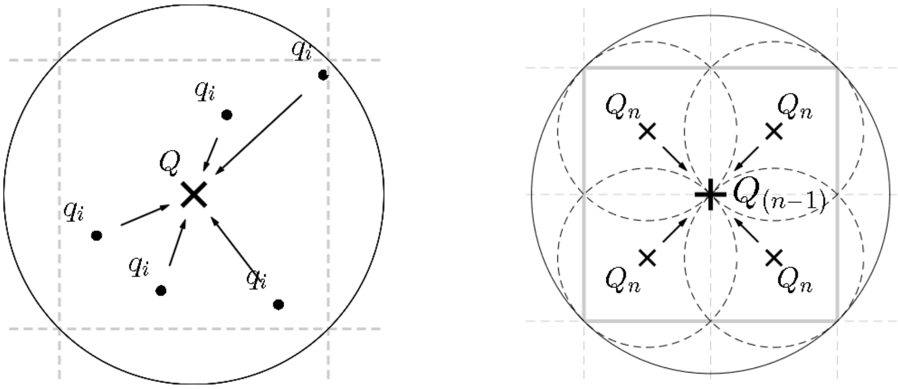

(a) Collecting expansions (b) Traversing the tree

Figure 4.2: *For each leaf box, the influence of each individual particle within the box is collected at the center of the box as a multipole expansion (a). Thereafter, the multipole expansions from the 8 child boxes (but depicted as 4 boxes in 2D) at level n are collected at the center of the box of the parent box at level n-1 of the tree, starting from the leafs down to level 2 (b).*

Step 3, Calculating the interactions:
Successful calculation of the influence of the multipole expansion around source Q at target P requires that Q and P are well-separated from each other (figure 4.3a). In other words, the ratio of the diameter d of the circle around Q holding all the individual particles divided by the distance D between P and Q has to be bigger than 1, or otherwise the solution would not converge. This criterion is captured by the acceptance factor θ. The bigger the acceptance factor is taken, the further away the multipole expansion of a certain size has to be to get accepted by target P, but also the more accurate the solution and the faster the convergence. To ensure convergence, θ has to be at least 1.

In a close region around source P, the source and target are not well-separated for any level of refinement, and direct particle-particle interactions become necessary. On the other hand, the further away from the target, expansions from lower levels in the tree can be accepted, reducing the computational effort (figure 4.3b).

Note that up till now each figure depicts a circle as wide as the diagonal of the box centered around the middle of the box (figures 4.2a and 4.2b). The current implementation, however, calculates the center of the box $\boldsymbol{x}^Q$ like in equation 4.1 as a weighted average of all the particles $\boldsymbol{x}_i^q$ contained in that box, with the diameter d being as wide as MAX $\left(2 \cdot \left\|\boldsymbol{x}_i^q - \boldsymbol{x}^Q\right\|\right)$. This also implies that multipole expansions of directly neighbouring boxes can be accepted, as long as the center of the multipole expansion is far away enough or the expansion diameter small enough.

$$\boldsymbol{x}^Q = \frac{\sum_i \boldsymbol{x}_i^q \cdot \boldsymbol{\alpha}_i^q}{\sum_i \boldsymbol{\alpha}_i^q} \tag{4.1}$$

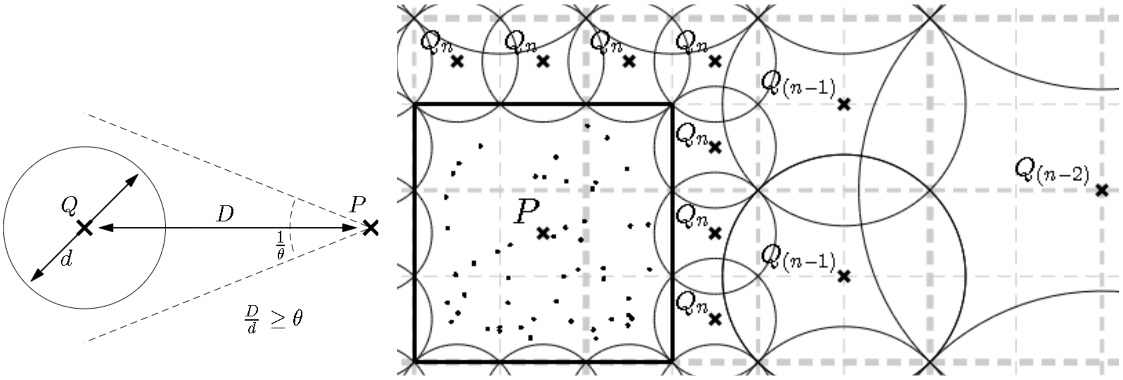

(a) Acceptance factor (b) Near- and far-field interactions

Figure 4.3: *Interactions between the multipole expansions around source Q with target point P can take place as long as the ratio of D/d is greater than the acceptance factor θ (a). Figure (b) shows that further away, multipole expansions of boxes lower in the tree can be taken. In the near-field (shown as the box around target point P) the interactions have to be taken directly, though, as the centers of the surrounding boxes are too close to P.*

4.2 Analytical description of the FMM

The description of the multipole expansion technique presented here follows to a great extent the Greengard-Rokhlin formulation as used in the work of Koumoutsakos [17].

The potential Φ induced by a source of unit-strength $Q(\boldsymbol{x}^Q)$ on a target point $P(\boldsymbol{x}^P)$ in a spherical coordinate system is described by equation 4.2, in which $\boldsymbol{x}^P = \{\rho_P, \theta_P, \phi_P\}$ and $\boldsymbol{x}^Q = \{\rho_Q, \theta_Q, \phi_Q\}$ (for an explanation of the spherical coordinate system used, the reader is referred to figure 4.4).

$$\Phi(\boldsymbol{x}^P; \boldsymbol{x}^Q) = \frac{1}{\|\boldsymbol{x}^P - \boldsymbol{x}^Q\|} \tag{4.2}$$

The general solution to Laplace's equation for the potential can also be expressed in the form of a generating formula for Legendre polynomials P_n, as in equation 4.3. This equation gives the far-field potential at point P, due to a unit-strength charge at source Q.

$$\Phi(\boldsymbol{x}^P; \boldsymbol{x}^Q) = \sum_{n=0}^{\infty} \frac{\rho_Q^n}{\rho_P^{n+1}} P_n(u) \tag{4.3}$$

The Legendre functions P_n are then expressed through spherical harmonics Y_n^m (equation 4.4), and the spherical harmonics in their turn through the associated Legendre polynomials P_n^m (equation 4.5). The Legendre functions are here expressed as a function of the cosine of angle γ, which denotes the angle between points P and Q. Note that the superindices in both these cases indicate the order, and not a power.

$$P_n(\cos\gamma_{P\to Q}) = \sum_{m=-n}^{n} Y_n^{-m}(\theta_Q,\phi_Q)Y_n^m(\theta_P,\phi_P) \tag{4.4}$$

$$Y_n^m(\theta,\phi) = \sqrt{\frac{(n-|m|)!}{(n+|m|)!}}P_n^{|m|}\cos(\theta)e^{im\phi} \tag{4.5}$$

P_n^m are dependent on their preceding terms, and described by the recurrence formula in equation 4.6, with the boundary conditions of equations 4.7 and 4.8. Note that !! indicates the double factorial which is the product of the odd integers only.

$$P_n^m(u) = \frac{(2n-1)uP_{n-1}^m(u) - (n+m-1)P_{n-2}^m(u)}{n-m} \tag{4.6}$$

$$P_{m+1}^m(u) = (2m+1)uP_m^m(u) \tag{4.7}$$

$$P_m^m(u) = (-1)^m(2m-1)!!(1-u^2)^{m/2} \tag{4.8}$$

Combining equations 4.3 and 4.4, and by introducing a particle dependent charge, a far-field representation of a collection of particles centered around point Q, that induce a potential at point P, is thus described by equation 4.9.

$$\Phi(\boldsymbol{x}^P;\{\boldsymbol{x}^{q_i}\}) = \sum_{n=0}^{\infty}\sum_{m=-n}^{n}\sum_{i=1}^{N_v} q_i\frac{\rho_i^n}{\rho_P^{n+1}}Y_n^{-m}(\theta_i,\phi_i)Y_n^m(\theta_P,\phi_P) \tag{4.9}$$

The terms describing the collection of particles centered around Q are collected, forming the multipole expansion coefficients M_n^m as in equation 4.10 and 4.11.

$$\Phi(\boldsymbol{x}^P;\{\boldsymbol{x}^{q_i}\}) = \sum_{n=0}^{\infty}\sum_{m=-n}^{n}\frac{M_n^m}{\rho_P^{n+1}}Y_n^m(\theta_P,\phi_P) \tag{4.10}$$

With,

$$M_n^m = \sum_{i=1}^{N_v} q_i\rho_i^nY_n^{-m}(\theta_i,\phi_i) \tag{4.11}$$

The solution of the potential is now described in the form of individual multipole expansions of each source particle contained in a leaf box centered around the center of that leaf. However, of interest are the multipole expansions of source particles described at the center of the leaf box, which requires a translation from $\boldsymbol{x}^{q_1} \rightarrow \boldsymbol{x}^{Q_{\text{leaf}}}$. Subsequently, these expansions have to be traversed over the tree to all the coarser levels, and repetitive translations $\boldsymbol{x}^{Q_{\text{child}}} \rightarrow \boldsymbol{x}^{Q_{\text{parent}}}$ are carried out from the leafs down the tree. The far-field representation at $\boldsymbol{x}^P$ from an expansion translated from the collection of particles to the center of that box $\boldsymbol{x}_i^q \rightarrow \boldsymbol{x}^{Q_0}$ and subsequently from that box to another box $\boldsymbol{x}^{Q_0} \rightarrow \boldsymbol{x}^{Q_1}$ is now described by equation 4.12 through 4.17, where the expansions are multiplied with inner and outer translation functions I and O to translate the multipole expansion coefficients M via C to D. The whole coordinate system is clarified in figure 4.4b.

$$\Phi(\mathbf{x}^P; \mathbf{x}^{Q_1}) = \sum_{l=0}^{\infty} \sum_{j=-l}^{l} D_l^j(\mathbf{x}_1^Q) O_n^m(\mathbf{x}^P - \mathbf{x}^{Q_1}) \tag{4.12}$$

$$D_l^j(\boldsymbol{x}^{Q_1}; \boldsymbol{x}^{Q_0}) = \sum_{n=0}^{l} \sum_{m=\text{MAX}(j+n-l,-n)}^{\text{MIN}(j+l-n,n)} C_n^m(\boldsymbol{x}^{Q_0}; \{\boldsymbol{x}^{q_i}\}) I_{l-n}^{j-m}(\boldsymbol{x}^{Q_1} - \boldsymbol{x}^{Q_0}) \tag{4.13}$$

$$C_n^m(\boldsymbol{x}^{Q_0}; \{\boldsymbol{x}^{q_i}\}) = \sum_{i=1}^{N_v} q_i \rho_i^n Y_n^m(\theta_i, \phi_i)(-1)^{-n} i^{-|m|} A_n^m \tag{4.14}$$

$$A_n^m = \frac{(-1)^n}{\sqrt{(n-m)!\,(n+m)!}} \tag{4.15}$$

$$I_{l-n}^{j-m}(\boldsymbol{x}^{Q_1} - \boldsymbol{x}^{Q_0}) = (-1)^{l-n} A_{l-n}^{j-m} \rho_{Q_0 \rightarrow Q_1}^{l-n} Y_{l-n}^{j-m}(\theta_{Q_0 \rightarrow Q_1}, \phi_{Q_0 \rightarrow Q_1}) \tag{4.16}$$

$$O_n^m(\boldsymbol{x}^P - \boldsymbol{x}^{Q_1}) = \frac{(-1)^j i^{|j|} Y_n^m(\theta_{Q_1 \rightarrow P}, \phi_{Q_1 \rightarrow P})}{A_l^j \rho_{Q_1 \rightarrow P}^{j+1}} \tag{4.17}$$

The FMM is now described in terms of the distant influence of a scalar potential at a target point due to a charge at a source point. Instead of the scalar potential due to a particle carrying a charge, of interest is the vector potential due to a particle carrying a vector strength. To this extent the potential Φ is replaced by the vector potential $\boldsymbol{\Psi}$ (the Green's function solution related to Poisson's equation), with the 3 components of the particle strength being the individual charges:

$$\Phi(\boldsymbol{x}^P; \boldsymbol{x}^Q) \rightarrow \boldsymbol{\Psi}(\boldsymbol{x}^P; \boldsymbol{x}^Q) = \frac{-1}{4\pi \left\| \boldsymbol{x}^P - \boldsymbol{x}^Q \right\|} \tag{4.18}$$

$$q_i \rightarrow \left\{ \alpha_x^p, \alpha_y^p, \alpha_z^p \right\} \tag{4.19}$$

The curl of the potential then gives the velocity: $\boldsymbol{u} = \nabla \times \boldsymbol{\Psi}$, but unfortunately the available FMM does not return any derivatives of the potential, and this relation has to be derived manually. This requires some effort, as the relevant terms are given in spherical coordinates. For a full derivation, the reader is referred to appendix B, but the final

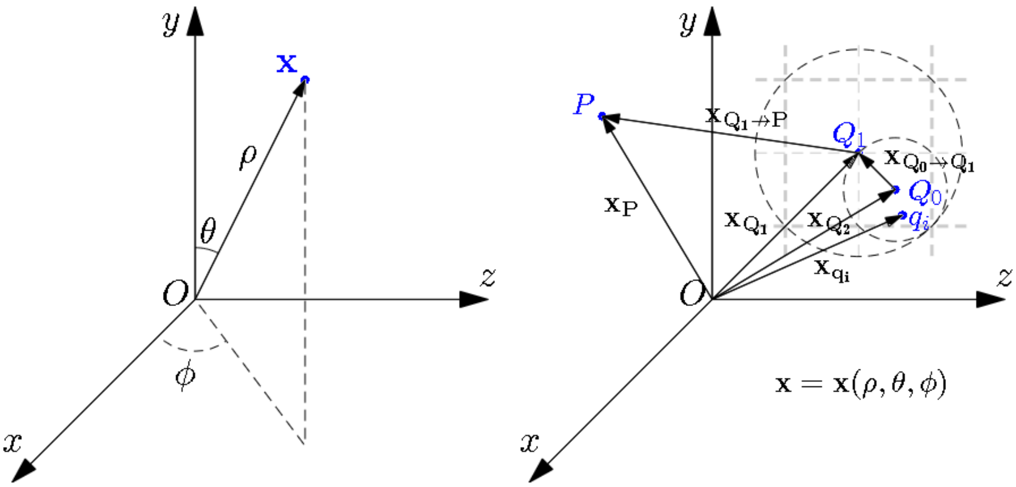

(a) Spherical coordinate system (b) Explanation of several coordinates

Figure 4.4: *Spherical coordinates centered around the origin are used throughout the analytical description of the FMM, with the angles defined as in (a). The vectors describing the target* P*, the centers* Q_0 *and* Q_1 *of two boxes at different levels in the tree, and a source particle* q_i *within box* Q_0 *are shown, along with two vectors describing the distance between* Q_1 *and* P*, and* Q_0 *and* Q_1*.*

outcome for the velocity is given in section 4.3.

The derivation for the vortex stretching is significantly longer and has not been carried out. The far-field stretching could might be ignored by using the fact that the influence of the stretching decays faster than for the velocity (with $\mathcal{O}(r^3)$ and $\mathcal{O}(r^2)$ respectively). Unfortunately, this assumption cannot be made. Even if a large radius of direct interactions is taken around the target, one would easily loose 10 % or more of stretching influence from the far-field. As the expressions for the far-field stretching are not available, one has to shift to taking finite differences from the potential at the target point. For this purpose a 3-point central difference stencil is applied which results in 6 extra computational nodes around the target point; 2 extra nodes for each dimension. As such, the gradient tensor of the velocity can be obtained. The computational effort of the FMM increases significantly, as the calculation of the extra multipole expansions on the stencil is very expensive. On the other hand, the direct derivative calculation at the original target point would be expensive too, and therefore it is interesting to investigate what the most efficient strategy is for obtaining the derivatives from the vector potential: via the direct derivative expressions or via finite differences. This investigation is presented in section 6.2.7.

Finally, it is noted that due to the fact that the original vector potential is based on a singular particle field, the resulting velocity and stretching terms are also singular. As a solution, a certain radius around the target point proportional to the particle smoothing radius is maintained in which all the interactions are solved directly. It is justifiable to take into account the interactions between the target point and all the sources outside this region through multipole expansions, as the smooth and singular solution converge with distance.

4.3 Derivation of the velocity

The relationship between the spherical multipole terms and the velocity in Cartesian coordinates can be formed into a short expression as stated in equation 4.20, with R^{-1} being the rotation matrix from spherical to Cartesian coordinates (equation 4.21), ∇O_n^m the gradient of O_n^m in spherical coordinates (equation 4.22), and $\boldsymbol{D}_n^m$ the vector holding the 3 components of D_n^m as a function of the individual components of the particle strength $\boldsymbol{\alpha}^p$ at the particle source location (equation 4.23). All the summation symbols have been left out, but all the order-terms have to be added up in between. The coordinate system (ρ, θ, ϕ) stands for the system $(\rho, \theta, \phi)_{Q_1 \to P}$ throughout the derivation. A derivation of expression 4.20 itself is presented in appendix B.

$$\boldsymbol{u}(x, y, z) = \left(R^{-1}(\theta, \phi) \nabla O_n^m(\rho, \theta, \phi)\right) \times \boldsymbol{D}_n^m(\alpha_x, \alpha_y, \alpha_z) \tag{4.20}$$

$$R^{-1}(\theta, \phi) = \begin{bmatrix} \sin\theta\cos\phi & \cos\theta\cos\phi & -\sin\phi \\ \sin\theta\sin\phi & \cos\theta\sin\phi & \cos\phi \\ \cos\theta & -\sin\theta & 0 \end{bmatrix} \tag{4.21}$$

$$\nabla O_n^m(\rho, \theta, \phi) = \frac{\partial O_n^m}{\partial \rho} \hat{\boldsymbol{\rho}} + \frac{1}{\rho} \frac{\partial O_n^m}{\partial \theta} \hat{\boldsymbol{\theta}} + \frac{1}{\rho \sin\theta} \frac{\partial O_n^m}{\partial \phi} \hat{\boldsymbol{\phi}} \tag{4.22}$$

$$\boldsymbol{D}_n^m(\alpha_x, \alpha_y, \alpha_z) = \{D_n^m(q_i = \alpha_x), D_n^m(q_i = \alpha_y), D_n^m(q_i = \alpha_z)\} \tag{4.23}$$

The gradient of O_n^m is taken by noting that $O_n^m(\rho, \theta, \phi)$, $Y_n^m(\theta, \phi)$, and $P_n^m(\theta)$. The derivative with respect to ρ therefore only requires differentiation of O_n^m itself, see equation 4.24.

$$\frac{\partial O_n^m}{\partial \rho} = -(m+1) \frac{(-1)^m i^{|m|} Y_n^m}{A_n^m \rho^{m+2}} \tag{4.24}$$

The differentiation with respect to θ is a bit more elongated, as also Y_n^m and each of the P_n^m terms require differentiation themselves. Note that by applying the chain rule, $\partial P_n^m / \partial \theta$ is turned into $-\sin\theta \cdot \partial P_n^m / \partial \cos\theta$, where P_n^m is a function of $\cos\theta$. The derivation is shown in equations 4.25 through 4.29.

$$\frac{\partial O_n^m}{\partial \theta} = \frac{(-1)^m i^{|m|}}{A_n^m \rho^{m+1}} \frac{\partial Y_n^m}{\partial \theta} \tag{4.25}$$

$$\frac{\partial Y_n^m}{\partial \theta} = \sqrt{\frac{(n-|m|)!}{(n+|m|)!}} \frac{\partial P_n^m}{\partial \cos\theta} (-\sin\theta)\, e^{im\phi} \tag{4.26}$$

$$\frac{\partial P_n^m}{\partial \cos\theta} = \frac{(2n-1)\left(P_n^m + \cos\theta \frac{\partial P_{n-1}^m}{\partial \cos\theta}\right) - (n+m-1)\frac{\partial P_{n-2}^m}{\partial \cos\theta}}{n-m} \tag{4.27}$$

$$\frac{\partial P_{m+1}^m}{\partial \cos\theta} = (2m+1)\left(P_m^m + \cos\theta \frac{\partial P_m^m}{\partial \cos\theta}\right) \tag{4.28}$$

$$\frac{\partial P_m^m}{\partial \cos\theta} = (-1)^{m-1}(2m-1)!!m\cos\theta(\sin\theta)^{m-2} \tag{4.29}$$

And finally the differentiation with respect to ϕ is concise, as ϕ only appears in an exponent within Y_n^m as shown in equations 4.30 and 4.31.

$$\frac{\partial O_n^m}{\partial \phi} = \frac{(-1)^m i^{|m|}}{A_n^m \rho^{m+1}} \frac{\partial Y_n^m}{\partial \phi} \tag{4.30}$$

$$\frac{\partial Y_n^m}{\partial \phi} = \sqrt{\frac{(n-|m|)!}{(n+|m|)!}} P_n^m i m e^{im\phi} \tag{4.31}$$

4.4 Conclusions

The theoretical content of an $\mathcal{O}(N \log N)$ Fast Multipole Method is outlined, which is a simplified version of the original $\mathcal{O}(N)$ FMM as proposed by Greengard and Rokhlin Greengard and Rokhlin [14]. In the current implementation, the multipole expansions are not turned into local expansions during traversing of the tree, which reduces the theoretical optimum efficiency, but also reduces the prefactor significantly.

The working principle of the FMM is by collecting the local source terms into multipole expansions, whereby far-field interactions between the target and source are taken through these expansions, while the near-field interactions are taken directly. To this extent, a data structure is constructed whereby the 3D domain is divided into an octa-tree, containing a further refinement of boxes over the tree levels. In the finest boxes, called the leafs of the tree, the expansions are shifted from the sources to the centers of the boxes, and accordingly from the child to the parent boxes over the coarser levels of the tree. The accuracy of the interactions is defined through the acceptance factor (measure of the distance from the target to the box) and the expansion order.

The currently implemented FMM gives the vector potential as output, though the velocity and vorticity stretching term are of interest. These terms are obtained through taking the first and second partial derivatives of the vector potential, which can be done directly or through finite differences. The velocity derivative has currently been obtained, while the stretching is taken through a 3-point central difference scheme from this velocity.

Chapter 5

Introduction to the Numerical VPM Code

In this chapter, an introduction is given into the numerical VPM and FMM code that has been developed along the theory stated in chapters 3 and 4. The code serves as a stand-alone tool where the in- and output on the client side takes place via text files. The basic features of the code are as follows:

- The VPM code offers a stand-alone numerical flow solver for the purely Lagrangian modelling of a space consisting of freely convecting and diffusing vorticity carrying particles.
- The design of the VPM is based on an existing VIC code, developed for the PhD dissertation of Rasmussen [25]. Only the routines regarding model initiation and memory allocation have been adopted. The routines related to the numerical solver have been (re)written. All algorithms are written in Fortran 90.
- The VPM makes use of the Parallel Particle-Mesh library [29] for (distributed) memory allocation, and for the FMM routines [30] and supporting modules. The PPM library is open-source and available online [39].
- The VPM is suitable for parallel computations (using MPI) when the FMM is not utilized. The FMM routines are written in parallel as well, but the present version of the FMM showed to be buggy in parallel mode. Future work is thus required to make the FMM usable for parallel computations.

5.1 The Parallel Particle-Mesh (PPM) library

The Parallel Particle-Mesh library, as the name suggests, is designed as a flexible, portable platform for both parallel particle and hybrid particle-mesh algorithms. It includes portability through the use of the Fortran 90 and C languages and the Message Passing Interface

(MPI) libraries for parallel communications. The infrastructure of the PPM covers topics such as domain composition and interpolation routines, processor load balancing and communication optimization techniques, and commonly applied numerical solvers such as the FFT and FMM methods.

The parallelization of the problem requires the space to be divided into sufficiently granular sub domains, such that a proper distribution of sub domains over the processors can be achieved . Such a decomposition in combination with the appropriate boundary conditions is known as a topology, and the PPM offers libraries for construction and communication between topologies, and the optimal load balancing over the processors.

Although the focus of the PPM functionality lies in the framework of parallel hybrid particle-mesh algorithms, only the purely Lagrangian functionality is exploited for the present thesis work.

5.2 The Fast Multipole Method (FMM) routines

The FMM is part of the PPM library, and consists of four main routines. These routines have to be called in sequence, and are outlined below:

Initiation of the FMM:
The first routine is associated with the allocation of relevant variables in the calculation of the multipole expansions, the construction of the data tree, the decomposition of tree levels into topologies, the conversion of leaf boxes into sub domains and the mapping of sub domains over the processors, and the construction of data lists of boxes containing information about neighbours and related particles. Furthermore, fundamental recurring series that appear throughout the calculation of the multipole expansions are calculated, and the box properties regarding the dimensions, box centers, and masses are computed.

Computation and traversing of the multipole expansions:
the multipole expansion coefficients are calculated by looping over the particles in each leaf of the finest tree level. The tree is subsequently traversed through which the expansion coefficients are shifted over the levels of the tree.

Computation of the potential:
In the original FMM the vector potential is computed on a set of target points as provided on the client side. This is the most relevant routine of the FMM, as this routine has been extensively rewritten with the purpose of obtaining the velocity and stretching terms.

Finalize:
In the final routine, all memory assigned to the FMM is deallocated.

5.3 Structure of the VPM program

A basic decomposition of the VPM program is demonstrated through the flowchart in figure 5.1. The program is started with calling the initiation routines. Here the input file from the client-side is read. The input file contains a user-specified number of parameter settings. If parameters are not defined by the client, default parameters are chosen by the program. Hereafter, the MPI standard is initiated, which allows the program to communicate over the processors, and the PPM is initialized.

Next, the model is set up, whereby all kind of parameters are allocated. The most important initiation involves the allocation of the particle set structure, holding all the information of the particles in the domain. Moreover, flowcase specific parameters are set, as defined through the input files.

Subsequently, the simulation is launched, whereby first the flowcase specific time dependent parameters are set, and the particle collection is updated to remove obsolete particle data. If parallel mode is enabled, the domain is now decomposed over the processors, after which the evolution equations are carried out (RHS). When enabled, the FMM is called from within the RHS module. Time integration does now take place, which is done through substeps when higher order schemes are applied. After all the substeps of the time integration have been carried out, data is deallocated, and the diagnostics for the output file are computed. This loop is repeated until the end of the simulation.

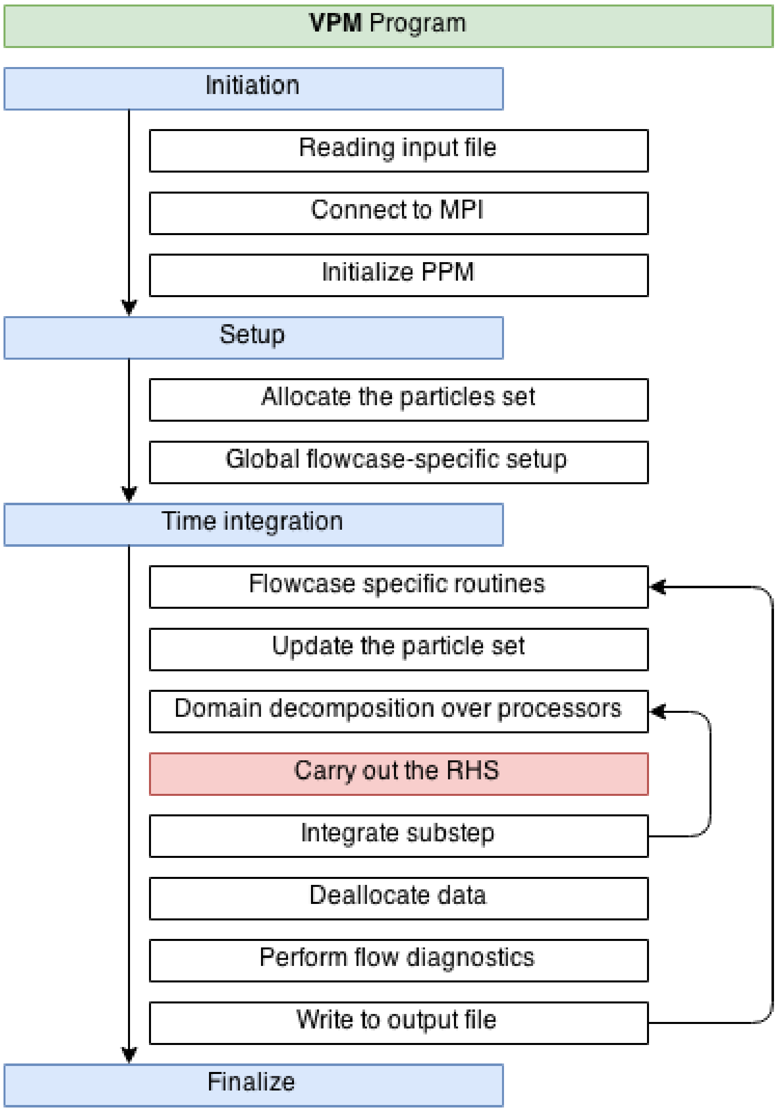
VPM Program
Initiation
Reading input file
Connect to MPI
Initialize PPM
Setup
Allocate the particles set
Global flowcase-specific setup
Time integration
Flowcase specific routines
Update the particle set
Domain decomposition over processors
Carry out the RHS
Integrate substep
Deallocate data
Perform flow diagnostics
Write to output file
Finalize

Figure 5.1: *Flowchart of the VPM program*

Chapter 6

Verification and Validation

In this chapter, the results of the simulations carried out with the VPM are presented. These simulations are discussed, and verified and validated with analytical, numerical, and experimentally obtained results from literature. Important topics to assess are the verification of the velocity and stretching computation of the VPM, the convergence and computational effort of the FMM, and the stability and accuracy of the VPM over time (especially regarding the divergence of particles). To this extent, the following test-cases are discussed in this chapter:

1. Section 6.1: **Single vortex ring**. A single circular vortex ring offers a fundamental problem to investigate, as it is axi-symmetric, not subject to stretching, and above all: simple analytical expressions are available for verification. The computation of the velocity is assessed and the influence of particle overlap and core size is investigated.

2. Section 6.2: **Double vortex rings (leapfrogging problem)**. This system consists of two circular vortex rings, sharing the same symmetry axis, for which also stretching occurs. Like for the single ring, analytical expressions are available, and the time evolution of leapfrogging problem can be assessed by applying time marching to a set of ODEs. Using the frogleaping problem, the stretching is verified and the convergence and computational effort of the FMM are analyzed.

3. Section 6.3: **Linked vortex rings (knot problem)**. The last geometric test-case consists of two circular vortex rings which are linked like a shackle. The problem is not axi-symmetric and as a result the geometry deforms over time into a complex pattern, which poses a modelling challenge regarding stability and accuracy. No simple analytical expressions or empirically obtained results are available, but the simulations are checked against numerical VPM results from literature. The influence of different numerical implementations of the VPM are assessed on the

stability and accuracy.

4. Section 6.4: **Axi-symmetrical actuator disk combined with an analytical far-wake description**. The wake of an axi-symmetric actuator disk is modelled using a wake sheet of vortex rings discretized by particles. The far-wake after 5 diameters is replaced by an analytical description of a straight vortex tube. With this set-up, cases are run from $C_t = 4/9 - 8/9$. Also simulations with highly loaded rotors from $C_t = 9/9 - 16/9$ are run, but without replacing the far-wake with an analytical description. The wake of the actuator disk is assessed regarding the wake expansion, velocity deficit, and the stability and expansion of the shear layer, using PIV results and the numerical results from a potential flow model from literature.

5. Section 6.5: **Rotating 3-bladed turbine with prescribed vorticity from the MEXICO experiment**. This case offers the validation of the VPM in a purely 3D set-up, whereby the formation of chaotic and therefore unstable flow regions pose a modelling challenge. The application of the classic and transpose scheme, and the application of viscous diffusion by PSE is investigated on the stability and accuracy of the wake. The simulations are compared to the experimental results from the MEXICO rotor.

6.1 Single vortex ring

6.1.1 Motivation

In this section a circular vortex ring with a finite but small thickness (also called a torus) is modelled using regularized particles over the circumference. It is a relevant case to investigate, as circular vortex rings form the wake of the actuator disk as simulated for this thesis work, see section 6.4.

The single vortex ring is of interest for analysis, as analytical approximations for the self-induced velocity over the circumference are available. The analytical expressions are however only valid for a thin-core approximation. It is therefore investigated to what core size these expressions are reasonably valid. Finally, the influence of the particle overlap is investigated on the accuracy of the self-induced velocity.

6.1.2 Problem statement

In figure 6.1 the problem of the single vortex ring is schematically depicted. The ring thickness is shown as a dashed outline around the ring. The vorticity is carried by particles with a finite core size, which is illustrated by circles of radius σ. The inter-particle spacing is denoted by h, and the ring radius from ring center to core center is given by R.

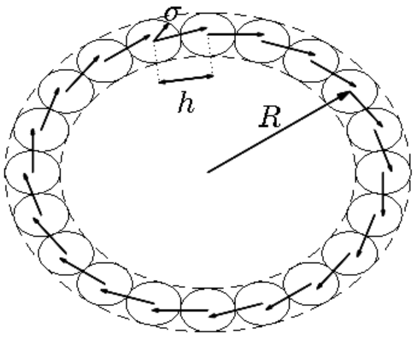

Figure 6.1: *A schematic overview of the ring decomposition by particles. Visible are 20 particles with the corresponding strength vector and core radius. The particle spacing h in this example equals two core radii, such that the overlap is $\lambda = \sigma/h = 0.5$.*

If sufficient overlap is present, the particle discretization approaches a continuous vorticity distribution over the ring. In that case, thin ring approximations are known for the velocity at the core center of the torus, see equation 6.1 (Sullivan et al. [32]). In this equation, β is dependent on the chosen core model, whereby the core has to be circular. The average velocity at the core center of the ring torus is indicated by the ring velocity in the remainder of this section.

$$U_{\text{core}} = \frac{\Gamma}{4\pi R}\left(\ln\left(\frac{8R}{\sigma}\right) - \beta\right) \tag{6.1}$$

A small parameter study is carried out to investigate the influence of both the core size and the overlap condition on the error convergence, whereby the error is defined as the difference between the simulated ring velocity and the analytical ring velocity as $\varepsilon = \|U_{\text{core}}/U_{\text{core,exact}} - 1\|$. In the first case, only the core size is adjusted. In the second case, the core size is kept constant, while the particle number is increased. An overview of parameters as applied for this problem is summarized in table 6.1. It is furthermore noted that the high order algebraic core is applied, and that the simulation is carried out without applying the FMM.

Table 6.1: *Overview of parameters as applied for the thin vortex ring problem*

Parameter	Value	Unit	Description
Γ	1	$[m^2 s^{-1}]$	Ring circulation
R	1	$[m]$	Ring radius
σ	0.001-0.1	$[m]$	Core size
NP	10-20000	-	Number of particles
h	0.00031-0.63	$[m]$	Particle spacing
λ	0.0016-6.28	-	Particle overlap
β	0.5	$[ms^{-1}]$	Analytical parameter (high-order algebraic)

6.1.3 Discussion on the ring velocity and overlapping condition by the direct method

Figure 6.2 shows the error convergence over the overlapping ratio, whereby the particle density is increased (decreasing h) and the core size σ is kept constant. The results for 5 different core sizes are presented altogether, ranging from a very small core size of $\sigma/R = 0.001$ to a relatively large core size of $\sigma/R = 0.1$.

If looked at the results for all the five different core sizes, the error convergence shows the same trend below an overlapping ratio of $\lambda < 1.5$, at which point the error is already smaller than 1 ‰for all cases. If the overlapping ratio is further increased, an underbound is reached as the thin core approximation of equation 6.1 is now responsible for the leading error term. Nevertheless, even for the largest core size of $\sigma/R = 0.1$ the error of approximation is only in the order of $\mathcal{O}(10^{-4})$.

It can be concluded that the solution of the thin ring converges to that of the analytical expression from equation 6.1, and thereby the VPM correctly resolves the velocity. Regarding the approximation of a continuous vortex filament with a finite thickness by regularized particles, it is important to maintain a certain overlap. This overlap needs to be at least $\lambda = 1$ to obtain an error of less than 1 % in the velocity calculation at the particle positions in a thin ring. This is in line with literature [8, 24, 36], where it is stated that an overlap of at least $\lambda = 1$ is required (see section 3.2).

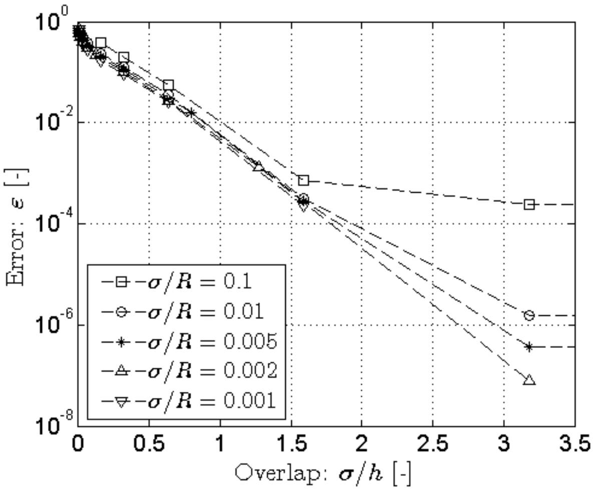

Figure 6.2: *The error for the velocity as taken at the center of the ring relative to an analytical approximation versus the overlapping ratio.*

6.2 Double or leapfrogging rings

6.2.1 Motivation

The single circular ring as applied for the velocity verification (section 6.1) does not involve vorticity stretching. To be able to assess the computation of stretching, a simple geometry of two leapfrogging rings is introduced, which stretch and shrink in a periodical sense. The leapfrogging behaviour is also relevant, as it is encountered in the unstable shear layer of the wake of a HAWT, as soon as vortices start pairing (see sections 2.2, 6.4, and 6.5).

The problem of the leapfrogging rings forms the basis of several investigations. First, the vortex stretching of the VPM is analyzed over time. Second, the computation of the velocity and stretching is used to verify the accuracy and computational effort of the FMM.

6.2.2 Problem statement

A double ring system is presented where the rings are oriented in the same plane and share a common symmetry axis, see figure 6.3. The description of the individual rings is similar as encountered in figure 6.2 from section 6.1. The only differences between the two rings are the size and overlapping ratio, but the other parameters (the number of particles, core size, circulation, and initial location of the ring center) are similar.

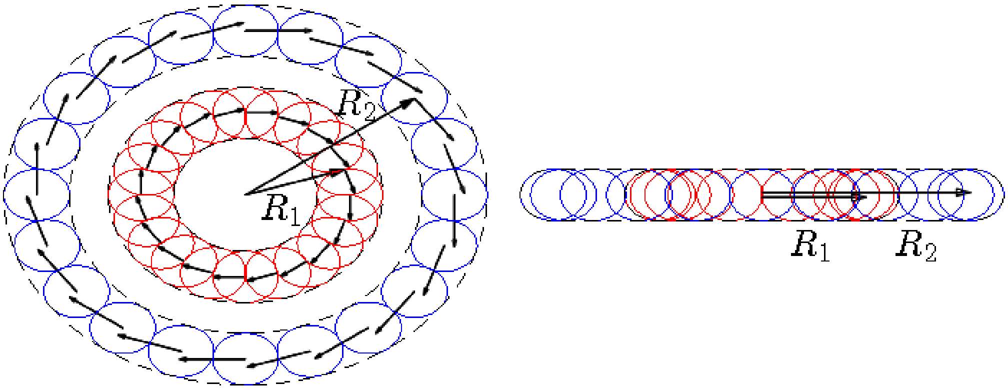

(a) Front view (b) Side view

Figure 6.3: *The front and side view of the initial position of the two vortex rings. The core size, number of particles, and circulation is equal for both rings.*

An example of the time evolution of this problem is shown in figure 6.4. As a result of the self-induced velocity and stretching, the two rings start rotating around each other in a periodical sense through a movement which is also known as leapfrogging. Both rings continuously switch positions at a constant rate in time.

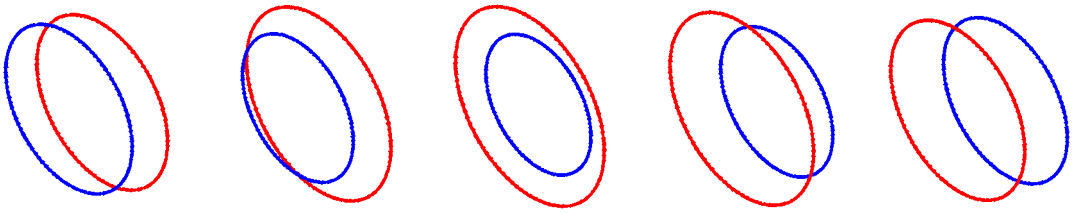

Figure 6.4: *Demonstration of the evolution of the leapfrogging configuration over time*

For the simulation, the set-up of table 6.2 is implemented. Both rings are identical, with the exception of the initial ring radius and thus also the initial particle overlap. A second order Runge-Kutta time integration scheme has been applied, with the high order algebraic kernel for regularization. Volume is not conserved, as the core size remains constant during stretching.

Table 6.2: *Overview of parameters as applied for the leapfrogging problem*

Parameter	Value	Unit	Description
$\Gamma_{1,2}$	1	$[m^2s^{-1}]$	Circulation
R_1	0.5	$[m]$	Ring 1 radius
R_2	1	$[m]$	Ring 2 radius
$\sigma_{1,2}$	0.1	$[m]$	Core size
$NP_{1,2}$	100	-	Number of particles per ring
λ_1	3.0	-	Ring 1 initial particle overlap
λ_2	1.5	-	Ring 2 initial particle overlap
D	0	[m]	Initial distance from ring center to center
Δt	0.01	[s]	Time step size

Investigation of the vortex stretching by the VPM:
The computation of the velocity has already been verified using the single ring in section 6.1. The computation of the vortex stretching is currently assessed by analyzing the periodic stretching and shrinking of the rings over time, and verified along known analytical expressions for a system of coaxial vortex rings (Cheng et al. [6]), which are summarized in appendix C. It requires the solving of a set of non-linear Ordinary Differential Equations (ODE). The vortex stretching is not directly verified, but the correct evolution of the leapfrogging problem over time can only occur whenever the stretching is accurately resolved. The FMM is not applied for this investigation.

Investigation of the velocity and stretching by the FMM:
For the verification of the FMM, the convergence of the velocity and vortex stretching over the expansion order and acceptance factor is assessed. The computation of the velocity through the direct expressions as derived in section 4.3 is compared to the velocity obtained through finite differences from the vector potential. The direct expressions for the stretching have not been derived, such that only the convergence of the stretching as

obtained through finite differences is analyzed.

Investigation of the computational effort of the FMM:
The growth of computational effort over the expansion order and the acceptance factor is assessed. Thereafter, the computational effort for a far-field (box) interaction is compared to that of a direct interaction, by which a guideline is obtained for the minimum amount of particles required in an individual leaf box. This includes a comparison between the velocity and stretching obtained by the direct derivative (see section 4.3) and finite differences from the vector potential. This is relevant, as the finite differences of the first partial derivatives require 6 extra nodes on the stencil, and if also the stretching is obtained through finite differences, a stencil of 25 nodes in total is required to obtain the second partial derivatives as well (see figure 6.5). It is therefore valuable to know what approach is computationally the most efficient.

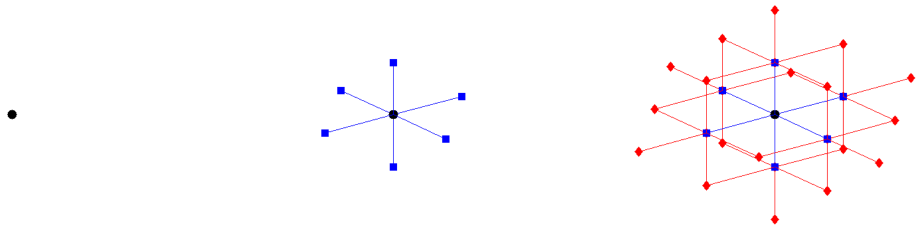
(a) Target point (b) 7-point stencil (c) 25-point stencil

Figure 6.5: *The application of a 3-point central difference stencil in 3 dimensions, results in 7 nodes for the first partial derivatives, and 25 nodes for the second partial derivatives.*

6.2.3 Verification of the vorticity stretching by the direct method

Figure 6.6 shows the radius of both rings of the leapfrogging problem, as obtained through the simulation with the VPM without FMM applied, versus the analytical expressions of appendix C. As the analytical expressions form a system of non-linear ODEs, a Eulerian time marching approach is used with a time step size of $\Delta t = 0.001[s]$.

It is visible that the simulation results correspond very well to those of the analytical expressions. The periodic behaviour of the stretching and shrinking of the rings is clearly visible, whereby both rings follow exactly the same trajectory and change positions with a 180 degrees phase shift. These results indicate that the VPM correctly resolves the vortex stretching.

As will become apparent throughout the remainder of this chapter, the handling of the stretching over time is not necessarily straightforward due to divergence of the vorticity field. The discussion on vortex stretching is therefore continued in section 6.3, using the more demanding knot problem.

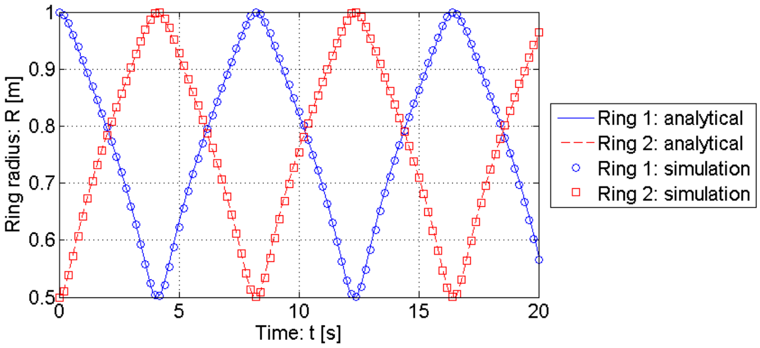

Figure 6.6: *The radius of both simulated rings over time compared to the analytical result.*

6.2.4 Verification of the velocity by the FMM using finite differences

This subsection is devoted to the analysis of the velocity field as taken by finite differences directly from the potential. The velocity as obtained directly from the multipole expansions is assessed in subsection 6.2.5.

Two parameters mainly contribute to the accuracy of the FMM. Those are:

1. The acceptance factor θ
2. The order of the expansions

Convergence of the error is expected both over an increase in acceptance factor or an increase in expansion order. It thus has to be analyzed what combination of acceptance factor and expansion order gives the fastest convergence. To this extent, figure 6.7 is constructed, which gives the error convergence over the expansion order for a range of acceptance factors ($0.5 \leq \theta \leq 4.0$). From left to right, the subplots give the solution for a singular core, a small core of $\sigma/R = 0.01$ (overlapping ratio of 1.6), and finally a large core of $\sigma/R = 0.1$ (overlapping ratio of 16). The reason the result for multiple core sizes is presented, lies in the fact that the potential is singular. This influences the accuracy of the real solution which is smooth in case of a non-singular core.

The error is defined as $\epsilon = \|U_{FMM}/U_{N^2} - 1\|$, and it is taken as the average velocity over half of one of the two rings. Theory states that convergence is not guaranteed for $\theta < 1.0$, and that the larger the acceptance factor becomes, the faster the error convergences over the expansion order (see section 4.1). Indeed, if looked at the solution for a singular core in figure 6.7a, barely any convergence is visible for $\theta = 0.5$ and the convergence increases with increasing acceptance factor. The result for the minor core size of $\sigma/R = 0.01$ (figure 6.7b) approaches that of a singular core (figure 6.7a), indicating that in case of a small core size the application of the singular FMM is valid.

When the core size is further increased (figure 6.7c), it is visible that the initial error for the first order term is larger and that the convergence quickly smooths out over the higher order terms. The reason is that the velocity due to the FMM will converge to the singular solution instead of the smooth solution. An underbound in the error is therefore visible, which decreases with increasing acceptance factor, as a wider range around the target point is solved directly. It is therefore advisable to maintain a certain cut-off radius of a few core sizes around the target point in which the solution is smooth and should be solved through direct interactions. Whenever the source and target point are sufficiently separated, the singular solution of the FMM can be taken into account as the singular and smooth solution converge with distance.

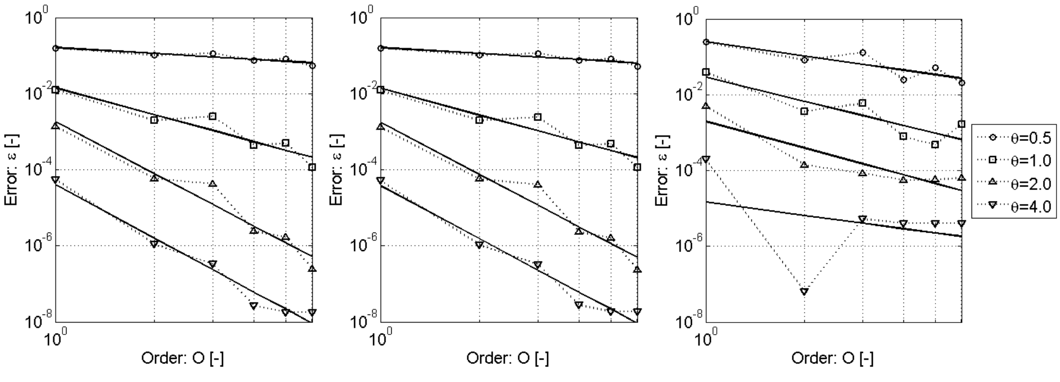

(a) σ = singular (b) $\sigma/R = 0.01$ (c) $\sigma/R = 0.1$

Figure 6.7: *The convergence of the velocity error over the expansion order for a range of acceptance factors, whereby the velocity is taken through finite differences.*

6.2.5 Verification of the velocity by the FMM using the direct derivative expressions

In subsection 6.2.4 it was demonstrated that by obtaining the partial derivatives from the potential by finite differences, the correct error convergence for the velocity is obtained as outlined in chapter 4. A major drawback is the use of 6 extra computational nodes for the finite differences, as interactions involving multipole expansions are very expensive to calculate. If one also wants to resolve the vortex stretching, the velocity on each of these 7 stencil nodes has to be computed first, which requires a 3-point central difference stencil for each individual node. A large part of these nodes are shared between neighbouring stencils, but in the end 25 computational nodes are required for the computation of the vector potential (see figure 6.5). I.e. the computation of the stretching at the central target point requires the computation of the velocity at the 6 surrounding nodes, which on its turn requires the computation of the vector potential on 25 nodes in total.

To reduce the necessity for such a large stencil, the direct expressions for the velocity derivative from the vector potential have been obtained (see section 4.3). If subsequently the stretching is solved through finite differences, the total stencil size is reduced from 25 nodes back to 7 nodes.

Figure 6.8 is constructed in the same way as 6.7 from subsection 6.2.4, but now the velocity is obtained through the direct expressions. It is visible that the convergence over the order terms is very limited; it seems that the error quickly reaches an underbound, even for the singular case. The origin of this anomaly is unknown, and requires a future inspection of the derivation and implementation of the velocity derivatives. Nonetheless, if looked at the first order term, the convergence of the acceptance factor shows a very good agreement with the results from the potential for all cases (figure 6.7). The systematic error thus decreases considerably with acceptance factor, through which very accurate results can be obtained.

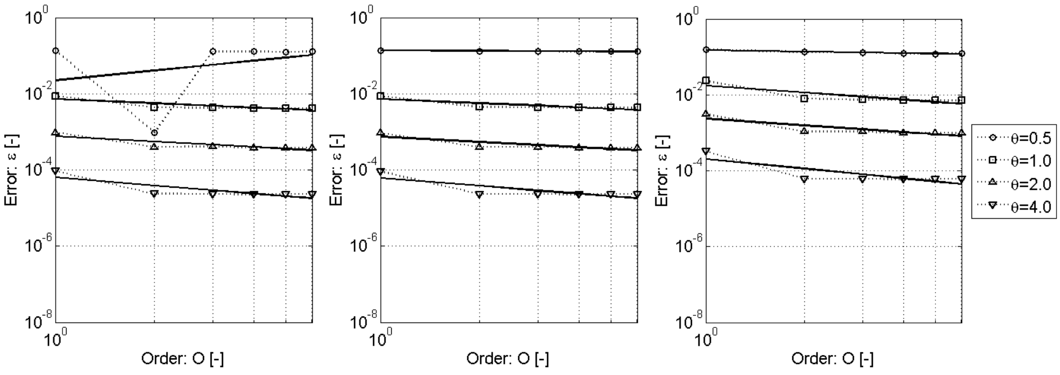

(a) σ = singular (b) $\sigma/R = 0.01$ (c) $\sigma/R = 0.1$

Figure 6.8: *The convergence of the velocity error over the expansion order for a range of acceptance factors, whereby the velocity is taken through the direct derivative expressions.*

6.2.6 Discussion on the verification of the stretching by the FMM using finite differences

Finally, the error convergence of the stretching term is analyzed, with the error defined as $\epsilon = \|(D\omega/Dt)_{FMM}/(D\omega/Dt)_{N^2} - 1\|$. A second derivation of the expansion is not carried out, such that the stretching has to be resolved through a 3-point central difference stencil from the velocity around the target point (just like the velocity has been obtained from the potential in subsection 6.2.5). The results are presented in figure 6.9, whereby the velocity is obtained directly and the stretching is obtained through finite differences, allowing for a stencil with only 7 nodes in total. It is visible that the error convergence over the acceptance factor is faster for the stretching than for the velocity from figures 6.7 and 6.8. The reason is that the influence of stretching decreases more rapidly over distance than for the velocity.

6.2.7 Analysis of the computational effort of the FMM

In this subsection, the computational effort will be assessed against the accuracy of the FMM. All cases have been run on a single core of the Intel Core i7-3537U CPU with a basic clock speed of 2.00 GHz (maximum turbo frequency: 2.50 GHz).

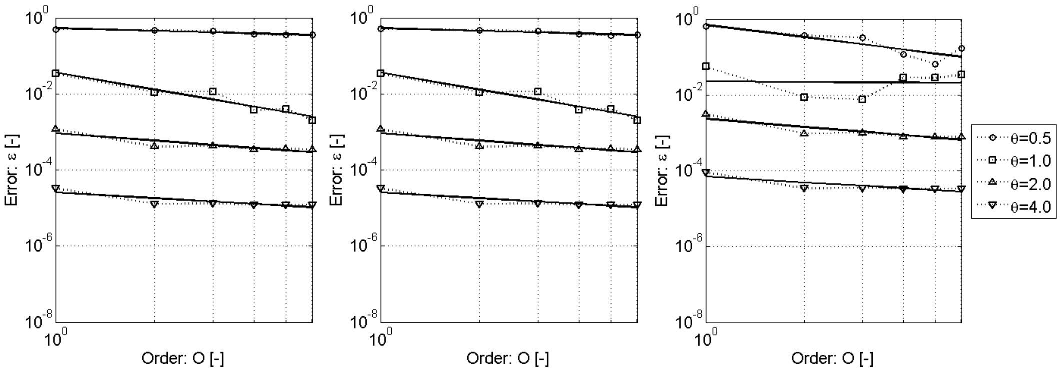

(a) σ = singular (b) $\sigma/R = 0.01$ (c) $\sigma/R = 0.1$

Figure 6.9: *The convergence of the stretching error over the expansion order for a range of acceptance factors, whereby the velocity is taken via the direct derivative expressions and the stretching through finite differences from the velocity partial derivatives.*

The computational effort versus the expansion order and acceptance factor are plotted in figure 6.10. Both subplots contain the same information, but show the trends of the order and acceptance factor individually. The results for the computational effort have been normalized over the computational effort of a direct simulation. Therefore, if the computational effort surpasses $10^0 = 1$, the simulation using the FMM would in fact be slower than taking all the interactions directly. It is noted that the performance of the FMM is very dependent on the particle distribution in space. The FMM will result in a faster computation whenever a lot of particle clustering is present, than when particles are evenly spread out.

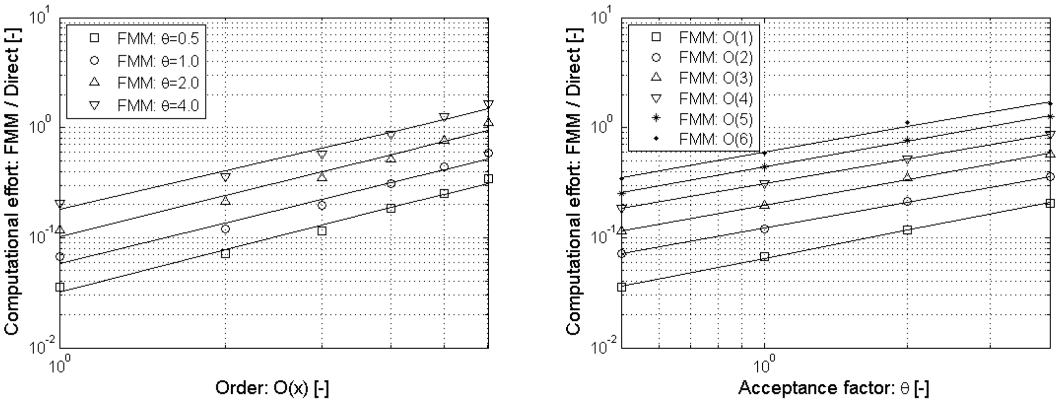

(a) Computational effort vs. expansion order (b) Computational effort vs. acceptance factor

Figure 6.10: *The computational effort of the FMM normalized to the computational effort of a direct simulation, with a growth rate between* $0.52 \sim 0.58$ *in computational effort over the expansion order, and a growth rate of about* $0.56 \sim 0.65$ *in computational effort over the acceptance factor.*

From figure 6.10, it follows that the growth rate of computational time over the expansion order and the acceptance factor is comparable. Doubling either the order or the acceptance factor results in a 52% to about 65% increase in computational time. Therefore, Increasing the expansion order or the acceptance factor results in the same order of computational increase.

It is now of interest to look at the computational effort of an interaction involving expansions versus a direct interaction. An interaction involving expansions is expensive, and it is therefore more efficient to take the interactions individually for a small amount of particles in a box, see figure 6.11. A small study is therefore carried out to obtain the minimum amount of particles required in a box to allow for the acceptance of a common interaction via multipole expansions instead of individual direct interactions. Besides, the relative computational effort of interactions involving either finite differences or the direct derivative expressions are obtained.

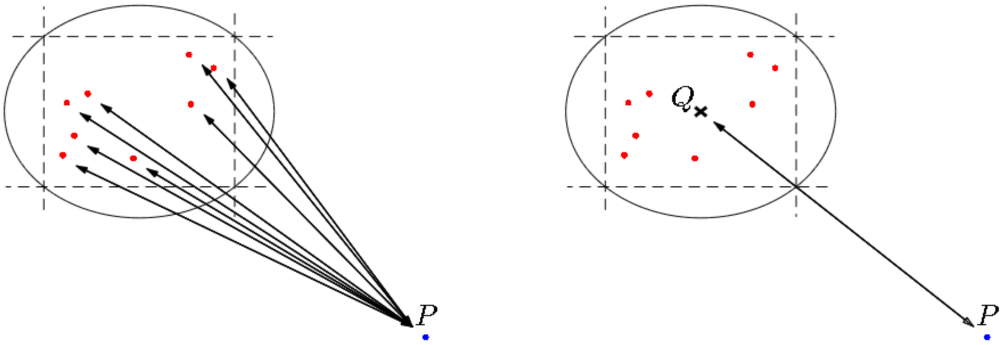

(a) Direct interactions

(b) Multipole interaction

Figure 6.11: *Two possibilities of computing the interactions in a box: (a) via direct interactions between the target P and all the individual particles, or (b) between the multipole expansion around the box center Q and target P.*

Table 6.3 gives an overview of the relative computational effort of an interaction through a multipole expansion versus one direct interaction. For instance, the value 14.3 indicates that at least 15 particles have to be in a box for the interaction via expansions to be more efficient. Horizontally, the computational effort is given for an increasing expansion order. It is visible that interactions via expansions become significantly more expensive for an increasing expansion order. Vertically, 4 different set-ups of the FMM are presented, which are:

1. Velocity taken through finite differences, stretching ignored (7 nodes required on the stencil).
2. Velocity and stretching taken through finite differences (25 nodes required on the stencil).
3. Velocity taken through the derived expressions, stretching ignored (no stencil required, only the target point).

4. Velocity taken through the derived expressions, stretching taken through finite differences (7 nodes required on the stencil).

If the first and third row of results from table 6.3 are compared, it turns out that the velocity computation via finite differences (case 1) is only about 2 times as expensive as for the derived expressions (case 3), even though 6 extra computational nodes are required. If looked at the second and fourth row of results, where also the stretching is taken into account, then it is visible that the computation via finite differences on the stencil with 25 nodes (case 2) is actually faster than when the velocity is obtained via the derived expressions and the stretching via finite differences (case 4). It must be stated that the implementation of the direct expressions for the velocity computation have not been optimized, but the results from 6.3 gives rise to the question whether the derived expressions for the vortex stretching would actually lead to a faster computation than for case 2.

Table 6.3: *Computational efforts of a box (expansion) interaction relative to a direct (particle-particle) interaction*

Case:	Velocity:	Stretching:	Stencil nodes:	$\mathcal{O}(1)$	$\mathcal{O}(2)$	$\mathcal{O}(3)$	$\mathcal{O}(4)$	$\mathcal{O}(5)$	$\mathcal{O}(6)$
1	central diff.	none	7	14.3	26.5	42.0	63.1	88.0	119
2	central diff.	central diff.	25	34.9	74.2	129	199	282	382
3	derived	none	1	6.76	13.7	23.5	36.4	52.2	71.4
4	derived	central diff.	7	42.3	86.0	146	224	322	443

6.3 The knot problem of linked vortex rings

6.3.1 Motivation

The last vortex ring geometry that will be assessed is the knot problem, which consists of two linked vortex rings. Opposite to the cases with the single and double vortex rings of sections 6.1 and 6.2, the current test-case has no direct physical relevance regarding the wake of a HAWT turbine. Instead, the knot problem is chosen to allow for a stability analysis of complex flow structures.

The knot problem is not axi-symmetric. Under their self-induced velocity and stretching, the two rings will start travelling and deforming. At some point, the two rings will inevitably get entangled, due to the fact that the rings are linked. Subsequently, highly stretched filament structures will form, where sharp curvatures and vortex roll-up will be manifested. As the two rings become entangled, those will connect after some time and form one large vortex ring.

Even though the knot problem is not encountered in the wake of a wind turbine, the emerging phenomena are actually very relevant. Highly stretched filaments can be formed locally in the wake, with the just described phenomena as a result. An example for the wake of a HAWT turbine is given by the root vortices, which form a narrow helical structure of vortices of opposite circulation, which easily become entangled. The VPM has difficulty in maintaining the accuracy and stability of the simulation of these complex flow patterns. It is therefore important to identify the behaviour of the VPM regarding these phenomena and to assess methods that can mitigate the formation of complex stretched flow structures.

In this section, the stability and accuracy of different numerical set-ups of the VPM will be analyzed over time. The performance of the classic stretching scheme is assessed against the transpose scheme. As the transpose scheme is very sensitive to divergence, the implementation of the divergence relaxation by Pedrizzetti (see section 3.3.2) is considered. Furthermore, the effect of the core model, size and growth, and the particle overlapping condition is investigated, for which a particle splitting scheme is applied (see section 3.5.1). Finally, viscous diffusion is modelled by a PSE scheme (see section 3.4.3), to be able to simulate reconnection of vortex rings and the mitigation of stretched flow. To allow for a quantitative analysis, use is made of the linear and quadratic diagnostics, as outlined in section 3.6

6.3.2 Problem Statement

The initial geometry of the knot problem as applied for the simulations in this section is presented in figure 6.12. Visible are two circular tori which are linked like a shackle.

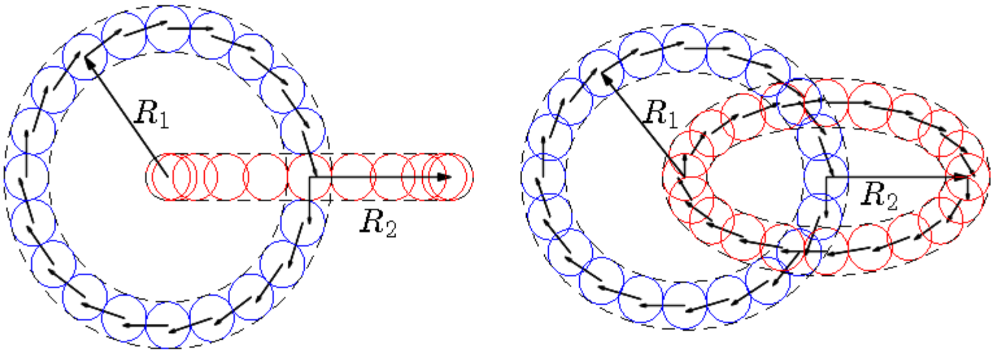

(a) Front view (b) Three-quarter view

Figure 6.12: *The front and side view of the initial position of the two vortex rings. The core size, number of particles, and circulation is equal for both rings.*

Under the influence of the self-induced velocity and stretching, the knot structure will deform over time. This is demonstrated in figure 6.13. The regions of stretching and compression are visualized by red and blue respectively. After a certain amount of time both rings meet each other at two points. It is visible in the last frame that these regions are deepred, which indicates that the most stretching is occurring at these positions. It is likely that the simulation will fail hereafter, as it is difficult to maintain the stability in the simulation locally at these two points. The result will be a blow-up of the simulation, by which the particle vectors at the instability grow to extremely large values in a very short period of time, destroying the physical representation. A demonstration of this blow-up behaviour is given in figure 6.14 for a single ring. Notice also the short time span in which this blow-up occurs.

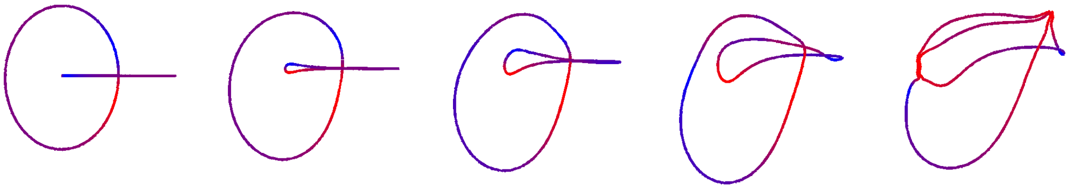

Figure 6.13: *Impression of the knot problem over time. Red indicates regions of filament stretching, and blue regions of compression. The second ring is in a perpendicular plane to the observer.*

In figure 6.15a the situation from the last frame of figure 6.13 is magnified (though from another viewing angle). The points where the two rings first meet are encircled. These

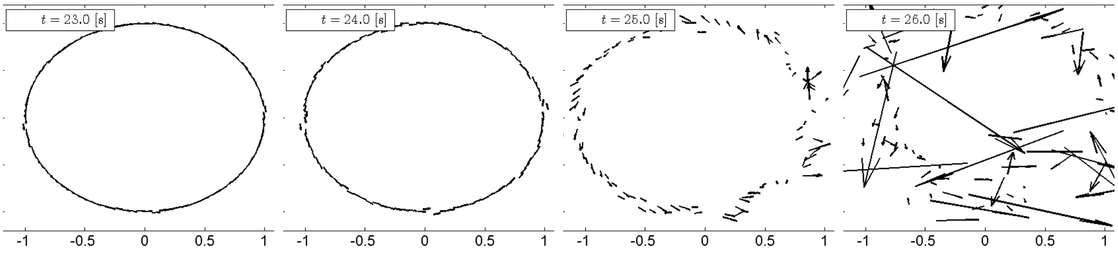

(a) $t = 23(s)$ (b) $t = 24(s)$ (c) $t = 25(s)$ (d) $t = 26(s)$

Figure 6.14: *Demonstration of the phenomenon of blow-up in a simulation. Visible is a single vortex ring subject to some anomalies in the particle alignment. In a short amount of time these anomalies make the whole structure unstable and the simulation ceases to exist.*

points are referred to as the (re)connection points, as the two rings would connect here to form one large ring in case of a viscous flow. The remainder of the two rings are aligned with opposite circulation, as indicated by the arrows, and would therefore cancel each other out through viscous diffusion. This is visualized in figure 6.15a. These reconnection points and the aligned filament sections form critical regions in the flow, regarding the stability of the simulation. To obtain a better insight in the time evolution of the knot problem, the reader is referred to appendix E.

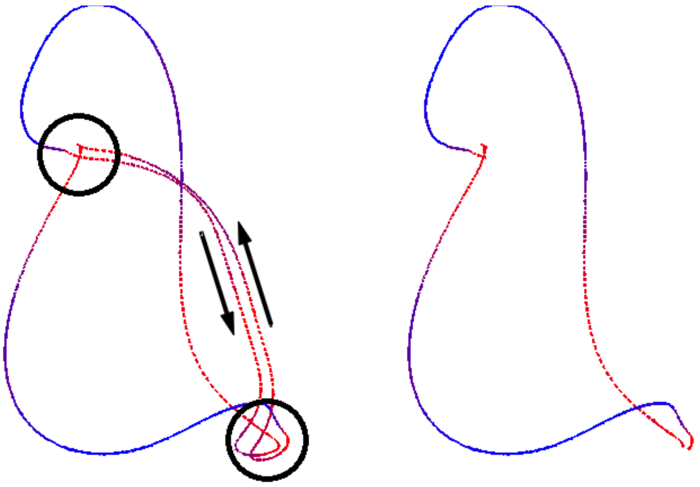

(a) (b)

Figure 6.15: *Impression of the reconnection process, whereby the two rings form one ring through viscous diffusion. The encircled areas show the reconnection points, and the vectors indicate the opposite circulation of the aligned filaments. These are critical regions regarding stability.*

An overview of initial parameter settings is presented in table 6.4. Throughout the simulations, a second order Runge-Kutta time integration scheme is applied (RK2), and a high order algebraic kernel implemented. The FMM is not enabled.

Table 6.4: *Overview of parameters as applied for the knot problem*

Parameter	Value	Unit	Description
$\Gamma_{1,2}$	1	$[m^2s^{-1}]$	Initial circulation
$R_{1,2}$	1	$[m]$	Initial radius
$\sigma_{1,2}$	0.1	$[m]$	Initial core size
$NP_{1,2}$	250	-	Initial number of particles
$\lambda_{1,2}$	4.0	-	Initial particle overlap
$\lambda_{1,2}$	3.0	-	Minimum particle overlap
D	1	[m]	Initial distance from ring center to center
Δt	0.01-0.0001	[s]	Time step size
ν	0/0.001	$[m^2s^{-1}]$	Kinematic viscosity

6.3.3 Comparison of the knot problem with numerical results from literature

The knot problem is a purely theoretical configuration of vortex rings, for which no known empirically obtained experimental results are available. As the problem is not axi-symmetric, like the single and double vortex rings systems from sections 6.1 and 6.2, analytical results are also not straightforward to obtain. Nonetheless, the problem has been numerically modelled by others, allowing for a qualitative comparison.

Figure 6.16 shows the time evolution of the knot problem for a simulation using the VPM (frames 6.16a through 6.16d) compared to the numerical results from Winckelmans and Leonard [37] (frames 6.16e through 6.16h). The transpose stretching scheme has been applied with a high-order algebraic core for the regularization. The current simulation is subject to a constant core with particle splitting to maintain the overlap. The reference simulation is subject to a growing core to fulfil the overlapping condition, whereby no particle splitting is applied.

Although the simulation set-up differs slightly, the results compare very well. At 4.5 seconds divergence is being manifested for both simulations at the same position. Due to the particle splitting, the vectors are smaller for the simulation with the current VPM code. After 5.0 seconds the two vortex rings start connecting, and a stable simulation cannot be maintained any further with this set-up. Again, both simulations show divergence at the same positions, although the particle splitting helps to better maintain the filament integrity.

Figure 6.17 shows the linear impulse, angular impulse, total energy, and helicity for both simulations. It is visible in figure 6.17b that the angular impulse is better conserved for the current simulation. The reason is unsure, but a possibility is that the splitting scheme reduces the amount of particle divergence. The linear impulse, helicity, and angular impulse compare very well.

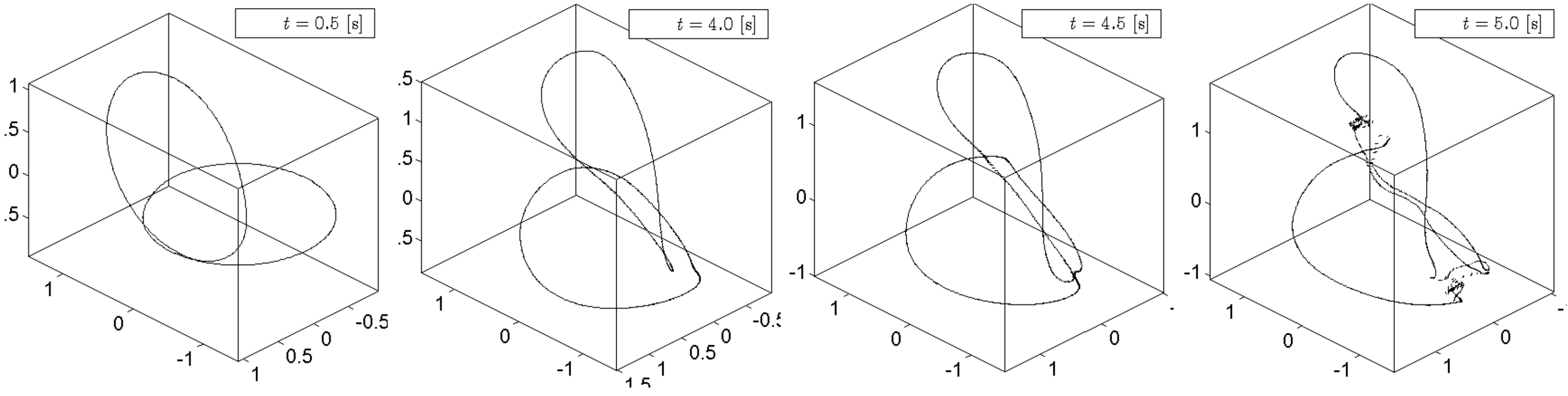

(a) $t = 0.5(s)$ (b) $t = 4.0(s)$ (c) $t = 4.5(s)$ (d) $t = 5.0(s)$

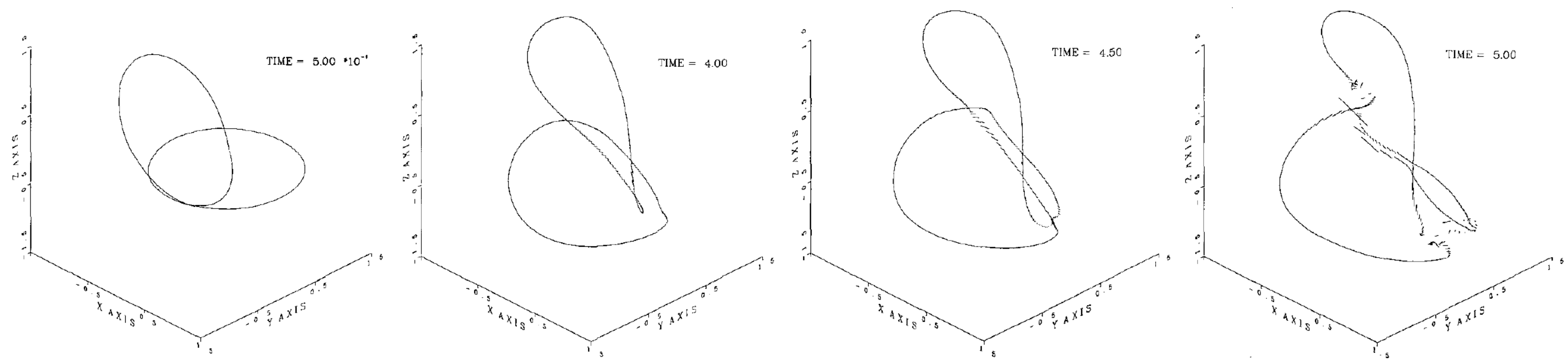

(e) $t = 0.5(s)$ (f) $t = 4.0(s)$ (g) $t = 4.5(s)$ (h) $t = 5.0(s)$

Figure 6.16: *The knot problem as simulated by the VPM (frame (a) through (d)) and simulated by Winckelmans and Leonard [37] (frame (e) through (h)).*

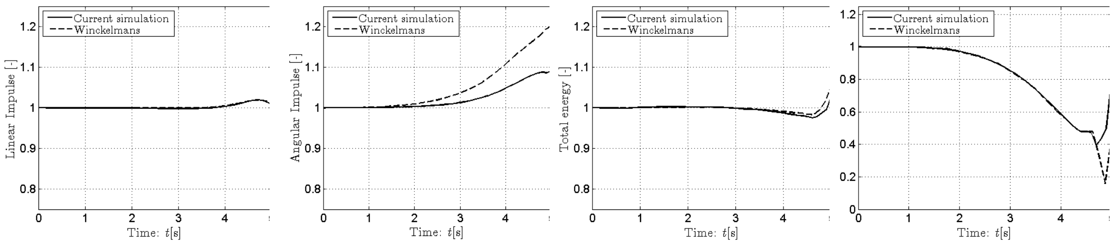

(a) Lin. impulse (b) Ang. impulse (c) Total energy (d) Helicity

Figure 6.17: *A comparison of quadratics for the knot problem between the VPM code from this thesis and the numerical results from Winckelmans and Leonard [37].*

6.3.4 Analysis of the results with the classic stretching scheme

The classic stretching scheme is applied, and the core is allowed to shrink during stretching to conserve the volume. A time step size of 0.01 seconds is applied with an initial core size of 0.1 meter, which results in an initial overlapping ratio of 4.0 (well above the minimum requirement of 1.0). Figure 6.18 shows vertically 4 different set-ups of the simulation, and horizontally each time the last 0.3 seconds of the simulation before blow-up. In red are the regions of intense stretching, and blue indicates compression.

The first row (figures 6.18a through 6.18c) shows the case with the set-up as described in the first paragraph. The simulation fails at the two points where both rings meet. In these regions the stretching is intense, and therefore the overlap is under-resolved as the number of particles remains constant. The blow-up phenomenon as demonstrated in figure 6.14 is manifested, whereby the diverting straight line sections are the distorted particle vectors.

To guarantee overlap, a remeshing scheme is now applied in the form of particle splitting in filament direction whenever the overlapping ratio drops below a threshold value of $\lambda = 3.0$. The result is presented in figures 6.18d through 6.18f but now the simulation fails earlier as another problem arises. There is an underlimit in core size and circulation for which the time step size can support a stable simulation, as effectively the particles approach a singular state for a too thin core. Therefore the particles start diverging at the regions of the most intense stretching, even though the overlap is maintained. Note that no blow-up is visible at 3.4 seconds, although it does occur a very short amount of time later. As it happens so rapidly, it is easily overlooked whenever results are outputted.

To reobtain a stable simulation for a longer period of time, the time step size is now decreased from $\Delta t = 0.01[s] \rightarrow \Delta t = 0.002[s]$, with the results shown in figures 6.18g through 6.18i. Again the simulation fails at the point of reconnection.

Finally, the time step is decreased even further towards $t = 0.0001[s]$, but it will not result in a significantly longer stable simulation. The reason is that stretching continues to happen and very fine rolled-up vortex sections are formed. To exemplify this phenomenon,

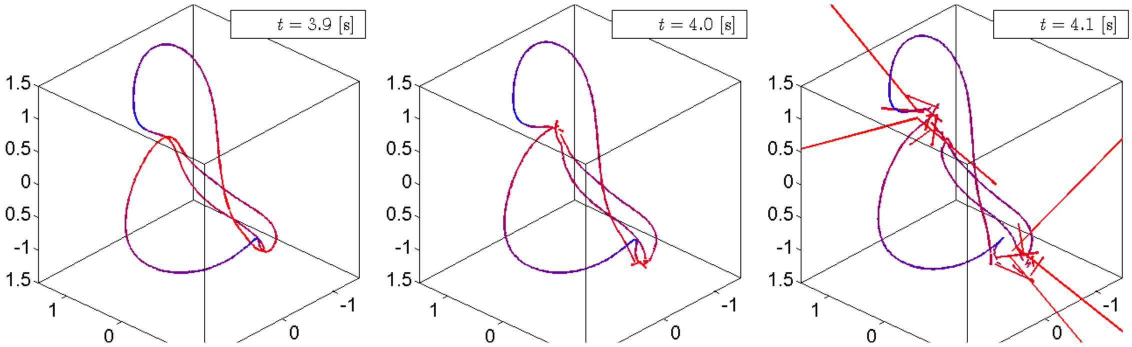

(a) $\Delta t = 0.01(s)$, no split, $t = 3.9(s)$

(b) $\Delta t = 0.01(s)$, no split, $t = 4.0(s)$

(c) $\Delta t = 0.01(s)$, no split, $t = 4.1(s)$

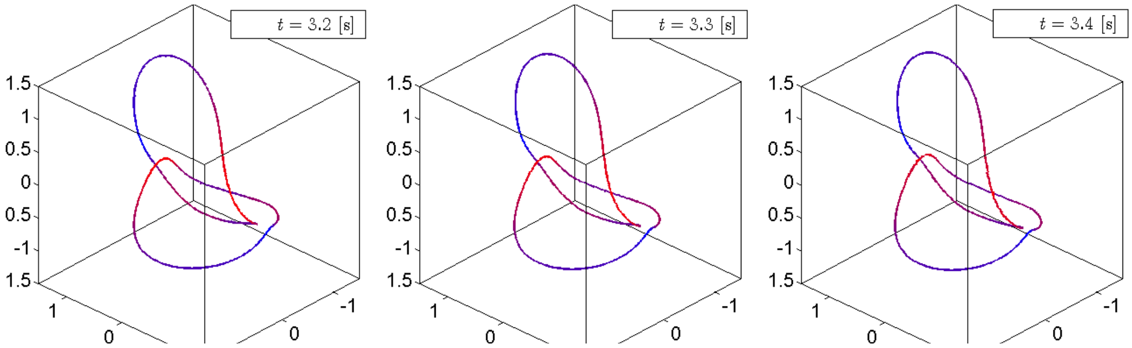

(d) $\Delta t = 0.01(s)$, $t = 3.2(s)$

(e) $\Delta t = 0.01(s)$, $t = 3.3(s)$

(f) $\Delta t = 0.01(s)$, $t = 3.4(s)$

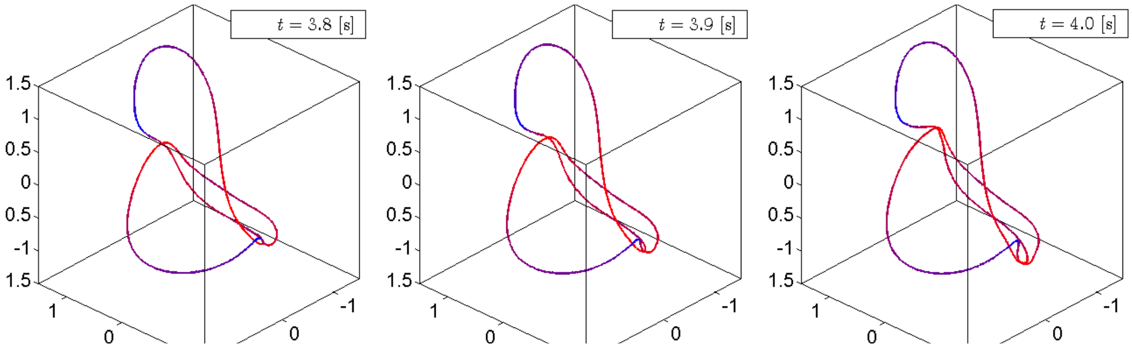

(g) $\Delta t = 0.002(s)$, $t = 3.8(s)$

(h) $\Delta t = 0.002(s)$, $t = 3.9(s)$

(i) $\Delta t = 0.002(s)$, $t = 4.0(s)$

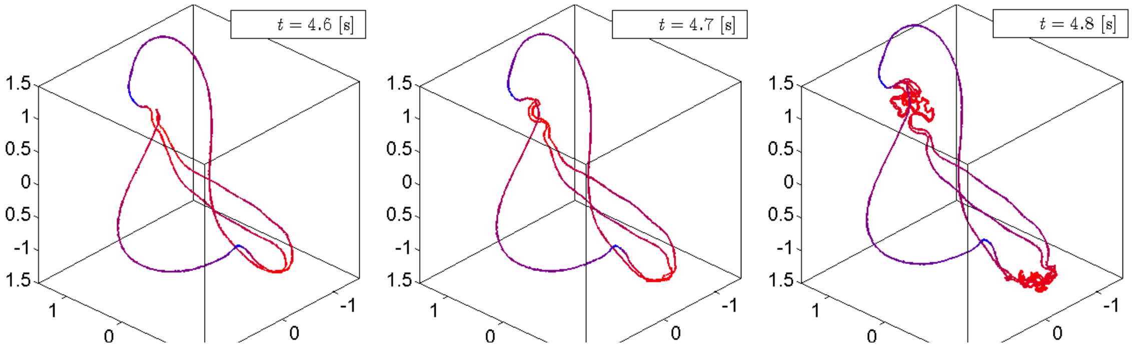

(j) $\Delta t = 0.0001(s)$, $t = 4.6(s)$

(k) $\Delta t = 0.0001(s)$, $t = 4.7(s)$

(l) $\Delta t = 0.0001(s)$, $t = 4.8(s)$

Figure 6.18: *Vertically, 4 different cases are shown: (a-c) constant amount of particles, (d-f) particle splitting applied, (g-i) reduction of time step size, (j-l) reduction of both time step size and overlapping ratio. Horizontally, the frames of the last 0.3 seconds before blow-up are visualized. Red indicates a region of stretching, and blue indicates compression.*

the under-limit for the overlap during splitting is lowered to $\lambda = 1.5$, as vortex roll-up is intensified as the overlap is reduced. The results are shown in figures 6.18j through 6.18l, where it is apparent that in a very short amount of time a very complex flow structure has formed due to intense stretching. This roll-up behaviour at intense stretching and a lower particle overlap is typical for the classic scheme; it has not been encountered with the transpose scheme.

6.3.5 Analysis of the results with the transpose scheme and divergence relaxation applied

In a solenoidal fluid, the classic and transpose scheme should lead to the same exact solution, as explained in section 3.2.3. Simulations using the VPM are subject to divergence, such that the performance between these schemes differ. For singular particles, the transpose scheme is favourable as it manages to conserve vorticity exactly during vorticity stretching (Winckelmans [36]). For the regularized case, both schemes perform equally well (or bad), although Cottet and Koumoutsakos [8] favour the classic scheme due to a better performance regarding particle divergence, as has been explained in section 3.3.

In this subsection the performance of the transpose scheme is assessed on the knot problem. For the first case, the same set-up is used as for the first case of the classic scheme from subsection 6.3.4 and figures 6.18a through 6.18c. The result for the transpose scheme is shown in figures 6.19a through 6.19c. The simulation with the transpose scheme survives for a longer period of time than for the classic scheme. This is mainly due to the fact that the particles start diverging in the region where the two vortex rings meet and the stretching is thus somewhat delayed. The particle divergence is most clearly seen in figure 6.19b and it results locally in a difference in the result between the classic and transpose scheme. It is a phenomenon that is not encountered with the classic scheme, and it is independent from the overlap or time integration applied. It occurs for the transpose scheme when two filaments with a different orientation are closely situated.

To overcome the problem of particle divergence, the relaxation by Pedrizzetti [24] is used (see section 3.3.2). A small relaxation of $f = 0.02$ is chosen. This time, also particle splitting is applied. The results are shown in figures 6.19d through 6.19f. If compared with the results for the classic scheme in figures 6.18d through 6.18f, it is visible that the simulation with the transpose scheme survives for a significant longer time span (3.4 seconds versus 4.3 seconds). Even though the chosen time step size is too coarse, the simulation with the transpose scheme survives by diffusing the particles in radial direction, thereby reducing the rotation in the stretched filament regions. Due to the relaxation applied, both rings manage to approach each other closely, without manifestation of a large divergence (Compare figure 6.19e with 6.19b). Finally, at time $t = 4.3[s]$ also this simulation blows up.

For the last case in the analysis with the transpose scheme, the time step size is decreased to $t = 0.01[s] \rightarrow t = 0.005[s]$ and the relaxation filter is increased to $f = 0.02 \rightarrow f = 0.1$. The results are shown in figures 6.18g through 6.18i. Due to the smaller time step size, no

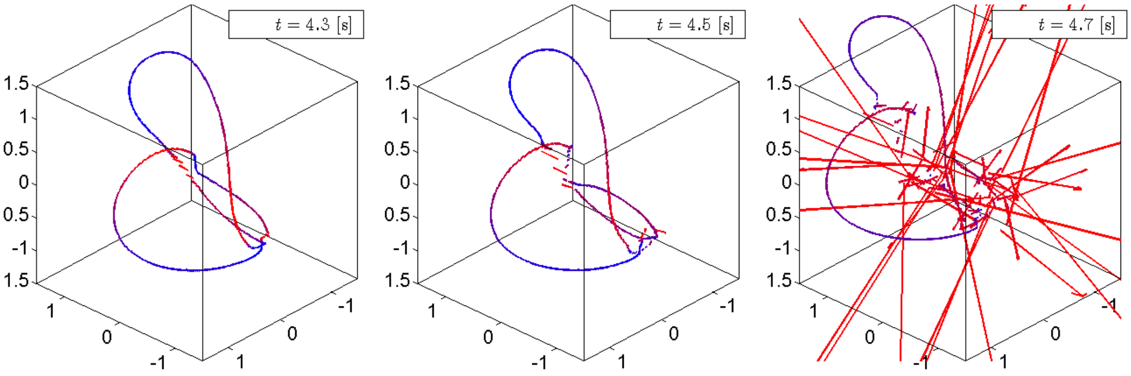

(a) $\Delta t = 0.01(s)$, no split, $t = 4.3(s)$

(b) $\Delta t = 0.01(s)$, no split, $t = 4.5(s)$

(c) $\Delta t = 0.01(s)$, no split, $t = 4.7(s)$

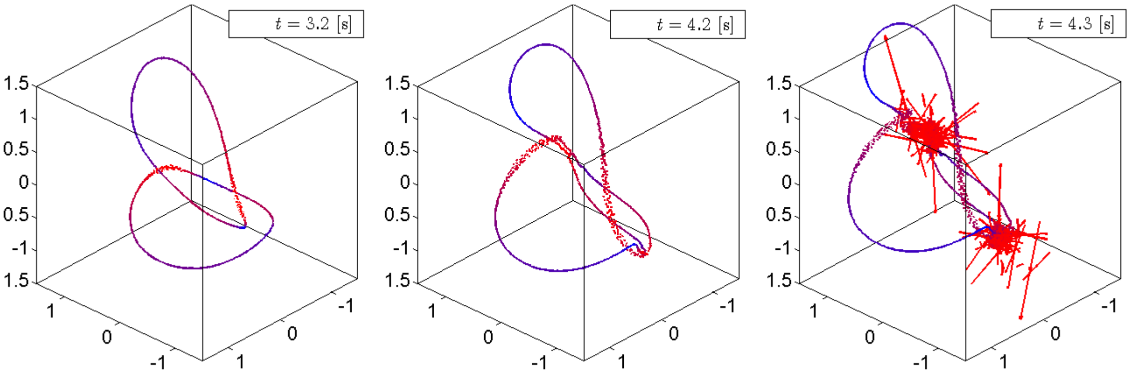

(d) $\Delta t = 0.01(s)$, $t = 3.2(s)$

(e) $\Delta t = 0.01(s)$, $t = 4.2(s)$

(f) $\Delta t = 0.01(s)$, $t = 4.3(s)$

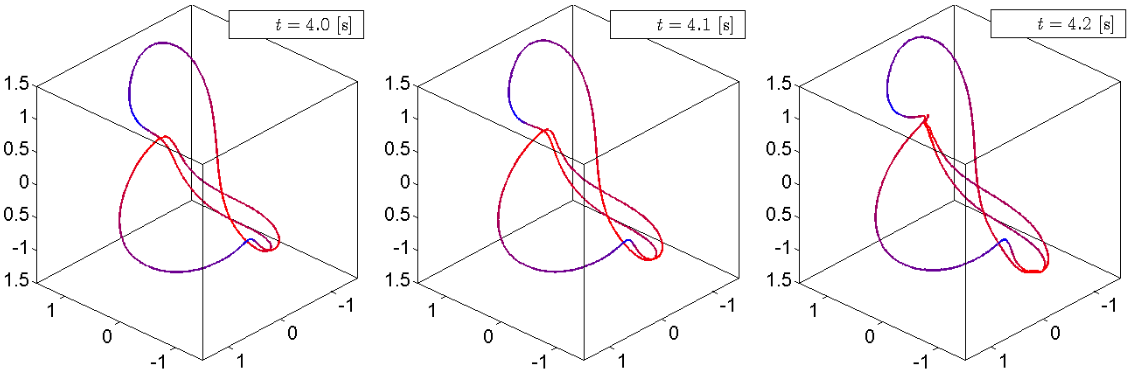

(g) $\Delta t = 0.005(s)$, $t = 4.0(s)$

(h) $\Delta t = 0.005(s)$, $t = 4.1(s)$

(i) $\Delta t = 0.005(s)$, $t = 4.2(s)$

Figure 6.19: *Vertically, 3 different cases are shown with the transpose scheme applied: (a-c) constant amount of particles, (d-f) particle splitting and relaxation applied, (g-i) reduction of time step size and relaxation increased. Horizontally, the frames of the last instances in time before blow-up are visualized. Red indicates a region of stretching, and blue indicates compression.*

radial diffusion of particles is apparent, and also the divergence is oppressed successfully by the increased relaxation. To this extent, compare figure 6.19i with 6.19b, where it is clearly visible that the particles now remain aligned and both rings are able to approach each other closely. At this point very sharp curvatures are visible, and the simulation does not maintain to keep stability any further.

If the results from the transpose scheme of figures 6.19g through 6.19i are compared with the results from the classic scheme from figures 6.18g through 6.18i, it is visible that both solutions look very comparable. This supports the statement that both the classic and transpose scheme lead to the same solution when the divergence-free condition is preserved (see section 3.2.3).

6.3.6 Comparison between the classic and transpose scheme regarding the diagnostics

In this section, a comparison between the classic and transpose scheme regarding the linear and angular quadratics is presented. An extensive explanation about the quadratics can be found in section 3.6.

Figure 6.20 shows the linear and quadratic diagnostics of the knot problem over time, for the classic scheme and for the transpose scheme with different relaxation factors applied. Figures 6.20a and 6.20b show the linear and angular impulse, which should in theory remain constant. For the linear impulse, it is visible that the classic scheme shows the best conservation over time, while the transpose scheme without divergence filtering results in the biggest difference. If relaxation is applied ($f = 0.02$ and $f = 0.1$) the linear impulse is better conserved, and the result of the transpose scheme approaches that of the classic scheme. The same applies for the angular impulse, where it is visible that the result for the transpose scheme with $f = 0.1$ almost overlaps with the result for the classic scheme.

In theory, also the results for the energy and helicity (figures 6.20c and 6.20d) have to remain constant if the flow is inviscid. It is noted that the used expressions for the regularized quadratic diagnostics are approximations, such that this conservation is not obtained. It is visible for the energy, that the results for the classic and transpose scheme without relaxation match closely. It could be that this is a coincidence, as the results for the higher relaxation factors converge to a result that is slightly offset from the result with the classic scheme. This is also visible in the result for the helicity, where the results for the transpose scheme with relaxation applied show a slightly better conservation.

In contrast to the energy and helicity, the transpose results with relaxation do converge to the result of the classic scheme in case of the enstrophy (figure 6.20e). Enstrophy is not conserved in either viscid or inviscid flows. It is a measure of rotation, and it increases with stretching, which explains the large increase in enthalpy over time for these results.

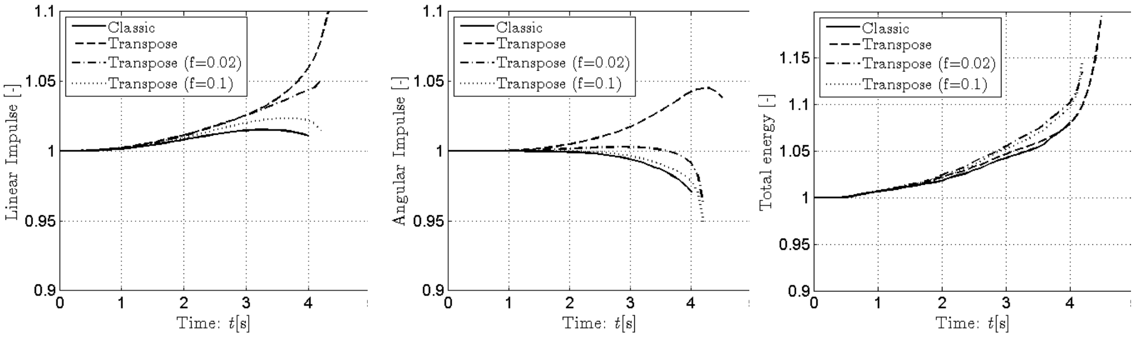

(a) Linear impulse (b) Angular impulse (c) Total energy

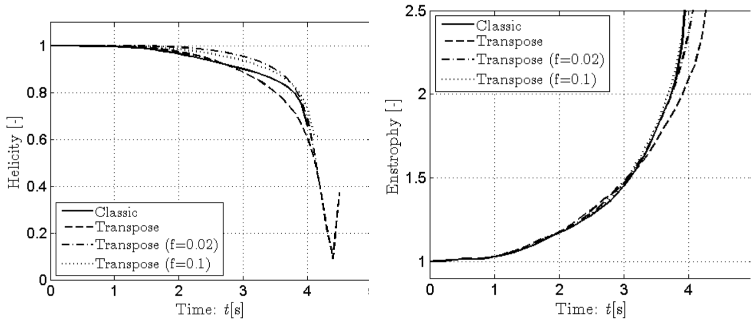

(d) Helicity (e) Enstrophy

Figure 6.20: *The linear and quadratic diagnostics for several cases of the knot problem.*

6.3.7 Analysis of the results with the PSE scheme applied for mitigation of intensely stretched flow structures

Although the application of the transpose scheme in combination with relaxation of the particle divergence seems to be effective for handling intense stretching, it does not offer a solution for the entanglement and sharp curvatures at the point of reconnection of the two rings. As the reconnection of vortex rings is a viscous process, a good strategy is to look into diffusion of the local vorticity by application of a Particle Strength Exchange scheme (PSE). Diffusion also offers a viable prospective regarding the mitigation of entangled filaments with opposite circulation and sharp curvatures, as will become apparent.

As a demonstration, a close-up of one of the two points where the filaments meet is presented in figure 6.22 (at the circled areas in figure 6.15). In this case the transpose scheme is applied and in the first image (figure 6.21a) it is shown that particles diffuse radially in a region of stretching (red). The reason is a too course time integration.

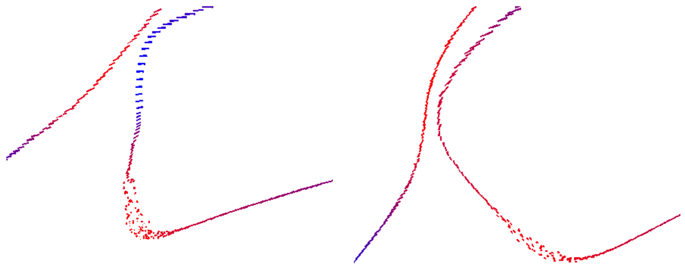

(a) Clean (b) $f = 0.02$

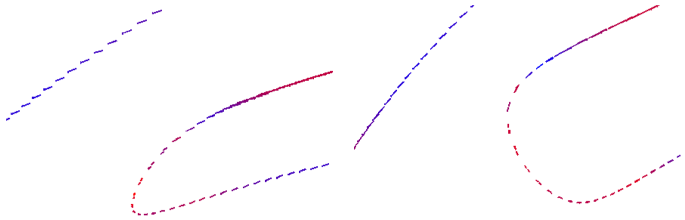

(c) $\nu = 0.001 (m^2/s)$ (d) $f = 0.02$, $\nu = 0.001 (m^2/s)$

Figure 6.21: *Mitigation of the divergence during stretching with the transpose scheme applied*

In the region where the spacing between the two filaments is the smallest, the particles start to divert, which has been explained in subsection 6.3.5 to be a phenomenon specific to the transpose scheme. Figure 6.21b shows again the simulation with the transpose scheme, but with a relaxation of $f = 0.02$ applied. The divergence in the region of neighbouring filaments is effectively suppressed, while the radial diffusion of particles is still present.

The PSE scheme is now applied with a viscocity of $\nu = 0.001[m^2/s]$. The results are shown with and without relaxation ($f = 0.02$) applied in figures 6.21c and 6.21d. The reduced particle vectors indicate that the circulation is reduced locally by diffusion. Without having to decrease the time step size, the radial diffusion of particles is not present anymore, although still divergence is visible in the result without relaxation. In the result with relaxation applied, the particle alignment is much better maintained.

6.3.8 Analysis of the results with different core types applied

In the analysis of the knot problem, the core has been treated as a physical (or real) core which is allowed to shrink during stretching, as to satisfy the volume preservation constraint ($\partial(\sigma^2 L)/\partial t = 0$). In the analysis in this subsection, results with a real core will be compared to results with a constant core, which functions purely as a numerical smoothing tool for alleviation of the singular behaviour and to allow for communication between particles (overlap). In the latter case, the core is referred to as a vorton. The rationale for a constant core is that stretching will less likely result in the formation of fine roll-up structures. Other advantages are that stretching with a constant core results in a reduced addition of split particles, and that a coarser time integration can be afforded.

Results with the classic scheme and the transpose scheme (the latter with $f = 0.02$ applied) are presented in figure 6.22 for a real core and a vorton smoothing. In addition, a PSE scheme with a viscosity of $\nu = 0.001[m^2/s]$ is applied for all cases. For each case, 3 frames of the simulation are shown at the same moment in time for easy comparison. An exception is formed by the result in figure 6.22i, where a blow-up of the simulation occurred at 5.9 seconds (the actual blow-up is not visible in the figure). The other three cases did not experience a blow-up at least up to 7 seconds. Note that the two cases with the vorton applied are presented in black, as the amount of stretching was tracked using the local core size as a measure.

If figure 6.22 is compared to figures 6.18 and 6.19, an important result is that all the simulations survive for a much longer period of time, whereby it is meant that no blow-up occurs. The first case (figures 6.22a through 6.22c), for which the classic scheme and a real core is applied, shows that the alignment of particles is very well conserved up till 5.5 seconds and reasonably well up till 7 seconds. The second case (figures 6.22d through 6.22f) shows the results with the classics scheme, but now with a constant core applied. If figure 6.22f is compared to figure 6.22c it is visible that the amount of added particles is much reduced (as indicated by NP). The particles remain aligned, with the exception of the region near the points of reconnection. At 7.1 seconds, the simulation with the real core blows up in the neighbourhood of the reconnection points (not shown), while no blow-up of the simulation with the constant core has been recorded. The particle divergence around the reconnection points (figure 6.22f) does however amplify over time.

Figures 6.22g through 6.22i show the results for the transpose scheme with the real core applied. It has been experienced that the transpose scheme has difficulty with keeping

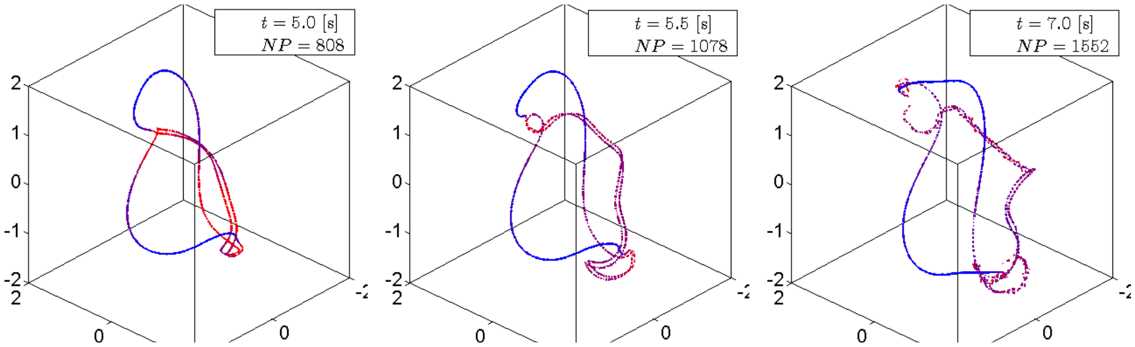

(a) Classic, real core, $t = 5.0(s)$ (b) Classic, real core, $t = 5.5(s)$ (c) Classic, real core, $t = 7.0(s)$

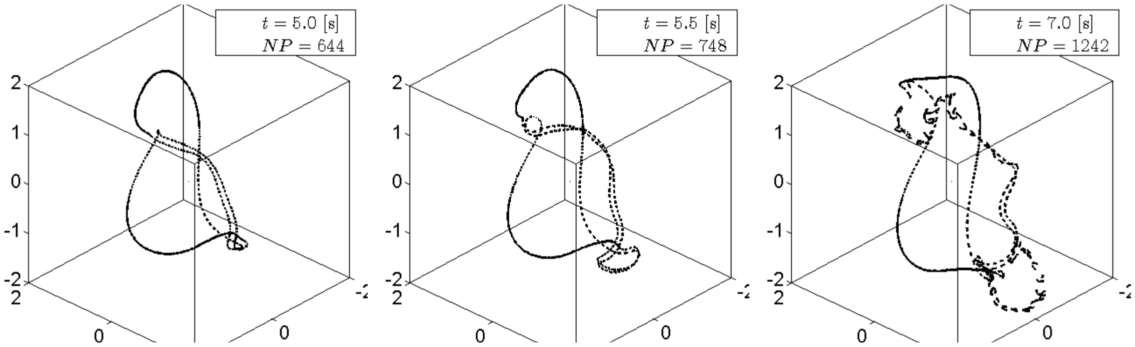

(d) Classic, vorton, $t = 5.0(s)$ (e) Classic, vorton, $t = 5.5(s)$ (f) Classic, vorton, $t = 7.0(s)$

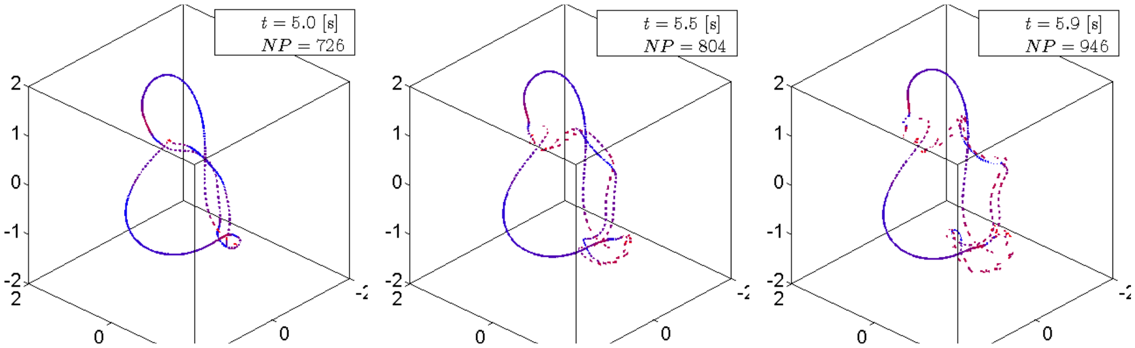

(g) Transpose, real core, $t = 5.0(s)$ (h) Transpose, real core, $t = 5.5(s)$ (i) Transpose, real core, $t = 5.9(s)$

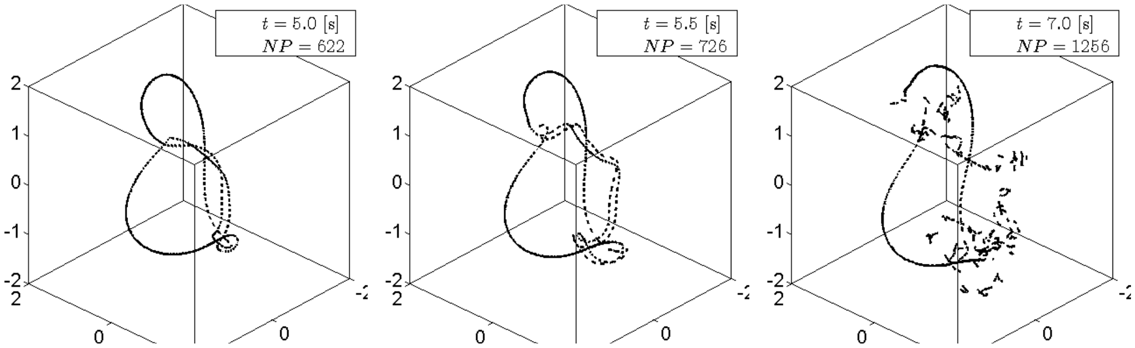

(j) Transpose, vorton, $t = 5.0(s)$ (k) Transpose, vorton, $t = 5.5(s)$ (l) Transpose, vorton, $t = 7.0(s)$

Figure 6.22: *Vertically, 4 different cases are shown, all with a PSE scheme applied: (a-c) classic scheme with a real (time dependent) core, (d-f) classic scheme with a constant core (vorton), (g-i) transpose scheme with a real (time dependent) core, (j-l) transpose scheme with a constant core (vorton). For the cases with the transpose scheme, a relaxation factor of* $f = 0.02$ *is applied. Horizontally, for each case 3 images in time are shown. Red indicates a region of stretching, and blue indicates compression.*

the filaments divergence-free whenever filaments of different orientation approach each other, which is the case in the region of aligned filaments with opposite circulation. The divergence relaxation applied cannot prevent the simulation from blowing up after 5.9 seconds. Finally, the simulation with the transpose scheme and the real core applied do not experience a quick blow-up (figures 6.22j through 6.22l), but a large particle-divergence is experienced in the region of the aligned filaments (figure 6.22l).

As a final assessment the quadratics are plotted in figure 6.23 which correspond to the results of figure 6.22. Figure 6.23e shows a steep drop in enstrophy around $t = 5[s]$ for the results with the classic scheme applied, which marks the point of reconnection of both rings. The enstrophy drops as the PSE scheme successfully mitigates the stress of the intense stretching of the filaments. This is also visible by a steeper decline in energy at that point, see figure 6.23d. It is noted that the largest rate of energy decay corresponds with the peak of enthalpy, as the enthalpy is proportional to the rate of energy decline. The enthalpy peak in case of the classic scheme with vortons applied is much smaller, as no core shrinking is manifested during stretching, and thus the intensity of rotation is less.

Figure 6.23e also shows that the simulations with the transpose scheme with the real core applied fails in mitigating the intense stretching. No reduction in enthalpy is visible, and as a consequence the simulation blows-up just before $t = 6.0[s]$. The simulation with the transpose scheme and vortons applied does perform somewhat better, but the stretching is not as well mitigated as for the simulations with the classic scheme applied.

In theory, the linear impulse and angular impulse should remain constant during viscous diffusion (figures 6.23a and 6.23b), although this is not the case for the current results. It is possible that this is due to the fact that currently the viscosity is not allowed to diffuse to the void area in space, as no particles are present to collect any vorticity. Therefore, the diffusion is not correctly resolved in a physical manner.

Finally, note the peaks in the helicity plot (figure 6.23c) after $t = 5.0[s]$ for the simulation with the transpose scheme and vortons applied. These peaks indicate divergence, as was visualized in figure 6.22l. In other words, the simulation does not experience a blow-up, but the physical interpretation of the simulation is still lost.

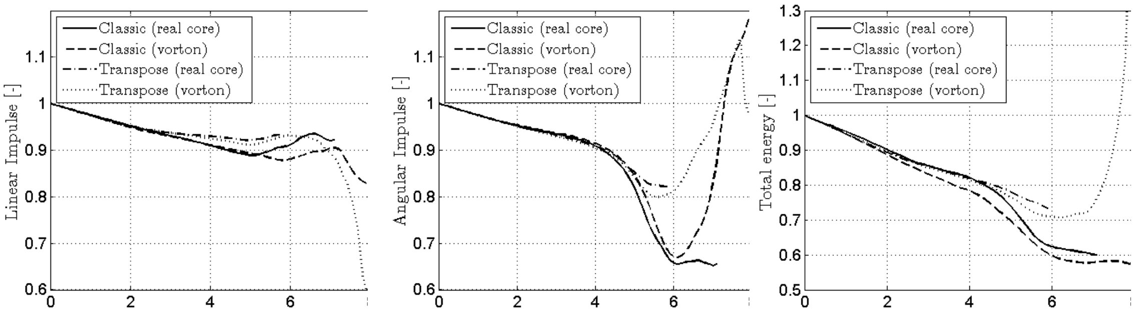

(a) Lin. impulse (b) Ang. impulse (c) Total energy

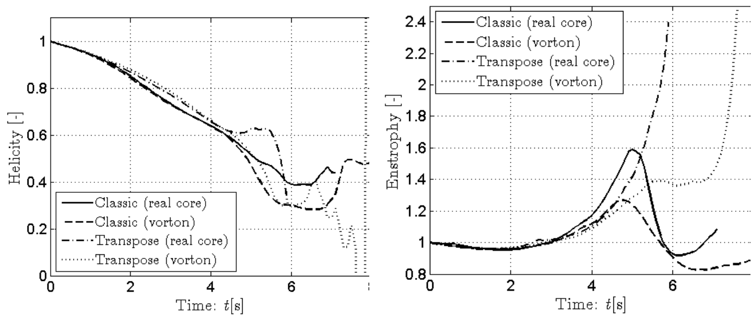

(d) Helicity (e) Enstrophy

Figure 6.23: *The linear and quadratic diagnostics for several cases of the knot problem.*

6.4 Actuator disk combined with an analytical model for the far-wake

6.4.1 Motivation

The actuator disk offers an appropriate first validation case for the wake of a HAWT, by isolating the wake specific phenomena and ignoring the aerodynamic effects of a rotating blade. A range of thrust coefficients both below and beyond the Betz limit ($C_t = 8/9$) are applied, and for the lower thrust coefficients the far-wake is replaced by an analytical expression. Furthermore, the axisymmetry of the problem is exploited, resulting in a very significant computational reduction.

6.4.2 Problem statement

An actuator disk with a continuous, constant pressure distribution is modelled by shedding vortex rings of constant circulation from the disk edges. The shed vortex rings are discretized through particles, see figure 6.1 in section 6.2. The strength of the particles is dependent on the time step, the disk dimensions, particle discretization, and thrust coefficient. This relationship (for a constant disk loading) is as follows:

$$\Gamma = \frac{\|\alpha^p\|}{\Delta l} = \frac{\|\alpha^p\| \, N_P}{2\pi R} = C_t \frac{1}{2} U_\infty^2 \Delta t \tag{6.2}$$

To maintain a small core size, but at the same time a sufficient overlap, a large amount of particles is required for the wake discretization. In the current simulations, a number of particles in the order of $\mathcal{O}(10^5)$ and a number of time steps of $\mathcal{O}(10^3)$ is applied. To reduce the computational effort, use is made of the axisymmetry of the problem: as each of the vortex rings consists between 20 to a 100 particles, the computational effort can be brought down by the same amount. Furthermore, the far-wake is replaced by an analytical model from 5 diameters downstream onwards, called the semi-infinite vortex tube. A description of this model is given by Gibson [12] and Branlard and Gaunaa [1], and an explanation is added in appendix D.

The parameter set-up for all cases is presented in table 6.5. The FMM is enabled using the derived expressions for the velocity and finite differences for the stretching. RK2 time integration is applied and the particle core is high order algebraic. Overlap is not maintained during stretching of the rings (no particle splitting is allowed).

Several experiments are carried out using the combined model of the actuator disk with the analytical wake tube. First, a general outline is given of the shape and properties of the wake. Then, the application of the FMM is verified by checking the results of the wake expansion and velocity deficit against a purely direct simulation. Thereafter, the accuracy and stability of the simulation results for different time steps and schemes, overlapping ratios, and core sizes is checked. Finally, the results of a range of thrust coefficients is investigated, including those of highly loaded rotors with wake reversal ($C_t \geq 1$) for which the expressions of the semi-infinite tube are not valid anymore.

Table 6.5: *Overview of parameters as applied for the actuator disk problem*

Parameter	Value	Unit	Description
C_t	4/9-16/9	-	Thrust coefficient
R	1	$[m]$	Radius
z_{tube}	10	$[m]$	Start of the tube in axial direction
NP	20-100	-	Number of particles per shed ring
σ	Singular-0.1	$[m]$	Core size
Δt	0.025	$[s]$	Time step size and ring shedding interval
t	75	$[s]$	Total simulation time
$\mathcal{O}$	2	-	FMM expansion order
θ	2.0	-	FMM acceptance factor

6.4.3 Analysis of the wake and shear layer for $C_t = 8/9$

Figure 6.24 shows the axial velocity field for a thrust coefficient of 8/9 (Betz limit). The vertical black line represents the actuator disk, and the dashed lines demarcate the contour of the semi-infinite vortex tube. The particles are shed at the edge of the actuator disk and form a vortex sheet and thus a sheer layer enclosing the wake. Only one half of the actuator disk and wake is shown, as the result is symmetric.

At about 1.5 diameters downstream, an onset of the Kelvin-Helmholtz instability is visible due to the steepness of the shear layer. By plotting the vorticity (figure 6.25) this phenomenon is more clearly visualized. Notice the roll-up behaviour at the instability onset, as demonstrated by Rosenhead [26]. The integrity of the vortex sheet cannot be maintained by the simulation and the wake sheet breaks up into clouds of particles. These clouds of particles start pairing and rotating around each other, which is also known as leapfrogging (see section 6.2), through which the shear layer starts expanding over the axial direction downstream.

To get more insight into this unstable behaviour of the shear layer, the results of an experiment carried out by Lewis [19] is presented in figure 6.26 . In figure 6.26a a straight sheet of particles with an equal circulation of $\Gamma = 1.0$, a time step size of $\Delta t = 0.001$, and a particle spacing of $h = 0.033333$ is visible. To trigger the Kelvin-Helmholtz instability, the two central particles have been displaced by $\Delta x = \Delta y = 0.01$, after which the sheet starts to roll-up locally. It is visible that after 30 time steps the sheet cannot sustain the increasing roll-up and that the sheet breaks up into two sections. At this instance in time also a wave pattern is visible in the sheet, which is probably caused by instabilities originating from the disturbances by the roll-up eddies. Subsequently, both ends of the sheet are rolled-up into two separate clouds of particles. It is thus demonstrated that a small initial disturbance results in a breakdown of the whole wake sheet.

Figure 6.26b shows the same experiment as for figure 6.26a, but without initial forced disturbance. Even though no instabilities have been introduced at time zero, the numerical round-off errors over time trigger instabilities over the whole sheet. Again small clusters of particles are formed which coalesce with neighbouring clusters to form larger clouds

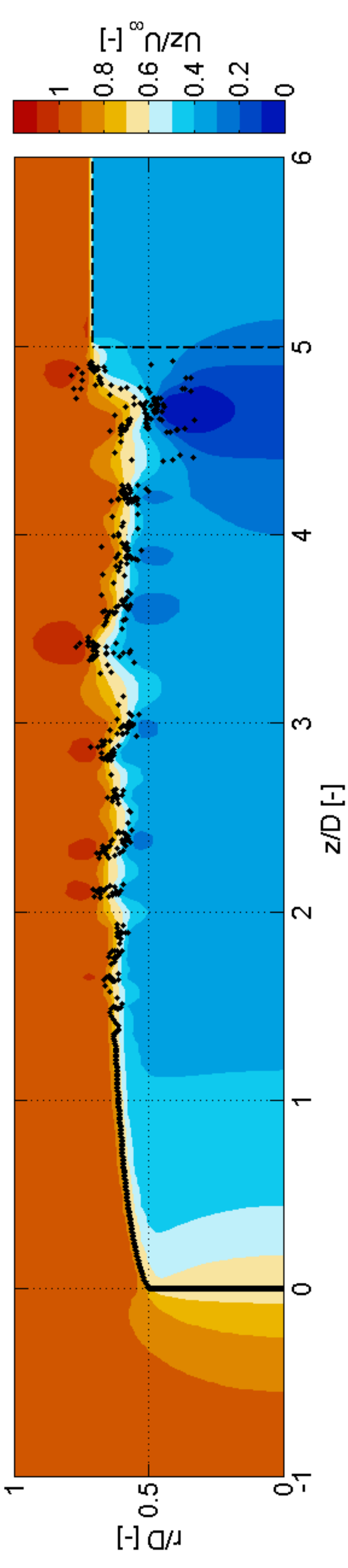

Figure 6.24: The axial velocity contour plot with the particle street projected on top for $C_t = 8/9$ and the semi-infinite vortex tube applied.

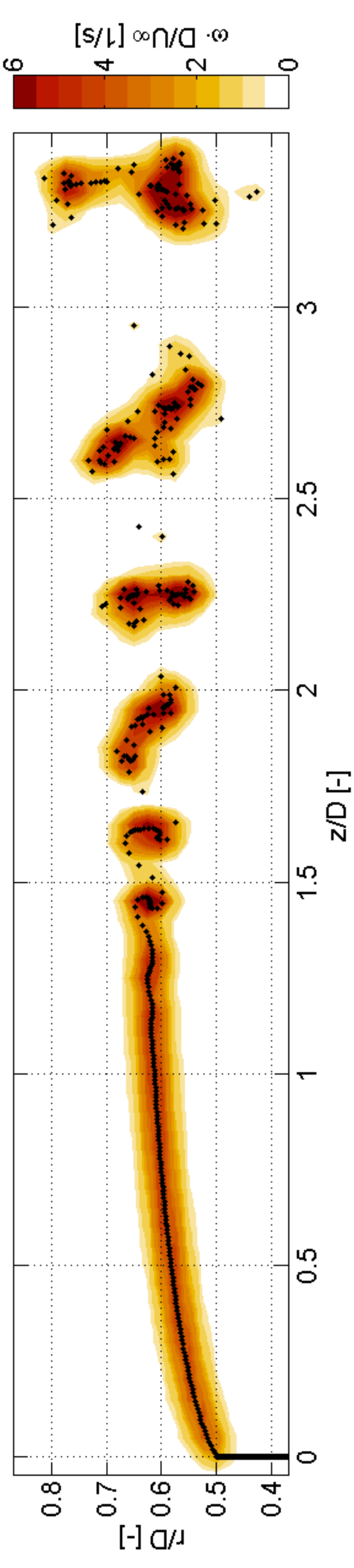

Figure 6.25: The vorticity contour plot with the particle street projected on top for $C_t = 8/9$ and the semi-infinite vortex tube applied. Close-up of the near-wake.

of particles. Lewis [19] comments on this behaviour as: "In effect our theoretical vortex sheet has undergone a form of transition from an initially laminar style of configuration to one in which the vorticity is repacked by its own natural convective motions into an array of eddies which have the appearance of two-dimensional turbulence.".

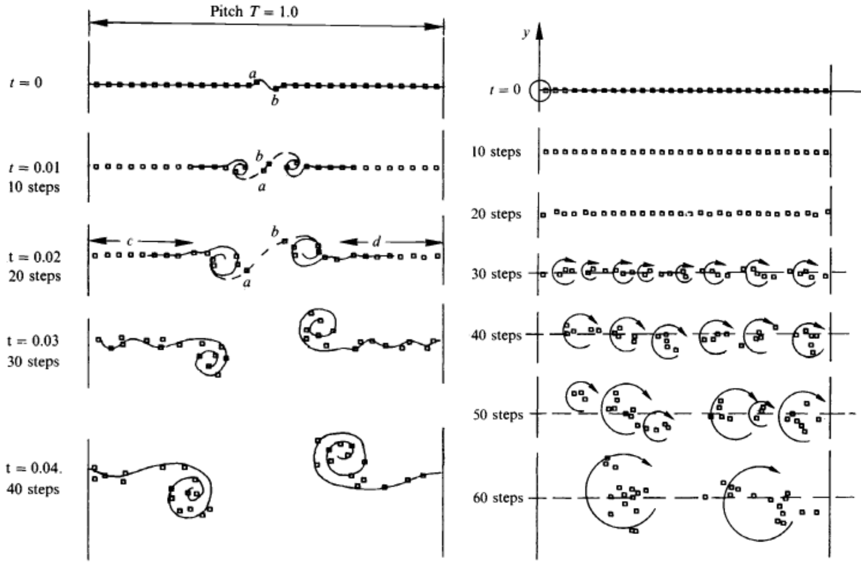

(a) Forced initial instability (b) Instability by computational round-off errors

Figure 6.26: *Kelvin-Helmholtz instability of a vortex sheet (Lewis [19]). Sheet modelled by 30 vortex elements of strength* $\Delta\Gamma = 1.0$, $\Delta t = 0.001$.

In figure 6.27 the mean of the axial velocity is presented. As a comparison, the experimental results from Lignarolo et al. [20] for an actuator disk at the same thrust coefficient of $C_t = 8/9$ are given in figure 6.28, and the difference in axial velocity between figures 6.27 and 6.28 is presented in figure 6.29. Regarding figure 6.28, no data has been obtained in the blank region due to limitations in the experimental PIV set-up.

The results for the numerical and the PIV experiment show a similar wake expansion, and also the shear layer expansion matches reasonably well (figures 6.27 and 6.28). The wake expansion results in a reduction of axial velocity in downstream direction, for which the PIV results show a slightly larger velocity deficit, see figure 6.29. The results also show that a narrow region of axial velocity increase relative to the free-stream velocity is present, just aft of the disk up to 1 diameter downstream.

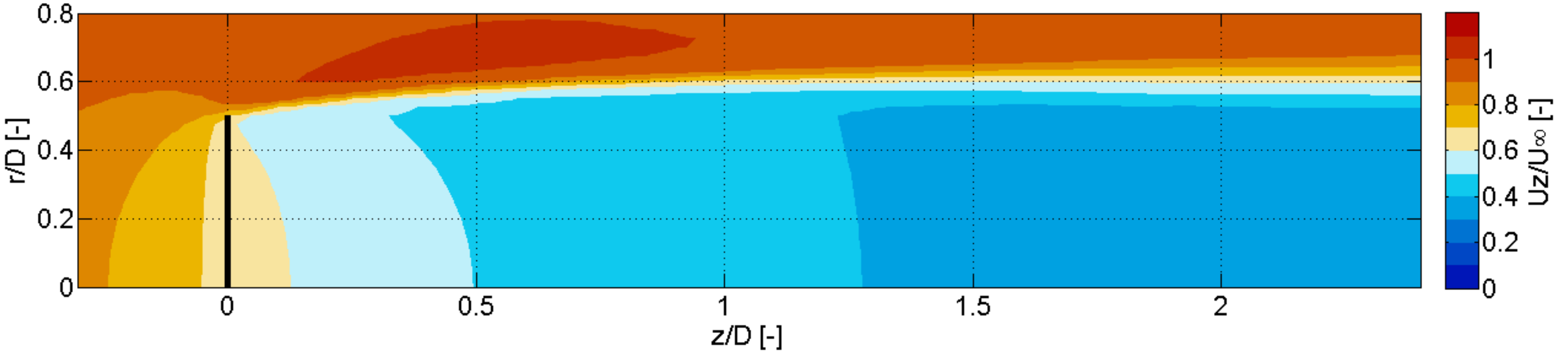

Figure 6.27: *The mean axial velocity contour plot (100 samples) with the particle street projected on top for* $C_t = 8/9$ *and the semi-infinite vortex tube applied. Close-up of the near-wake.*

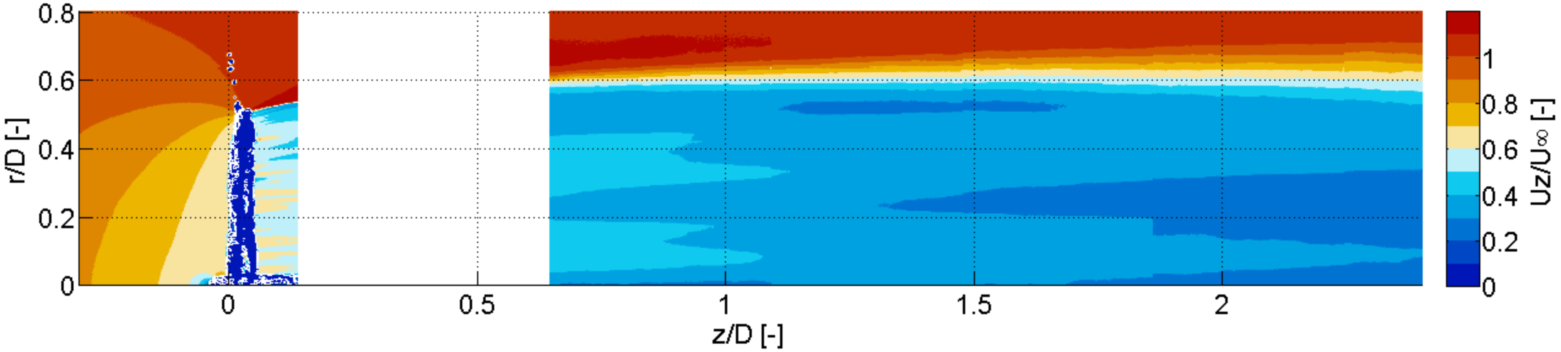

Figure 6.28: *The mean axial velocity contour plot of the reference experiment (Lignarolo et al. [20]).*

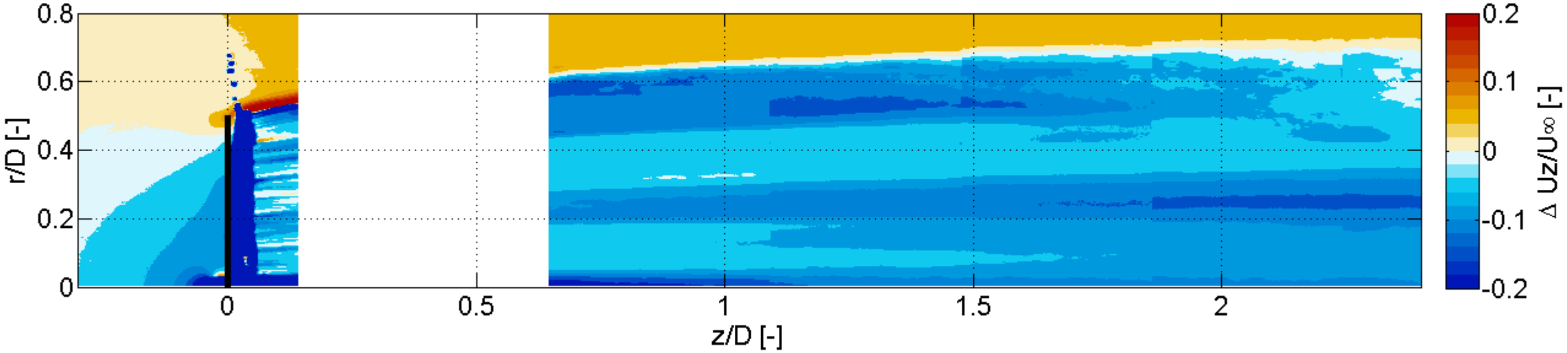

Figure 6.29: *The difference in mean axial velocity between figures 6.27 and 6.28.*

6.4.4 Analysis of the results for a direct computation versus the FMM

In this section, the validity of the simulation with the FMM applied is verified against the purely direct (N^2) solution. Furthermore, the result of a simulation with the FMM applied, but without taking the far-field stretching into account is added. For validation, the results are compared to the numerical results by van Kuik and Lignarolo [33], for which the model is outlined hereafter.

van Kuik and Lignarolo [33] have developed a potential flow model for the actuator disk, whereby the wake sheet is discretized into a finite number of vortex rings. The far-wake from 15 diameters downstream and beyond is replaced by an analytical description of the wake as also applied for the actuator disk simulations in the current thesis work. The far-wake and the first vortex ring at the actuator disk are fixed in time and space, while the vortex rings in between experience a degree in freedom regarding the strength and position. By applying the boundary conditions of no force and normal velocity on the rings, the position and strength of the rings are determined by iteration. Accurate results have been obtained with an error in wake expansion of only 0.7 ‰.

For the validation in this section, figures 6.30 and 6.31 are constructed. Figure 6.30 shows the centerline velocity over the axial direction, while figure 6.31 gives the axial velocity deficit or wake profile for different axial positions. For both figures the results from the model by van Kuik and Lignarolo [33] are added for comparison. It has to be noted that for figure 6.31 only the wake expansion is a result from van Kuik and Lignarolo [33] (red dotted line). The accompanying straight velocity deficit has been obtained by applying the continuity equation.

If looked at figure 6.30, the result without far-field stretching (NS) shows a decrease in velocity deficit relative to the other results. As the wake expands, the lack of stretching results in a loss of circulation in the vortex rings, and thus a decrease in the axial induction. If now the FMM with stretching applied is compared with the direct result, both curves match very well up to about 1 diameter downstream, where the onset of instability differs between both simulations. The centerline velocity of the direct and FMM result also match with the results from van Kuik and Lignarolo [33], up to about 2 diameters downstream, after which the results from the VPM show a significant offset. The reason for this offset lies in the fact that the wake expansion with the VPM is less than for the analytical tube. I.e. the near-wake does not connect smoothly to the far-wake and it contracts a bit, through which the centerline velocity is decreased between 2 and 5 diameters downstream.

That the wake expansion does not reach the theoretical value is also visible in figure 6.31, where the axial velocity deficit for several axial positions are presented. The velocity deficit is smooth right from the onset at the actuator disk, due to the large core size applied ($\sigma/R = 0.1$). Subsequently, it is visible how the shear layer expands over the axial direction. Finally, note that the FMM without stretching applied shows a large offset in axial velocity deficit over the whole wake between the actuator disk and analytical tube, while the velocity deficit profile of the other two results match closely.

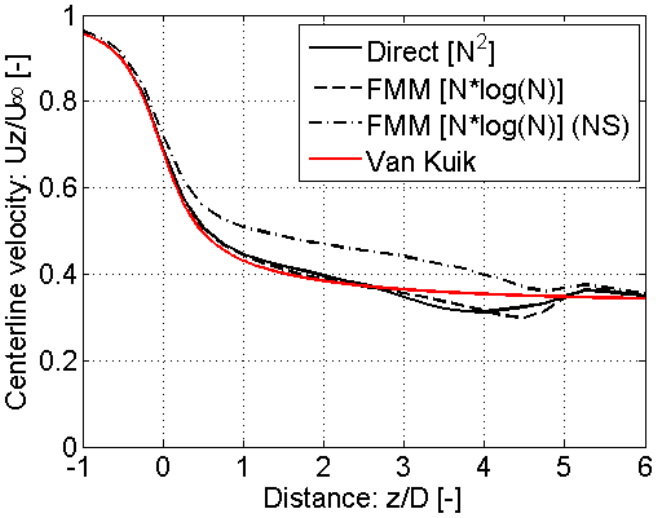

Figure 6.30: *A comparison between the direct simulation and the simulation with the FMM applied for the centerline velocity over the wake, with $C_t = 8/9$. Note, NS stands for No far-field Stretching applied.*

6.4.5 Analysis of the results for different core sizes and overlapping ratios

Results for the centerline velocity (figure 6.34) and axial velocity deficit over the wake (figures 6.32 and 6.33), for a thrust coefficient of $C_t = 8/9$ are presented. The influence of the particle overlap ($\lambda = \sigma/h$) and the core size (σ/R) is investigated.

It is visible in figure 6.34a that the particle overlap of $\lambda = 0.8$ and $\lambda = 1.6$ follow the correct centerline velocity profile quite closely (even though $\lambda = 0.8$ results in fact in a slightly under-resolved overlap). The smallest particle overlap of $\lambda = 0.3$ does result in a relatively large reduction in both velocity deficit and wake expansion, see figure 6.32. Further downstream, the wake profile differs between all results (between 4 and 5 diameters), due to the instability of the wake.

The comparison between the core sizes is now discussed. It has to be noted that the number of particles per ring is kept constant, which results in a decrease in overlap for a smaller core size. It is visible that the velocity deficit profile between the different core sizes is very comparable up to 1 diameter downstream. The reason that the shear layer for the smaller core sizes is as smooth as for the largest core size, has possibly to do with the fact that the shear layer is unstable right from the wake onset for the smaller core sizes. It is also visible that between 2 to 3 diameters downstream, the shear layer consisting of the smaller core sizes is smoother than for the largest core size. At that point the shear layer with the largest core size is also becoming unstable, and the shear layer is almost completely similar between all core sizes at 4 diameters downstream. Probably, the Kelvin-Helmholtz instability and the subsequent breakdown of the vortex sheet is the dominant factor in the shape of the shear layer, and particle specific parameters such as

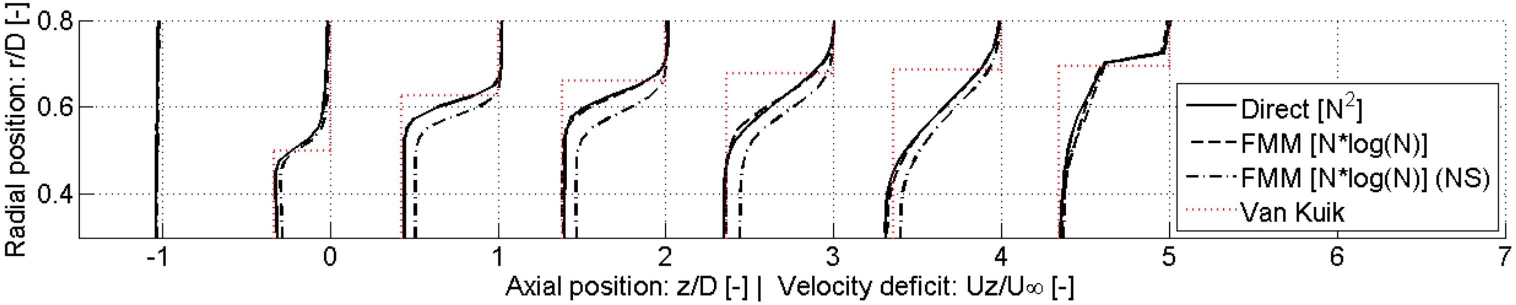

Figure 6.31: *The axial velocity deficit for different axial positions over the wake at $C_t = 8/9$. Comparison between the direct simulation, the FMM, and the FMM with No Stretching (NS) applied.*

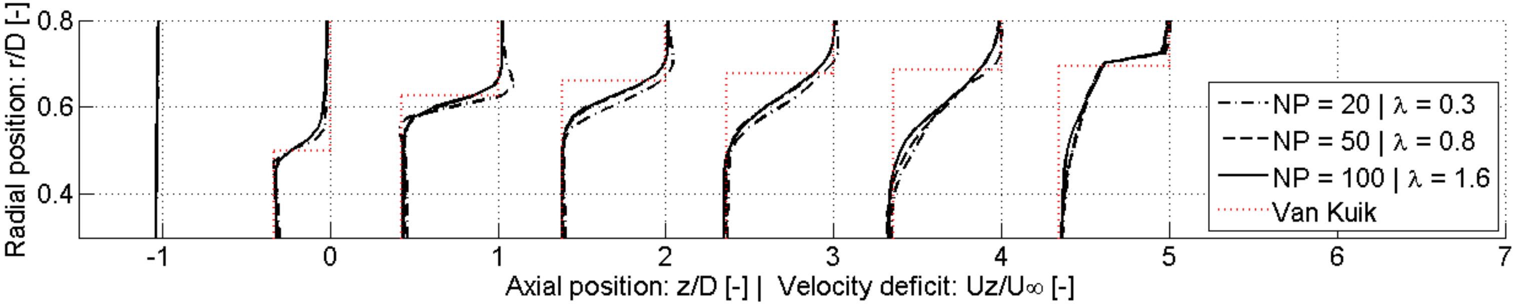

Figure 6.32: *The axial velocity deficit for different axial positions over the wake at $C_t = 8/9$. Comparison between different overlapping ratios.*

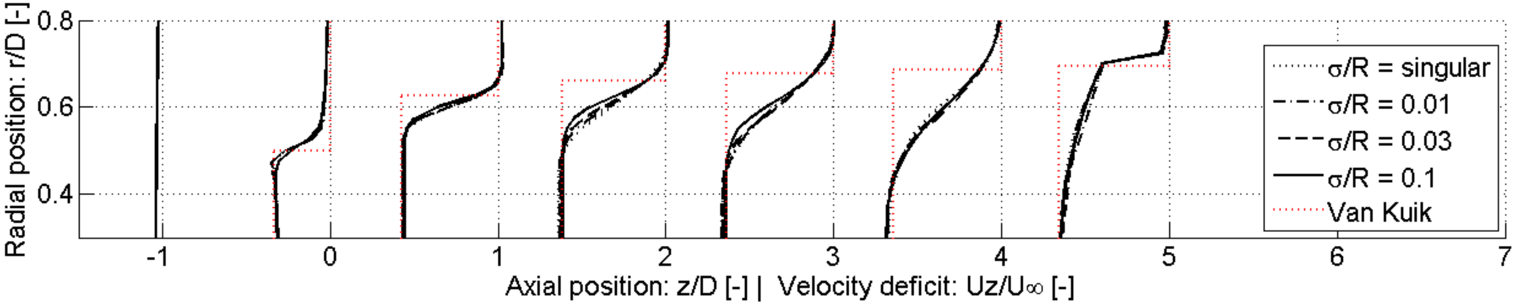

Figure 6.33: *The axial velocity deficit for different axial positions over the wake at $C_t = 8/9$. Comparison between different core sizes.*

the overlap and cores size have a relatively small influence on the shear layer expansion. In all cases, the shear layer starts expanding quickly after initiation, and reaches the centerline at about 4 to 5 diameters downstream, which is in line with what has been stated in section 2.2 about the theory on wake aerodynamics.

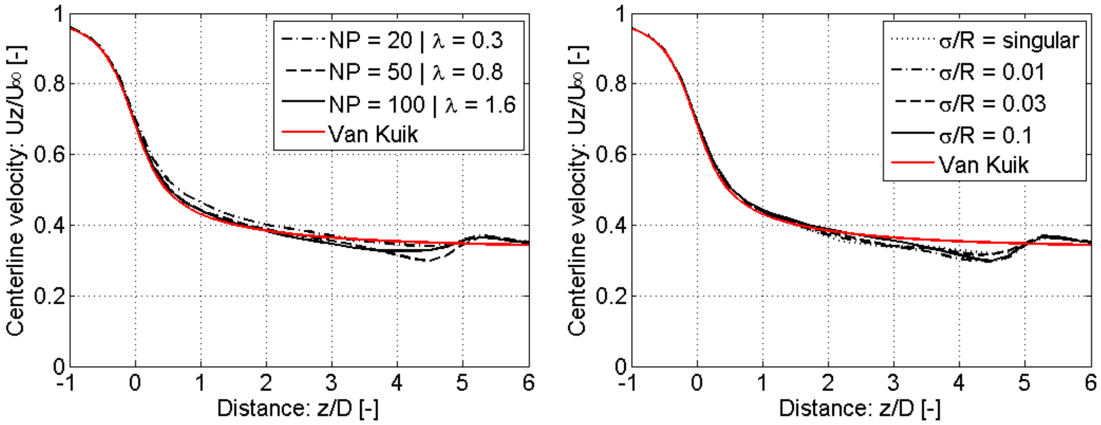

(a) Comparison for overlap

(b) Comparison for core size

Figure 6.34: *A comparison between different overlapping ratios and core sizes for the centerline velocity over the wake, with $C_t = 8/9$.*

6.4.6 Analysis of results for different thrust coefficients

A comparison of the axial velocity over a range of thrust coefficients is presented in figure 6.35. For the simulations between $C_t = 4/9 - 8/9$ the semi-infinite vortex tube is applied. For the results of $C_t = 9/9 = 1$ the wake expansion would theoretically go to infinity, and for higher thrust coefficients flow reversal takes place, such that the analytical vortex tube expression is undefined in these cases. In all cases, it has been encountered that an instability arises in the shear layer. From $C_t = 7/9$ and above the vortex street starts to break up already before 2 diameters downstream, such that it will have a significant effect on the induction factor at the rotor, and the wake expansion at 5 diameters downstream is not reached. The case for $C_t = 9/9$ has a special significance as the demarcation of highly loaded rotors, whereby in theory the wake should expand to infinity. This should result in an induction factor of $a = 0.5$ at the actuator disk and thus a flow stand-still in the far-wake. Due to the instabilities arising, the induction is reduced to $a = 0.4$ at the rotor plane and the wake manages to survive. However, higher thrust coefficients result in flow-reversal, and a periodic shedding in upstream direction of vorticity is visible. For clarification, the evolution over time for the thrust coefficients between $C_t = 8/9$ and $C_t = 16/9$ has been added in appendix F.

Figure 6.36a shows the centerline velocities over the wake for the range of thrust coefficients between $C_t = 4/9 - 8/9$. The horizontal red dashed lines indicate the theoretical asymptotes of the corresponding centerline velocities at full wake expansion, and the red circular dots denote the theoretical centerline velocities at the AD. For $C_t = 4/9$ and

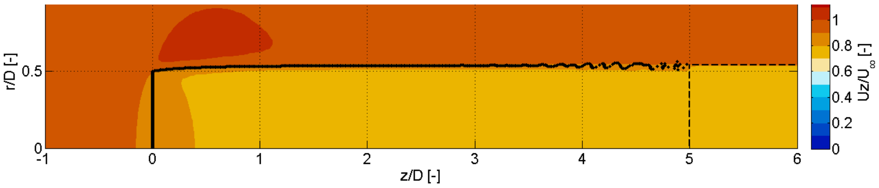

(a) $C_t = 4/9$

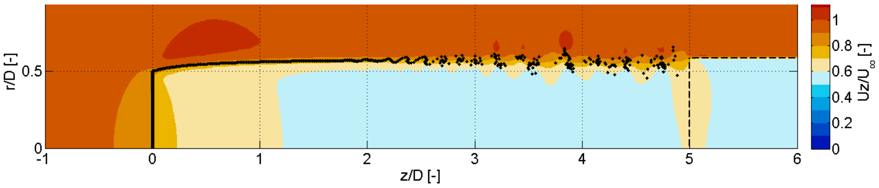

(b) $C_t = 6/9$

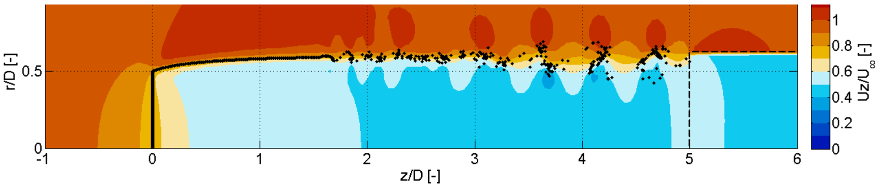

(c) $C_t = 7/9$

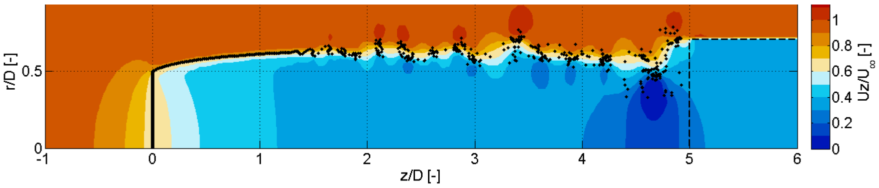

(d) $C_t = 8/9$

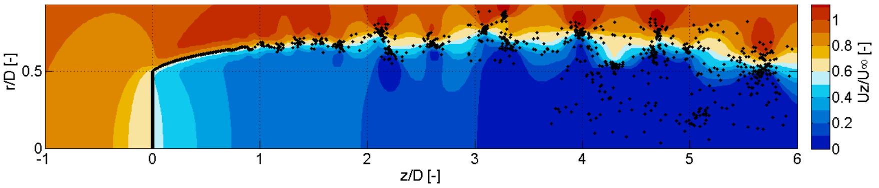

(e) $C_t = 9/9$

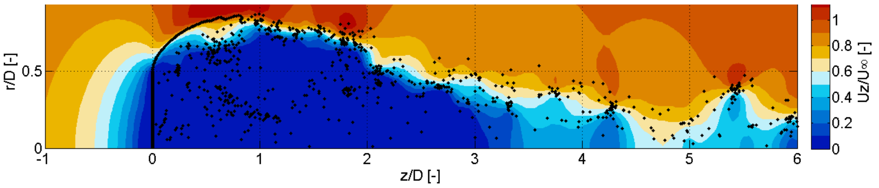

(f) $C_t = 12/9$

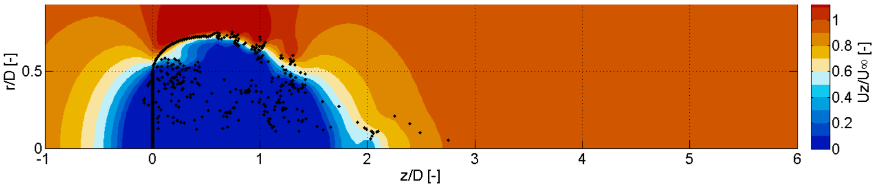

(g) $C_t = 16/9$

Figure 6.35: *The contour map of the axial velocity over a range of thrust coefficients. The semi-infinite vortex tube is only applied for thrust coefficients of* $C_t = 8/9$ *and lower.*

$C_t = 6/9$, the full wake expansion occurs already in front of the start of the semi-infinite tube, and the connection is reasonably smooth. For $C_t = 7/9$ and $C_t = 8/9$, the vortex sheet contracts just before the start of the analytical tube, as the wake expansion is not fully reached. Therefore, the centerline velocity overshoots the theoretical value.

Finally, figure 6.36b shows the theoretical relationship between the thrust coefficient and the induction factor, along with the Glauert correction for highly loaded rotors, and the corrections by Burton and Wilson (Buhl [2]). A collection of empirically obtained results are added (red crosses) and the results of simulations from the VPM (blue circles). Above $C_t = 8/9$ the wake starts to become highly loaded, and the turbine enters the turbulent wind mill state. The thrust coefficients of $C_t = 12/9$ and $16/9$ end up in the large scattered region beyond $a = 0.5$ for which inverse flow is manifested. The induction factors for the highest thrust coefficients are taken here as under-bounds, as it is difficult to define the induction factor due to the periodic wake shedding.

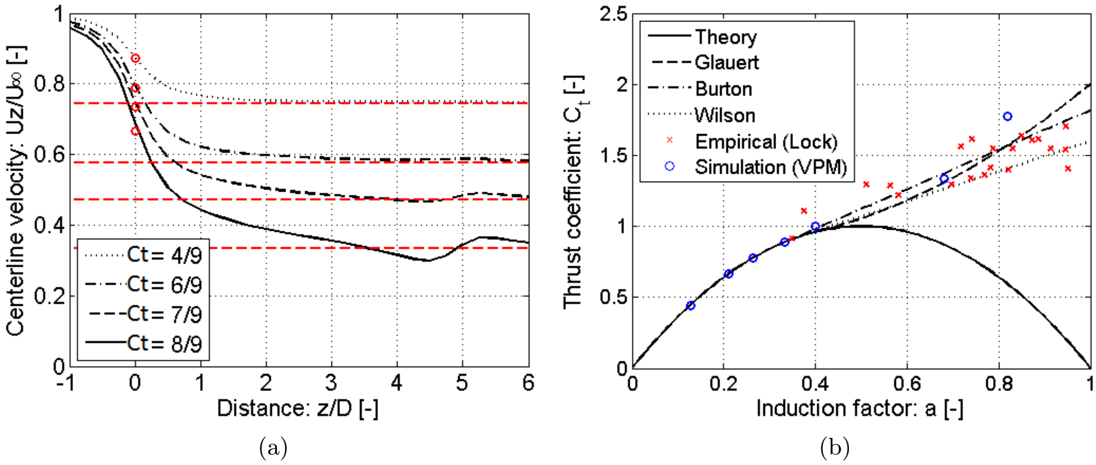

(a) (b)

Figure 6.36: *(a) The centerline velocity over the wake for different thrust coefficients. (b) The induction factor versus the thrust coefficient for theoretical, empirical, and simulated results.*

6.5 Simulation of the 3-bladed MEXICO rotor with prescribed circulation

6.5.1 Motivation

As a final validation case, a 3-bladed rotating HAWT turbine has been modelled. Where the stability and solenoidal condition of the simulation was guaranteed in case of the actuator disk due to the axi-symmetry involved, the objective for the current test-case was to investigate the stability in a purely 3D environment. It is aimed for to obtain stable and accurate results over the near-wake, up to about 3 to 4 rotor diameters downstream. For all the cases that will be discussed in this section, results showing the time evolution of the wake are presented in appendix G.

6.5.2 Problem statement

As the rotor performance is not explicitly modelled, constant prescribed trailing circulation is shed from the rotor blades. As an input for this prescribed circulation, empirical results are used from the MEXICO (Model rotor EXperIments under COntrolled conditions) experiment (figure 6.37) [22, 23]. In this experiment, a 3-bladed small-scale wind turbine (4.5 meter rotor diameter) has been investigated in the German-Dutch Wind Tunnels (DNW) for a chordwise Reynolds number of $Re = 600,000$ at 75% radial position. For the current simulations, a tip speed ratio of $\lambda = 6.67$ has been applied.

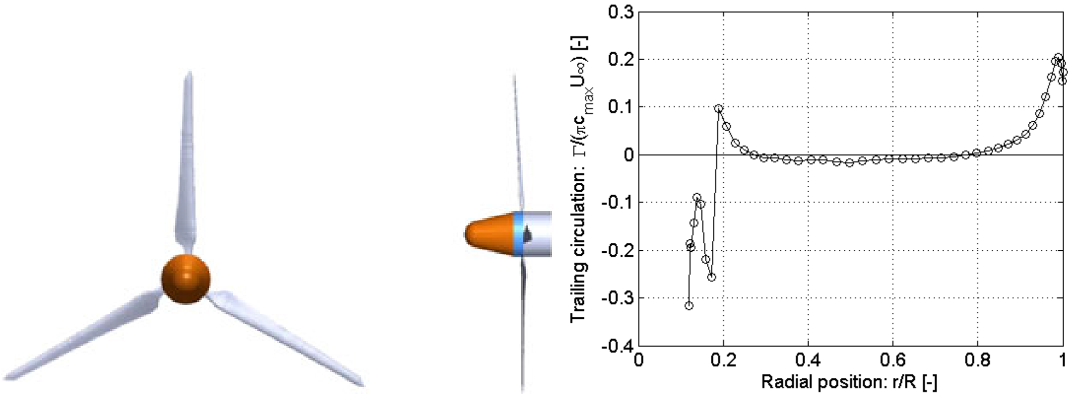

(a) Turbine geometry (b) Trailing circulation over one blade

Figure 6.37: *The configuration of the MEXICO rotor and the normalized trailing circulation over each blade. Image (a) is borrowed from Micallef et al. [22]. Note, The diameter of the MEXICO turbine is 2.25 [m] with c_{max} being 0.24 [m].*

The simulation set-up is described in table 6.6. The FMM is enabled with the direct derivatives for the velocity and finite differences for the vortex stretching. As stability is an issue, RK4 time integration is applied. The core is high order algebraic, and particle splitting is present to guarantee overlap.

Table 6.6: *Overview of parameters as applied for the simulation of the MEXICO rotor*

Parameter	Value	Unit	Description
TSR	6.67	-	Tip speed ratio
U_∞	0.942	$[ms^{-1}]$	Free-stream velocity
R	1	$[m]$	Radius
c_{max}	0.107	$[m]$	Maximum chord width
NB	3	-	Number of blades
NP	9	-	Number of spanwise trailing vortices per blade
σ	0.1	$[m]$	Core size
λ	1.5	$-$	Minimum core overlap
ν	0-0.0001	$[m^2s^{-1}]$	Kinematic viscosity
Δt	0.05	$[s]$	Time step size and shedding interval
t	5-15	$[s]$	Total simulation time
$\mathcal{O}$	2	-	FMM expansion order
θ	2.0	-	FMM acceptance factor

6.5.3 Qualitative discussion of the wake

Figure 6.38 shows the typical wake geometry as appearing throughout the simulations. 9 trailing vortices are shed per blade, forming a helical structure of 27 vortices in total. The thickness indicates the circulation strength, through which it is visible that circulation is mainly arising at the root and the tip of the blade. Although figure 6.38 suggests the use of filaments, visible are particle vectors normalized to the local respective filament element length. As long as the particles stay divergence-free, the vectors will remain aligned.

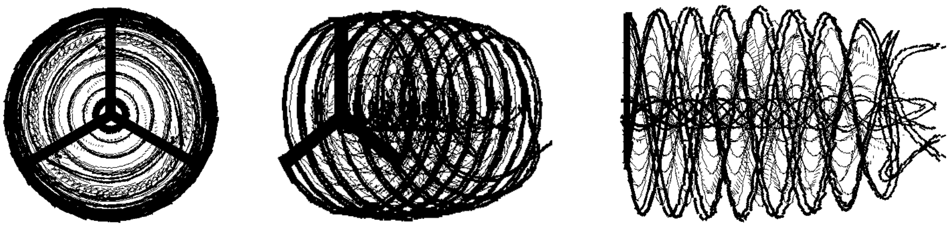

(a) Front view (b) Three-quarter view (c) Side view

Figure 6.38: *A typical illustration of the wake of a HAWT as modelled through the VPM. As the particle vectors are alligned, a representation of the trailing vortex filaments is visible. The thickness is an indication of the circulation strength.*

Figure 6.39 gives a demonstration of the axial velocity contour in the wake. The particle vectors are projected on top to obtain a qualitative impression of the integrity of the trailing vortices. Over the first 2 diameters downstream, the particles remain reasonably well connected, through which the representation of the shear layer at the tip and root is maintained. Due to these shear layers, a wake expansion and flow deficit is visible. Note also the region around the centerline, in which the axial flow velocity actually increases. In reality, this phenomenon would not occur as a rotor hub would be present resulting in a blocking effect. At the extremity of the wake, the root vortices start forming complex, highly stretched patterns in which the tip vortices are getting entangled as well. The prevention or mitigation of vorticity of these distorted regions is important, as these chaotic flow patters infringe on the stability of the simulation. The result is either a blow-up of the simulation, or the addition of an unacceptable amount of particles in highly stretched flow regions.

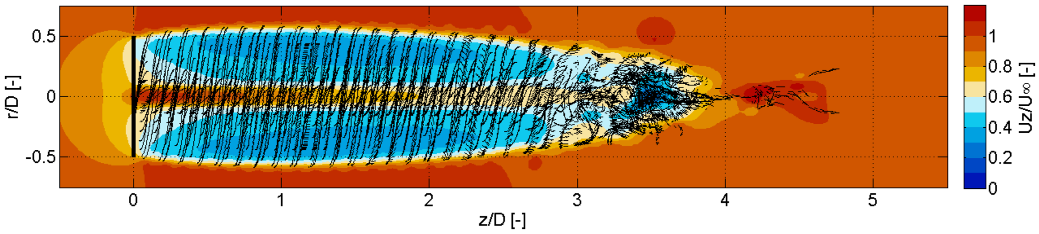

Figure 6.39: *Demonstration of the wake of the 3-bladed MEXICO turbine, simulated by the VPM. The black lines represent the trailing vortices discretized by particle vectors.*

6.5.4 Comparison between results with and without PSE applied for the classic scheme

Figure 6.40 shows the wake for a simulation with a constant particle core, a classic scheme for stretching, and without any form of viscous diffusion handling applied. Figure 6.40a shows a break-up of the shear layer with wave patterns in the helical particle structure forming. The unstable shear layer results in the wake becoming chaotic after 2 diameters downstream, which is visible in figures 6.40b and 6.40c. The chaotic wake part is built up of highly stretched and entangled vortices. Due to this behaviour, a simulation with the real core applied (which is allowed to shrink during stretching) would have already blown up, and no meaningful results have been obtained for a wake that has travelled more than 2 diameters downstream with a real core.

A very effective measure against the intensely stretched and entangled flow regions, is by the application of a Particle Strength Exchange (PSE) scheme, through which the particles are allowed to exchange vorticity to simulate viscous diffusion. Figure 6.41 shows the result by the application of a viscosity of $\nu = 0.0001 [m^2/s]$ with a rotor scale Reynolds number of $Re = D \cdot U_\infty / \nu = 18840$. The wake region beyond 2 diameters downstream shows a smoother construction, and the regions of intense vorticity have been alleviated, when compared with figure 6.40. The root vortices diffuse with axial direction due to the opposite circulation of the triple root vortex system, see figure 6.41c. The vortices in the shear layer remain well aligned, and while the shear layer shows a minor fluctuating pattern, no break down of the shear layer is visible. Although the shear layer looks reasonably stable from figure 6.41c, it is visible in figure 6.41a that the particles tend to form wave patterns again, as was encountered in figure 6.40a. This results in an incorrect reduction of the strength of the vortex sheet, and the wake expansion and velocity deficit further down the wake are reduced, as visible in figure 6.41b.

It is expected that the formation of wave patterns in the shear layer are a result of the coarse time integration. To this extent, the simulation with the classic scheme and PSE applied, but with a 2.5 times decreased time step size is presented in figure 6.42. It is visible in figure 6.42a that the wave pattern in the shear layer is not encountered, and the helical structure is well maintained. In figure 6.42b it is visible that the wake expansion and flow deficit are far better modelled than in figure 6.41b.

6.5.5 Analysis of the results with a PSE scheme applied using the transpose scheme

In this section, the same viscous simulation with the PSE applied as in section 6.5.4 is carried out, but now with the transpose stretching scheme applied. Figure 6.43 shows the results for the transpose scheme without relaxation, while for figure 6.44 the transpose scheme with a large relaxation of $f = 0.1$ is applied.

Figure 6.43a shows that the root vortices just aft of the rotor loose connection and are averaged out under influence of the transpose scheme. I.e. the physical representation of the root vortex system is quickly lost. As a result, a narrow region of large flow deficit is visible between 1 and 2 rotor diameters in figure 6.43b. This behaviour is also visible far down the wake, where a complex flow geometry is forming. On the other hand, the outer shear layer is very well maintained: the vortices remain aligned and breakdown of the wake sheet is not visible before 2.5 rotor diameters downstream (figure 6.43c). That the outer shear layer remains intact is also visible in figure 6.43a, where it is shown that the tip vortices remain alligned, with just a minor wave pattern formation occurring. The transpose scheme thus shows a better modelling capability than for the classic scheme for a coarse time integration, regarding the outer shear layer.

As a remedy against the divergence of the root vortices, a divergence relaxation of $f = 0.1$ is applied, which is shown in figure 6.44. If figure 6.44a is compared to figure 6.43a it is visible that the large strip of divergence around the centerline has been resolved. Figure 6.44b shows that the shear layer of the root vortices is well maintained over the wake. Also, the chaotic flow pattern at the end of the wake has been mitigated to a large extent, as the very large flows deficit which was visible in figure 6.43b has been largely reduced in figure 6.44b.

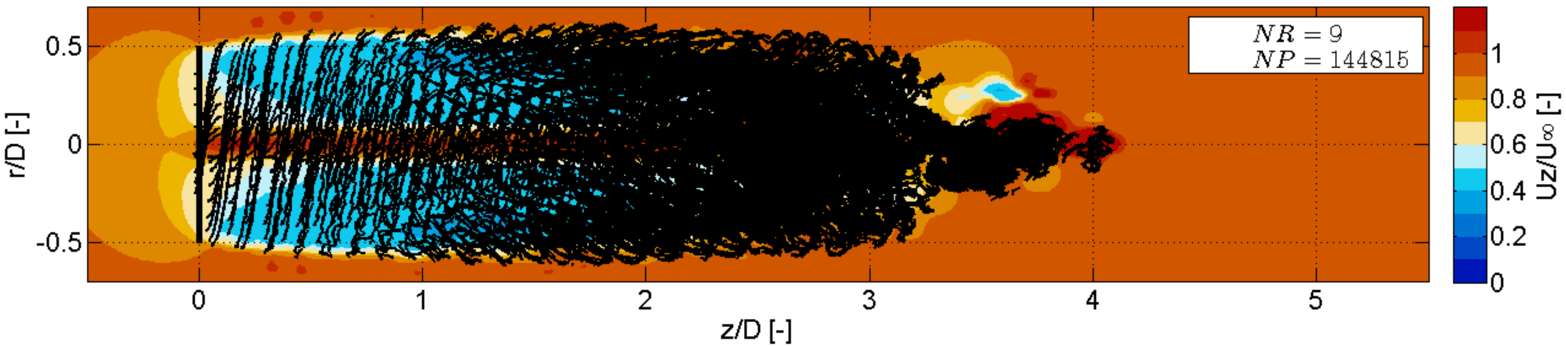

(a) Axial velocity with projection of particles

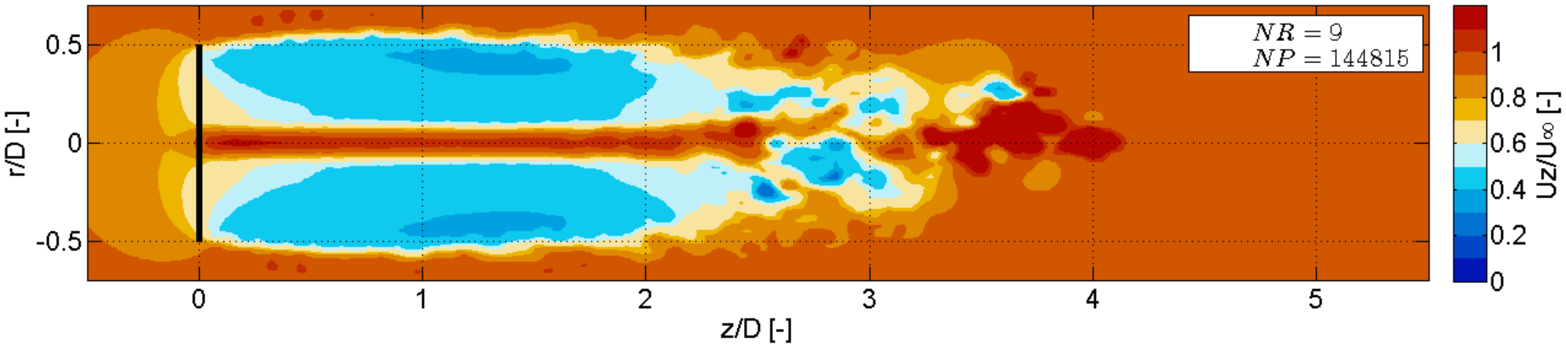

(b) Axial velocity

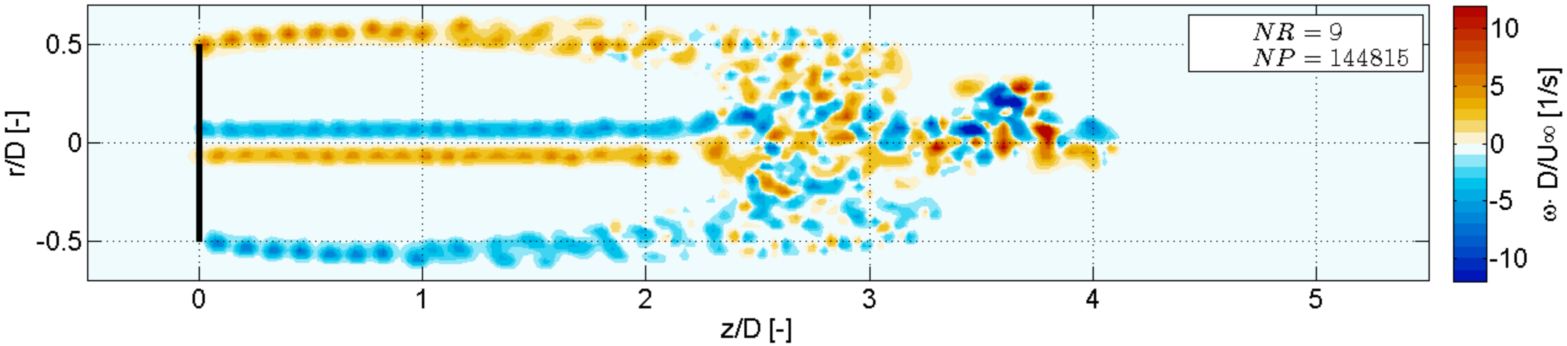

(c) Vorticity

Figure 6.40: *The wake with the classic scheme, without PSE applied. Visualization after 9 rotations.*

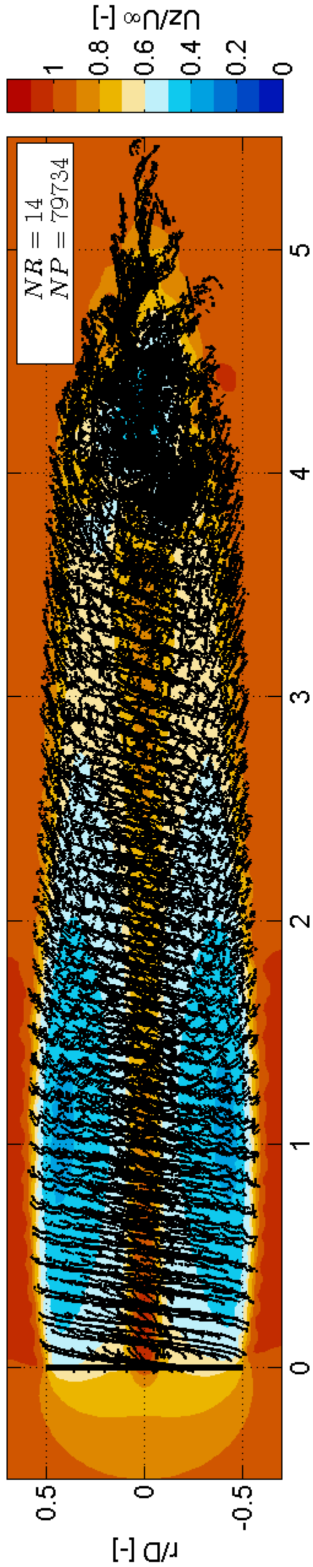

(a) Axial velocity with projection of particles

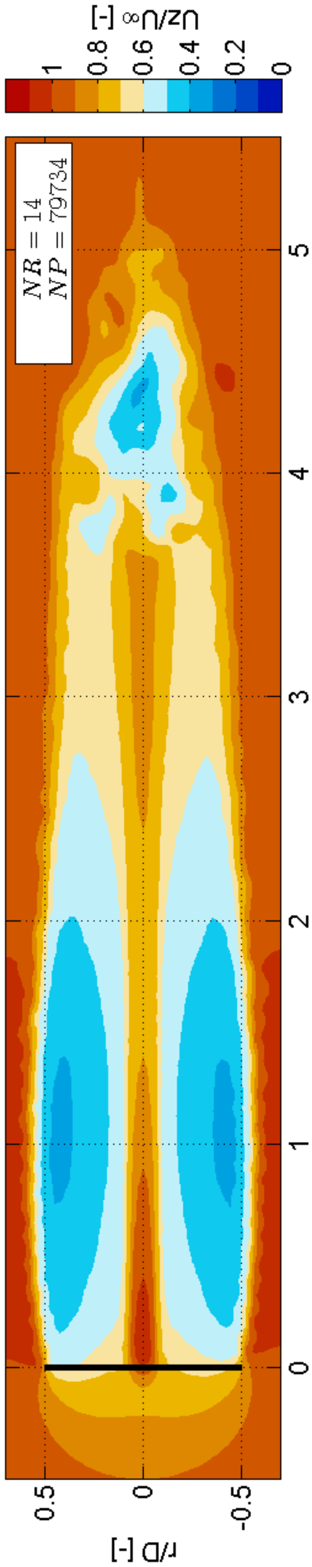

(b) Axial velocity

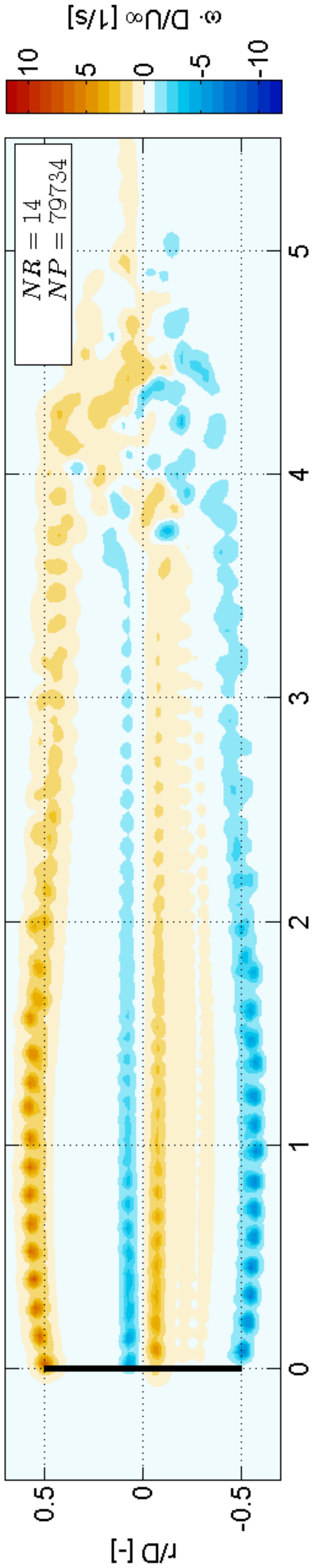

(c) Vorticity

Figure 6.41: *The wake with the classic scheme, with PSE applied. Visualization after 14 rotations.*

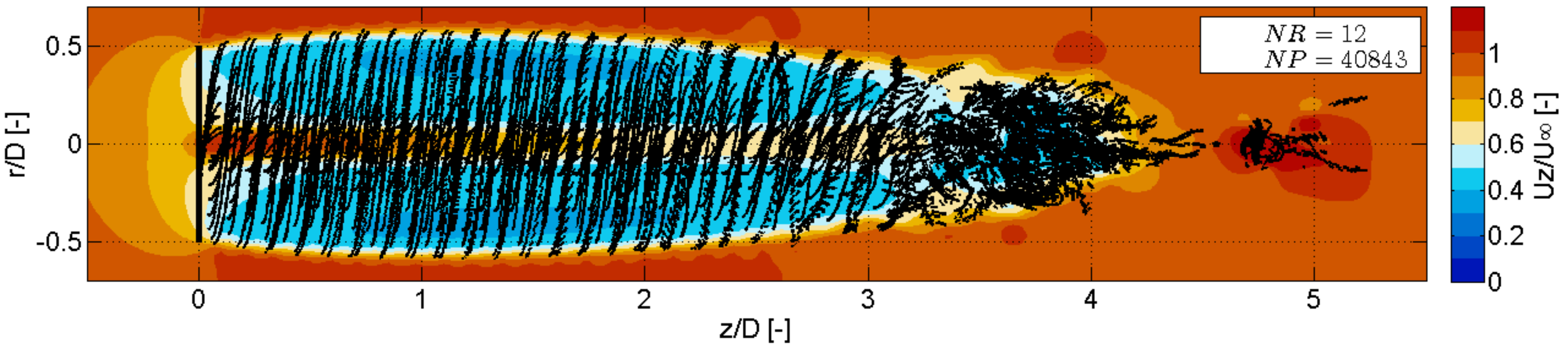

(a) Axial velocity with projection of particles

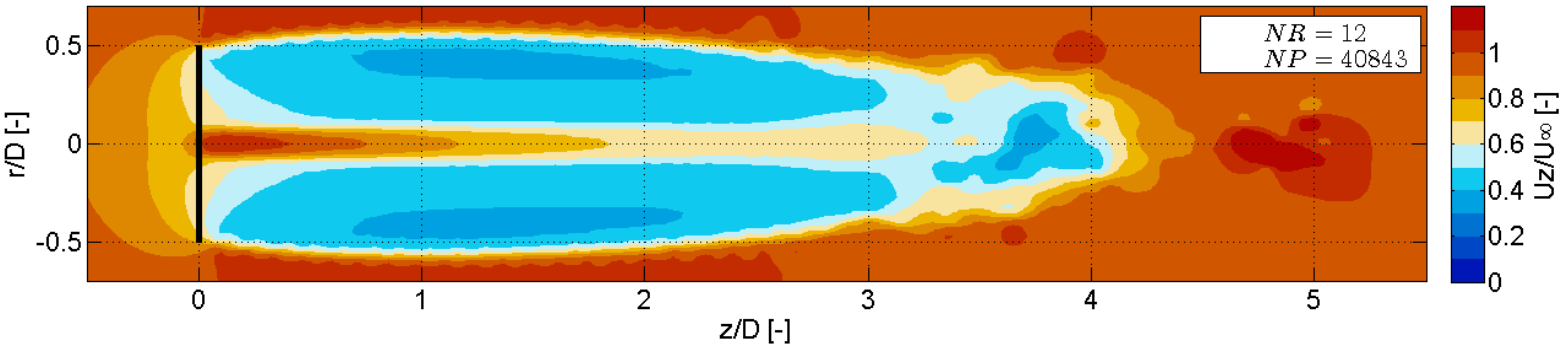

(b) Axial velocity

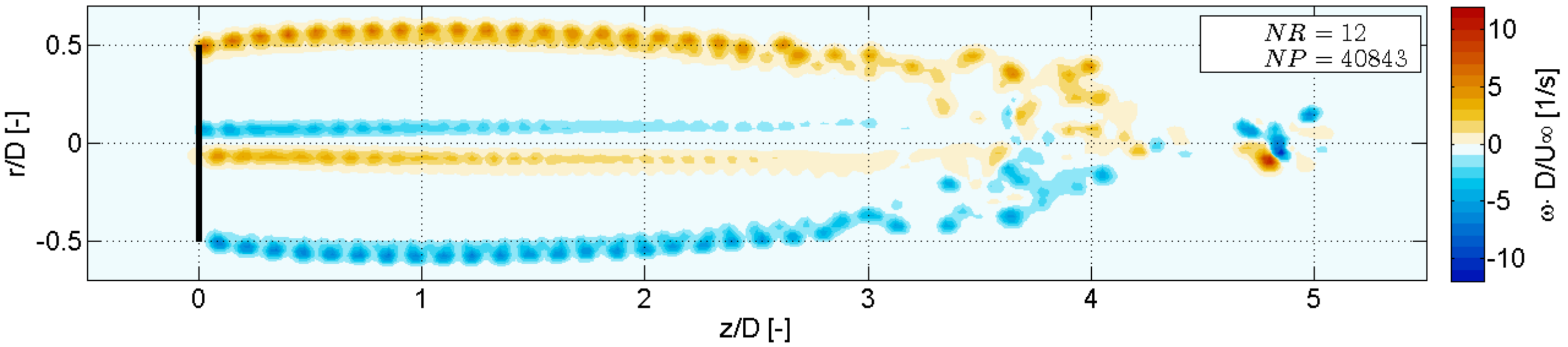

(c) Vorticity

Figure 6.42: *The wake with the classic scheme, with PSE applied. Visualization after 12 rotations.*

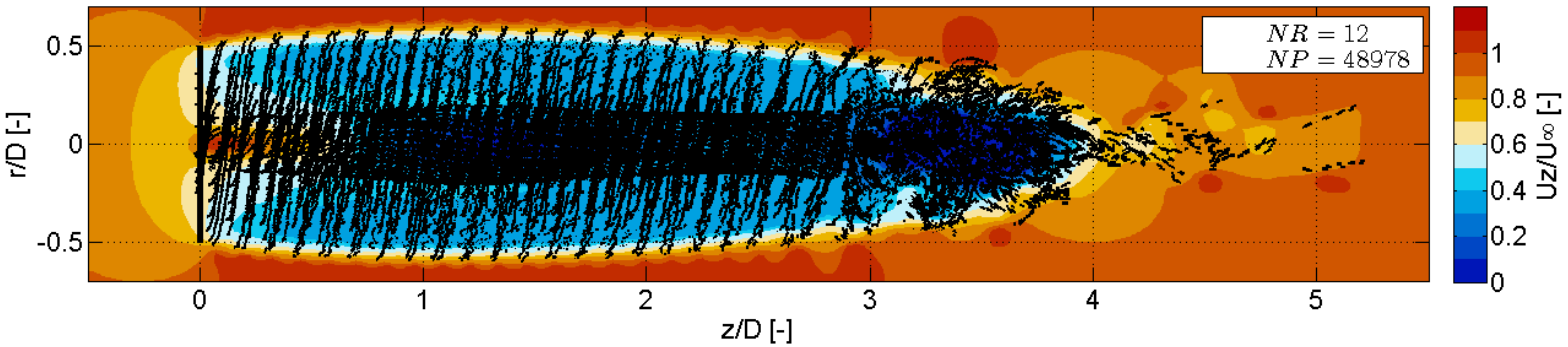

(a) Axial velocity with projection of particles

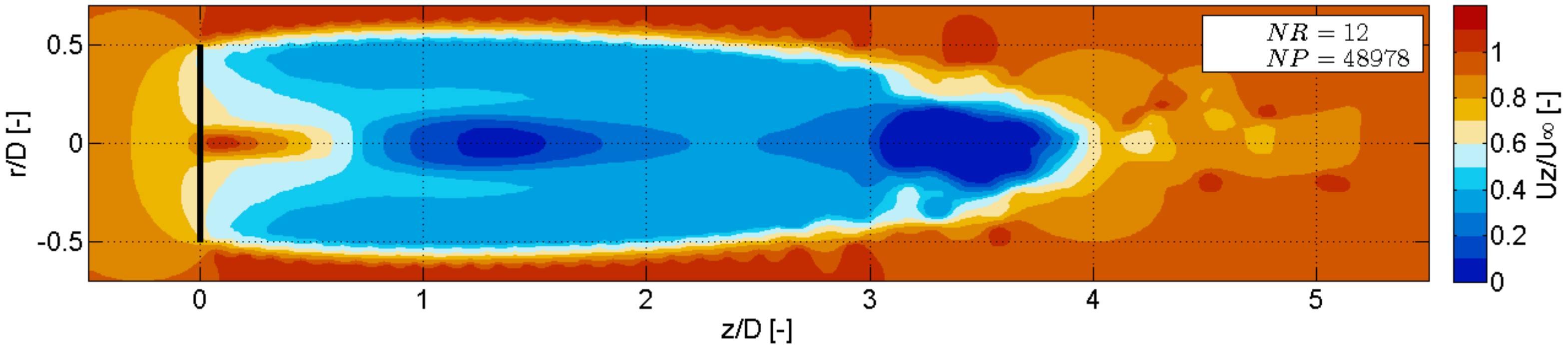

(b) Axial velocity

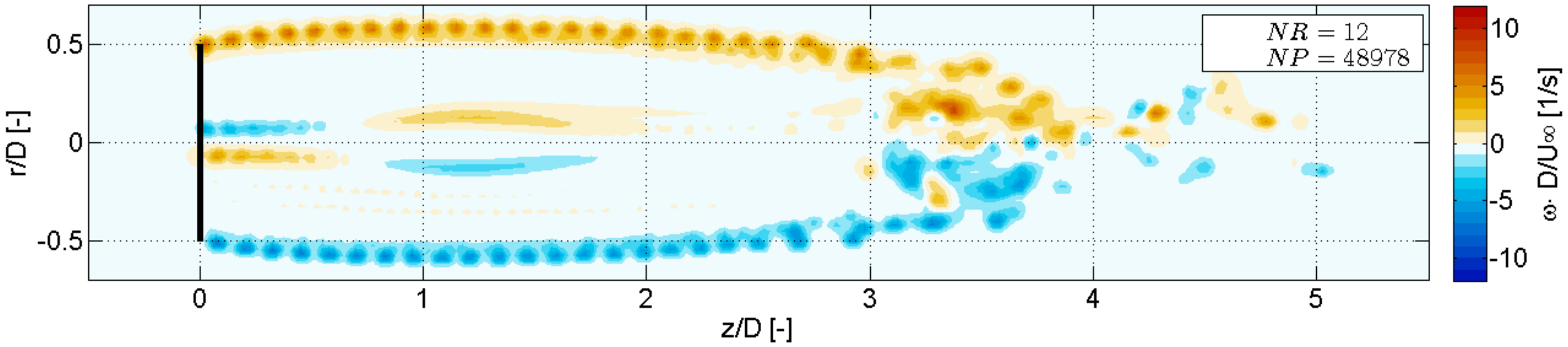

(c) Vorticity

Figure 6.43: *The wake with the transpose scheme without relaxation, but with PSE applied. Visualization after 12 rotations.*

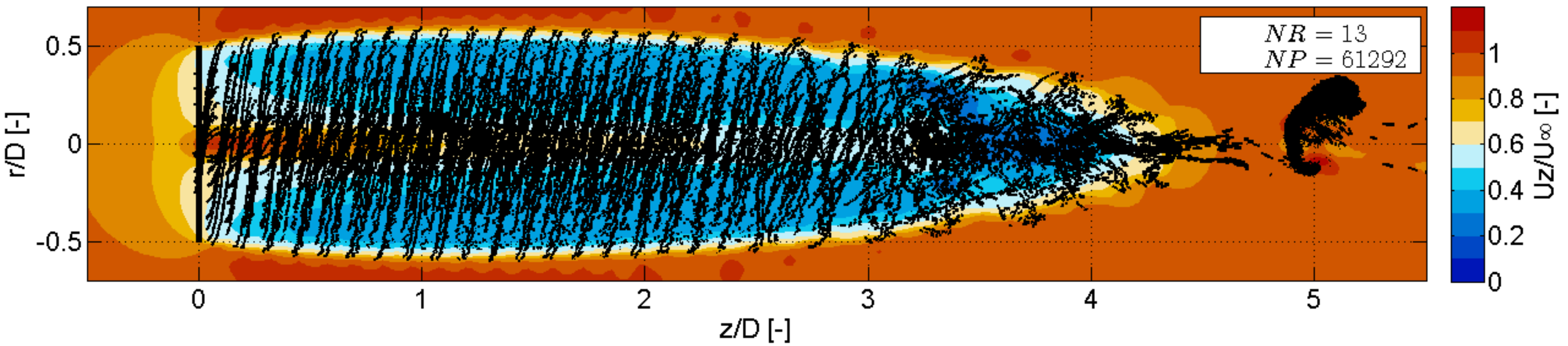

(a) Axial velocity with projection of particles

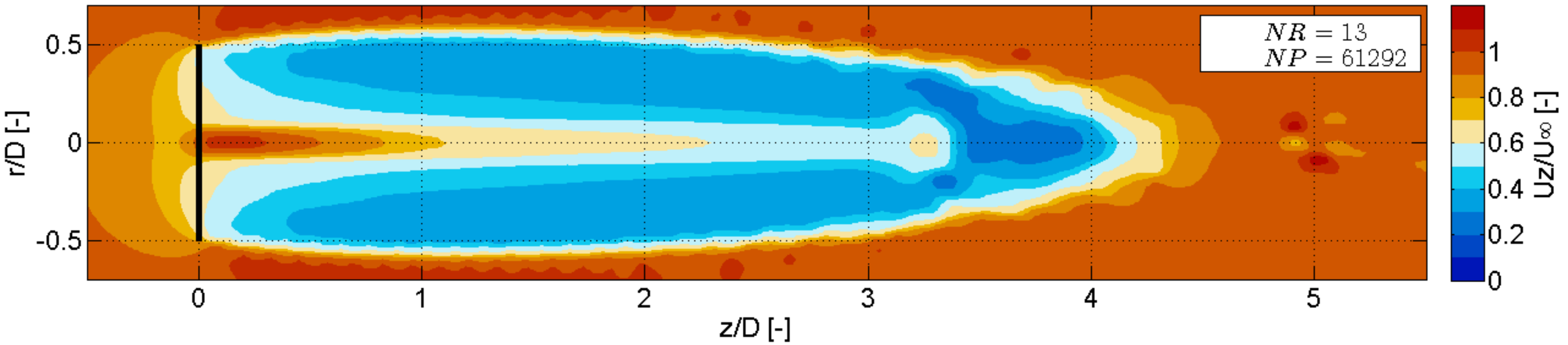

(b) Axial velocity

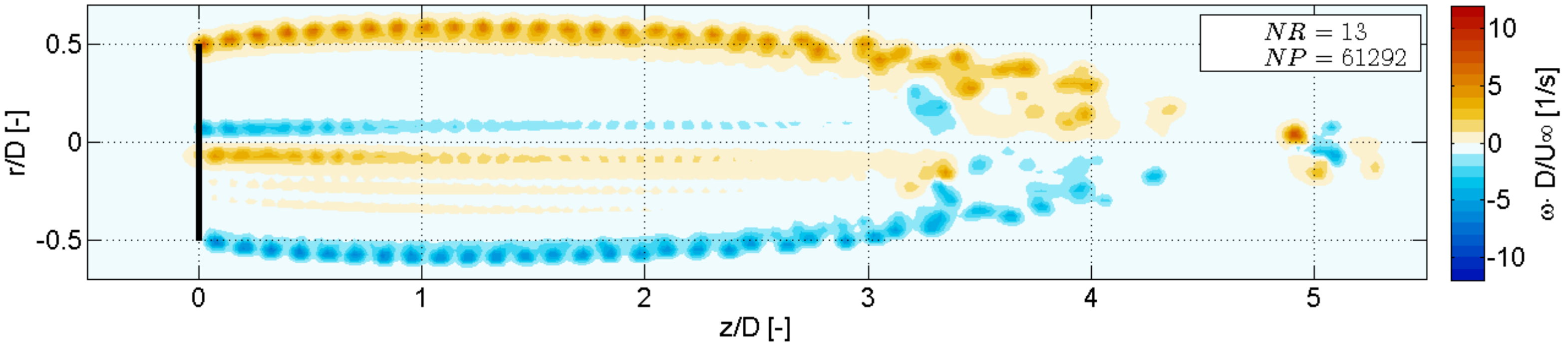

(c) Vorticity

Figure 6.44: *The wake with the transpose scheme with relaxation ($f = 0.1$) and PSE applied. Visualization after 13 rotations.*

6.5.6 Comparison between the numerical and experimental wake

Although the transpose scheme shows divergence of the root vortices, the result from the classic scheme would also be incorrect due to absence of the rotor hub modelling. To obtain insight into this effect, figure 6.45 shows the axial velocity for the case with the transpose scheme applied ($f = 0.02$). For comparison, figure 6.46 shows the empirical result for a 2-bladed turbine subject to a tip speed ratio of 6.0 and a thrust coefficient of $C_t = 8/9$ (Betz limit), as presented by Lignarolo et al. [20]. In the blank area just aft of the rotor, no results have been obtained due to limitations in the PIV test set-up.

Although the actual turbine configuration and operational conditions differ between both results, a comparable wake geometry is obtained. However, the presence of a physical rotor results in a large flow deficit behind the hub, up to flow-reversal. Ironically, the transpose scheme which was subject to divergence in the root vortices, results in a flow deficit profile around the root which compares better to the results of 6.46, than with the classic scheme applied.

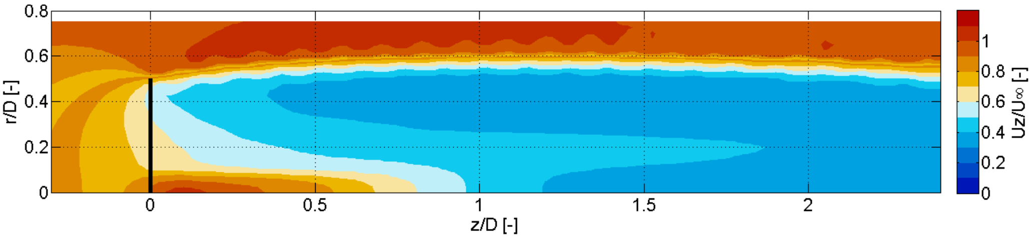

Figure 6.45: *Axial velocity of a VPM simulation with the transpose stretching scheme, a numerical core, and the PSE scheme applied.*

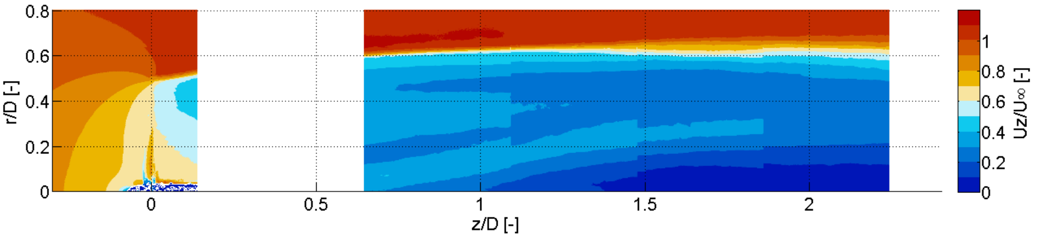

Figure 6.46: *Axial velocity of a physical 2-bladed turbine, obtained by PIV (Lignarolo et al. [20]).*

6.5.7 Comparison between the numerical and empirical results of the axial and radial velocity

In this subsection, the axial and radial velocity profiles at different radial positions around the rotor region will be discussed. Figure 6.47 shows the axial and radial velocity contours for four different radial positions on the rotor, from 52% tot 91% of the blade span. The empirical results originate from Nilsson et al. [23]. The results for the simulation with the classic scheme with and without PSE applied, and the transpose scheme with PSE applied and a small relaxation ($f = 0.02$) are presented. All simulations are subject to the same time step size of $\Delta t = 0.05[s]$. The empirical results from the MEXICO rotor are included for comparison. It has to be noted that the region from the rotor to 1 diameter downstream for $r/R = 0.52$, shows a large velocity deficit in axial direction for the empirical results. This is caused by the reflections of the laser beams on the rotor hub during the PIV experiments. This phenomenon is also visible for the result of $r/R = 0.60$, although being it to a far lesser extent. The results outside this region, and for the other radial positions are valid nonetheless.

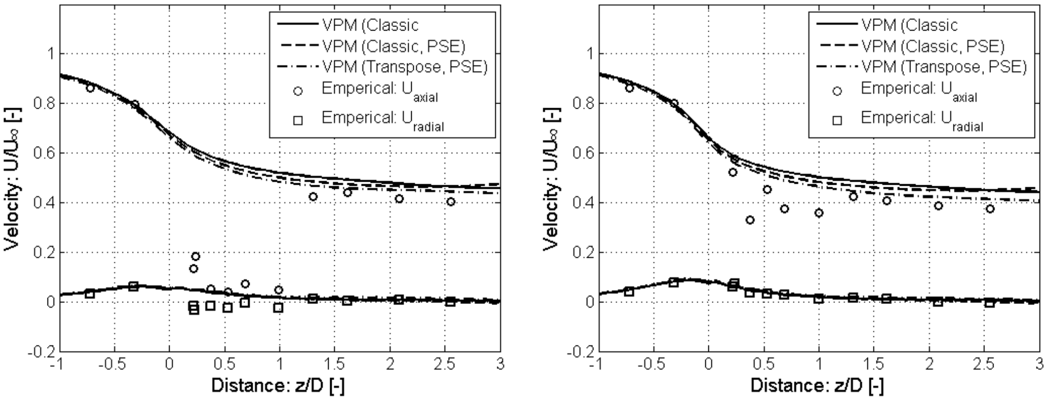

(a) $r/R = 0.52$ (b) $r/R = 0.60$

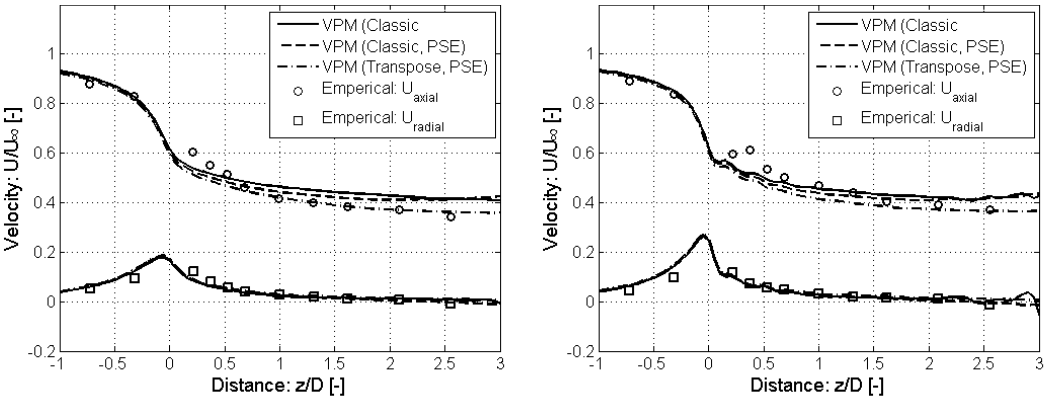

(c) $r/R = 0.82$ (d) $r/R = 0.91$

Figure 6.47: *The axial and radial velocity for different radial positions in the near-wake. The rotor is positioned at* $z/D = 0$. *The empirical results are borrowed from Nilsson et al. [23]*

All the results show the correct trend of decreasing axial velocity over the wake and a peak in radial velocity around the rotor. Outside the region which is influenced by PIV reflections, the radial velocity follows the empirical results quite closely. The axial induction at the rotor is a bit overestimated, although the axial velocity deficit closer to the far-wake is underestimated for the cases with the classic stretching scheme applied. In case of the transpose scheme, the empirical results for the axial velocity are better approximated. The reason is that the transpose scheme better maintained the structure of the outer shear layer, by which the wake expansion and flow deficit was more accurately modelled.

6.5.8 Analysis of the computational effort

The final investigation concerns the computational effort and number of particles over time of the simulation with the MEXICO rotor. All cases have been given 240 hours of simulation time on a single core of the Intel Xeon CPU E5-2670v2 with a clock speed of 2.5 GHz. The FMM is subject to an expansion order of 2 and an acceptance factor of 2.0, using direct expressions for the velocity and finite differences for the stretching.

Figure 6.48a shows the number of particles in the wake over the number of rotations of the turbine. The results with the PSE scheme applied show a mutual agreement and a linear growth up to about 12 rotations, indicating that few particles are added during vortex stretching. Over the last few rotations, a sharp increase is visible in the number of particles added over time, as the formation of complex flow structures requires the addition of a significant amount of extra particles locally. For the result without PSE applied, this behaviour is already present from 5 rotations onwards, as the simulation is heading towards a blow-up.

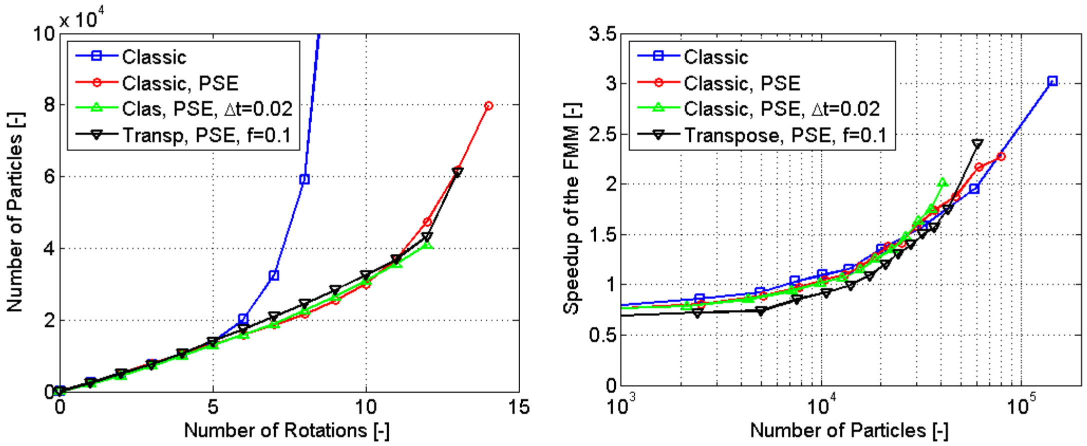

(a) (b)

Figure 6.48: *(a) Impression of the number of particles over the number of turbine rotations. (b) The speedup of the FMM relative to a direct simulation versus the number of particles in the domain.*

Figure 6.48b shows the computational efficiency of the FMM as the speedup ratio over a purely direct (N^2) simulation, versus the number of particles in the wake. I.e. when the curve exceeds unity, the simulation is faster with the FMM than without. It is visible that this break-even point for the presented results is around $0.6 - 1.4 \cdot 10^4$ number of particles. After $4 - 7 \cdot 10^4$ number of particles, simulations with the FMM are twice as fast. The result with the largest number of particles present shows a triple speedup for $1.5 \cdot 10^5$ particles in the wake. A number of particles in the range of $\mathcal{O}(10^4)$ thus results in a modest speedup.

Chapter 7

Conclusions and Recommendations

The objective of the present thesis work was to develop a fully Lagrangian Vortex Particle Method (VPM) for wind energy purposes, and to couple the VPM to a Fast Multiple Method (FMM) to reduce the computational effort. The code was written in Fortran 90 within the framework of the Parallel Particle-Mesh (PPM) library [30]. The FMM has been modified such that the velocity and stretching terms could be obtained.

For this thesis it was aimed to investigate the applicability of the VPM for the modelling of the near-wake of an actuator disk and a 3-bladed HAWT with prescribed circulation from the MEXICO experiment [22]. Focus lied on the accuracy, computational effort, and stability of the method. To obtain more insight in the modelling aspects of the VPM, several simple vortex geometries have been modelled and assessed against known analytical and numerical solutions. The conclusions from these investigations are enlisted hereafter.

7.1 Conclusions

- An existing FMM has been modified to obtain the velocity and vortex stretching terms as partial derivatives from the vector potential. The convergence and computational effort of this modified FMM were checked along the leapfrogging problem:
    - The velocity and stretching have been obtained as the first and second partial derivatives from the vector potential, through either finite differences and the derived expressions. Convergence was shown for the finite differences over both the expansion order and the acceptance factor. For the derived expressions, convergence was only visible over the acceptance factor; an underbound in the error was present when the order was increased. The origin of this anomaly was unknown, but a similar accuracy as for the finite differences was obtained by increasing the acceptance factor instead.

  - For the FMM to become more efficient than using purely direct interactions, a particle size of at least $\mathcal{O}(10^4)$ was required. Moreover, the expressions of the partial derivatives of the vector potential to obtain the velocity were expensive to compute. If also the stretching was taken into account, it was demonstrated that using finite differences resulted in a more efficient computation.

- Investigations with simple vortex ring geometries showed that the VPM is subject to an unstable behaviour over time, whereby local anomalies in the vortex structure would result in a global blow-up of the simulation. Blow-up has to be understood as a phenomenon whereby the particles start diverging and the strength vectors grow towards infinitely large values. Investigations with the knot-problem resulted in the following outcomes:

  - The application of a higher order time integration scheme improves the stability of the VPM significantly, but nor a smaller time step size or improved time integration can prevent the simulation from becoming unstable. The reason is that as time passes, the ongoing vortex stretching (especially through vortex roll-up and filament entanglement) results in unacceptably intense rotational scales with the manifestation of particle divergence. It is essential to apply smoothing of the singular field, and it is advisable to keep a constant core or underbound in the core size for stability.
  - The classic vortex stretching scheme is not inherently subject to particle divergence, under the conditions of a proper time integration and sufficient particle overlap. If the overlap is under-resolved, the vortices will start to roll-up locally, which the VPM cannot sustain over time. If the rotation becomes too intense locally, a sudden particle divergence will be manifested, blowing-up the simulation.
  - The transpose stretching scheme shows an automatic stabilizing effect when divergence or vortex roll-up appears. This allows for a coarser time integration and less particle overlap to be applied. A major drawback is that the stretching scheme is therefore inherently subject to divergence in regions of neighbouring filaments with different orientations. As a remedy, the application of divergence relaxation [24] has been successfully applied.
  - To be able to maintain stability, it is of vital importance to diminish vorticity from regions of intense vortex rotation. To this extent, a Particle Strength Exchange (PSE) scheme has been successfully applied for modelling viscous diffusion, increasing the simulation survival time significantly.

- The VPM has been applied for modelling the near-wake of an axi-symmetric actuator disk subject to a constant thrust over the rotor. It was of interest to investigate the wake expansion, wake velocity deficit, and the shear layer expansion as modelled by the VPM for thrust coefficients up to the Betz limit. Moreover, the simulation performance of highly loaded rotors is investigated.

  - Simulations have been run with a thrust coefficient ranging from $C_t = 4/9$ to the Betz limit of $C_t = 8/9$, with the replacement of the far-wake by an

  analytical description. Comparisons with momentum theory and a numerical potential model [33] indicated a correct modelling of axial velocity over the centerline of the wake.
  - A visualization of the wake showed the formation of the Kevin-Helmholtz instability, the subsequent break-down of the vortex sheet, the recovery through the clustering of particles, and the leapfrogging behaviour of the particle clusters. As a result, the shear layer started expanding and reached the centerline at about 5 diameters downstream. Due to the break-down of the vortex sheet, the wake expansion was less than momentum theory predicts.
  - The simulations using purely direct interactions and those using the FMM showed a very close mutual comparison. The results with the FMM whereby the far-field stretching was ignored showed a large reduction in axial flow deficit, due to a numerical loss of circulation during stretching of the vortex rings.
  - The influence of parameters describing the regularization of the vorticity field (core radius, number of particles, and particle overlap) showed to have a minor influence on the wake profile, as the effects of the Kelvin-Helmholtz instability and break-down of the vortex sheet were dominant phenomena in the expansion of the shear layer.
  - The VPM was able to simulate highly loaded rotors ($C_t = 9/9 - 16/9$), for which flow-reversal and periodic vortex shedding in upstream direction occurred. The results showed a departure from momentum theory, and a rough comparison with Glauert's correction for highly loaded rotors.

- The final investigation involved the simulation of the near-wake of a 3-bladed turbine, whereby the rotor was modelled using prescribed circulation from the MEXICO experiment [22] for a tip speed ratio of $\lambda = 6.67$. Opposed to the simulation with the actuator disk, the present wake was purely 3D and therefore subject to divergence and other instabilities.

  - Simulations with the classic stretching scheme did not show divergence in the tip or root vortices, but the formation of roll-up structures in the outer shear layer significantly reduced the expansion and flow deficit in the wake. As a remedy, a much smaller time step size was required.
  - With the transpose scheme a larger time step size could be afforded. The wake expansion and flow deficit were very well maintained over the wake, as the filaments in the outer shear layer did not show divergence and vortex roll-up. On the contrary, the root vortices showed a large divergence appearing. Application of relaxation effectively resolved this issue up to a few diameters downstream.
  - In any case, chaotic flow was present in the outer region of the wake, as the filament ends started rolling up and diverging. It resulted in a local region of non-physical flow reversal and stable simulations for more than 2 diameters downstream were not obtained. The application of PSE successfully diffused vorticity within these chaotic regions, thereby guaranteeing stability for an extended period of time. With PSE applied, stable simulations have been obtained up to 4 rotor diameters downstream.

  - A comparison with experimental results from the MEXICO rotor showed that accurate results have been obtained for the axial and radial velocity profiles in the near-wake.

7.2 Recommendations

Further investigation into the computational efficiency of the FMM:
It is recommended to investigate the computational efficiency of the FMM for a larger collection of particles and on the particle distribution in space. Regarding the partial derivatives of the vector potential, no study into the computational optimization has been carried out of the velocity derivation, and the derivation of the stretching term has not been resolved at all. To be able to obtain a fair comparison with the method of finite differences regarding computational efficiency, the current computations have to be checked, and the stretching derivation has to be obtained.

Obtaining a comparison between the computational efficiency of the Eulerian and Lagrangian VPM:
Often a Eulerian-Lagrangian form of the VPM is applied, as the regular mesh allows for the straightforward acquisition of partial derivatives, the remeshing of the distorted particle field, and the application of Poisson solvers (FFT). It is valuable to know what the computational effort is of the Lagrangian VPM combined with an FMM relative to a Eulerian-Lagrangian VPM combined with an FFT.

Preparing the VPM and FMM for parallel computations:
The currently developed VPM code is to a large extent written for a parallel implementation. However, the available FMM and certain routines within the PPM library proved to be buggy regarding the parallel functionalities, and it has not been succeeded in fully resolving these issues. It is therefore left as a future project to properly implement the parallel functionality of the VPM code.

Replacing the far-wake of the MEXICO rotor by an analytical model:
It was visible that a chaotic flow was formed at the outer region of the wake during the simulations of the MEXICO rotor. It is advised to investigate the stability of the near wake when the far-wake is replaced by an analytical description, like for the actuator disk. As such, the influence of the starting wake can be eliminated.

Computational gain by merging particles:
For the present thesis work, particle splitting is applied to guarantee overlap during stretching. On the other side, particle merging is not investigated, while stretching may result in regions with a large number of particles containing often a very limited amount of vorticity. It is expected that a large computational gain can be obtained by merging closely spaced particles or eliminating particles where most vorticity has been diffused away.

References

[1] E. Branlard and M. Gaunaa. Cylindrical vortex wake model: right cylinder. *Wind Energy*, 2014. ISSN 10991824, 10954244.

[2] M.L. Buhl. *A new empirical relationship between thrust coefficient and induction factor for the turbulent windmill state.* National Renewable Energy Laboratory Golden, CO, 2005.

[3] D. Castelein. *Dynamic Stall on Vertical Axis Wind Turbines.* PhD thesis, TU Delft, Delft University of Technology, 2015.

[4] P. Chatelain, A. Curioni, M. Bergdorf, D. Rossinelli, W. Andreoni, and P. Koumoutsakos. Billion vortex particle direct numerical simulations of aircraft wakes. *Computer Methods in Applied Mechanics and Engineering*, 197(13-16):1296–1304, 2008. ISSN 00457825, 18792138.

[5] P. Chatelain, S. Backaert, G. Winckelmans, and S. Kern. Large eddy simulation of wind turbine wakes. *Flow Turbulence and Combustion*, 91(3):587–605, 2013. ISSN 15731987, 13866184.

[6] M. Cheng, J. Lou, and T.T. Lim. Vortex ring with swirl: A numerical study. *Physics of Fluids (1994-present)*, 22(9):097101, 2010.

[7] Chorin. Numerical study of slightly viscous flow. *Journal of Fluid Mechanics*, 57: 785–796, 1973. ISSN 00221120, 14697645.

[8] G.H. Cottet and P.D. Koumoutsakos. *Vortex methods: theory and practice.* Cambridge university press, 2000.

[9] S. Degond, P.and Mas-Gallic. The weighted particle method for convection-diffusion equations. i. the case of an isotropic viscosity. *Mathematics of computation*, 53(188): 485–507, 1989.

[10] C.S. Ferreira, M. Barone, A. Zanon, R. Kemp, and P. Giannattasio. Airfoil optimization for stall regulated vertical axis wind turbines.

[11] C.S. Ferreira, H. Aagaard Madsen, M. Barone, B. Roscher, P. Deglaire, and I. Arduin. Comparison of aerodynamic models for vertical axis wind turbines. *Journal of Physics: Conference Series (online)*, 524(1), 2014. ISSN 17426588, 17426596.

[12] I.S. Gibson. On the velocity induced by a semi-infinite vortex cylinder: with extension to the short solenoid. *Aeronautical Journal*, 78(762):262–266, 1974. ISSN 00019240.

[13] H. Glauert. Elements of aerofoil and airscrew theory. *Elements of Aerofoil and Airscrew Theory*, (2), 1947.

[14] L. Greengard and V. Rokhlin. A fast algorithm for particle simulations. *Journal of Computational Physics*, 73(2):325–348, 1987. ISSN 00219991, 10902716.

[15] M.O.L. Hansen. *Aerodynamics of wind turbines.* Earthscan, 2009. ISBN 1844074382, 9781844074389.

[16] M.M. Hejlesen, P. Rasmussen, J.T.and Chatelain, and J.H. Walther. A high order solver for the unbounded poisson equation. *Proceedings of the 25th Nordic Seminar on Computational Mechanics*, 2012.

[17] P. Koumoutsakos. Fast multipole methods for three-dimensional n-body problems. 1995.

[18] A. Leonard. Vortex methods for flow simulation. *Journal of Computational Physics*, 37(3):289–335, 1980.

[19] Reginald I. Lewis. *Vortex element methods for fluid dynamic analysis of engineering systems*, volume 1. Cambridge University Press, 2005.

[20] L.E.M. Lignarolo, D. Ragni, C. Krishnaswami, Q. Chen, C.J. Simão Ferreira, G.J.W. van Bussel, and Q. Chen. Experimental analysis of the wake of a horizontal-axis wind-turbine model. *Renewable Energy, Renew. Energy*, 70:31–46, 2014. ISSN 09601481, 18790682.

[21] L. Manickathan. *Hybrid Eulerian-Lagrangian Vortex Particle Method: A fast and accurate numerical method for 2D Vertical-Axis Wind Turbine.* PhD thesis, TU Delft, Delft University of Technology, 2014.

[22] D. Micallef, G. van Bussel, C.S. Ferreira, and T. Sant. An investigation of radial velocities for a horizontal axis wind turbine in axial and yawed flows. *Wind Energy*, 16(4):529–544, 2013. ISSN 10991824, 10954244.

[23] K. Nilsson, W.Z. Shen, J.N. Sorensen, S.P. Breton, and S. Ivanell. Validation of the actuator line method using near wake measurements of the mexico rotor. *Wind Energy*, 18(3):499–514, 2015. ISSN 10954244, 10991824.

[24] G. Pedrizzetti. Insight into singular vortex flows. *FLUID DYNAMICS RESEARCH*, 10(2):101–115, 1992. ISSN 01695983, 18737005.

[25] J.T. Rasmussen. Particle methods in bluff body aerodynamics, 2011.

[26] L. Rosenhead. The formation of vortices from a surface of discontinuity. *Proceedings of the Royal Society of London. Series A, Containing Papers of a Mathematical and Physical Character*, pages 170–192, 1931.

[27] L.F. Rossi. Resurrecting core spreading vortex methods: A new scheme that is both deterministic and convergent. *SIAM Journal on Scientific Computing*, 17(2): 370–397, 1996.

[28] B. Sanderse. Aerodynamics of wind turbine wakes. *Energy Research Center of the Netherlands (ECN), ECN-E–09-016, Petten, The Netherlands, Tech. Rep*, 2009.

[29] I.F. Sbalzarini, J.H. Walther, M. Bergdorf, S.E. Hieber, E.M. Kotsalis, and P. Koumoutsakos. Ppm–a highly efficient parallel particle–mesh library for the simulation of continuum systems. *Journal of Computational Physics*, 215(2):566–588, 2006.

[30] I.F. Sbalzarini, J.H. Walther, B. Polasek, P. Chatelain, M. Bergdorf, S.E. Hieber, E.M. Kotsalis, and P. Koumoutsakos. A software framework for the portable parallelization of particle-mesh simulations. In *Euro-Par 2006 Parallel Processing*, pages 730–739. Springer, 2006.

[31] C.J. Simão Ferreira. *The near wake of the VAWT: 2D and 3D views of the VAWT aerodynamics*. PhD thesis, TU Delft, Delft University of Technology, 2009.

[32] I.S. Sullivan, J.J. Niemela, Robert E. Hershberger, D. Bolster, and R.J. Donnelly. Dynamics of thin vortex rings. *Journal of Fluid Mechanics*, 609:319–347, 2008. ISSN 00221120, 14697645.

[33] G.A.M. van Kuik and L. Lignarolo. Potential flow solutions for energy extracting actuator disc flows. *Wind Energy*, 2014.

[34] L.J. Vermeer, J.N. Sørensen, and A. Crespo. Wind turbine wake aerodynamics. *Progress in aerospace sciences*, 39(6):467–510, 2003.

[35] S.G. Voutsinas. Vortex methods in aeronautics: how to make things work. *International Journal of Computational Fluid Dynamics*, 20(1):3–18, 2006. ISSN 10290257, 10618562.

[36] G.S. Winckelmans. *Topics in vortex methods for the computation of three-and two-dimensional incompressible unsteady flows*. PhD thesis, California Institute of Technology, 1989.

[37] G.S. Winckelmans and A. Leonard. Contributions to vortex particle methods for the computation of three-dimensional incompressible unsteady flows. *Journal of Computational Physics*, 109(2):247–273, 1993.

[38] W. Yu, C.J. Simão Ferreira, G.A.M. van Kuik, and D. Baldacchino. Vortex ring model analysis of an actuator disc with dynamic and non-uniform load. *Wind Energy*, 2015.

[39] ETH Zürich. Parallel particle-mesh library. `http://www.ppm-library.org/`. Accessed: 05-May-2015.

Appendix A

Regularized Evolution Equations

In this appendix the regularized vorticity evolution equations are presented, along with tables of relevant regularization functions. Table A.1 holds for some well-known kernel types, the regularization functions for the vorticity, stream function, velocity, and the derivative of the velocity kernel as used for the stretching scheme.

Table A.1: *Overview of several relevant terms of common regularization functions*

Kernel type	$\zeta(\rho)$	$\chi(\rho)$	$g(\rho)$	$\frac{d}{d\rho}\left(\frac{g(\rho)}{\rho^3}\right)$
2^{nd} order Gaussian	$\frac{3}{4\pi}e^{-\rho^3}$		$\frac{1}{4\pi}\left(1-e^{-\rho^3}\right)$	$-\frac{3}{4\pi}\frac{1-e^{-\rho^3}\left(1+\rho^3\right)}{\rho^4}$
0^{th} low order algebraic (Rosenhead-Moore)	$\frac{3}{4\pi}\frac{1}{(\rho^2+1)^{\frac{5}{2}}}$	$\frac{1}{4\pi}\frac{1}{(\rho^2+1)^{\frac{1}{2}}}$	$\frac{1}{4\pi}\frac{\rho^3}{(\rho^2+1)^{\frac{3}{2}}}$	$-\frac{3}{4\pi}\frac{\rho}{(\rho^2+1)^{\frac{5}{2}}}$
2^{nd} high order algebraic (Winckelmans-Leonard)	$\frac{18}{5\pi}\frac{1}{(\rho^2+1)^{\frac{7}{2}}}$	$\frac{1}{4\pi}\frac{\left(\rho^2+\frac{3}{2}\right)}{(\rho^2+1)^{\frac{3}{2}}}$	$\frac{1}{4\pi}\frac{\rho^3\left(\rho^2+\frac{5}{2}\right)}{(\rho^2+1)^{\frac{5}{2}}}$	$-\frac{3}{4\pi}\frac{\rho\left(\rho^2+\frac{7}{2}\right)}{(\rho^2+1)^{\frac{7}{2}}}$

In equations A.1 through A.4, the vorticity evolution equations are shown. The scalar parts used in these equations as function of the velocity kernel and the derivative of the velocity kernel are presented in table A.2. Note that $\rho = \frac{\|\boldsymbol{r}_{qp}\|}{\sigma}$, with $\|\boldsymbol{r}_{qp}\| = \boldsymbol{x}^p - \boldsymbol{x}^q$, and f being a mixing factor between 0 and 1.

$$\frac{d\boldsymbol{x}^p}{dt} = \boldsymbol{u}^p = -\sum_q \frac{\sigma^3}{\rho^3} g(\rho)\left(\boldsymbol{r}_{qp} \times \boldsymbol{\alpha}^q\right) \tag{A.1}$$

$$\left.\frac{D\boldsymbol{\alpha}^p}{Dt}\right|_{\sigma}^{classic} = -\sum_q \left\{\frac{\sigma^3}{\rho^3} g(\rho)\left(\boldsymbol{\alpha}^p \times \boldsymbol{\alpha}^q\right) + \frac{1}{\sigma^5 \rho}\frac{d}{d\rho}\left(\frac{g(\rho)}{\rho^3}\right)\left(\boldsymbol{\alpha}^p \cdot \boldsymbol{r}_{qp}\right) \cdot \left(\boldsymbol{r}_{qp} \times \boldsymbol{\alpha}^q\right)\right\} \tag{A.2}$$

Table A.2: *Terms used in the calculation of the particle evolution equations, for a variety of smoothing kernels*

Kernel type	$\frac{\sigma^3}{\rho^3} g(\rho)$	$\frac{1}{\sigma^5 \rho} \frac{d}{d\rho} \left(\frac{g(\rho)}{\rho^3} \right)$
Laplacian (Singular)	$\frac{1}{4\pi} \frac{1}{\lVert \boldsymbol{r}_{qp} \rVert^3}$	$-\frac{3}{4\pi} \frac{1}{\lVert \boldsymbol{r}_{qp} \rVert^5}$
2nd order Gaussian	$\frac{1}{4\pi} \frac{1-e^{-\frac{\lVert \boldsymbol{r}_{qp} \rVert^3}{\sigma^3}}}{\lVert \boldsymbol{r}_{qp} \rVert^3}$	$-\frac{3}{4\pi} \frac{1-\left(1+\frac{\lVert \boldsymbol{r}_{qp} \rVert^3}{\sigma^3}\right) e^{-\frac{\lVert \boldsymbol{r}_{qp} \rVert^3}{\sigma^3}}}{\lVert \boldsymbol{r}_{qp} \rVert^5}$
0th low order algebraic (Rosenhead-Moore)	$\frac{1}{4\pi} \frac{1}{\left(\lVert \boldsymbol{r}_{qp} \rVert^2+\sigma^2\right)^{\frac{3}{2}}}$	$-\frac{3}{4\pi} \frac{1}{\left(\lVert \boldsymbol{r}_{qp} \rVert^2+\sigma^2\right)^{\frac{5}{2}}}$
2nd high order algebraic (Winckelmans-Leonard)	$\frac{1}{4\pi} \frac{\lVert \boldsymbol{r}_{qp} \rVert^2+\frac{5}{2}\sigma^2}{\left(\lVert \boldsymbol{r}_{qp} \rVert^2+\sigma^2\right)^{\frac{5}{2}}}$	$-\frac{3}{4\pi} \frac{\lVert \boldsymbol{r}_{qp} \rVert^2+\frac{7}{2}\sigma^2}{\left(\lVert \boldsymbol{r}_{qp} \rVert^2+\sigma^2\right)^{\frac{7}{2}}}$

$$\left.\frac{D\boldsymbol{\alpha}^p}{Dt}\right|_{\sigma}^{transpose} = \sum_q \left\{ \frac{\sigma^3}{\rho^3} g(\rho) \left(\boldsymbol{\alpha}^p \times \boldsymbol{\alpha}^q\right) + \frac{1}{\sigma^5 \rho} \frac{d}{d\rho} \left(\frac{g(\rho)}{\rho^3} \right) \left(\boldsymbol{\alpha}^p \cdot \left(\boldsymbol{r}_{qp} \times \boldsymbol{\alpha}^q\right)\right) \cdot \boldsymbol{r}_{qp} \right\} \tag{A.3}$$

$$\begin{aligned} \left.\frac{D\boldsymbol{\alpha}^p}{Dt}\right|_{\sigma}^{mixed} = \sum_q \Bigg\{ \frac{1}{\sigma^5 \rho} \frac{d}{d\rho} \left(\frac{g(\rho)}{\rho^3} \right) \Big[& (1-f) \left(\boldsymbol{\alpha}^p \cdot \left(\boldsymbol{r}_{qp} \times \boldsymbol{\alpha}^q\right)\right) \cdot \boldsymbol{r}_{qp} \\ & -f \left(\boldsymbol{\alpha}^p \cdot \boldsymbol{r}_{qp}\right) \cdot \left(\boldsymbol{r}_{qp} \times \boldsymbol{\alpha}^q\right) \Big] \Bigg\} \end{aligned} \tag{A.4}$$

That the classical and the transpose scheme hold identical information, i.e. that $[\nabla \boldsymbol{u}][\boldsymbol{\omega}] = [\nabla \boldsymbol{u}]^{\boldsymbol{T}}[\boldsymbol{\omega}]$, is shown in the derivation in equation A.5, with the additional remark that $\boldsymbol{\omega} = \nabla \times \boldsymbol{u}$, but $\tilde{\boldsymbol{\omega}} \neq \nabla \times \tilde{\boldsymbol{u}}$, explaining why these schemes are not identical for a discretized field.

$$\begin{aligned} [\nabla \boldsymbol{u}] [\boldsymbol{\omega}] - [\nabla \boldsymbol{u}]^T [\boldsymbol{\omega}] &= \begin{bmatrix} \frac{\partial u_x}{\partial x} & \frac{\partial u_y}{\partial x} & \frac{\partial u_z}{\partial x} \\ \frac{\partial u_x}{\partial y} & \frac{\partial u_y}{\partial y} & \frac{\partial u_z}{\partial y} \\ \frac{\partial u_x}{\partial z} & \frac{\partial u_y}{\partial z} & \frac{\partial u_z}{\partial z} \end{bmatrix} \begin{Bmatrix} \omega_x \\ \omega_y \\ \omega_z \end{Bmatrix} - \begin{bmatrix} \frac{\partial u_x}{\partial x} & \frac{\partial u_x}{\partial y} & \frac{\partial u_x}{\partial z} \\ \frac{\partial u_y}{\partial x} & \frac{\partial u_y}{\partial y} & \frac{\partial u_y}{\partial z} \\ \frac{\partial u_z}{\partial x} & \frac{\partial u_z}{\partial y} & \frac{\partial u_z}{\partial z} \end{bmatrix} \begin{Bmatrix} \omega_x \\ \omega_y \\ \omega_z \end{Bmatrix} \\ &= \begin{Bmatrix} \frac{\partial u_y}{\partial x}\omega_y + \frac{\partial u_z}{\partial x}\omega_z - \frac{\partial u_x}{\partial y}\omega_y - \frac{\partial u_x}{\partial z}\omega_z \\ \frac{\partial u_x}{\partial y}\omega_x + \frac{\partial u_z}{\partial y}\omega_z - \frac{\partial u_y}{\partial x}\omega_x - \frac{\partial u_y}{\partial z}\omega_z \\ \frac{\partial u_x}{\partial z}\omega_x + \frac{\partial u_y}{\partial z}\omega_y - \frac{\partial u_z}{\partial x}\omega_x - \frac{\partial u_z}{\partial y}\omega_y \end{Bmatrix} = \begin{Bmatrix} \omega_y(\frac{\partial u_y}{\partial x} - \frac{\partial u_x}{\partial y}) - \omega_z(\frac{\partial u_x}{\partial z} - \frac{\partial u_z}{\partial x}) \\ \omega_z(\frac{\partial u_z}{\partial y} - \frac{\partial u_y}{\partial z}) - \omega_x(\frac{\partial u_y}{\partial x} - \frac{\partial u_x}{\partial y}) \\ \omega_x(\frac{\partial u_x}{\partial z} - \frac{\partial u_z}{\partial x}) - \omega_y(\frac{\partial u_z}{\partial y} - \frac{\partial u_y}{\partial z}) \end{Bmatrix} \\ &= \boldsymbol{\omega} \times \begin{Bmatrix} \frac{\partial u_z}{\partial y} - \frac{\partial u_y}{\partial z} \\ \frac{\partial u_x}{\partial z} - \frac{\partial u_z}{\partial x} \\ \frac{\partial u_y}{\partial x} - \frac{\partial u_x}{\partial y} \end{Bmatrix} = \boldsymbol{\omega} \times (\nabla \times \boldsymbol{u}) = \boldsymbol{\omega} \times \boldsymbol{\omega} = 0 \end{aligned} \tag{A.5}$$

Appendix B

Profound Derivation of the Velocity

The currently implemented FMM returns the potential due to a source strength, although of interest are the derivatives of this potential, namely the velocity and the vector stretching terms. This appendix is dedicated to the derivation of the velocity only, which is related to the potential as $\boldsymbol{u} = \nabla \times \boldsymbol{\Psi}$, which is given in spherical coordinates as in equation B.1.

$$\begin{aligned} \boldsymbol{u} = \nabla \times \boldsymbol{\Psi} = \hat{\boldsymbol{\rho}} \frac{1}{\rho \sin\theta} & \left[\frac{\partial \sin\theta \Psi_\phi}{\partial \theta} - \frac{\partial \Psi_\theta}{\partial \phi} \right] \\ + \hat{\boldsymbol{\theta}} & \left[\frac{1}{\rho \sin\theta} \frac{\partial \Psi_\rho}{\partial \phi} - \frac{1}{\rho} \frac{\partial \rho \Psi_\phi}{\partial \rho} \right] \\ + \hat{\boldsymbol{\phi}} \frac{1}{\rho} & \left[\frac{\partial d\rho \Psi_\theta}{\partial \phi} - \frac{\partial \Psi_\rho}{\partial \theta} \right] \end{aligned} \tag{B.1}$$

This formulation of the curl requires the calculation of the partial derivatives of the potential. All the necessary differentiation-terms are written out in equations B.3 through B.8, where $\boldsymbol{D}_n^m$ is transformed into spherical coordinates with the rotation-matrix R (equation B.2). The differentiation-terms of O_n^m have been derived earlier on and can be found in section 4.3. Note that the summation symbols of all the order terms have been left out for brevity, but in reality all the individual order-terms have to be summed up in between, before multiplication with other terms.

$$R = \begin{bmatrix} \sin\theta\cos\phi & \sin\theta\sin\phi & \cos\theta \\ \cos\theta\cos\phi & \cos\theta\sin\phi & -\sin\theta \\ -\sin\phi & \cos\phi & 0 \end{bmatrix} \tag{B.2}$$

$$\begin{aligned} \frac{\partial \left(\Psi_\phi \sin\theta \right)}{\partial \theta} = & \left(\frac{\partial O_n^m}{\partial \theta} \begin{bmatrix} -\sin\theta\sin\phi & \sin\theta\cos\phi & 0 \end{bmatrix} \boldsymbol{D}_n^m \right. \\ & \left. + O_n^m \begin{bmatrix} -\cos\theta\sin\phi & \cos\theta\cos\phi & 0 \end{bmatrix} \boldsymbol{D}_n^m \right) \end{aligned} \tag{B.3}$$

$$\begin{aligned}\frac{\partial \Psi_\theta}{\partial \phi} = & \frac{\partial O_n^m}{\partial \phi} \begin{bmatrix} \cos\theta\cos\phi & \cos\theta\sin\phi & -\sin\theta \end{bmatrix} \boldsymbol{D}_n^m \\ & + O_n^m \begin{bmatrix} -\cos\theta\sin\phi & \cos\theta\cos\phi & 0 \end{bmatrix} \boldsymbol{D}_n^m\end{aligned} \tag{B.4}$$

$$\begin{aligned}\frac{\partial \Psi_\rho}{\partial \phi} = & \frac{\partial O_n^m}{\partial \phi} \begin{bmatrix} \sin\theta\cos\phi & \sin\theta\sin\phi & \cos\theta \end{bmatrix} \boldsymbol{D}_n^m \\ & + O_n^m \begin{bmatrix} -\sin\theta\sin\phi & \sin\theta\cos\phi & 0 \end{bmatrix} \boldsymbol{D}_n^m\end{aligned} \tag{B.5}$$

$$\frac{\partial \left(\Psi_\phi \rho\right)}{\partial \rho} = \left(\rho \frac{\partial O_n^m}{\partial \rho} + O_n^m\right) \begin{bmatrix} -\sin\phi & \cos\phi & 0 \end{bmatrix} \boldsymbol{D}_n^m \tag{B.6}$$

$$\frac{\partial (\Psi_\theta \rho)}{\partial \rho} = \left(\rho \frac{\partial O_n^m}{\partial \rho} + O_n^m\right) \begin{bmatrix} \cos\theta\cos\phi & \cos\theta\sin\phi & -\sin\theta \end{bmatrix} \boldsymbol{D}_n^m \tag{B.7}$$

$$\begin{aligned}\frac{\partial \Psi_\rho}{\partial \theta} = & \frac{\partial O_n^m}{\partial \theta} \begin{bmatrix} \sin\theta\cos\phi & \sin\theta\sin\phi & \cos\theta \end{bmatrix} \boldsymbol{D}_n^m \\ & + O_n^m \begin{bmatrix} \cos\theta\cos\phi & \cos\theta\sin\phi & -\sin\theta \end{bmatrix} \boldsymbol{D}_n^m\end{aligned} \tag{B.8}$$

In equations B.9 through B.11, all the just-mentioned derivative terms are combined to form the 3 components of the velocity in spherical coordinates. It follows that all the O_n^m-terms cancel out.

$$\begin{aligned}u_\rho = & \frac{1}{\rho\sin\theta} \bigg(\frac{\partial O_n^m}{\partial \theta} \begin{bmatrix} -\sin\theta\sin\phi & \sin\theta\cos\phi & 0 \end{bmatrix} \boldsymbol{D}_n^m \\ & - \frac{\partial O_n^m}{\partial \phi} \begin{bmatrix} \cos\theta\cos\phi & \cos\theta\sin\phi & -\sin\theta \end{bmatrix} \boldsymbol{D}_n^m \bigg)\end{aligned} \tag{B.9}$$

$$\begin{aligned}u_\theta = & \frac{1}{\rho\sin\theta} \frac{\partial O_n^m}{\partial \phi} \begin{bmatrix} \sin\theta\cos\phi & \sin\theta\sin\phi & \cos\theta \end{bmatrix} \boldsymbol{D}_n^m \\ & - \frac{\partial O_n^m}{\partial \rho} \begin{bmatrix} -\sin\phi & \cos\phi & 0 \end{bmatrix} \boldsymbol{D}_n^m\end{aligned} \tag{B.10}$$

$$\begin{aligned}u_\phi = & \frac{\partial O_n^m}{\partial \rho} \begin{bmatrix} \cos\theta\cos\phi & \cos\theta\sin\phi & -\sin\theta \end{bmatrix} \boldsymbol{D}_n^m \\ & - \frac{1}{\rho} \frac{\partial O_n^m}{\partial \theta} \begin{bmatrix} \sin\theta\cos\phi & \sin\theta\sin\phi & \cos\theta \end{bmatrix} \boldsymbol{D}_n^m\end{aligned} \tag{B.11}$$

Multiplication with the rotation-matrix from spherical to Cartesian coordinates R^-1 (which is the Transpose of R), results in equation B.12. A further rearrangement leads to the final result in equation B.15.

$$\begin{aligned}\mathbf{u}(x,y,z) = R^{-1}\mathbf{u}(\rho,\theta,\phi) = \frac{\partial O_n^m}{\partial \rho}&\left\{\begin{array}{c} -\cos\theta D_y + \sin\theta\sin\phi D_z \\ \cos\theta D_x - \sin\theta\cos\phi D_z \\ -\sin\theta\sin\phi D_x + \sin\theta\cos\phi D_y \end{array}\right\} \\ +\frac{1}{\rho}\frac{\partial O_n^m}{\partial\theta}&\left\{\begin{array}{c} \sin\theta D_y + \cos\theta\sin\phi D_z \\ -\sin\theta D_x - \cos\theta\cos\phi D_z \\ -\cos\theta\sin\phi D_x + \cos\theta\cos\phi D_y \end{array}\right\} \\ +\frac{1}{\rho\sin\theta}\frac{\partial O_n^m}{\partial\phi}&\left\{\begin{array}{c} \cos\phi D_z \\ \sin\phi D_z \\ -\cos\phi D_x - \sin\phi D_y \end{array}\right\}\end{aligned} \tag{B.12}$$

$$\begin{aligned}\mathbf{u}(x,y,z) = R^{-1}\mathbf{u}(\rho,\theta,\phi) = \frac{\partial O_n^m}{\partial \rho}&\left\{\begin{array}{c} -\cos\theta D_y + \sin\theta\sin\phi D_z \\ \cos\theta D_x - \sin\theta\cos\phi D_z \\ -\sin\theta\sin\phi D_x + \sin\theta\cos\phi D_y \end{array}\right\} \\ +\frac{1}{\rho}\frac{\partial O_n^m}{\partial\theta}&\left\{\begin{array}{c} \sin\theta D_y + \cos\theta\sin\phi D_z \\ -\sin\theta D_x - \cos\theta\cos\phi D_z \\ -\cos\theta\sin\phi D_x + \cos\theta\cos\phi D_y \end{array}\right\} \\ +\frac{1}{\rho\sin\theta}\frac{\partial O_n^m}{\partial\phi}&\left\{\begin{array}{c} \cos\phi D_z \\ \sin\phi D_z \\ -\cos\phi D_x - \sin\phi D_y \end{array}\right\}\end{aligned} \tag{B.13}$$

$$\begin{aligned}\mathbf{u}(x,y,z) = &\left(\left[\begin{array}{ccc} \sin\theta\cos\phi & \cos\theta\cos\phi & -\sin\phi \\ \sin\theta\sin\phi & \cos\theta\sin\phi & \cos\phi \\ \cos\theta & -\sin\theta & 0 \end{array}\right]\left\{\begin{array}{c} \frac{\partial O_n^m}{\partial\rho} \\ \frac{1}{\rho}\frac{\partial O_n^m}{\partial\theta} \\ \frac{1}{\rho\sin\theta}\frac{\partial O_n^m}{\partial\phi} \end{array}\right\}\right) \\ &\times\left\{\begin{array}{c} D_n^m(\theta_x) \\ D_n^m(\theta_y) \\ D_n^m(\theta_z) \end{array}\right\}\end{aligned} \tag{B.14}$$

$$\mathbf{u}(x,y,z) = \left(R^{-1}\nabla O_n^m\right) \times \mathbf{D}_n^m \tag{B.15}$$

Appendix C

The Analytical Expressions for a System of Coaxial Vortex Rings

In this appendix the expressions for the axial and radial velocity for a system of coaxial vortex rings (vortex rings that share a symmetry axis) are presented (Cheng et al. [6]). The expressions are valid for any amount of vortex rings, but are used in this thesis for the verification of the double ring or leapfrogging problem (see section 6.2).

The radial velocity $\dot{R}$ and axial velocity $\dot{Z}$ of a circular thin core ($\sigma \ll R$) vortex ring are given in equations C.1 and C.2. R and Z represent the radial and axial position of the ring circumference relative to the symmetry-axis. σ and Γ are the core size and circulation respectively. The subindex i indicates the ring of interest, and the subindex j points to the other vortex rings in the system, with N being the total amount of vortex rings.

$$\dot{Z}_i = \frac{\Gamma_i}{4\pi R_i}\left[\ln\left(\frac{8R_i}{\sigma_i}\right) - \beta\right] + \sum_{j=1}^{N} \frac{\Gamma_j}{2\pi R_i}\frac{\partial I_{ij}}{\partial R_i} \tag{C.1}$$

$$\dot{R}_i = -\sum_{j=1}^{N} \frac{\Gamma_j}{2\pi R_i}\frac{\partial I_{ij}}{\partial Z_i} \tag{C.2}$$

I_{ij} is given in equation C.3, and is itself a function of the elliptic parameter k_{ij} (equation C.4) and the complete elliptic integrals of the first and second kind, being K and E respectively (equations C.5 and C.6).

$$I_{ij} = \sqrt{R_i R_j \left[\left(\frac{2}{k_{ij}} - k_{ij}\right) K(k_{ij}^2) - \frac{2}{k_{ij}} E(k_{ij}^2)\right]} \tag{C.3}$$

$$k_{ij}^2 = \frac{4R_iR_j}{(R_i + R_j)^2 + (Z_i + Z_j)^2} \tag{C.4}$$

$$K(k_{ij}^2) = \frac{\pi}{2}\sum_{n=0}^{\infty}\left[\frac{(2n)!}{2^{2n}(n!)^2}\right]^2 \left(k_{ij}^2\right)^n \tag{C.5}$$

$$E(k_{ij}^2) = \frac{\pi}{2}\sum_{n=0}^{\infty}\left[\frac{(2n)!}{2^{2n}(n!)^2}\right]^2 \frac{\left(k_{ij}^2\right)^n}{1-2n} \tag{C.6}$$

For the leapfrogging problem in section 6.2, the derivatives of I_{ij} with respect to the radius R_i and the axial distance Z_i ($\frac{\partial I_{ij}}{\partial R_i}$ and $\frac{\partial I_{ij}}{\partial Z_i}$) are obtained through a 3-point central differences scheme.

Appendix D

The Analytical Expressions for the Semi-Infinite Circular Vortex Tube

This appendix contains the expressions for the analytical straight semi-infinite circular vortex tube as applied for the actuator disk test-case (see 6.4). Assuming that the wake has fully expanded in the far-wake, the strength per unit length γ and tube diameter R_{tube} can be calculated through Froude's momentum theory, see equations D.1 and D.2.

$$\gamma = \frac{\Gamma}{\Delta s} = \frac{\frac{1}{2} C_t U_\infty^2 \Delta t}{U_\infty (1-2a)} = \frac{C_t U_\infty}{2-4a} \tag{D.1}$$

$$R_{\text{tube}} = R_{\text{disk}} \sqrt{\frac{1-a}{1-2a}} \tag{D.2}$$

With the axial induction factor a at the disk given as in equation D.3.

$$a = \frac{1-\sqrt{1-C_t}}{2} \tag{D.3}$$

The velocity field that the analytical tube induces in radial and axial direction, are given in equations D.4 and D.5 (Branlard and Gaunaa [1]).

$$u_r = -\frac{\gamma}{2\pi}\sqrt{\frac{R}{r}} \left[\frac{2-k^2}{k} K(k^2) - \frac{2}{k} E(k^2) \right] \tag{D.4}$$

$$u_z = \frac{\gamma}{2} \left[\frac{R-r+|R-r|}{2\,|R-r|} + \frac{zk}{2\pi\sqrt{rR}} \left(K(k^2) + \frac{R-r}{R+r} \Pi({k_0}^2, k^2) \right) \right] \tag{D.5}$$

With k being the elliptic eccentricity, and K, E, and Π being the complete elliptical integrals of the first, second, and third kind respectively. K and E appear in the expressions for a coaxial system of vortex rings, and have been presented in appendix C in equations C.5 and C.6. The values for k, k_0 and Π are shown in equations D.6 through D.8.

$$k^2 = \frac{4rR}{(r+R)^2 + z^2} \tag{D.6}$$

$${k_0}^2 = \frac{4rR}{(r+R)^2} \tag{D.7}$$

$$\Pi({k_0}^2, k^2) = \int\limits_0^{\pi/2} \frac{d\theta}{\left(1 + {k_0}^2 \sin^2\theta\right)\sqrt{1 - k^2 \sin^2\theta}} \tag{D.8}$$

Appendix E

Results over Time for the Knot Problem

In this appendix a demonstration is given regarding the time evolution of the knot-problem (see section 6.3). The specifications of this problem are presented in table E.1. The simulation is run with a real high-order algebraic core, PSE, particle splitting, and RK2 time integration applied.

Table E.1: *Overview of parameters as applied for the knot problem in figure E.1*

Parameter	Value	Unit	Description
$\Gamma_{1,2}$	1	$[m^2s^{-1}]$	Initial circulation
$R_{1,2}$	1	$[m]$	Initial radius
$\sigma_{1,2}$	0.1	$[m]$	Initial core size
$NP_{1,2}$	250	-	Initial number of particles
$\lambda_{1,2}$	4.0	-	Initial particle overlap
$\lambda_{1,2}$	3.0	-	Minimum particle overlap
D	1	[m]	Initial distance from ring center to center
Δt	0.002	[s]	Time step size
ν	0.001	$[m^2s^{-1}]$	Kinematic viscosity

The results from 0 to 5.5 seconds are given in figure E.1. Visible is the deformation of both rings under influence of the self-induced velocity and vortex stretching. After 4 seconds, both rings have deformed enough to meet each other. Due to the resulting alignment of filaments, a rapid increase in the rate of stretching (and thus addition of particles) is visible. In a viscous flow, both rings would decouple and reconnect to form one large ring. This is occurring in the present results at 5.5 seconds. The remaining section of aligned filaments possess opposite circulation and will diffuse each other away.

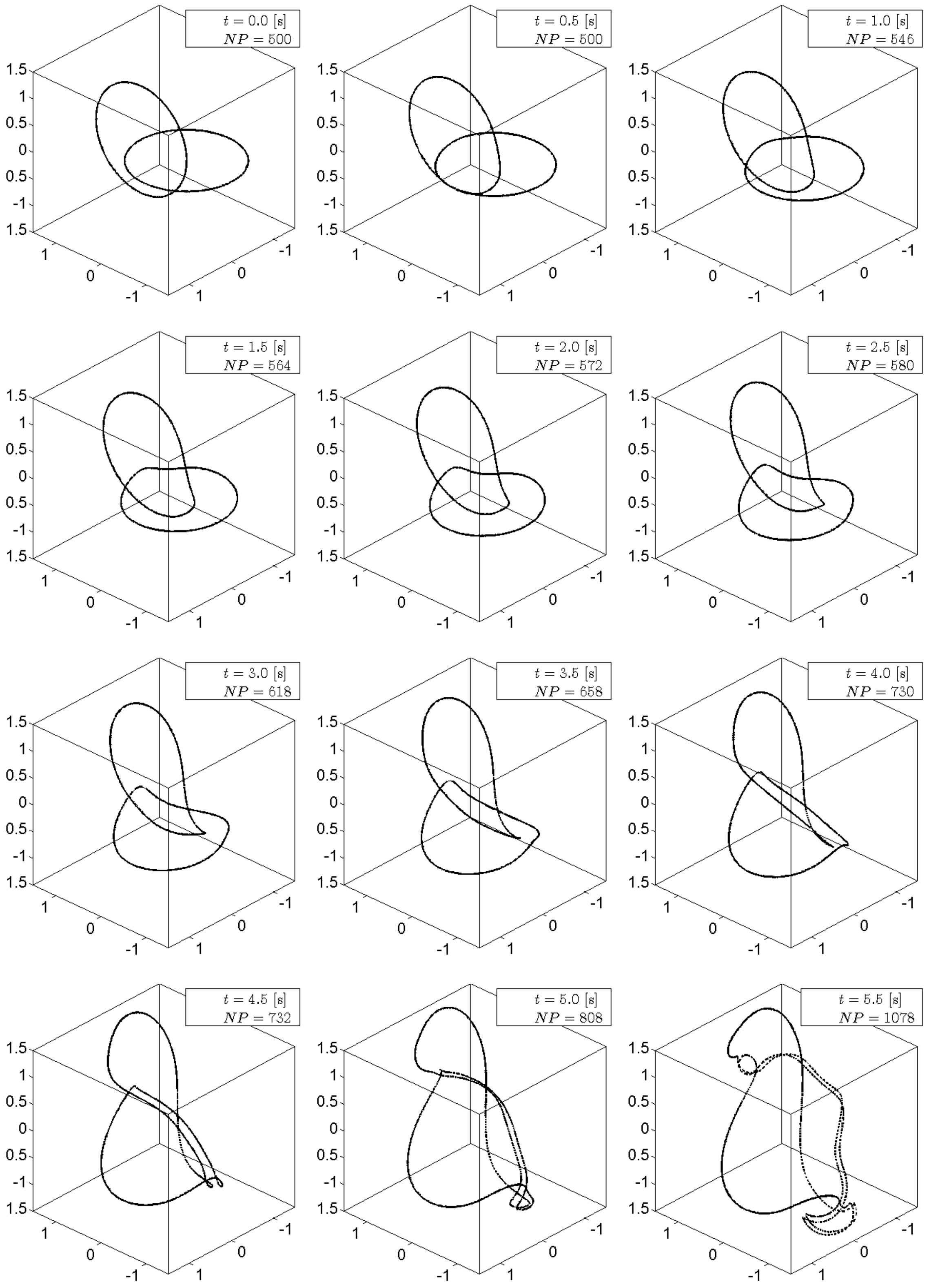

Figure E.1: *Demonstration of the time evolution of the knot-problem.*

Appendix F

Actuator Disk Results over Time for the Betz Limit and Highly Loaded Rotors

In this appendix, a demonstration is given of the near-wake development of the actuator disk (see section 6.4) from initiation up to 25 seconds. In no event is the far-wake replaced by an analytical model. The results for the following cases are presented:

- Section F.1: $C_t = 8/9$ (Betz limit)
- Section F.2: $C_t = 9/9$ (flow standstill in the far-wake)
- Section F.3: $C_t = 12/9$ (periodic flow reversal)
- Section F.4: $C_t = 16/9$ (periodic flow reversal)

F.1 Results for $C_t = 8/9$ (Betz limit)

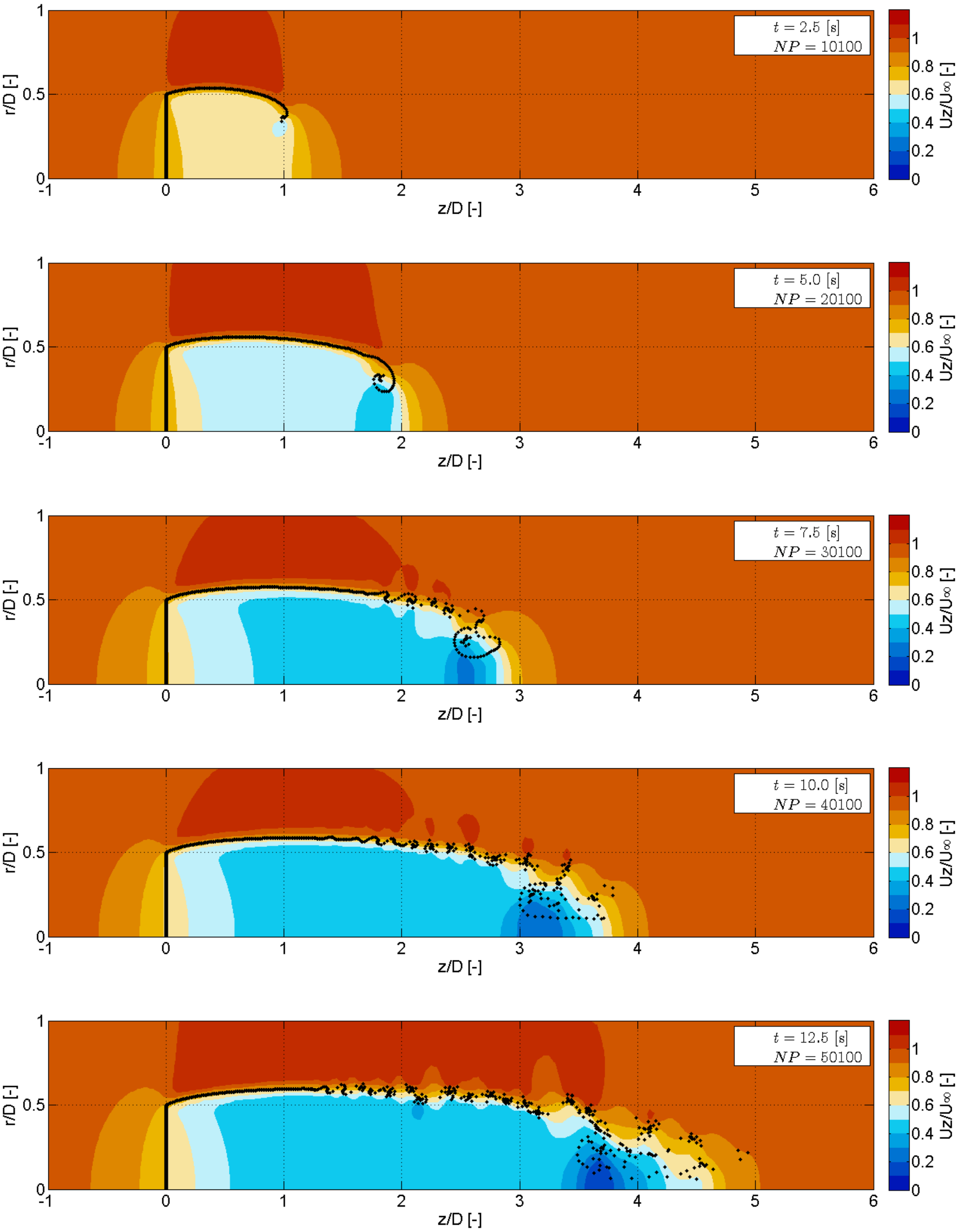

Figure F.1: *Axial velocity. $C_t = 8/9$. NP stands for Number of Particles, of which 1 particle is shown per shed vortex ring (50 particles per ring).*

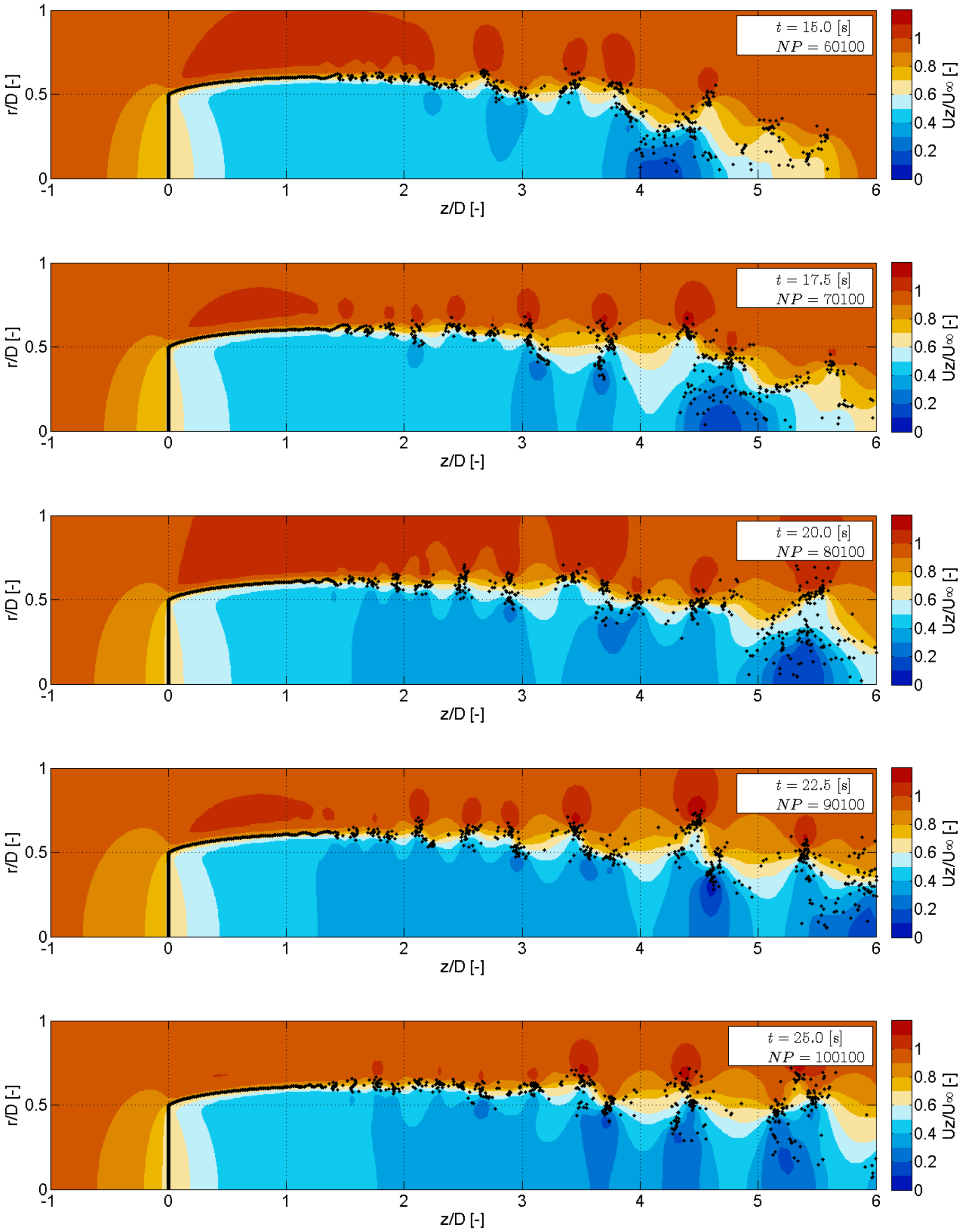

Figure F.2: *Continuation of figure F.1. Axial velocity.* $C_t = 8/9$. *NP stands for Number of Particles, of which 1 particle is shown per shed vortex ring (50 particles per ring).*

F.2 Results for $C_t = 9/9$

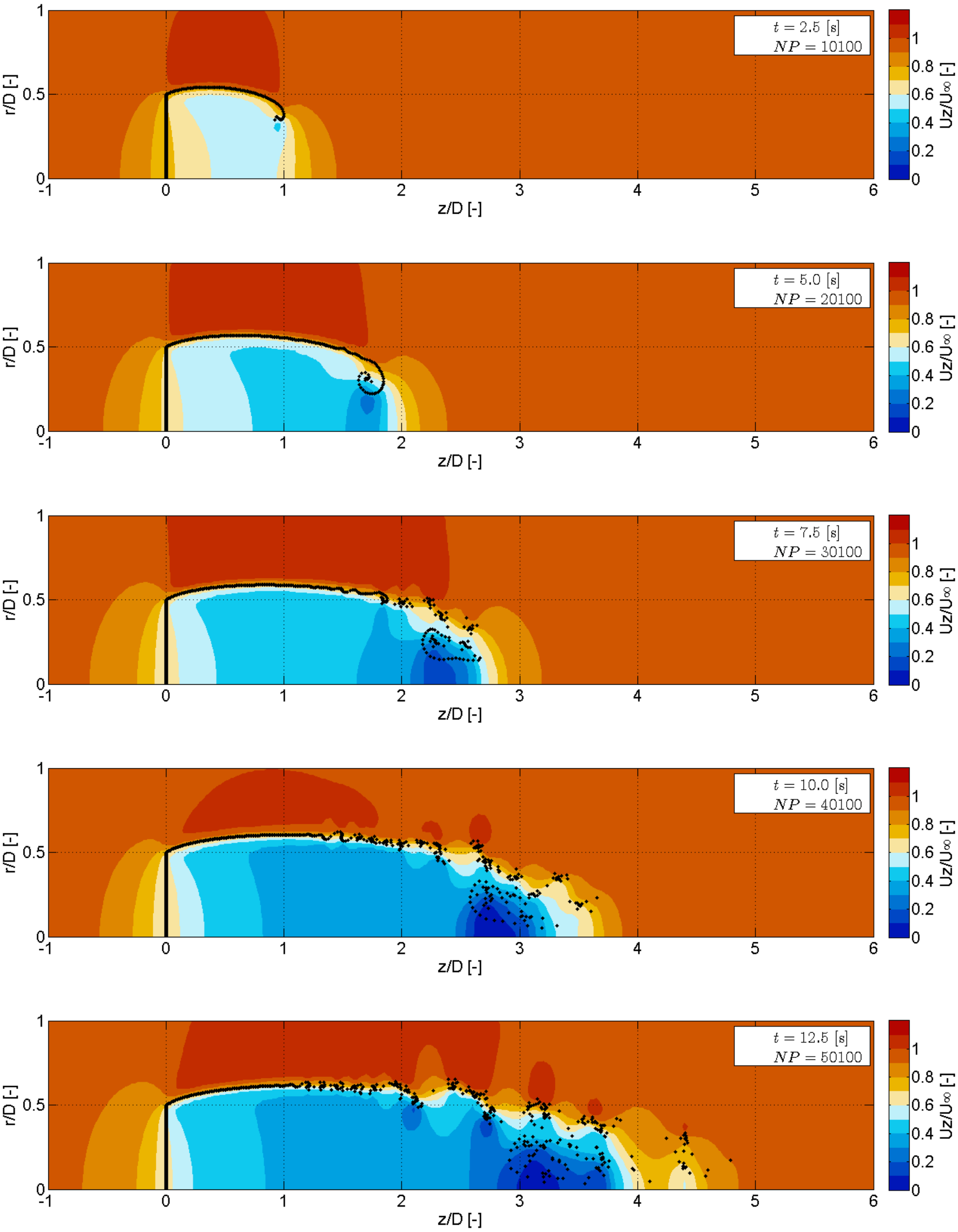

Figure F.3: *Axial velocity.* $C_t = 9/9$. *NP stands for Number of Particles, of which 1 particle is shown per shed vortex ring (50 particles per ring).*

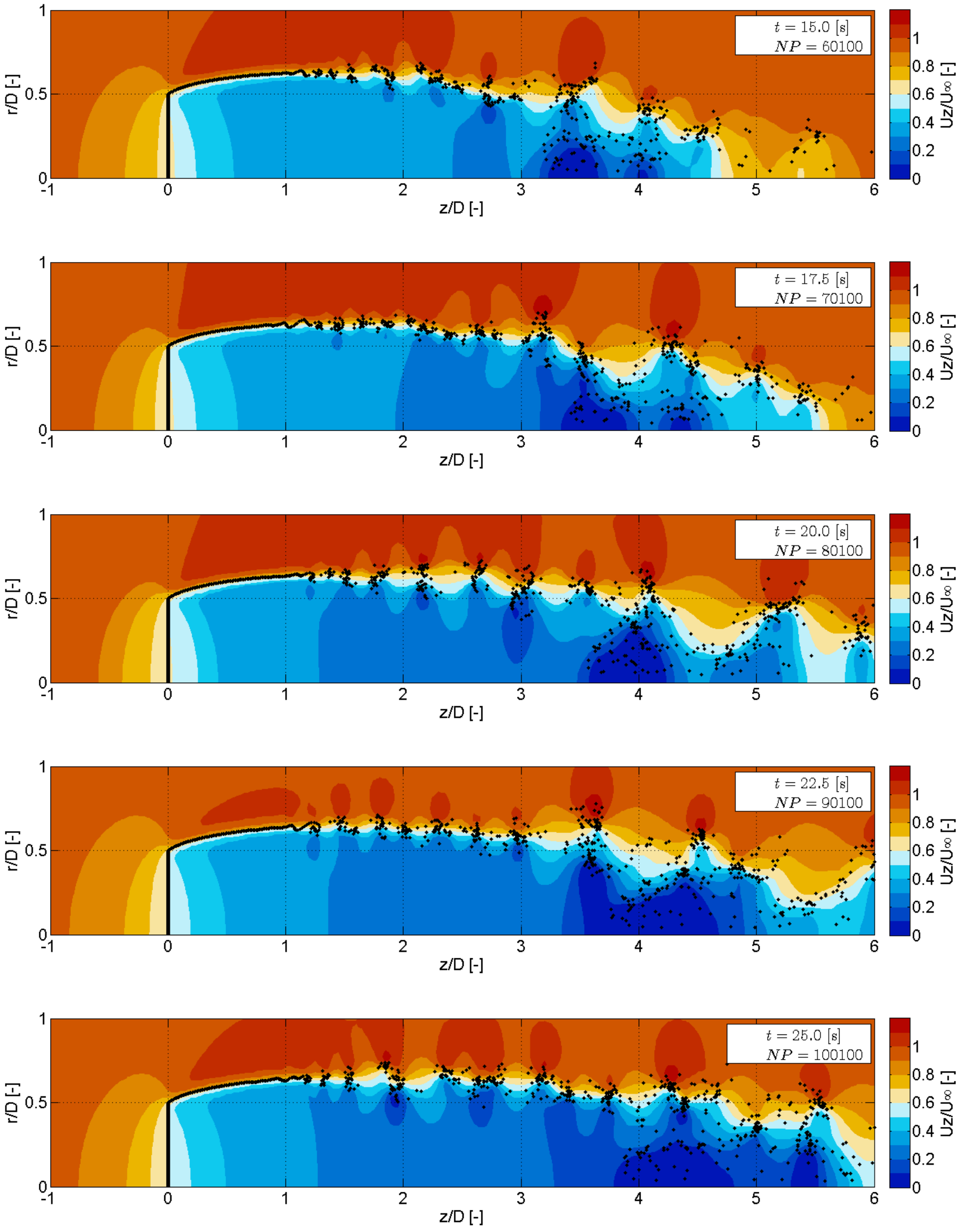

Figure F.4: *Continuation of figure F.3. Axial velocity.* $C_t = 9/9$. NP *stands for Number of Particles, of which 1 particle is shown per shed vortex ring (50 particles per ring).*

F.3 Results for $C_t = 12/9$

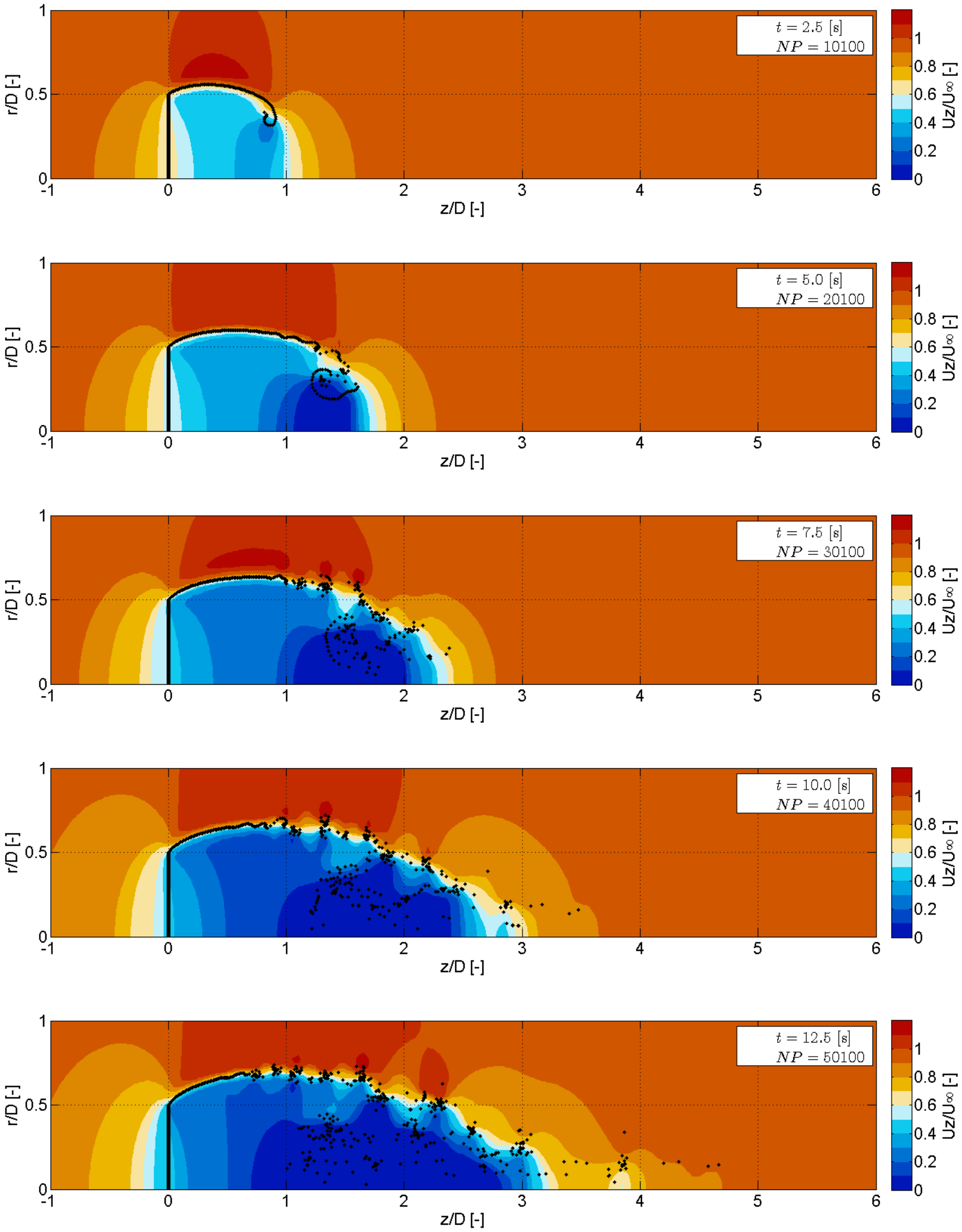

Figure F.5: *Axial velocity.* $C_t = 12/9$. *NP stands for Number of Particles, of which 1 particle is shown per shed vortex ring (50 particles per ring).*

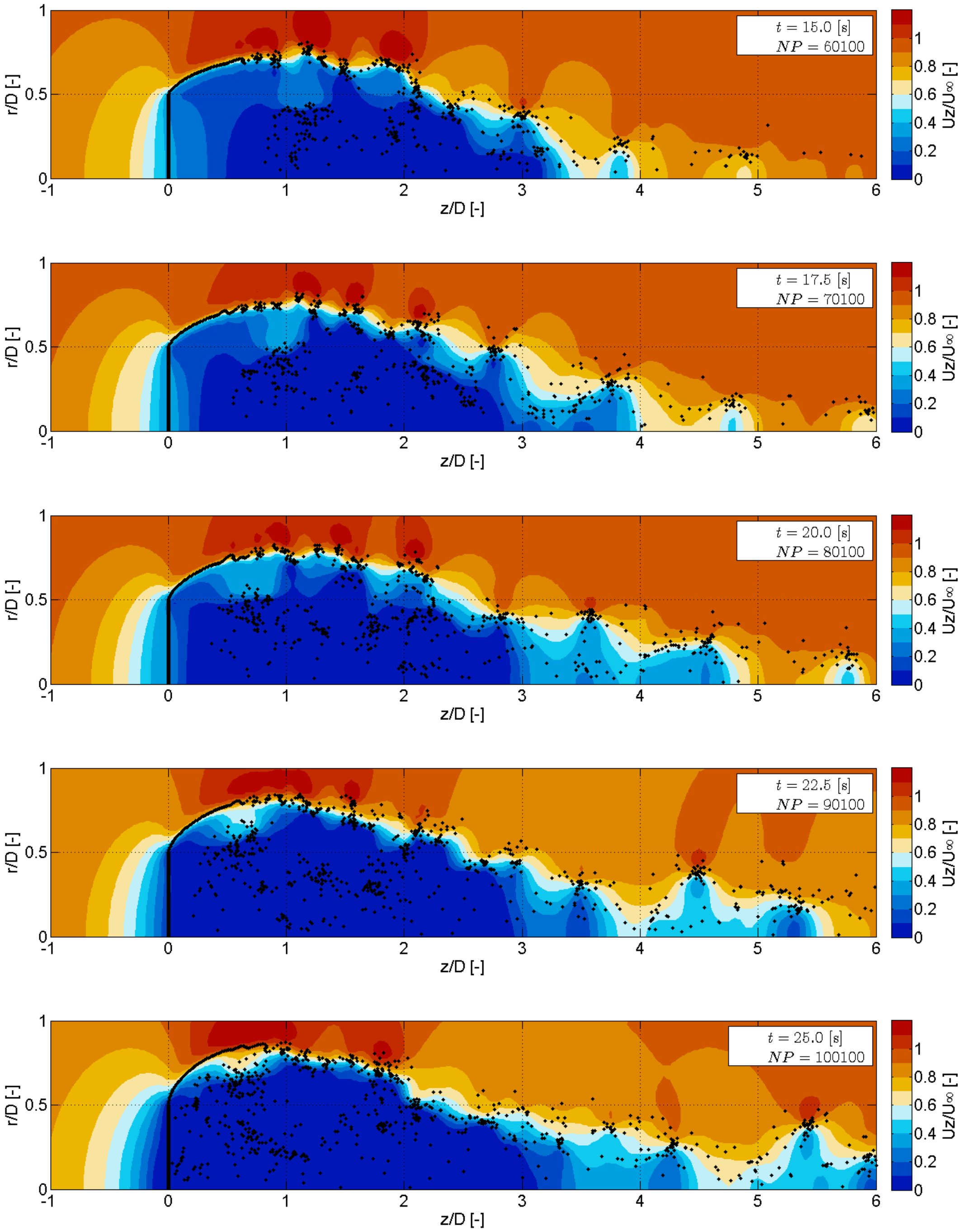

Figure F.6: *Continuation of figure F.5. Axial velocity. $C_t = 12/9$. NP stands for Number of Particles, of which 1 particle is shown per shed vortex ring (50 particles per ring).*

F.4 Results for $C_t = 16/9$

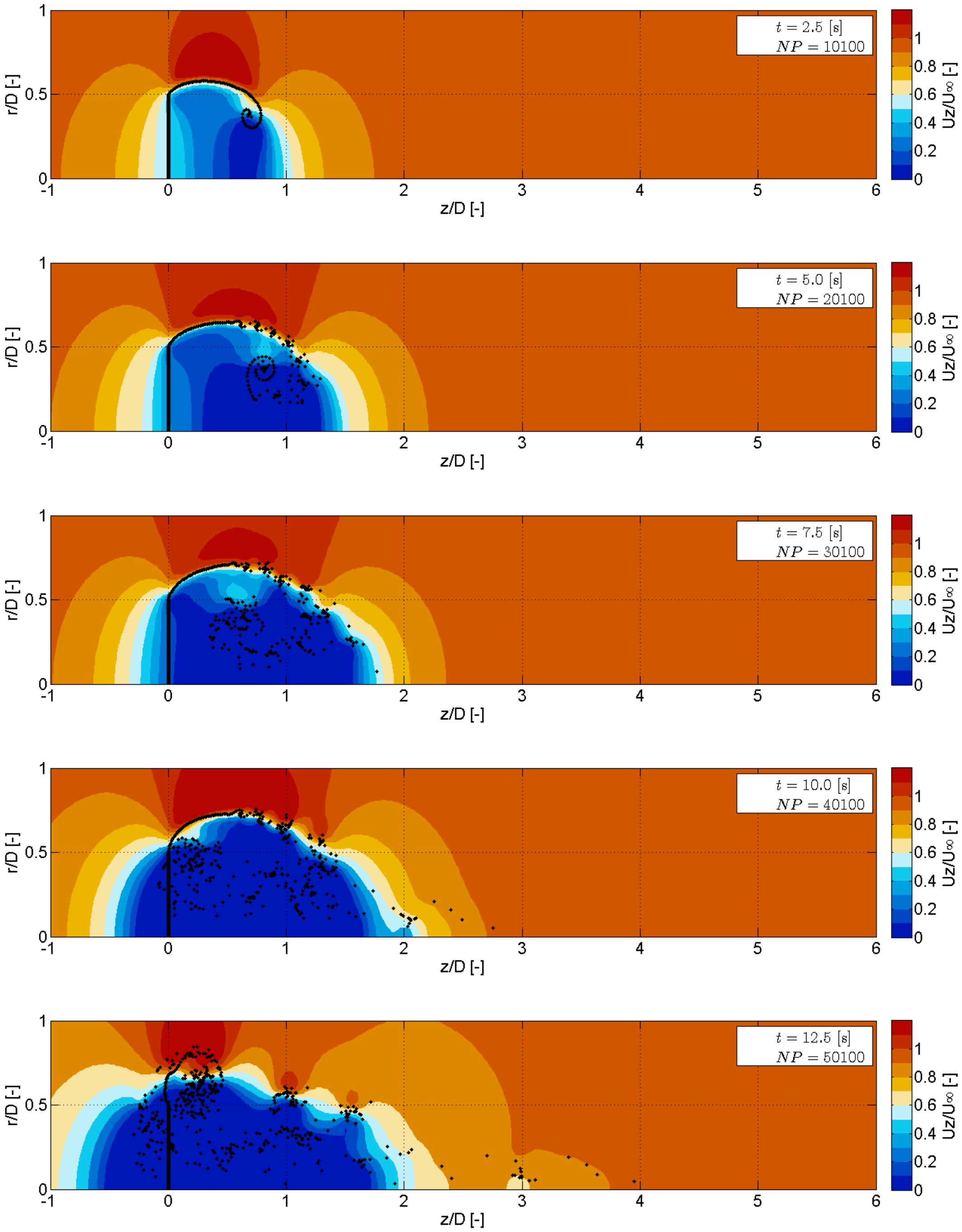

Figure F.7: Axial velocity. $C_t = 16/9$. *NP stands for Number of Particles, of which 1 particle is shown per shed vortex ring (50 particles per ring).*

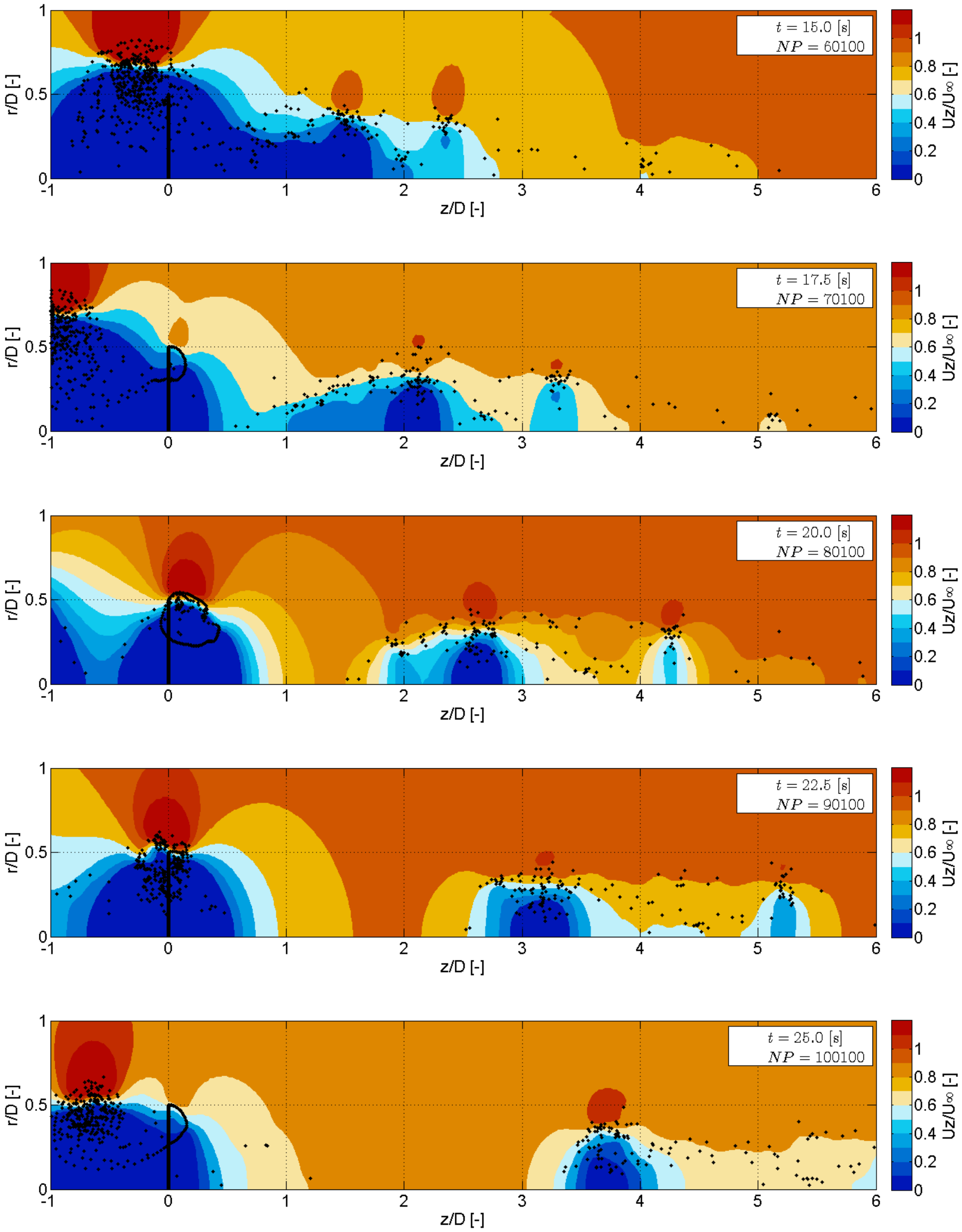

Figure F.8: *Continuation of figure F.7. Axial velocity. $C_t = 16/9$. NP stands for Number of Particles, of which 1 particle is shown per shed vortex ring (50 particles per ring).*

Appendix G

Results over Time for the MEXICO Rotor

In this section the results over time for a rotating turbine with prescribed circulation from the MEXICO experiment (Micallef et al. [22]) are presented, as discussed in section 6.5. The time evolution of the following five cases is demonstrated:

- Section G.1: classic stretching scheme applied.
- Section G.2: classic stretching scheme with PSE ($\nu = 0.0001[m^2 s^{-1}]$) applied.
- Section G.3: classic stretching scheme with PSE ($\nu = 0.0001[m^2 s^{-1}]$) and a smaller time step size ($\Delta t = 0.02[s]$) applied.
- Section G.4: transpose stretching scheme with PSE ($\nu = 0.0001[m^2 s^{-1}]$) applied.
- Section G.5: transpose stretching scheme with PSE ($\nu = 0.0001[m^2 s^{-1}]$) and divergence relaxation ($f = 0.1$) applied.

G.1 Results for the classic scheme

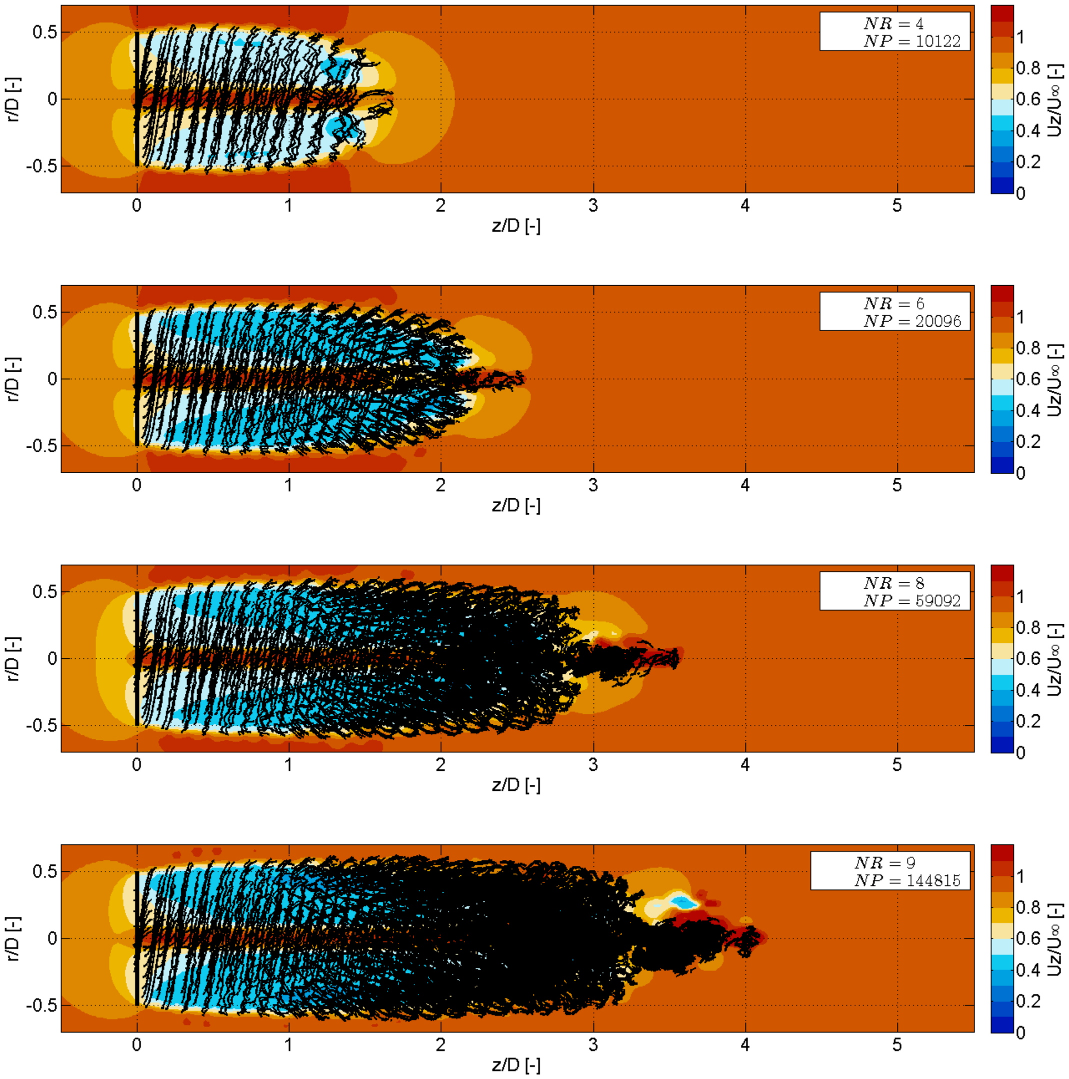

Figure G.1: *Filaments. Set-up: classic stretching scheme, $\Delta t = 0.05(s)$. NR and NP stand for Number of Rotations and Number of Particles respectively.*

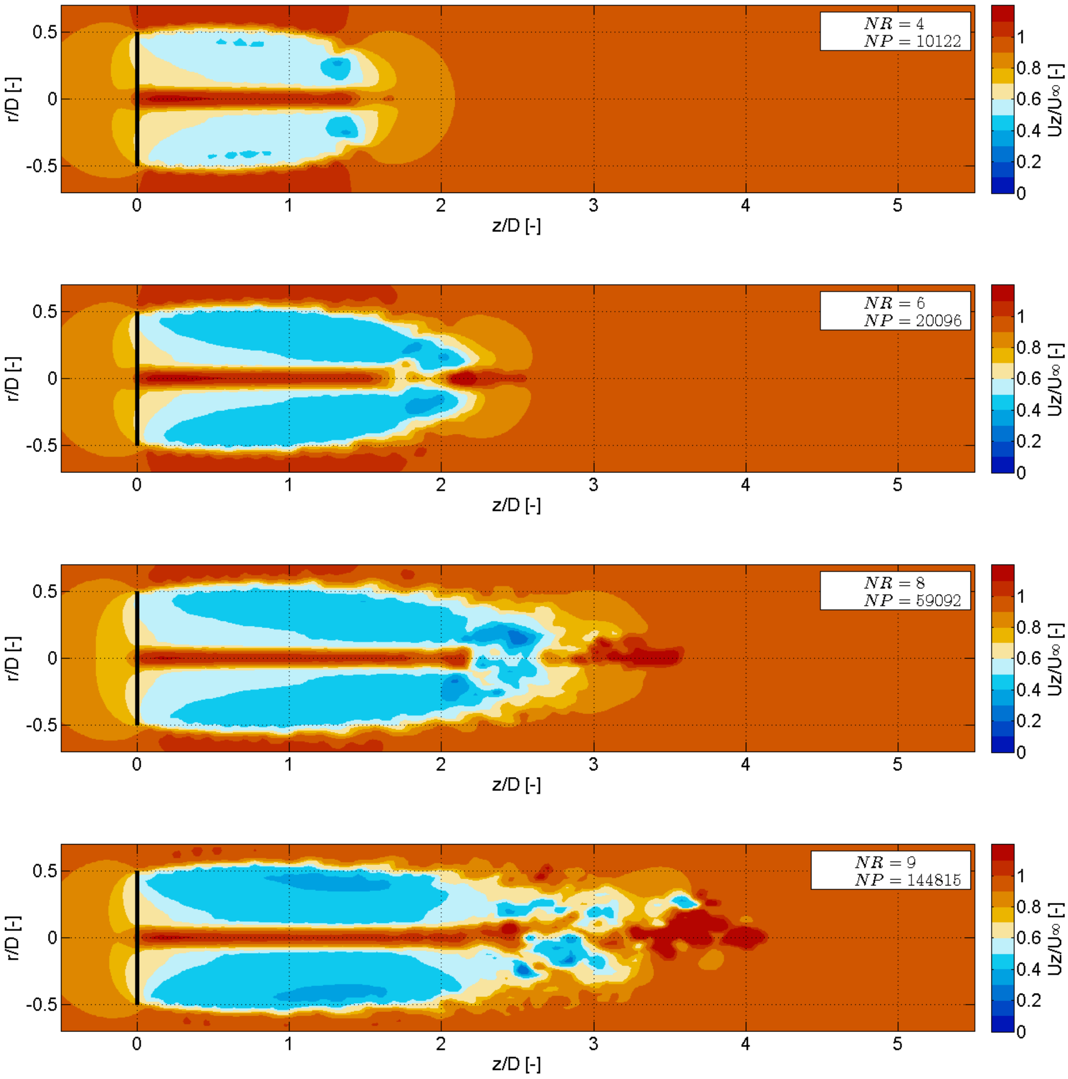

Figure G.2: *Axial velocity. Set-up: classic stretching scheme,* $\Delta t = 0.05(s)$*.* NR *and* NP *stand for Number of Rotations and Number of Particles respectively.*

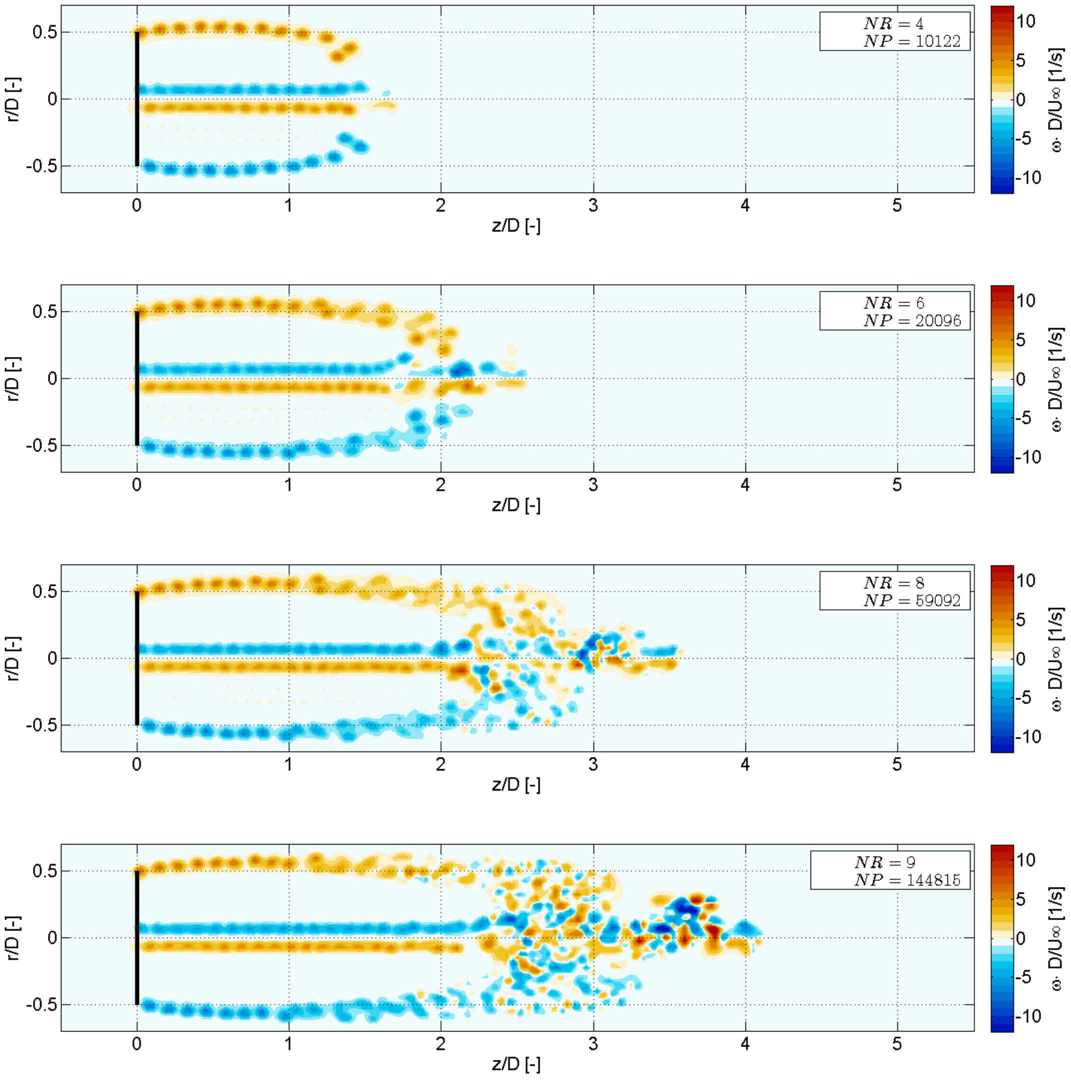

Figure G.3: *Vorticity. Set-up: classic stretching scheme,* $\Delta t = 0.05(s)$*.* NR *and* NP *stand for Number of Rotations and Number of Particles respectively.*

G.2 Results for the classic scheme with PSE applied

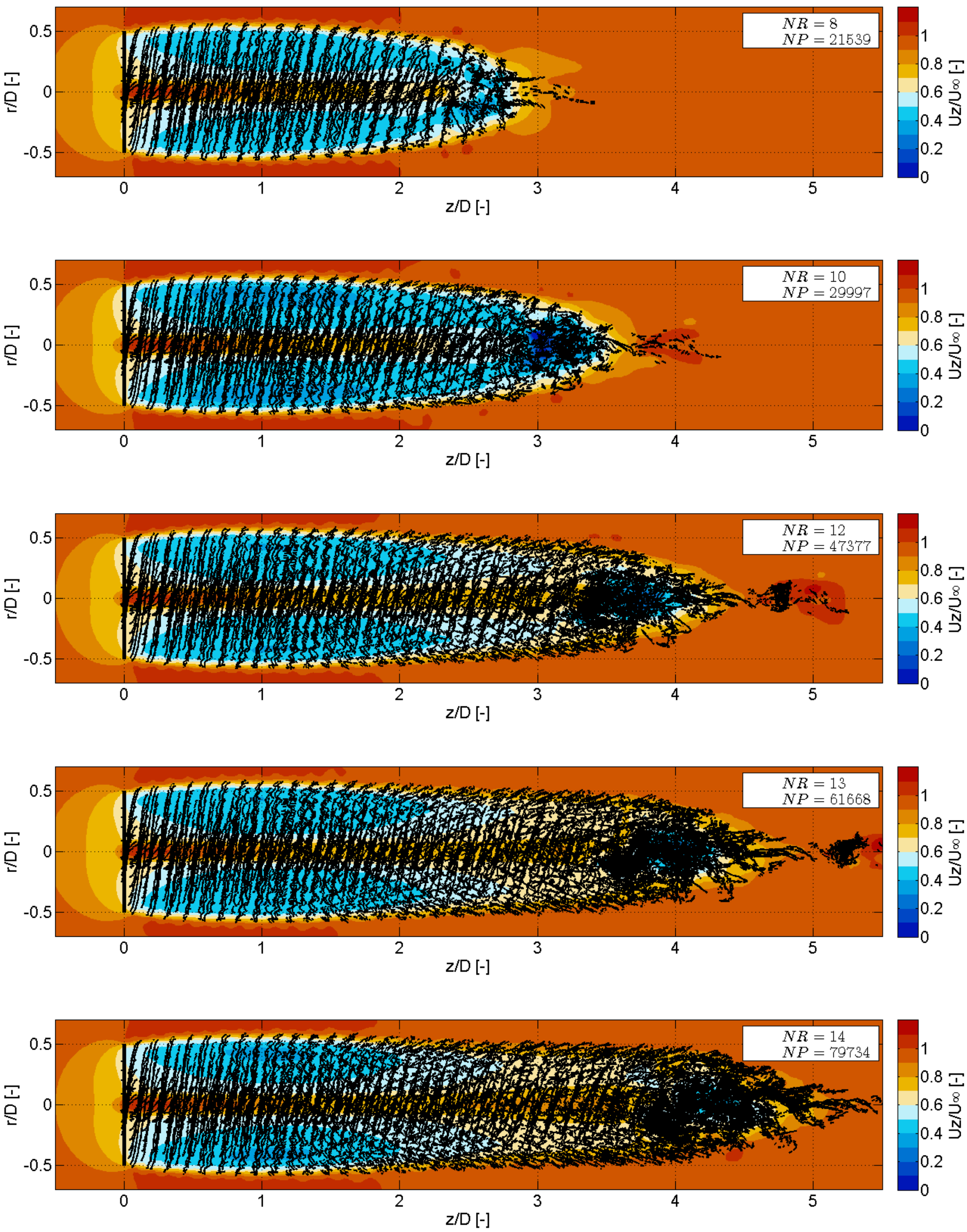

Figure G.4: *Filaments. Set-up: classic stretching scheme, $\Delta t = 0.05(s)$, $\nu = 0.0001[m^2/s]$. NR and NP stand for Number of Rotations and Number of Particles respectively.*

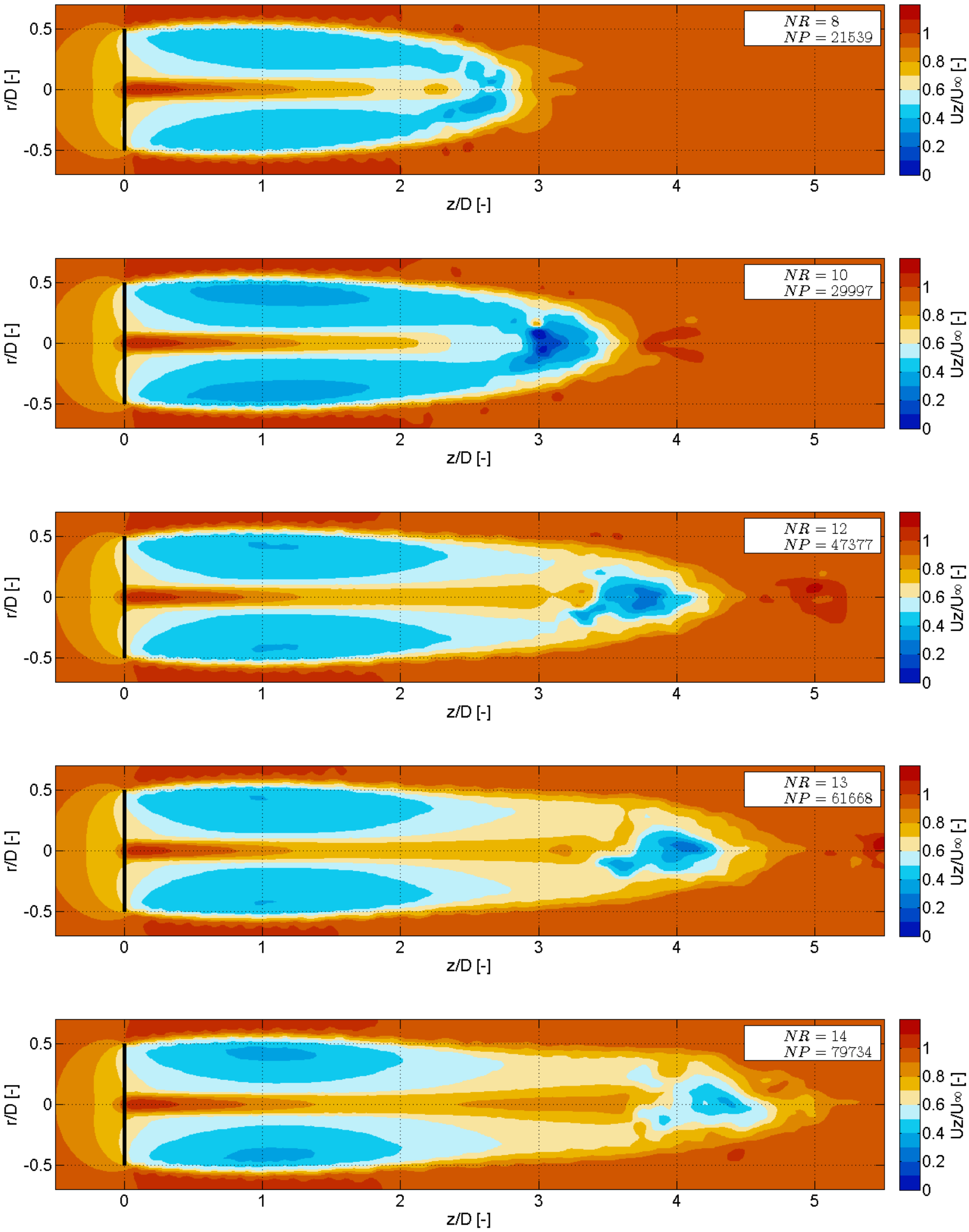

Figure G.5: *Axial velocity. Set-up: classic stretching scheme,* $\Delta t = 0.05(s)$, $\nu = 0.0001[m^2/s]$. NR *and* NP *stand for Number of Rotations and Number of Particles respectively.*

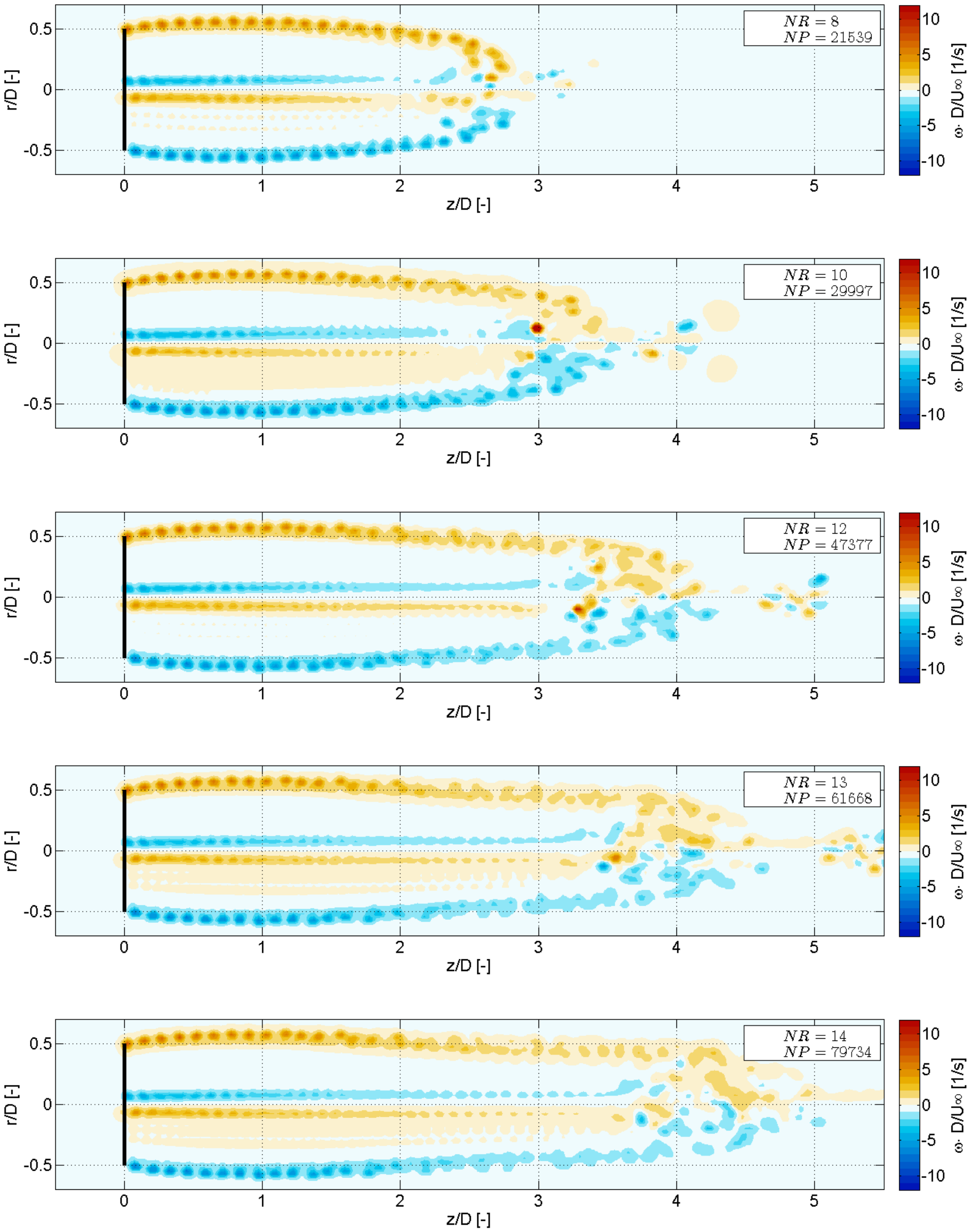

Figure G.6: *Vorticity. Set-up: classic stretching scheme, $\Delta t = 0.05(s)$, $\nu = 0.0001[m^2/s]$. NR and NP stand for Number of Rotations and Number of Particles respectively.*

G.3 Results for the classic scheme with the PSE scheme applied using a small time step size

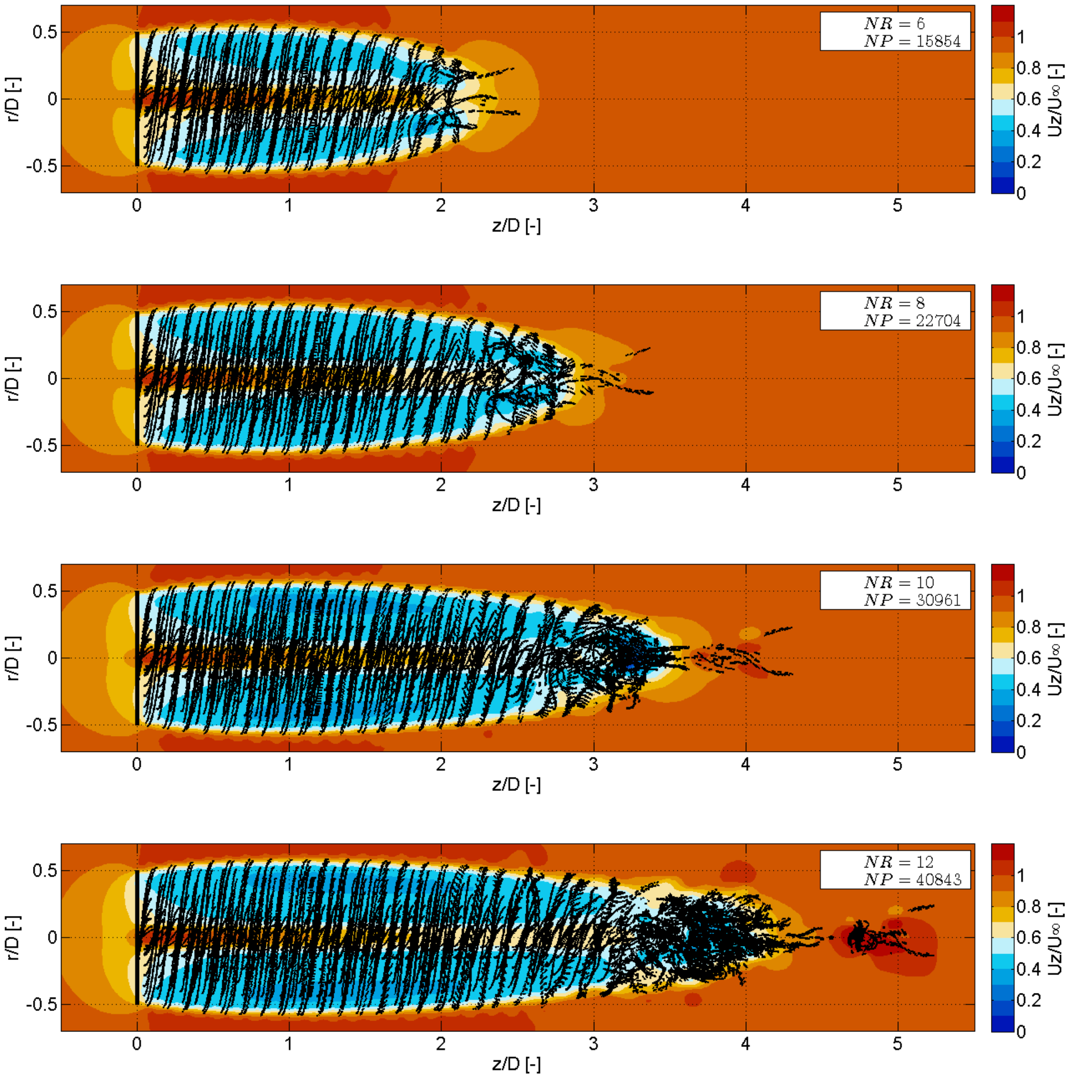

Figure G.7: *Filaments. Set-up: classic stretching scheme, $\Delta t = 0.02(s)$, $\nu = 0.0001[m^2/s]$. NR and NP stand for Number of Rotations and Number of Particles respectively.*

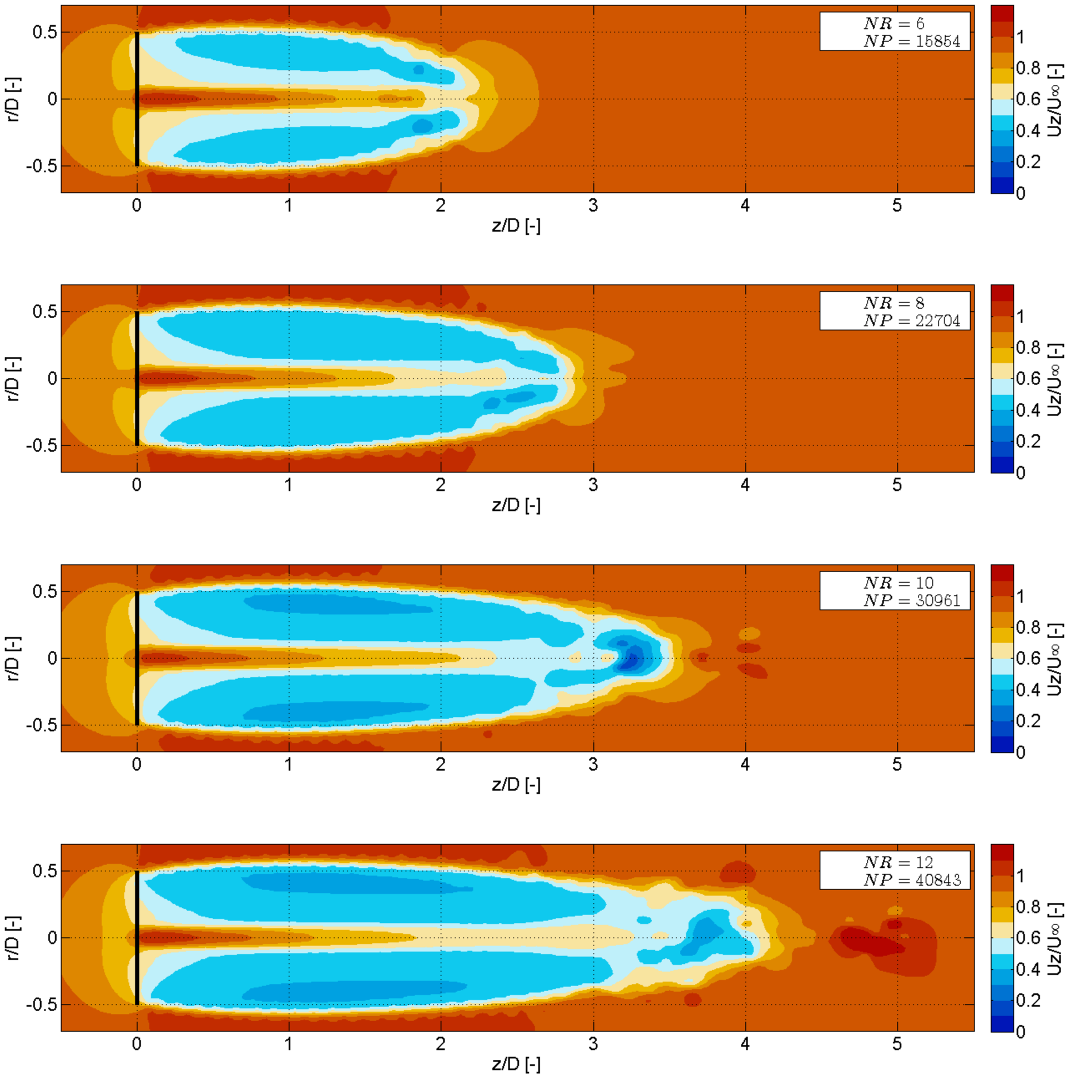

Figure G.8: *Axial velocity. Set-up: classic stretching scheme,* $\Delta t = 0.02(s)$, $\nu = 0.0001[m^2/s]$. NR *and* NP *stand for Number of Rotations and Number of Particles respectively.*

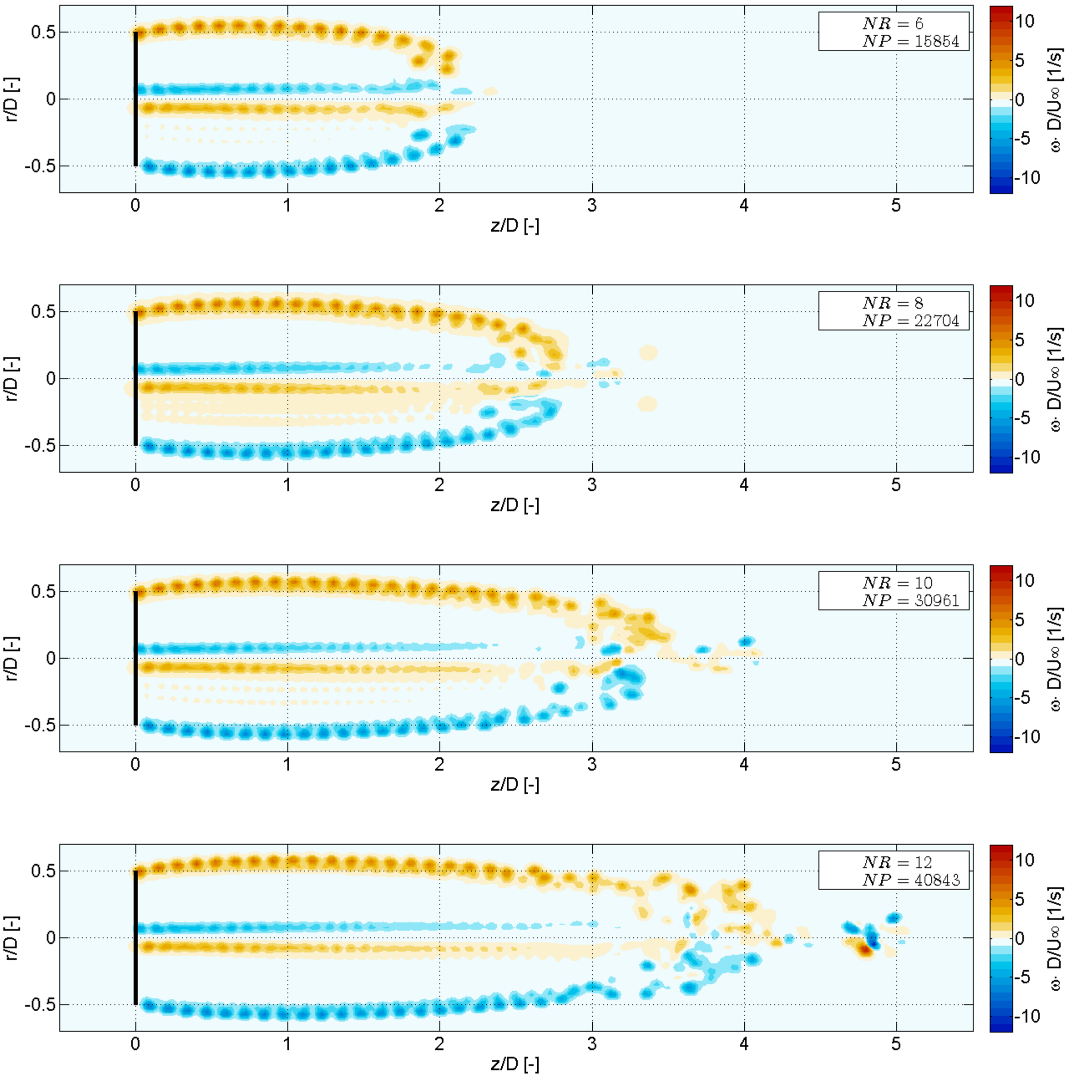

Figure G.9: *Vorticity. Set-up: classic stretching scheme,* $\Delta t = 0.02(s)$, $\nu = 0.0001[m^2/s]$. NR *and* NP *stand for Number of Rotations and Number of Particles respectively.*

G.4 Results for the transpose scheme with PSE applied

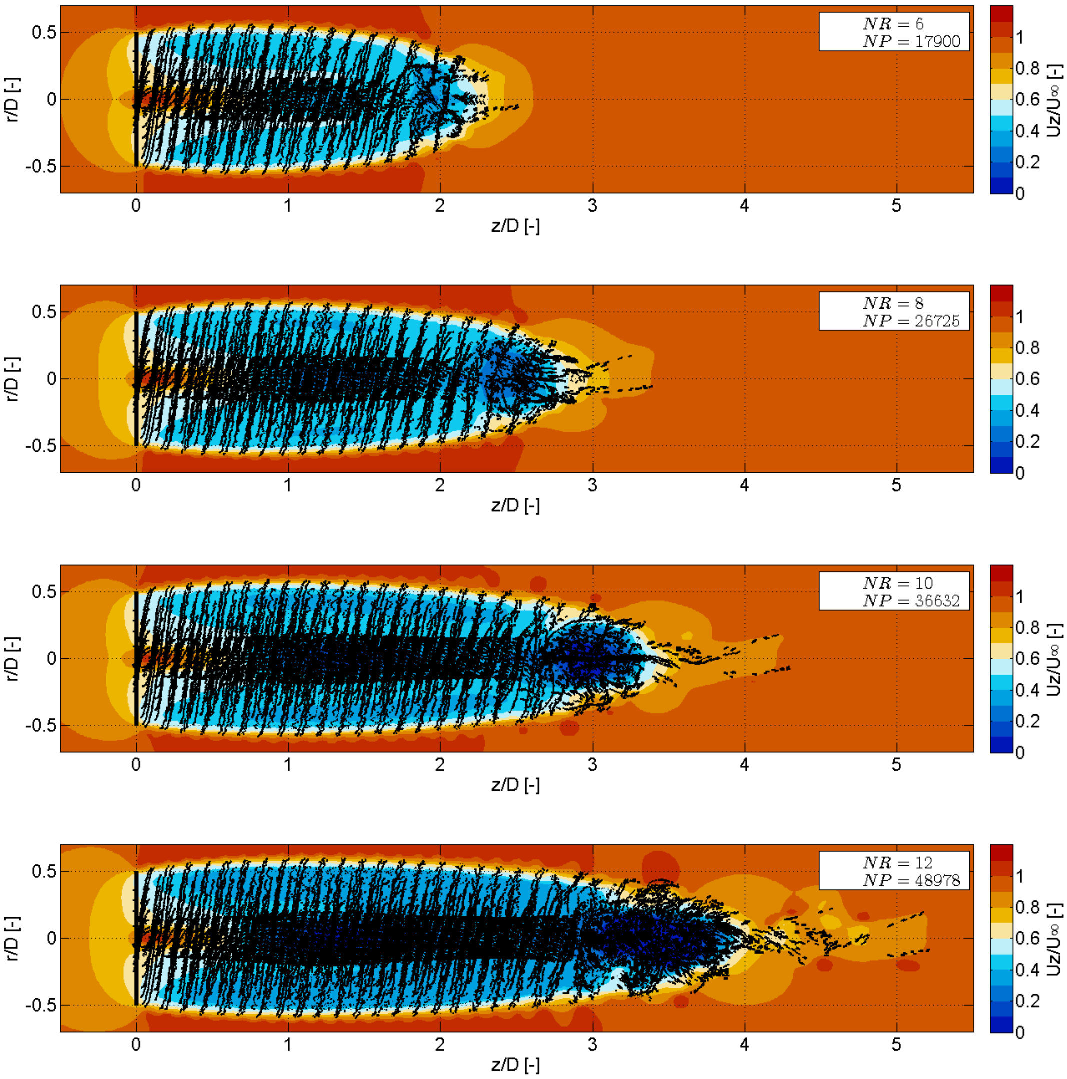

Figure G.10: *Filaments. Set-up: transpose stretching scheme,* $\Delta t = 0.05(s)$*,* $\nu = 0.0001[m^2/s]$*.* NR *and* NP *stand for Number of Rotations and Number of Particles respectively.*

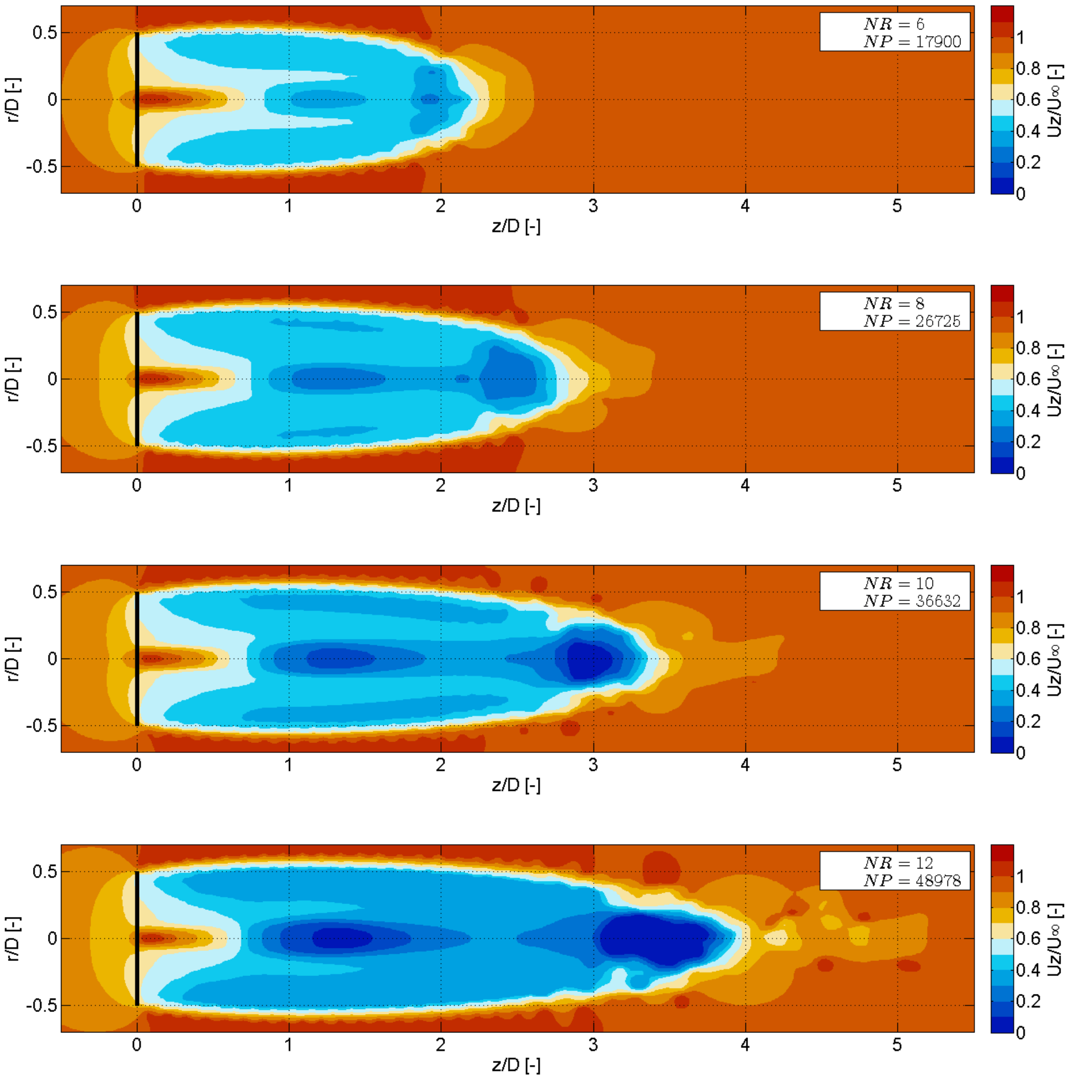

Figure G.11: *Axial velocity. Set-up: transpose stretching scheme,* $\Delta t = 0.05(s)$, $\nu = 0.0001[m^2/s]$. *NR and NP stand for Number of Rotations and Number of Particles respectively.*

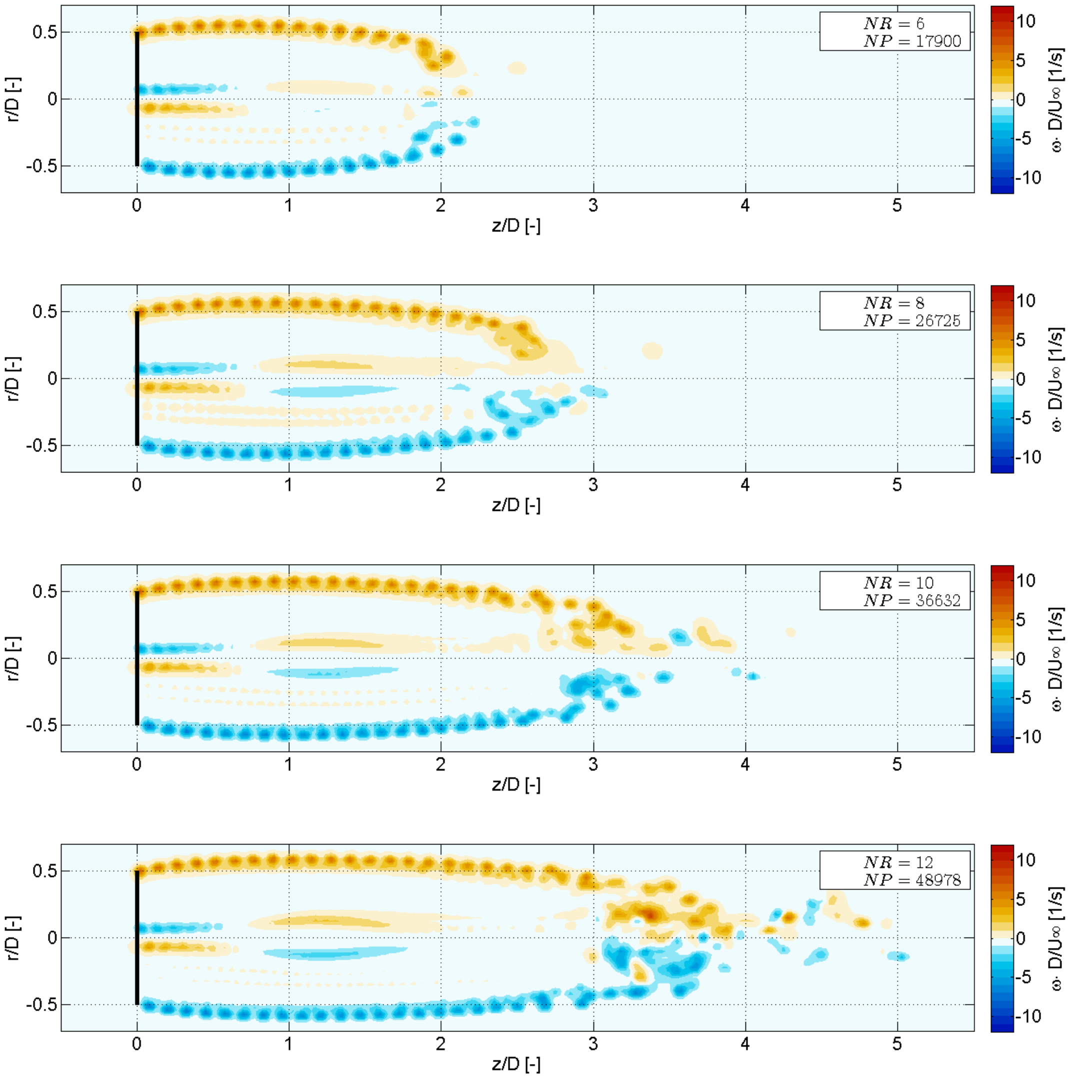

Figure G.12: *Vorticity. Set-up: transpose stretching scheme,* $\Delta t = 0.05(s)$, $\nu = 0.0001[m^2/s]$. *NR and NP stand for Number of Rotations and Number of Particles respectively.*

G.5 Results for the transpose scheme with relaxation and PSE applied

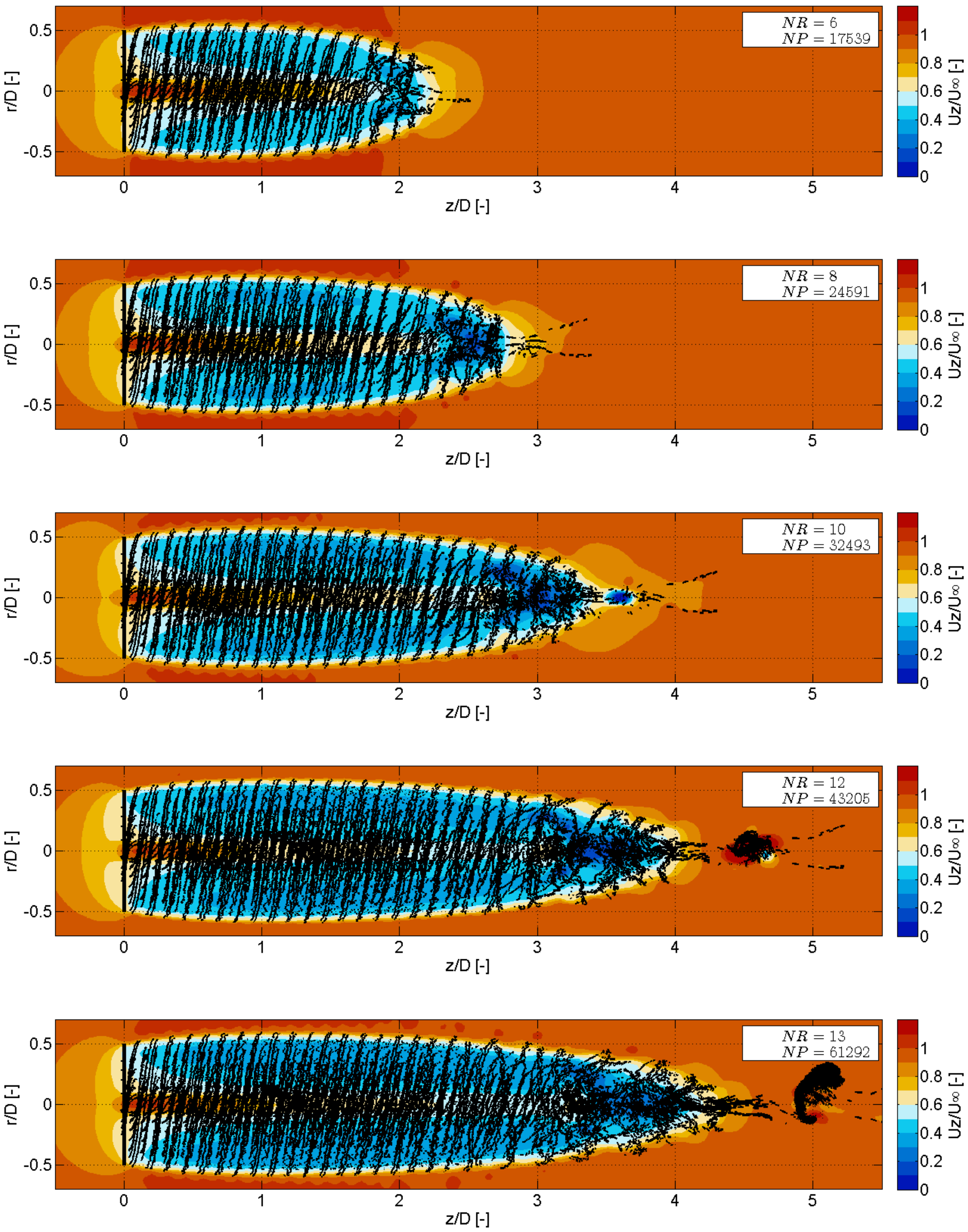

Figure G.13: *Filaments. Set-up: transpose stretching scheme, $f = 0.1$, $\Delta t = 0.05(s)$, $\nu = 0.0001[m^2/s]$. NR and NP stand for Number of Rotations and Number of Particles respectively.*

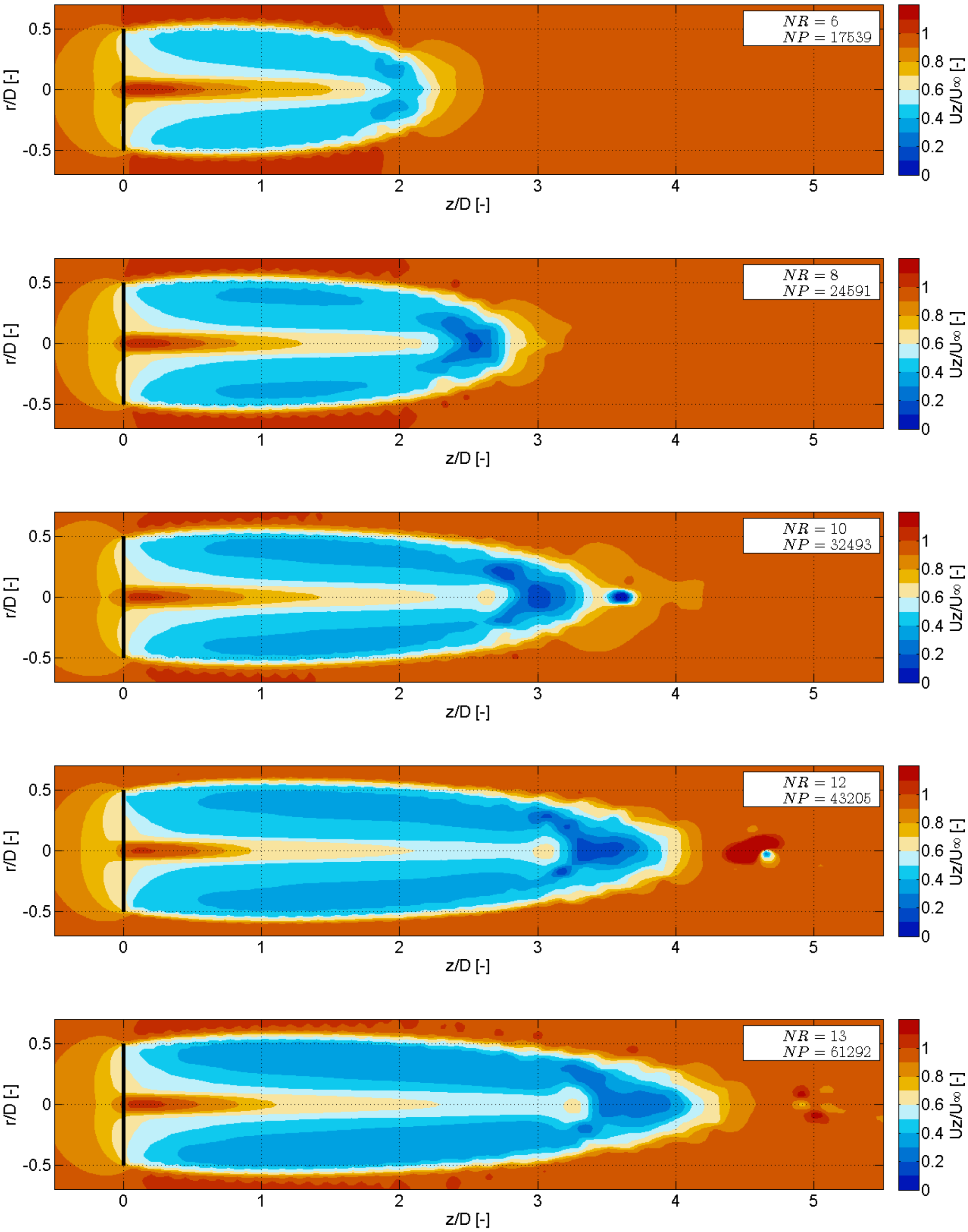

Figure G.14: *Axial velocity. Set-up: transpose stretching scheme,* $f = 0.1$, $\Delta t = 0.05(s)$, $\nu = 0.0001[m^2/s]$. *NR and NP stand for Number of Rotations and Number of Particles respectively.*

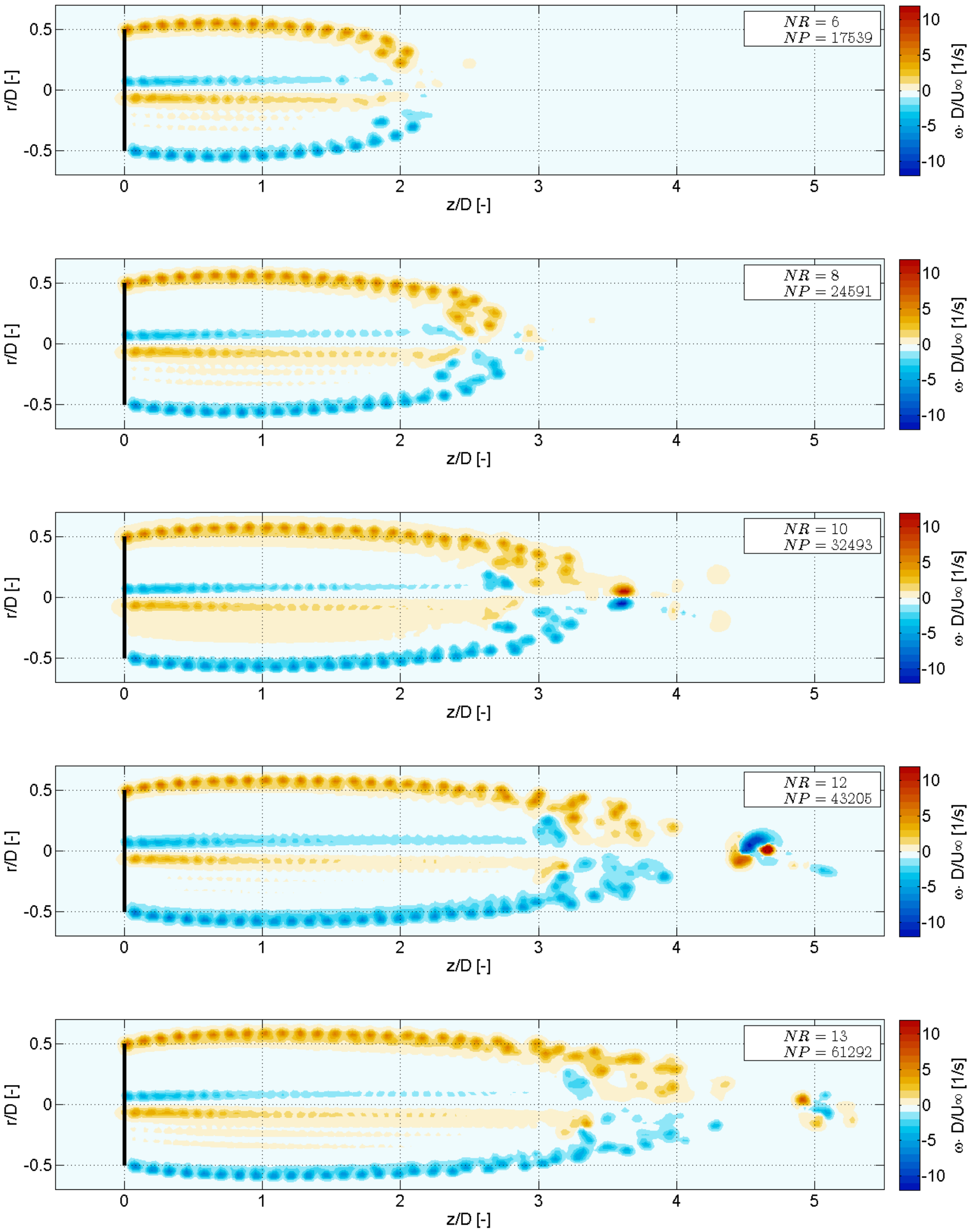

Figure G.15: *Vorticity. Set-up: transpose stretching scheme,* $f = 0.1$, $\Delta t = 0.05(s)$, $\nu = 0.0001[m^2/s]$. *NR and NP stand for Number of Rotations and Number of Particles respectively.*